Stellingen (*Propositions*)

behorende bij het proefschrift

Digital Testing of High-Voltage SF_6 Circuit Breakers

Pieter H. Schavemaker

Delft, 12 november 2002

1. Het digitaal testen van vermogenschakelaars kan het beproeven in het kortsluitlaboratorium niet vervangen, wel aanvullen.

   Digital testing of high-voltage circuit breakers can supplement but not replace the testing in the high-power laboratory.

2. Het is mogelijk om voor het eigenlijke afschakelmoment van de schakelaar al een gegronde uitspraak te doen over de kans op onderbreking.

   It is possible to make a well-founded statement on the chance of successful interruption of the breaker before the actual interruption moment takes place.

3. Een universeel toepasbaar schakelaarmodel met een beperkt aantal parameters bestaat niet.

   A universally applicable circuit breaker model with a limited number of parameters does not exist.

4. Om snelle én nauwkeurige boog-circuit-interactieberekeningen te maken, is een oplossingsmethode met een variabele stapgrootte noodzakelijk.

   In order to make both accurate and time-saving arc-circuit interaction computations, a numerical solver with a variable step size is necessary.

5. Het is onbegrijpelijk dat jongeren nog ingenieurswetenschappen gaan studeren in plaats van rechten, economie of iets dergelijks: je moet één jaar langer studeren, je gaat minder verdienen en uiteindelijk beland je allemaal toch achter een pc.

   It is incomprehensible that there are still young people who want to study engineering instead of law, economics, and such: you have to study an extra year, you will earn less and in the end all graduates end up behind a pc anyway.

6. De steeds verdergaande individualisering van de lasten van de burger in Nederland zal er toe leiden dat straks ook het broodje bij de bakker inkomensafhankelijk is.

The ever-increasing individualization of the costs of Dutch citizens will result in a situation where even the bread at the bakery is income dependent.

7. Kinderopvang is niet duur. Ontslag nemen of je arbeidsduur verkorten en zelf voor de kinderen zorgen, dat is pas duur!

   Day care is not expensive. Quitting your job or reducing your working hours in order to take care of your children yourself, that is expensive!

8. Crèches zijn primair bedoeld om ouders aan het werk te houden; het belang van het kind is ondergeschikt.

   Day care centres are primarily intended to keep the parents working; the child's interests are subsidiary.

9. Vakbonden behartigen alleen hun eigen 'achterban'. Wie niet betaalt, heeft geen inspraak in de eigen arbeidsomstandigheden.

   Labor unions represent only their own 'members'. Those who do not pay do not have a say in their own conditions of employment.

10. Het tekort aan huisartsen kan direct worden opgelost door voor iedereen een eigen risico van €500 in te voeren.

    The shortage in family doctors can be solved immediately by introducing an excess amount of €500 for everyone.

Digital Testing of High-Voltage SF_6 Circuit Breakers

PROEFSCHRIFT

ter verkrijging van de graad van doctor
aan de Technische Universiteit Delft,
op gezag van de Rector Magnificus prof. dr. ir. J.T. Fokkema,
voorzitter van het College voor Promoties,
in het openbaar te verdedigen op dinsdag 12 november 2002 om 16.00 uur
door

Petrus Hendrikus SCHAVEMAKER
elektrotechnisch ingenieur
geboren te Velsen.

Dit proefschrift is goedgekeurd door de promotor:
Prof. ir. L. van der Sluis

Samenstelling promotiecommissie:
Rector Magnificus, voorzitter
Prof. ir. L. van der Sluis, Technische Universiteit Delft, promotor
Prof. ir. W.L. Kling, Technische Universiteit Delft/Eindhoven, Tennet
Prof. dr. J.J. Smit, Technische Universiteit Delft
Prof. dr. ir. R.P.P. Smeets, Technische Universiteit Eindhoven, KEMA
Prof. ir. G.C. Damstra, Technische Universiteit Eindhoven
Prof. dr. W.R. Rutgers, Technische Universiteit Eindhoven, KEMA
Prof. dr. V. Kertész, Technical University of Budapest, KEMA
Prof. dr. ir. J.A. Ferreira, Technische Universiteit Delft, reservelid

Printed by:
Ridderprint Offsetdrukkerij B.V.
Ridderkerk, the Netherlands.

ISBN 90-9016125-2

In memory of Theo Schavemaker
To Saskia, Olov and Annika

Summary

High-voltage circuit breakers play an important role in transmission and distribution systems. They must clear faults and isolate faulted sections rapidly and reliably. Apart from power electronic devices, the only physical mechanism that can change in a short period of time from a conducting to an insulating state at a certain voltage is the plasma arc. It is this principle on which all circuit breakers are based.

The breaker's capabilities must be tested in the high-power laboratory. In the laboratory, a test circuit is set up that matches the real network as closely as possible to establish the correct arc-circuit interaction. Yet, these tests are rather cost intensive and only demonstrate whether or not a circuit breaker interrupts. Therefore, computational techniques can be applied to extend the information obtained during the tests. Thus 'digital testing' of circuit breakers is introduced.

All computations and results presented in this thesis are based on actual measurements that have been performed on various circuit breaker types of different manufacturers. These measurements have been executed within the framework of an international consortium with the aim to realize 'digital testing of high-voltage circuit breakers'. Four commercially available SF_6 circuit breakers have been subjected to Short Line Fault (SLF) tests in the KEMA High-Power Laboratory in the Netherlands. SLF testing has been applied as this is one of the most severe faults for a circuit breaker to interrupt.

'Digital testing' as described in this thesis can take three forms.

Firstly, the measured data can be analyzed directly. Several indicators are presented that give information about the circuit breaker interruption performance. Analysis of the frequency contents of the measured voltages makes it clear that it is valid to model the test circuit by means of lumped circuit elements.

Secondly, the laboratory data can be enhanced by the application of arc models. A new Mayr-type arc model is introduced that shows good correspondence between the measured and computed current and voltage traces. Furthermore, the arc model shows an overall performance of 90%. That means that only in one out of ten cases an interruption is observed during the mea-

surements for which the arc model shows a reignition, or vice versa. By means of arc models, the failure probability, the quality of interruption and the critical line length are determined.

Thirdly, additional information can be extracted from the measurements by means of the voltage injection method. In the lumped-element representation of the laboratory test circuit the circuit breaker is modeled by means of a voltage source that injects the measured voltage across the circuit breaker into the network. This method has been applied successfully for an indirect verification of the current zero measurement system of KEMA. Moreover, the quality of interruption is computed, the severity of various artificial lines is compared and the arc-circuit interaction in SLF test circuits is studied.

Three different programs that can be used for arc-circuit interaction studies have been compared, namely EMTP96 v3.0, XTrans and MATLAB Simulink/Power System Blockset in combination with the Arc Model Blockset (developed by the author). Programs with a fixed step-size solver, such as the EMTP96, are less suitable for detailed arc-circuit interaction studies than programs with variable step-size solvers, such as XTrans and MATLAB Simulink/Power System Blockset.

Samenvatting

Vermogenschakelaars spelen een belangrijke rol in transmissie- en distributienetten. Ze hebben als taak foutstromen te onderbreken en gestoorde netdelen op een snelle en betrouwbare manier af te schakelen. Als we de vermogenselektronische halfgeleiders buiten beschouwing laten, is de (licht)boog het enige fysische mechanisme dat bij hoge drijvende spanning snel van een geleidende naar isolerende toestand kan overgaan. Op dit principe zijn dan ook alle vermogenschakelaars gebaseerd.

Vanwege de complexe fysische processen die bij het afschakelen van hoge vermogens komen kijken, moet de juiste werking van nieuw ontwikkelde prototypes geverifieerd worden middels beproevingen in het kortsluitlaboratorium. In het laboratorium wordt een testcircuit opgebouwd dat zo goed mogelijk overeenkomt met het echte net om de juiste boog-circuit-interactie te bewerkstelligen. Deze beproevingen zijn vrij kostbaar en geven alleen aan of de schakelaar heeft onderbroken of niet. Rekentechnieken kunnen toegepast worden om zoveel mogelijk informatie uit deze beproevingen te halen; hiermee introduceren we het 'digitaal testen' van vermogenschakelaars.

Alle berekeningen en resultaten die gepresenteerd worden in dit proefschrift zijn gebaseerd op metingen die zijn verricht aan verschillende typen schakelaars van verscheidene fabrikanten. De metingen zijn verricht in het kader van een internationaal consortium, met als doel het 'digitaal testen van vermogenschakelaars' te bewerkstelligen. Vier commercieel verkrijgbare SF_6 vermogenschakelaars zijn onderworpen aan kortelijnfout (SLF) beproevingen in het KEMA kortsluitlaboratorium te Arnhem; het onderbreken van deze fout is (thermisch) het zwaarst voor de schakelaar.

Het 'digitaal testen' zoals beschreven in dit proefschrift kan worden onderverdeeld in drie categorieen.

Het direct analyseren van de meetdata is de eerste, en meest voor de hand liggende, aanpak om extra kennis te verkrijgen. Verscheidene indicatoren worden geïntroduceerd die informatie verschaffen over de onderbrekingsprestatie van de schakelaar. Analyse van de frequentie-inhoud van de gemeten spanningen toont aan dat het toegestaan is om de testcircuits met behulp van geconcentreerde elementen te modelleren.

Het toepassen van boogmodellen is de tweede methode om aanvullende gegevens uit de metingen te verkrijgen. Een nieuw Mayr-type boogmodel wordt beschreven, dat goede overeenkomsten laat zien tussen de gemeten en berekende stroom- en spanningscurves. Het boogmodel geeft in 90% van de onderbrekingspogingen het juiste resultaat van de beproeving: onderbreking of herontsteking. Met behulp van boogmodellen worden de faalkans, de onderbrekingsprestatie en de kritieke lijnlengte van de schakelaar berekend.

De derde methodiek om extra informatie uit de meetdata te verwerven is het toepassen van de spanningsinjectiemethode. In de afbeelding van het testcircuit, dat is opgebouwd uit geconcentreerde elementen, wordt de vermogenschakelaar gemodelleerd als een spanningsbron die de gemeten spanning over de schakelaar in het netwerk injecteert. Deze aanpak is toegepast voor een indirecte verificatie van het current zero meetsysteem van KEMA. Bovendien is de onderbrekingsprestatie van de schakelaar berekend, zijn een aantal kunstlijnen vergeleken en is de boog-circuit interactie in SLF-circuits bestudeerd.

Drie verschillende programma's die toegepast kunnen worden voor boog-circuit-interactieberekeningen zijn onderling vergeleken: EMTP96 v3.0, XTrans en MATLAB Simulink/Power System Blockset in combinatie met de Arc Model Blockset (ontwikkeld door de auteur). Programma's die gebruik maken van een numerieke oplossingsmethode met een vaste stapgrootte, zoals het EMTP96, zijn minder geschikt voor gedetailleerde boog-circuit-interactieberekeningen dan programma's waarbij de stapgrootte variabel is, zoals XTrans en MATLAB Simulink/Power System Blockset.

Preface

High-voltage SF_6 circuit breakers are the key protective devices in transmission and distribution systems. They must clear faults and isolate faulted sections rapidly and reliably. The capabilities of the circuit breaker prototypes must be verified by practical tests in the high-power laboratory.

Due to the power and physical size of the equipment that is required and the fact that the tests are destructive for the test object, testing is rather expensive and time consuming. In order to obtain as much information of the circuit breaker as possible from the cost intensive tests, the following partners initiated a project: KEMA High-Power Laboratory (NL), Delft University of Technology (NL), Siemens AG (G), RWE Energie (G) and Laborelec cv (B). This project was sponsored by the Directorate General XII of the European Commission in Standards, Measurements and Testing Program under contract no. SMT4-CT96-2121.

This thesis is based on the work carried out by the author within the framework of the international consortium with the aim to realize 'digital testing of high-voltage circuit breakers'. Based on refined voltage and current measurements, computational techniques are developed and applied, named 'digital testing', to extend the information obtained during the tests in the high-power laboratory.

Voorhout, the Netherlands *P.H. Schavemaker*

November 2002

Table of Contents

Chapter 1

Introduction

1.1 High-voltage circuit breakers

A circuit breaker is a switching device which the ANSI (American National Standards Institute) [2] defines as: 'A mechanical switching device, capable of making, carrying and breaking currents under normal circuit conditions and also, making, carrying for a specified time and breaking currents under specified abnormal circuit conditions such as those of short circuit'. It adds, as a note: 'A circuit breaker is usually intended to operate infrequently, although some types are suitable for frequent operation'.

High-voltage circuit breakers play an important role in transmission and distribution systems. They must clear faults and isolate faulted sections rapidly and reliably. In short, they must possess the following qualities:

- In closed position, they are good conductors.
- In open position, they are excellent insulators.
- They can close a shorted circuit quickly and safely without unacceptable contact erosion.
- They can interrupt a rated short-circuit current, or lower current, quickly without generating an abnormal voltage.

Apart from power electronic devices, the only physical mechanism that can change in a short period of time from a conducting to an insulating state at a certain voltage is the plasma arc. It is this principle on which all circuit breakers are based.

The first circuit breaker was developed by J.N. Kelman in 1901. It was the predecessor of the oil circuit breaker and capable of interrupting a short-circuit current of 200 to 300 A in a 40 kV

system. The circuit breaker was made up of two wooden barrels containing a mixture of oil and water, in which the contacts were immersed. Since then, circuit breaker design has undergone a remarkable development. In 1996, successful development of an 1100 kV, 50 kA rated gas-insulated switchgear was reported [104].

SF_6 puffer circuit breakers and SF_6 self-blast (or self-compression) circuit breakers are the most frequently applied breakers in today's power systems. They are becoming the leading equipment in switchgear from the distribution voltage to the transmission (ultra-high) voltage level. The main difference between these two breaker types is that in puffer breakers, the mechanical energy provided by the operating mechanism is used to compress the gas, while self-blast (or self-compression) breakers use the heat energy produced by the arc to raise the gas pressure. The operating principle of a puffer circuit breaker is shown in figure 1-1. The physical layout of an interrupter chamber of a double-nozzle puffer circuit breaker and its working principle is shown in figure 1-2.

1.2 Testing in the high-power laboratory

In high-power laboratories the functionality of high-voltage circuit breakers is tested in test circuits which are in fact lumped-element representations of the power system. In the high-power laboratory, various types of circuit breaker tests are carried out, such as:

- Development tests: usually performed by the manufacturer, in order to improve the prototype.
- Acceptance tests: performed by a testing facility and commisioned by the user, in order to test a circuit breaker according to his instructions.
- Type tests: performed by an independent certified testing facility, in order to verify whether the manufacturer's final circuit breaker design meets the demands as prescribed in the international standards.

Type tests of circuit breakers include [32]:

- mechanical and environmental tests, including mechanical operation test at ambient air temperature, low- and high-temperature tests, humidity test, test to prove operation under severe ice conditions and static terminal load test
- short-circuit current making and breaking tests including terminal fault tests, short line fault test, and also out-of-phase test
- capacitive current switching tests, including line-charging, cable-charging, single capacitor bank and back-to-back capacitor bank tests
- magnetizing and small inductive current switching tests

Except for the mechanical and environmental tests, all the tests in the IEC-62271-100 type test requirements are designed to prove the interrupting ability of circuit breakers.

There are two types of high-power laboratories. One is the network (grid) testing station and the other the specially built short-circuit generator testing station. A network testing station is built in the power system network and uses the grid to provide the short-circuit power directly. Low costs together with easy operation and maintenance are its main advantages. The disad-

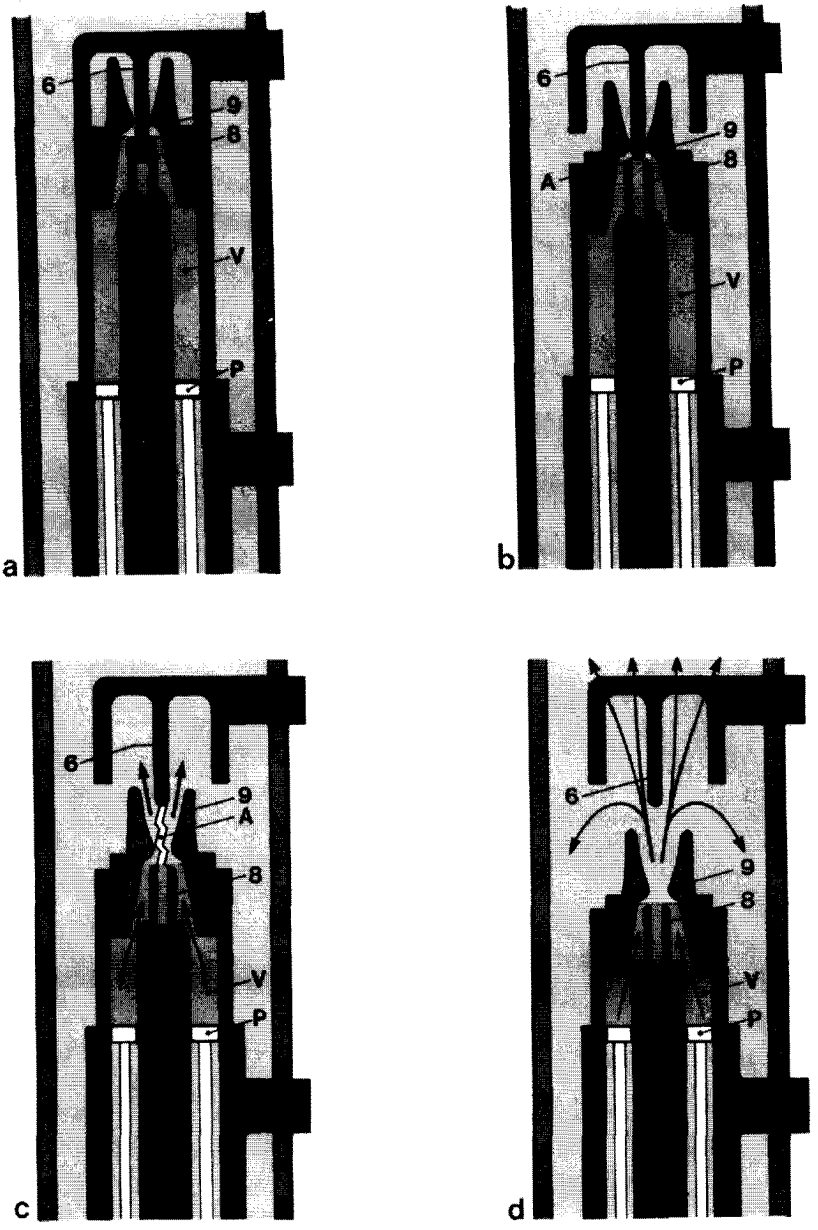

Figure 1-1. Puffer circuit-breaker operating principle [21]
(a) breaker closed, (b) start of opening, main contacts separate,
(c) arcing contacts separating, gas flow starts, (d) interruption completed.
A = arc, V = puffer volume, P = puffer piston, 6 & 8 = arcing contacts, 9 = interrupter nozzle.

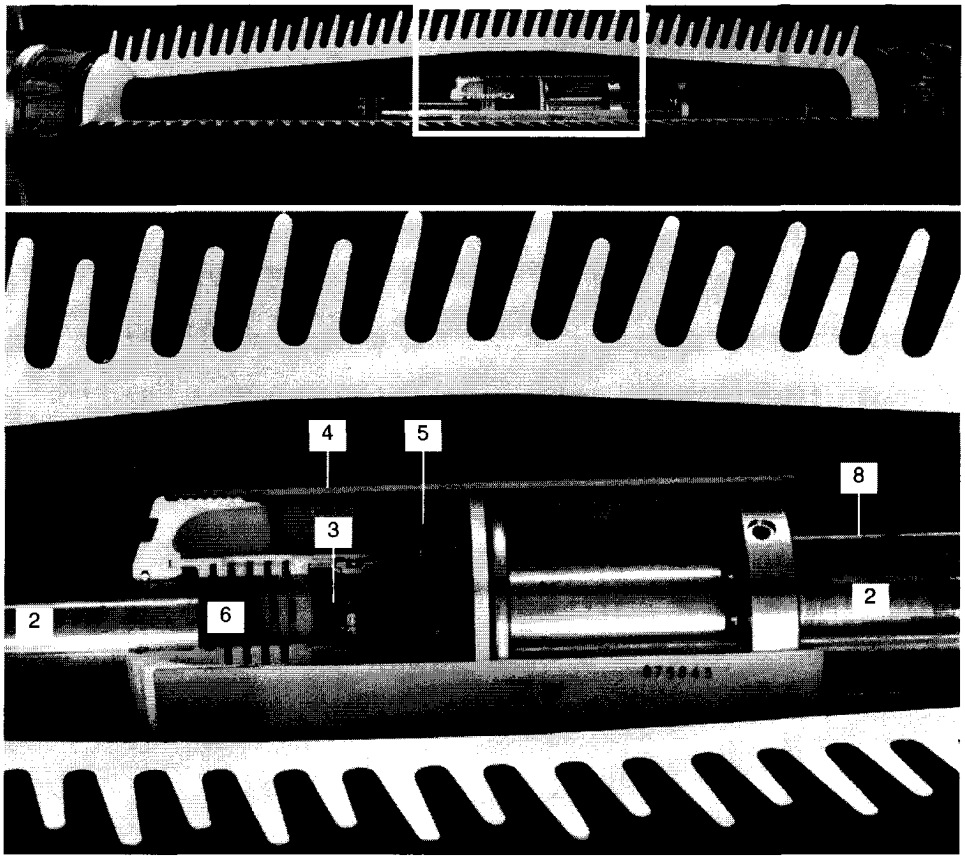

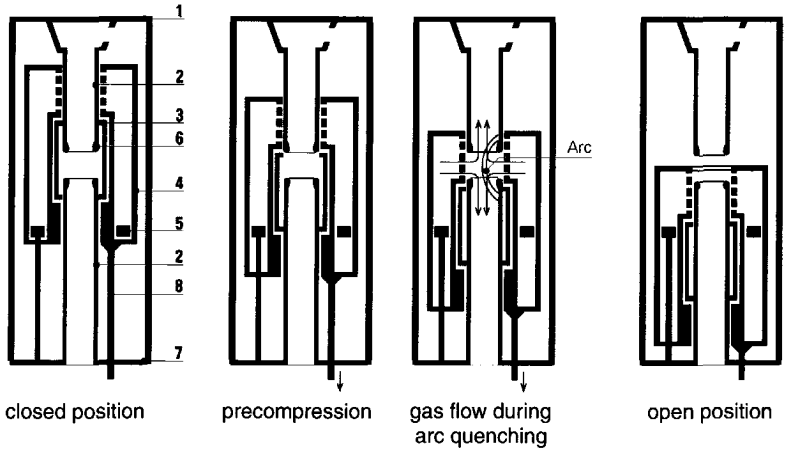

Figure 1-2. Physical layout and working principle of a double-nozzle puffer circuit breaker
1 - upper terminal plate, 2 - fixed tubes, 3 - moving contact tube, 4 - blast cylinder
5 - blast piston, 6 - arc quenching nozzles, 7 - lower terminal plate, 8 - operating rod

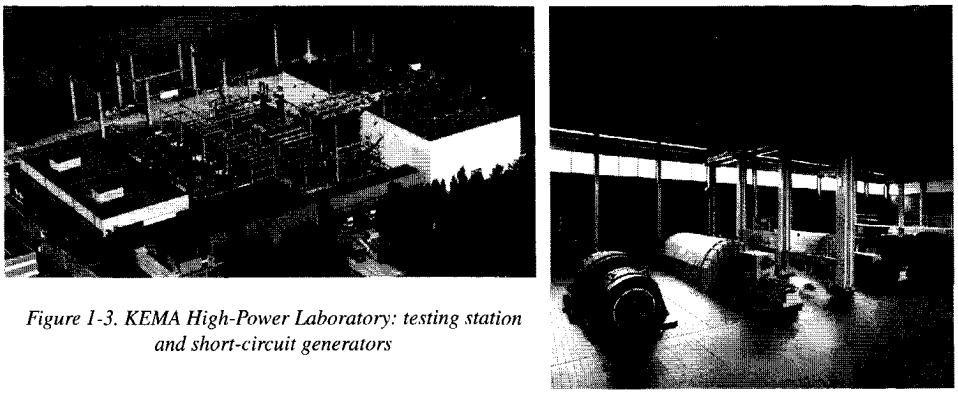

Figure 1-3. KEMA High-Power Laboratory: testing station and short-circuit generators

vantage of this kind of station is that the maximum test power is limited by the system capacity and stability. A generator testing station uses its own short-circuit generators to supply the testing power. Therefore, the grid power required by this type of station is rather low. Another advantage offered by this kind of station is the possibility to increase the testing capability by adding new short-circuit generators in parallel. The KEMA High-Power Laboratory is the largest testing station using short-circuit generators. The maximum direct testing power of the KEMA High-Power Laboratory in the test bay is 8400 MVA, delivered by four generators in parallel (figure 1-3).

As over the years the interrupting capability of the circuit breaker units has increased rapidly, the power available for direct tests was soon surpassed. Even the 8400 MVA installed at KEMA is only adequate to do direct three-phase testing of a 145 kV, 31.5 kA circuit breaker.

The synthetic testing method has been developed to overcome the problem of insufficient direct test power. In the synthetic testing method all of the current, or a major portion of it, is obtained from one source (current circuit), and the applied voltage and/or the recovery voltages (transient and power-frequency) are obtained wholly or in part from one or more separate sources (voltage circuits) [33]. When synthetic testing is applied, the KEMA High-Power Laboratory is able to do three-phase testing up to 245 kV, 63 kA or single-phase testing up to 550 kV, 100 kA [13,98].

1.3 Background and objective

The tests in a high-power laboratory are rather cost intensive and only demonstrate whether or not a circuit breaker interrupts. In this thesis computational techniques are described to extend the information obtained during the tests. Thus 'digital testing' of circuit breakers is introduced.

The thesis is based on the work carried out by the author within the framework of an international consortium with the aim to realize 'digital testing of high-voltage circuit breakers' [72,75,84]. This consortium had the following partners: KEMA High-Power Laboratory (NL), Delft University of Technology (NL), Siemens AG (G), RWE Energie (G) and Laborelec cv (B). The project was sponsored by Directorate General XII of the European Commission in the Standards, Measurements and Testing programme under contract no. SMT4-CT96-2121. The objective of the project as described in the 'Project proposal for financial support from the EC

for the community activities in the field of Research and Technological Development' is given hereunder.

In high-power / high-voltage laboratories components and installations for the supply of electrical energy are tested in order to verify their correct functioning under all conceivable circumstances. One of the key components in high-voltage electricity supply systems is the power circuit breaker, that has to interrupt short-circuit current arising as a result of a fault in such a system. In high-power laboratories, the ability to interrupt short-circuit currents is tested in test circuits, that are simulations of real high-voltage networks. These test circuits have the function to produce the correct waveforms for (short-circuit) current as well for the voltage that strikes the circuit breaker immediately after the breaker has interrupted the test current. The waveforms of current and voltage to which the test-object is subjected, have been laid down in standards, such as IEC-62271-100. These standardized waveforms are designed to be representative for the vast majority of the possible fault conditions in real power networks.

The objective of the project is to develop 'digital testing' of high-voltage power circuit breakers, i.e. a software product for testing of a model of such a device, once its characteristic 'fingerprints' are obtained from refined measurements during standard tests. (...)

The stages, that will ultimately lead to the objective are threefold:

- ***Introduction of measuring methods in the high-power laboratory with high resolution of relevant circuit breaker signals.***
  The transformation from analogue into digital acquisition of data from such tests, a stage through which the leading test-laboratories have been passing through in recent years, gives the opportunity to extract information from the test results that goes far beyond the classical oscillograms of the analogue era. With suitable measuring techniques, specific information can be gathered during the periods in which the circuit breaker experiences its maximum stress. Standard measuring techniques aimed to verify the functioning of the device, are not able to give insight in the very fast phenomena that accompany current interruption. Novel measuring techniques have to be developed that meet very stringent requirements regarding dynamic range, bandwidth and interference-free operation.
- ***Testing of the methods and the extraction of relevant parameters for characterization of the circuit breaker's interruption behavior in the test circuit.***
  Using digital signal processing techniques, that account for the non-linearity of the measuring transducers, specific parameters of the circuit breaker can be obtained with the aid of the instruments described above. These parameters characterize the circuit breaker with respect to its interrupting capability in the test circuit.
- ***The integration of the circuit breaker in a digital model of the circuit breaker and combination of this model with a circuit model.***
  These parameters will be integrated in arc-circuit interaction models so that predictions can be made of the (tested) circuit breaker's behavior in other circuits than the circuit in which the interrupter was actually tested. For this, existing models of arc-circuit interaction will be used as a starting point. The complicated physical processes that are involved in current interruption will be implemented in an engineering model for arc-circuit interaction.

After having reached the objective, 'digital testing' offers a wide range of new possibilities for users, manufacturers, standardizing bodies and test-laboratories for fine tuning of circuit breaker abilities, standards and real networks. These are summarized as follows:

- *Evaluation of the relevance of future standards with respect to realistic power networks*
- *Evaluation of the relevance of future standards for different circuit breaker technologies*
- *Estimation of the circuit breaker's limitations*
- *Reduction of testing in high-power laboratories*
- *Identification of network configurations that pose special difficulties to a circuit breaker*
- *Acceleration of development of new types of circuit breakers*
- *Monitoring of ageing processes of circuit breakers after long service*
- *Expansion of services for medium-size high-power laboratories*

The principle of 'digital testing' starting from high-resolution measurements and with the aims listed above, is an unprecedented activity in the world of power circuit breakers. (...)

1.4 Circuit breaker measurement data

All computations and results presented in this thesis are based on actual measurements that have been performed on various circuit breaker types of different manufacturers. These measurements have been executed within the framework of an international consortium with the aim to realize 'digital testing of high-voltage circuit breakers' (see also section 1.3). The four following, commercially available, SF_6 circuit breakers have been subjected to Short Line Fault (SLF) tests in the KEMA High-Power Laboratory in the Netherlands:

cb1 245 kV, 50 kA, 50 Hz; 90% SLF in a synthetic test circuit
cb2 72.5 kV, 31.5 kA, 60 Hz; 90% SLF in a direct test circuit.
cb3 145 kV, 31.5 kA, 60 Hz; 90% SLF in both a direct and a synthetic test circuit.
cb4 123 kV, 31.5 kA, 60 Hz; 90% SLF in a synthetic test circuit.

The test circuits used, the measurement information and the arc voltage and reignited current traces can be found in the appendix. Only for cb1, a 10 MHz measurement system has been used, whereas for the other circuit breakers a 40 MHz system has been applied (see also section 2.4.1).

1.4.1 Short Line Fault testing

The circuit breakers were subjected to SLF tests as a short line fault is one of the most severe faults it has to interrupt thermally. In the case of a short line fault, the fault is on a high-voltage transmission line a few kilometres away from the breaker terminals [23,95,99], as shown in figure 1-4. After current interruption, energy stored in the charged line segment is dissipated through travelling waves which reflect between the short-circuit point and the open end of the

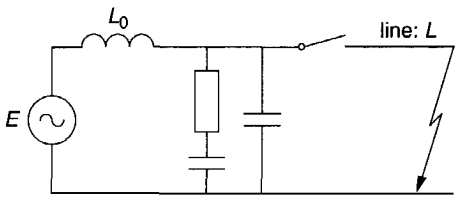

Figure 1-4. Typical short-line fault situation
E is the peak voltage of the supply
L_0 is the inductance of the supply
L is the inductance of the line

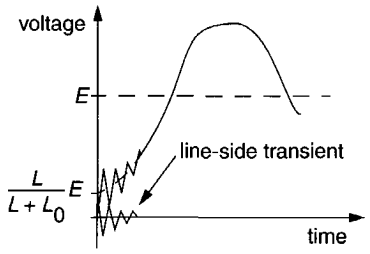

Figure 1-5. TRV resulting from the subtraction of the line-side transient from the source-side transient voltage

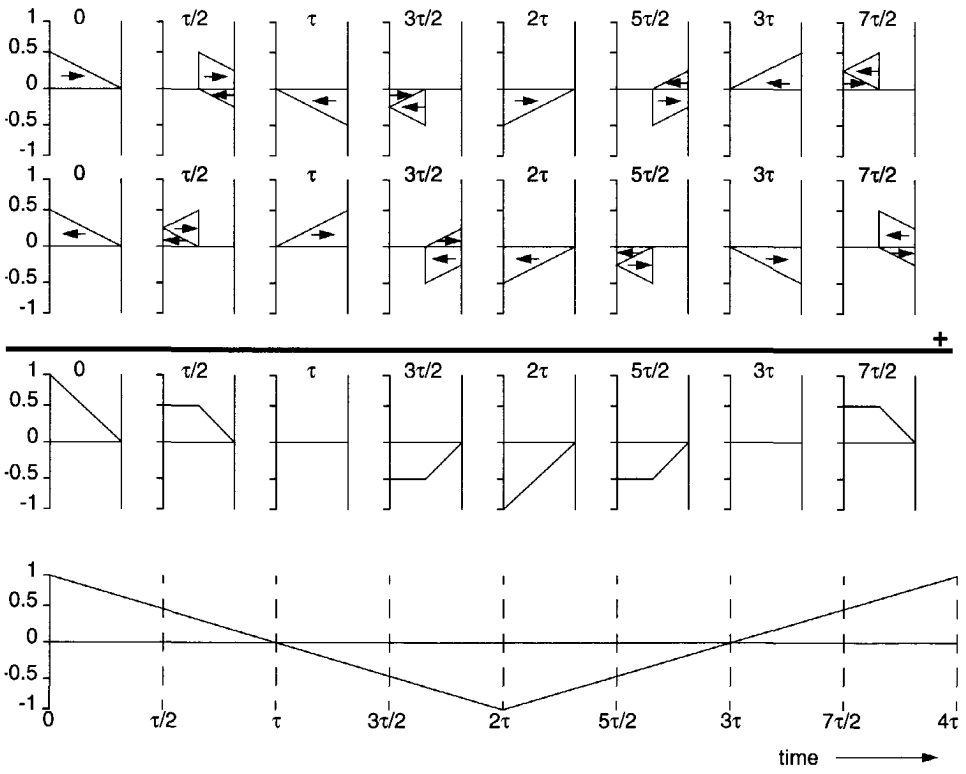

Figure 1-6. Triangular voltage at the line side of the circuit breaker
The first 3 graphs show the development of the voltage waves over the length of the line at 8 consecutive points in time:
1 - voltage wave travelling to the right (towards the short-circuit point)
2 - voltage wave travelling to the left (towards the open end at the breaker terminals)
3 - addition of the right- and left-travelling waves
The last graph shows the resulting triangular voltage at the breaker terminals
τ is the travelling time of the line

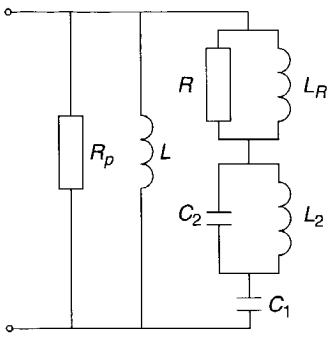

Figure 1-7. KEMA artificial line
%SLF is the ratio between the SLF current and the nominal rated current.
L_0 is the inductance of the supply.
Z is the characteristic impedance of the line.
R_p is put in parallel to reduce the peak factor from 1.8 to 1.6.

$$L = \frac{L_0}{\%SLF/100} - L_0$$

$$L_R = 0.145 \cdot L$$

$$L_2 = 0.0725 \cdot L$$

$$C_1 = \frac{1}{3} \cdot \frac{L}{Z_c^2}$$

$$C_2 = 2C_1$$

$$R = Z_c$$

$$R_p = 10Z$$

$$Z_c = \frac{R_p Z}{R_p - Z}$$

line at the breaker terminals, shown graphically in figure 1-6. A very steep, triangular-shaped waveform is the result, displayed in figure 1-5; it has a rate of rise of 5-10 kV/μs, and stresses the extinguishing medium between the contacts. The percentage SLF (%SLF) indicates to what extent the short-circuit current is reduced by the transmission line segment, e.g. when a short-circuit current of 40 kA is reduced to 36 kA we speak of a 90% SLF. In the IEC standard, 75% and 90% SLF tests are prescribed to test the SLF performance of high-voltage circuit breakers.

Due to the limited amount of space in the high-power laboratory, an artificial line is applied for short line fault testing. In the KEMA High-Power Laboratory, the artificial line as proposed by Van der Linden and Van der Sluis is used for these purposes [96]. The network topology of the KEMA artificial line is depicted in figure 1-7.

1.4.2 Example of an interruption (direct test)

As an example of an interruption, measurement #5021 of pole A of cb3 has been chosen. This is a direct SLF test where the arcing time is 8.1 ms. The measured voltage and current traces before current zero are shown in figure 1-8. It is evident that both current and voltage cross zero at the same time. Furthermore, the extinction peak of the arc voltage can clearly be recognized. The circuit breaker interrupts the current and the triangular-shaped voltage that builds up across the breaker can be observed in figure 1-9. The measured 'post-arc current', which results from the TRV over the non-infinite resistance of the arc channel, is depicted in figure 1-10. Clearly, the current shown here is not a post-arc current, as it becomes positive (as the TRV is negative, this would imply a negative arc resistance) after 0.1 μs. The post-arc current is very difficult to measure (see also Chapter 2), and cannot be considered to be a physical post-arc current for the measurements used in this thesis.

Note that in the titles of the figures, the measurement is indicated with the name #502103, which is also the default notation for direct tests in the rest of the thesis. The measurement system is capable of recording multiple voltage/current zero crossings (with a maximum number

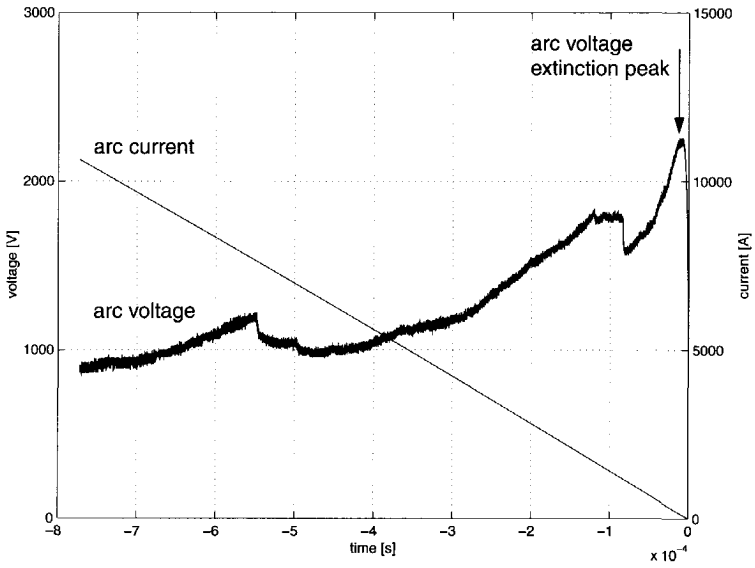

Figure 1-8. Measured arc voltage and current of #502103, pole A, direct test, cb3

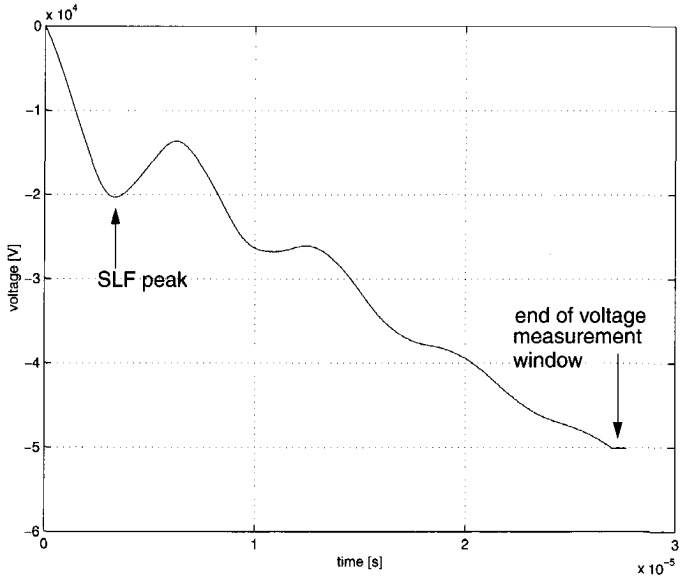

Figure 1-9. Measured TRV of #502103, pole A, direct test, cb3

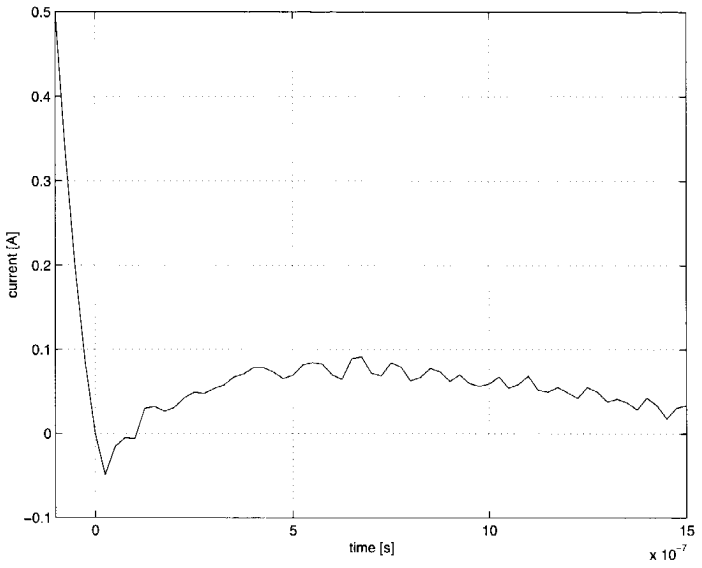

Figure 1-10. Measured 'post-arc current' of #502103, pole A, direct test, cb3

of four segments, see also section 2.4.1) during one test; the addition '03' indicates the segment of the measurement. In this case, the second segment (i.e. #502102) contains the data of a reignition, while the fourth segment (i.e. #502104) contains no data.

1.4.3 Example of a thermal reignition (synthetic test)

As an example for a thermal reignition, measurement #5109 of pole B of cb3 has been chosen. This is a synthetic SLF test where the arcing time is set to be 8.2 ms. The measured voltage and current traces before current zero are shown in figure 1-11. We can clearly distinguish the moment where the synthetic current starts to flow (about 1.3 ms before its current zero crossing), and the moment that the main current is interrupted by the auxiliary breaker (about 0.45 ms before the synthetic current crosses zero). The current continues to flow directly after the current zero crossing as illustrated in figure 1-12. The cooling power applied to the arc was not sufficient to extinguish the arc channel and a thermal reignition occurred.

For synthetic tests, there is only one relevant voltage/current zero crossing: the first current zero crossing of the synthetic current. Therefore, the four memory segments of the measurement system are combined into one large segment to record a longer time frame around this voltage/current zero crossing.

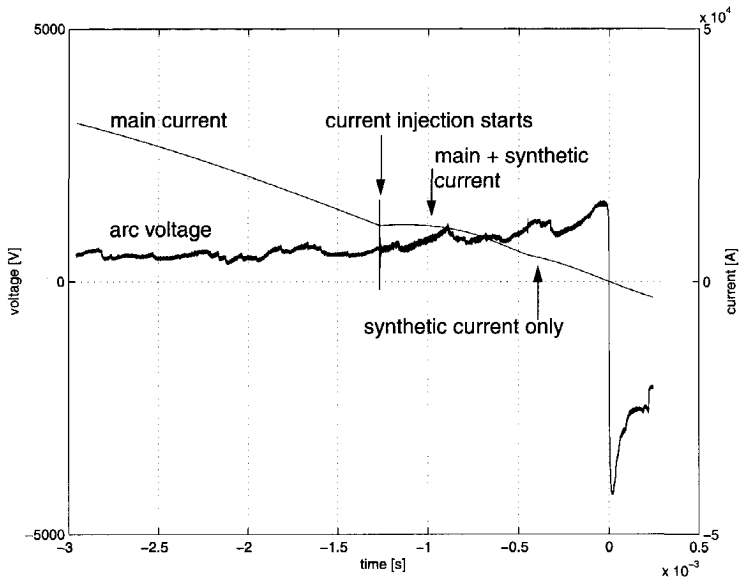

Figure 1-11. Measured voltage and current traces of #5109, pole B, synthetic test, cb3

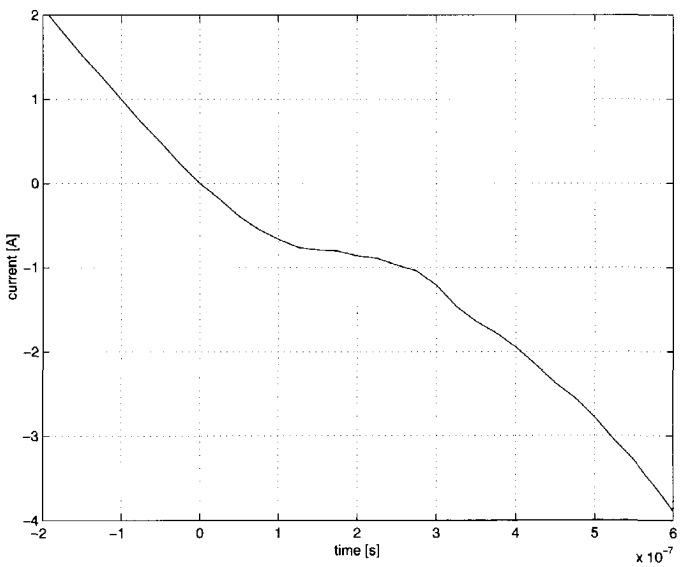

Figure 1-12. Measured current around current zero of #5109, pole B, synthetic test, cb3

1.5 Outline of the thesis

In this introduction general information and some facts concerning high-voltage circuit breakers and their testing are given. Furthermore, the interest and background of the research are outlined.

In chapter two, the general approach and specific problems concerning the measurements carried out in a high-power laboratory are discussed. The KEMA current zero measurement system is outlined, as this is the system on which the measurement data, as used in this thesis, are recorded. Furthermore, attention is paid to the (digital) processing of the measured signals.

In chapter three, the measurement data are analyzed as this is the most direct method to obtain extra information from the tests in the high-power laboratory. Several indicators are presented that give additional information about the circuit breaker performance. Wavelet analysis is presented and applied to investigate sudden jumps in the arc voltage. The frequency contents of the measured voltages are analyzed in order to make profound statements on the validity of the lumped-element modeling of the test circuit. The relation between the Maxwell equations and the lumped-element approximation is described.

In chapter four, (circuit breaker) arc models are applied in order to enhance the laboratory data. Starting from arc physics, the black-box arc models are derived. Based on the measurements, a new Mayr-type arc model is introduced. Several 'digital testing' applications of arc models are outlined, such as the determination of the failure probability, the quality of interruption and the critical line-length.

In chapter five, the voltage injection method is presented. In the lumped-element representation of the laboratory test circuit the circuit breaker is modeled by means of a voltage source that injects the measured voltage across the circuit breaker into the network. This method is applied for an indirect verification of the current zero measurement system of KEMA. Moreover, the quality of interruption is computed and artificial lines are compared.

In chapter six, numerical computations with arc models are addressed. Various computer programs can be used for arc-circuit interaction studies, namely EMTP96 v3.0, XTrans and MATLAB Simulink/Power System Blockset in combination with the Arc Model Blockset (developed by the author). The mathematical basis of these tools is described and they are compared in terms of computational performance.

In chapter seven, conclusions are drawn concerning the work and results presented in this thesis.

Chapter 2

Measuring in the high-power laboratory

2.1 Introduction

The 'switching action', the basic function of the circuit breaker, refers to the mutual conversion of conductor and insulating material at a given potential. In power circuit breakers, the intensity of the current flowing through the conductors and the voltage levels that must be sustained by the insulating material are very high, and at present the only practical approach is the use of arc plasma. During an opening operation, the net result of the conservation of flux linkages is that the current, flowing in the system inductances prior to switching, continues to flow when the contacts part. The final touching surface area of the contacts carries an extremely high current density and, because of the local heating, the contact surface literally 'explodes', thus initiating a gaseous conduction path and an arc plasma channel. Because of the non-zero resistance of the arc channel, the (short-circuit) current causes a voltage across the contacts of the circuit breaker: the arc voltage. The arc behaves as a non-linear resistance. Thus, both arc voltage and arc current cross the zero value at the same time instant. If the arc is cooled sufficiently, at the time the current goes through zero the circuit breaker interrupts the current because the electrical power input is zero. During current interruption, the arc resistance increases from practically zero to almost infinite in microseconds. Immediately after current interruption, the transient recovery voltage (TRV) builds up across the circuit breaker. As the gas mixture in the inter-electrode space does not change to a completely insulating state instantaneously, the arc resistance is finite at that time and a small current can flow: the post-arc current.

In high-power laboratories the ability of circuit breakers to interrupt short-circuit currents is verified in test circuits, which are in fact lumped-element representations of the power system. These test circuits must produce the correct waveforms for the short-circuit current as well as for the voltage that strikes the circuit breaker immediately after the breaker has interrupted the

test current. The waveforms of current and voltage to which the test object is subjected are laid down in ANSI and IEC standards. The current and voltage traces must be measured during the test in order to verify whether the test was in accordance with the prescriptions of IEC and ANSI or with the demands of the customer. Furthermore, the measurement data tell us whether or not the circuit breaker was successful in interrupting the current.

The high-power laboratory is a very hostile environment to perform measurements, because of the electromagnetism generated by the fast-changing high voltages and currents. Therefore, special measurement equipment must be used and precautions have to be taken in order to minimize disturbances on the measured signals.

The various methods to measure current and voltage in the high-power laboratory are outlined in the following sections. Thereafter, the current zero measurement system of the KEMA High-Power Laboratory, which we used for the measurements in this thesis, will be described.

2.2 Current measurement

For digital testing purposes, not only the large short-circuit current prior to current zero, but also the very small post-arc current is of great importance. After all, it is the small time period around the current zero crossing where most of the arc-circuit interaction occurs and where the circuit breaker does or does not interrupt the current.

However, the measurement of the post-arc current poses some special problems. In the high-current interval, the measurement equipment should be capable to measure currents of tens of kAs. Yet after the current zero crossing, post-arc currents with a magnitude of about 1 A or less should be measured. Additionally, the measurements are performed in an electromagnetically hostile environment.

In general there are 3 types of current measuring devices: shunts, current transformers and magneto-optical current transducers. These three types of measuring devices are described in the following sections.

2.2.1 Shunt

The shunt device is a calibrated ohmic resistance which is placed in the current-carrying path; the potential drop due to the current is recorded. This is also one of the drawbacks of the shunt: the device itself is part of the circuit in which the measurement is performed.

An ordinary shunt is not suitable for accurate current measurements in a high-power laboratory. The measuring leads create a loop where an EMF (electromotive force) is induced by the magnetic field from the current that is to be measured (figure 2-1).

To circumvent this problem, a coaxial shunt should be applied as depicted in figure 2-2 [23]. In this construction, the space inside the inner cylinder is field-free and the measurement will not be disturbed by the magnetic field.

When the shunt device is used for measuring both the arcing current and the post-arc current, a small resistance value and a high bandwidth should be applied, which leads to a poor sensitivity. Furthermore, the device must be able to withstand thermal overload. When an accurate measurement of the post-arc current is required, a high-ohmic shunt must be used. In that case,

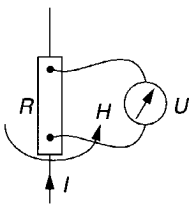

Figure 2-1. Shunt

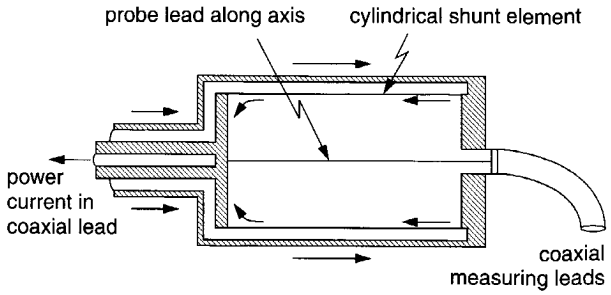

Figure 2-2. Coaxial shunt

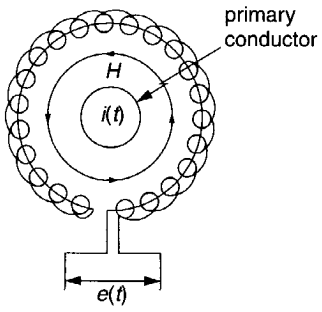

Figure 2-3. Rogowski coil

the shunt should be protected from the current in the high-current interval by means of bypass devices such as low-pressure gaps, vacuum switches or diodes.

2.2.2 Current transformer

Two types of current transformer can be distinguished: steel-core and air-core current transformers (CTs).

The steel-core CT has two major disadvantages which make the device inappropriate for current measurement in the high-power laboratory:

- increasing core losses at higher frequencies
- core saturation at lower frequencies

As an alternative to the steel-core CTs, air-core CTs can be used. These devices do not suffer from saturation. The principle of these devices is based on mutual inductance. They comprise a coil, which links to a part of the flux surrounding the primary or current-carrying conductor. The most widely used measuring device of this type is the Rogowski coil. A Rogowski coil consists of a homogeneously wound induction coil of constant section, which is closed upon itself around the current conductor and senses the magnetic field around the closed path as shown in figure 2-3.

The coil-induced voltage is [55]:

$$e(t) = M \cdot \frac{di}{dt} \qquad \text{with} \qquad M = 2\pi \cdot 10^{-7} \cdot \frac{NA}{r} \tag{2-1}$$

e the induced voltage [V]
i the time-varying current [A]
M the coefficient of mutual inductance [H]
N the number of windings
A the cross section of one winding of the Rogowski coil [m^2]
r the coil radius of the Rogowski coil [m]

As the voltage induced in the coil is proportional to the rate of change of the current, the current is obtained by integrating the voltage. Therefore, the device cannot measure a DC current. The main advantages of the Rogowski coil are:

- a potential-free measurement system
- a low-cost measurement system compared to a shunt or a steel-core CT
- a wide measurement range (from As to hundreds of kAs)
- a wide bandwidth
- a small and lightweight device

2.2.3 Magneto-optical current transducer

Optical measurement equipment offers a number of benefits, such as [64]:

- immunity for EMI (electromagnetic interference)
- high insulation level
- broad bandwidth

The magneto-optical current transducer is based on the Faraday effect in optical materials (circular birefringence), i.e., the rotation of the plane of polarization of linearly polarized light under the influence of a magnetic field parallel to the direction of light propagation [23]. The rotation angle can be written as follows:

$$\theta = V \int H dl \tag{2-2}$$

θ the rotation angle [rad]
V the Verdet constant [rad/A]
H the magnetic field [A/m]
l the length of the integration path [m]

When the optical path encloses the conductor, equation 2-2 becomes:

$$\theta = V \oint H dl = VNi \tag{2-3}$$

i the current enclosed by the light path [A]
N the number of loops of the light path around the current-carrying conductor

From equation 2-3, we can see that the rotation angle is directly proportional to the current.

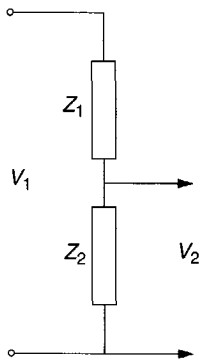

Figure 2-4. Voltage divider

The main advantages of this type of device, when applied for post-arc current measurement, are [24]:

- good linearity
- good sensitivity (by choosing a large number of turns N)
- immunity to high currents

A disadvantage of the optical current sensors is that circular birefringence is induced by a twist in the optical fibre as well, and that linear birefringence is induced by stress which depends on the temperature. Yet, a lot of research has been done to reduce or compensate the effects of these phenomena [64].

2.3 Voltage measurement

A voltage transformer has the same disadvantages as a CT and for that reason, it is not suitable for accurate voltage measurements at higher frequencies. Analogous to the current measurement, also an optical sensor can be applied for voltage measurement. This electro-optical voltage transducer is based on the Pockels effect in optical materials (linear birefringence), i.e., the refraction coefficient of a material changes under the influence of an electric field. Damstra and Kertész [14] state that the accuracy of the electro-optical transducers is too low and is difficult to maintain stable during high-power tests. Recently, however, an optical measurement system for voltages up to 400 kV in a bandwidth between DC and 30 MHz has been reported [66].

The most common device for voltage measurement is the voltage divider shown in figure 2-4. Voltage dividers must meet the following performance requirements [52]:

- appropriate dielectric strength
- sufficient thermal capacity for the AC recovery voltage
- good frequency response characteristic for measuring high frequencies

The output of the voltage divider is:

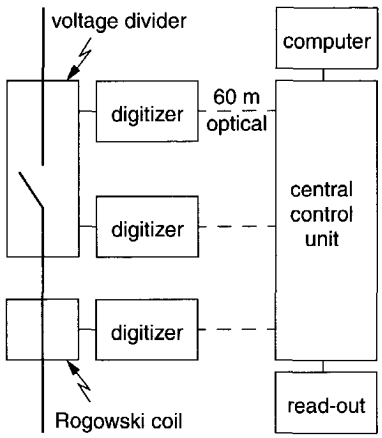

Figure 2-5. Schematical drawing of the KEMA current zero measurement system

$$V_2 = \frac{Z_2}{Z_1 + Z_2} V_1 \tag{2-4}$$

Most of the voltage dividers are of the resistive, the capacitive or the mixed type. Due to their thermal capacities, resistance voltage dividers cannot meet the performance requirements. For high frequencies and steep voltages, a capacitive divider is suitable. However, a capacitive divider cannot measure DC voltages. Therefore, the mixed (resistance-capacitance) voltage divider is commonly applied for voltage measurements in the high-power laboratory.

2.4 KEMA current zero measurement system

The current zero measurement system developed by KEMA in the context of the EU project 'digital testing of high-voltage circuit breakers' and applied for the measurements analyzed in this thesis will be described in the following sections [85]. A schematical drawing of the system is shown in figure 2-5; a practical setup in the test bay in figure 2-6.

The optical fibres are the galvanic isolation between the transducers and the recording equipment.

2.4.1 High-resolution high-frequency digitizing system

The digitizing system is a three-channel, 40 MHz, 12 bit system with 4x64k memories per channel. During the tests, data are stored in the local memory of the digitizer, and immediately after the test it is transferred over a serial optical link to a back-up memory of the central control unit in the control room. This unit is linked to a PC via an IEEE 488 bus. The memory of 256k samples per channel can be split in 1, 2 or 4 segments (giving a 6.4 ms time window at the highest sampling frequency) in which different current zero crossings during the arcing phase are recorded. The 4 memory blocks are used for recording multiple current zero cross-

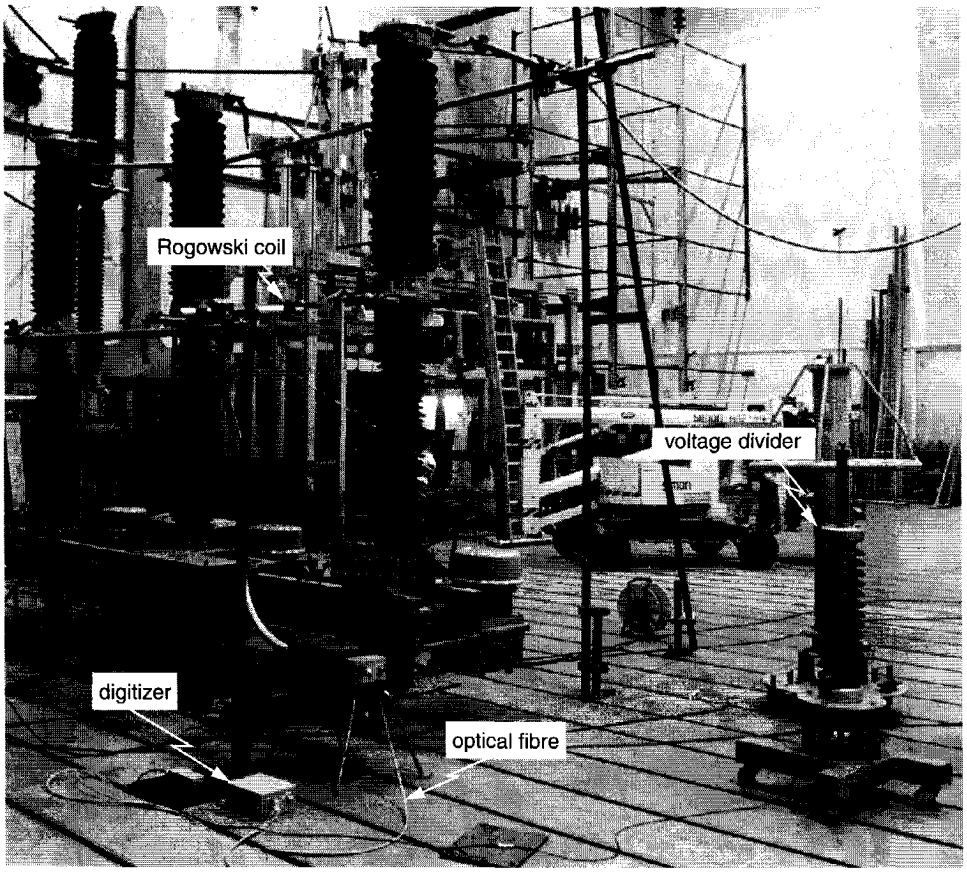

Figure 2-6. Measurement setup in the KEMA High-Power Laboratory

ings during direct tests. For synthetic tests, the 4 memory blocks are combined into 1 large block in order to record a longer time frame around the current zero crossing.

2.4.2 Measuring devices

KEMA manufactured its own Rogowski coil, which is shown in figure 2-7. The coil is placed in a shielded box to avoid interference by capacitive coupling, and slits in the shielded box eliminate eddy currents.

The Rogowski coil has a mutual inductance of 0.34 μH, so that the induced voltage is within the range of 3 - 10 V when a primary current with a slope of 10 - 30 A/μs is applied (see also equation 2-1 (section 2.2.2)). In the case of an ideal interruption at current zero, i.e., when the time derivative of the current changes from a constant value into zero instantaneously (see figure 2-8), the voltage induced in the coil will decay to zero with a time constant of $\tau = L/R$, with L the inductance of the coil and R the total resistance. In the case that the Rogowski coil is connected to the digital system by a 50 Ω coaxial cable, the time constant is approximately

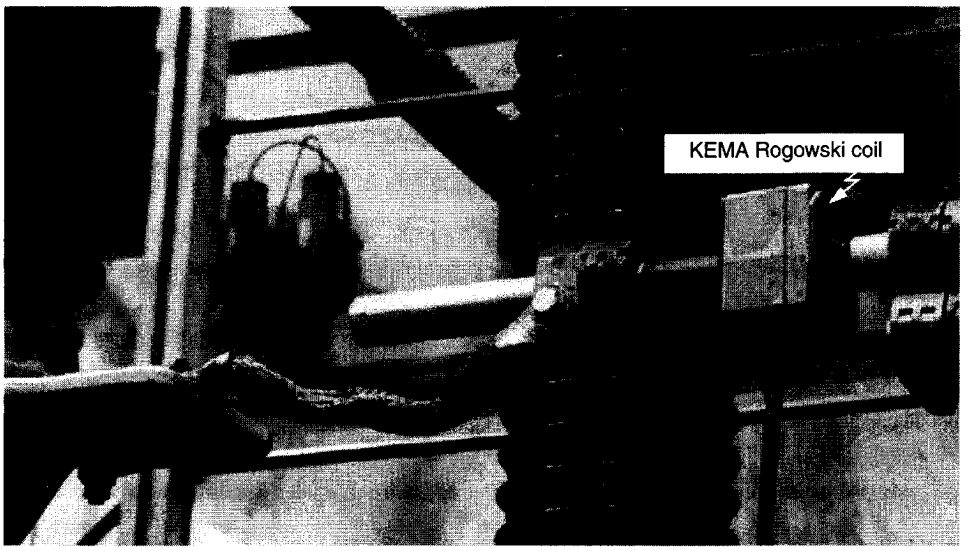

Figure 2-7. KEMA Rogowski coil

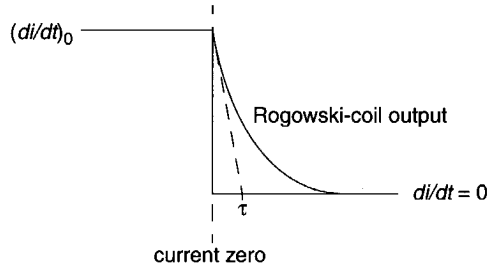

Figure 2-8. Time derivative of the interrupted current and the Rogowski-coil output in case of an ideal current interruption

450 ns. The relation between the time derivative of the primary current and the Rogowski-coil output is therefore given by the following equation:

$$M\frac{di}{dt} = e + \tau\frac{de}{dt} \tag{2-5}$$

i the primary current [A]
e the Rogowski-coil output [V]
M the coefficient of mutual inductance [H]
τ the time constant of the Rogowski coil [s]

The crossover frequency (-3 dB point) of the transfer function in equation 2-5 is approximately 350 kHz ($f = \omega/(2\pi) = 1/(2\pi\tau)$). This is the frequency above which the Rogowski-coil nature (output voltage proportional to the time derivative of the primary current) changes into a

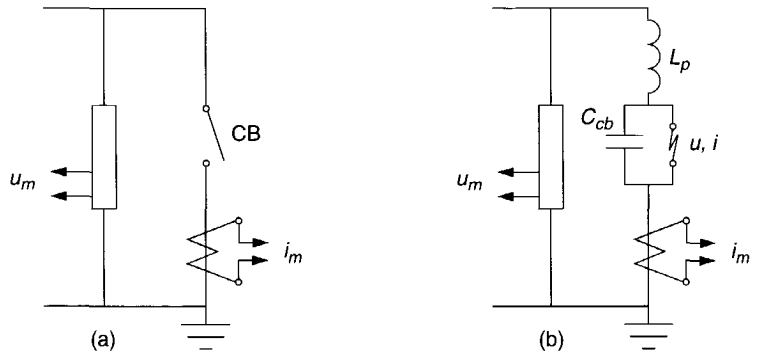

Figure 2-9. Arrangement (a) and principal scheme (b) of the arc voltage and arc current measurement. u_m, i_m - the measured voltage and current. u, i- the arc voltage and current. C_{cb} - the circuit breaker capacitance. L_p - a parasitic inductance.

current-transformer nature (output voltage proportional to the primary current) with ratio 1 : N, where N is the number of secondary turns.

For the voltage measurement, a commercial voltage divider was used (Haefely RCZ150 for voltages of 145 kV and lower).

2.4.3 Processing of the measured signals

The measured data must be treated in order to find the actual arc voltage and arc current [35,85]. It is not only necessary to integrate the Rogowski-coil output in order to determine the current; one must also take into account the non-ideal differentiating behavior of the device. Additionally, one should correct for the effect of the capacitive component in the measured current due to the flow of capacitive current through the stray capacitance of the circuit breaker. The voltage measurement has to be corrected for the voltage induced in the voltage measuring loop. The circuit relation between measured current and voltage and arc current and voltage is shown in figure 2-9.

From the measured traces, the arc voltage and arc current are computed by means of the following equations, which are derived from the circuit in figure 2-9 (b).

$$u = u_m - L_p \frac{di_m}{dt}$$

$$i = i_m - C_{cb}\frac{du}{dt} = i_m - C_{cb}\frac{du_m}{dt} + L_p C_{cb}\frac{d^2 i_m}{dt^2} \qquad (2\text{-}6)$$

u	the arc voltage [V]
i	the arc current [A]
u_m	the measured voltage [V]
i_m	the measured current [A]
C_{cb}	the circuit breaker capacitance [F]
L_p	a parasitic inductance [H]

In evaluating the current from the Rogowski-coil output, one should also take into account the non-ideal differentiating behavior (see section 2.4.2). The equation to obtain the current from the Rogowski-coil output is:

$$i_m(t) = i_m(0) + \frac{1}{M}\int_0^t e(s)d(s) + \frac{\tau}{M}e(t) \tag{2-7}$$

e the Rogowski-coil output [V]
M the coefficient of mutual inductance [H]
τ the time constant of the Rogowski coil [s]

The offset term $i_m(0)$ can be determined, considering the fact that the resistive component of the current, i.e. the arc current i, should be zero at voltage zero.

Chapter 3

Analysis of the measured data

3.1 Introduction

The most straightforward approach to obtain additional information from the tests in the high-power laboratory is by analyzing the measurement data directly. In the first section different indicators are introduced that give information about the circuit breaker performance.

The measured arc voltages are rather capricious, with a lot of sudden jumps, as can be seen from the graphics in the appendix. As the arc voltage is correlated with the cooling process of the circuit breaker arc, it is interesting to see whether the jumps (or other high-frequent phenomena) in the arc voltage are related to the observed ageing of the contacts, the nozzle or the degradation of the SF_6 gas. This is analyzed by means of wavelet analysis.

Finally, the frequency contents of the measured voltages are analyzed in order to be able to make an assessment of the validity of the lumped-element modeling of the test circuit. The relation between the Maxwell equations and the lumped-element approximation is discussed.

3.2 Direct analysis of measured data

The information that can be obtained from the measurement data directly gives quick insight into the performance of the circuit breaker in comparison with other measurements. This is also one of the drawbacks of the direct analysis: you cannot find an absolute boundary between interruption and failure from one single test. It is the collection of tests of a circuit breaker that gives you this information.

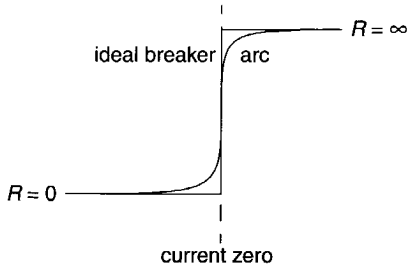

Figure 3-1. Resistance of an ideal breaker and arc resistance

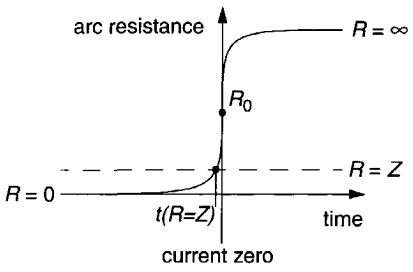

Figure 3-2. R_0 and t(R=Z)

3.2.1 Arc voltage

In the high current interval, a low arc voltage (< 1 kV for SF_6 circuit breakers) is observed. Only in the final 1 ms - 100 µs before current zero, the arc voltage increases to its extinction peak having a value of a few kV. The higher the extinction peak, the better the interruption probability. This can be clearly observed from the arc voltage plots in the appendix (e.g. figure A-16). It appears that a circuit breaker with an extinction peak higher than 2 kV is likely to interrupt the current. However, the arc voltage peak values do not give a sharp separation between the interruptions and the failures, in contrast to the indicator presented in the following section.

3.2.2 Arc resistance

The arc resistance is computed directly from the arc voltage and arc current. When an ideal circuit breaker interrupts a current, the resistance changes from a zero value to infinity instantaneously. The arc resistance changes gradually from a zero value to infinity in case of an interruption (figure 3-1). The quicker the arc resistance builds up, the more likely it is that the breaker interrupts the current. In particular the arc resistance value at current zero (R_0) is a valuable indicator (see figure 3-2). However, as the value of the current measured close to current zero is highly questionable, so is the value of the arc resistance that is obtained directly from the measured data. This can be circumvented by looking at the resistance value some time before the current zero crossing. Such an indicator is the time before current zero, where the arc resistance equals the characteristic impedance of the transmission line for an SLF test: $t(R=Z)$ (shown in figure 3-2). This is the point where the energy exchange between the arc and the artificial line is at its maximum.

The $t(R=Z)$ indicator can be determined from the measurement data directly and gives a clear distinction between the interruptions and the reignitions of the breaker. The closer the value of the indicator is to the current zero crossing, the more likely it is that the breaker will reignite. The $t(R=Z)$ values of cb4 are shown in figure 3-3; only one interruption (black bar) falls below the $t(R=Z)$ limit value, i.e., below the line separating the interruptions from the reignitions. The difference between the $t(R=Z)$ value that is obtained from a test and the $t(R=Z)$ limit value

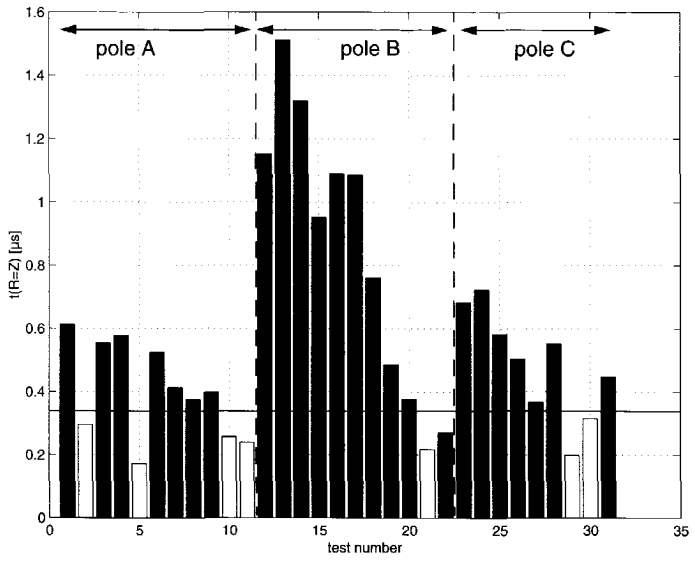

Figure 3-3. t(R=Z) values of cb4
Black bar: interruption. White bar: reignition.

gives an indication of the circuit-breaker performance during this test: the bigger this positive (negative) difference, the better (poorer) the circuit breaker performed.

Some remarkable observations can be made from figure 3-3. There is a clear overall decrease in the circuit-breaker performance during the progress of tests on every pole, reflecting the degradation of the circuit breaker by the tests. Furthermore, the effect of the amount of power frequency current stress (pole A: 28.4 kA_{RMS}, pole B: 13.9 .. 31.6 kA_{RMS}, pole C: 26.1 .. 35.4 kA_{RMS}) on the circuit-breaker performance can be clearly observed. The same tendencies have been found for cb2. These tendencies have not been found for cb3: this breaker did not show any signs of degradation, despite the large number of tests.

The *t(R=Z)* limit values of cb1, cb2, cb3 and cb4 are shown in table 3-1. Furthermore, the prediction power of the *t(R=Z)* indicator - its ability to separate the interruptions from the reignitions - is indicated as a percentage: the sum of the number of reignitions above and the number of interruptions below the limit value divided by the total number of measurements.

Table 3-1. t(R=Z) limit values for cb1, cb2, cb3 and cb4 and its prediction power

	cb1	cb2	cb3	cb4
t(R=Z) limit value [µs]	0.34	0.34	0.2	0.34
prediction power	100%	95%	96%	97%

The *t(R=Z)* indicator can be used to differentiate between circuit breakers as well. From table 3-1 it can be noted that the limit values of cb1, cb2 and cb4 are equal, while the limit value of

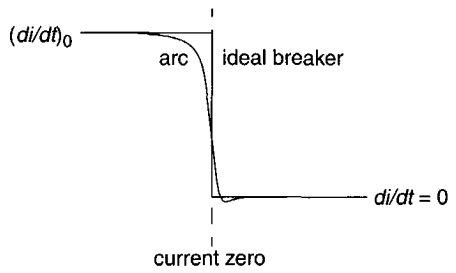

Figure 3-4. Time derivative of the interrupted current in case of an ideal breaker and an arc

cb3 is much lower. This indicates the better quality of cb3 when compared to cb1, cb2 and cb4: cb3 is able to interrupt even in cases with a much slower arc resistance buildup.

3.2.3 Time derivative of the arc current

When an ideal circuit breaker interrupts the current, the time derivative of the current changes instantaneously from a constant value to zero, as shown in figure 3-4. The time derivative of the arc current changes gradually from a constant value to zero in case of an interruption. That means that at the current zero crossing, the time derivative of the current has a certain value. The smaller the value of the time derivative at current zero, the more likely it is that the breaker interrupts the current.

The current measurements used in this thesis have been obtained with a Rogowski coil (see also section 2.4.2). The relation between the time derivative of the arc current and the Rogowski-coil output is therefore given by the following equation:

$$M\frac{di}{dt} = e + \tau\frac{de}{dt} \tag{3-1}$$

i the arc current [A]
e the Rogowski-coil output [V]
M the coefficient of mutual inductance [H]
τ the time constant of the Rogowski coil [s]

As an example, in figure 3-5, the current, its time derivative and the Rogowski-coil output derived by means of equation 3-1 for both an interruption and a reignition resulting from arc model computations are displayed. For the Rogowski-coil output, the same applies as for the time derivative of the current: the smaller the value at current zero, the more likely it is that the breaker interrupts the current. The Rogowski-coil outputs of cb3, where a more or less constant $(di/dt)_0$ (i.e. the average value of the arc current derivative from an interval of 100 µs before current zero to 5 µs before current zero (see figure 3-4)) is maintained during the tests, are shown in figure 3-6 and figure 3-7. The reignitions can be clearly identified from the interruptions.

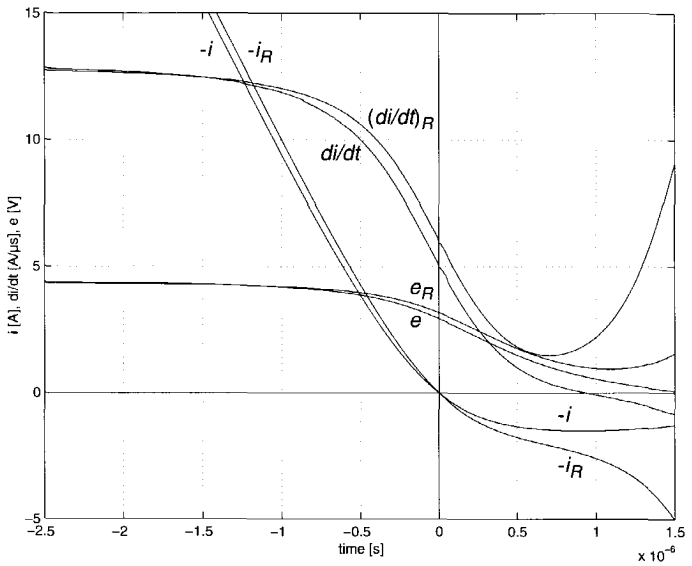

Figure 3-5. The current (i), di/dt and Rogowski-coil output (e) for both a computed interruption and a computed reignition (indicated with the subscript: R) (Rogowski-coil time constant τ = 450 ns, mutual inductance M = 0.34 µH)

3.3 Wavelet analysis in general

Despite the fact that the first mention of wavelets was in the early 1900s [25], the wavelet transform only recently gained popularity. One of the first publications introducing the application of wavelets to the field of power system engineering originates from 1996 [61]. Nowadays, the wavelet transform is a frequently applied tool in this field for the following applications:

- Analysis
  Wide area of applications, including: power-quality classification, fault detection and classification for protection relays, fault location, power system transient and harmonic studies, load forecasting.
- Compression and filtering
  Compression of power system disturbance data recorded by logging devices.
- Modeling and simulation
  Power system computations in the wavelet domain.

Wavelets are functions that satisfy certain mathematical requirements and are used for representing data or other functions. Wavelets are far more efficient for this application than Fourier analysis whenever a signal is dominated by transient behavior or discontinuities, as is the case

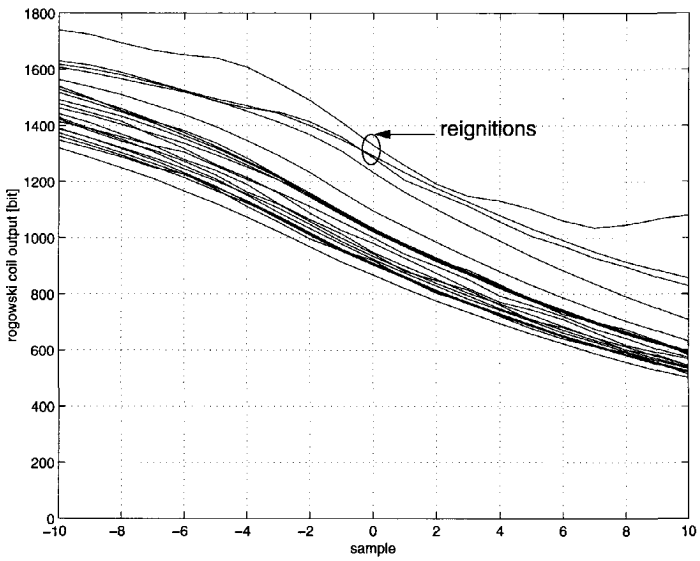

Figure 3-6. Rogowski-coil output (#500603... #503003, pole A, cb3)
(sample 0 corresponds to the current zero crossing)

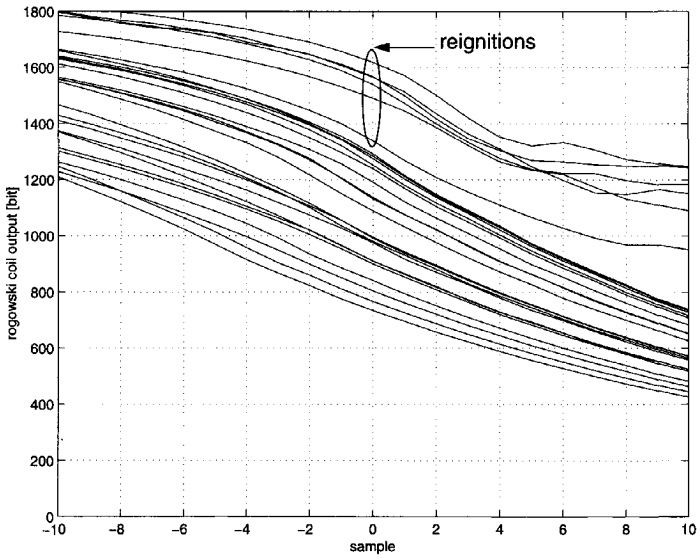

Figure 3-7. Rogowski-coil output (#5104... #5130, pole B, cb3)
(sample 0 corresponds to the current zero crossing)

with the measured arc voltages. The MATLAB Wavelet Toolbox has been applied for the wavelet computations in this thesis [46].

3.3.1 Wavelets compared to the Fourier transform

The Fourier transform of a time signal x is given in its continuous (FT) and discrete (DFT) form as:

$$FT(f) = \int_{-\infty}^{\infty} x(t)e^{-j2\pi ft}dt \tag{3-2}$$

$$DFT[k] = \sum_{n=0}^{N-1} x[n]e^{-j\frac{2\pi kn}{N}} \tag{3-3}$$

The Fourier transform breaks up a time signal into constituent sinusoids of different frequencies. Fourier analysis has a serious drawback. The basis functions used in Fourier analysis, sine and cosine waves, are located in frequency precisely but they exist for all time: after transformation to the frequency domain all time information is lost. It has become impossible to tell when a certain frequency occurred in time.

One technique that alleviates the problems to some extent is the windowed or Short-Time Fourier Transform (STFT). The STFT is similar to the FT except that the input signal is multiplied by a window function whose position is translated in time. The STFT of a time signal x is given in its continuous (STFT) and discrete (WDFT) form as:

$$STFT(f,\tau) = \int_{-\infty}^{\infty} x(t)w(t-\tau)e^{-j2\pi ft}dt \tag{3-4}$$

$$WDFT[k,m] = \sum_{n=0}^{N-1} x[n]w[n-m]e^{-j\frac{2\pi kn}{N}} \tag{3-5}$$

The simplest form for the window function w is a rectangular window, defined as follows:

$$w[n] = \begin{cases} 1 & \text{if } 0 \le n-m \le N-1 \\ 0 & \text{otherwise} \end{cases} \tag{3-6}$$

With the STFT, the input signal is chopped up into sections and each section is analyzed for its frequency contents separately, as shown in figure 3-8. The STFT has the limitation of a fixed window width, which means that the trade-off between frequency resolution and time resolution, which depends on the signal to be analyzed, must be fixed in advance in order to capture a certain phenomenon. A wide window gives good frequency resolution but a poor time resolution. Whereas a narrow window gives good time resolution but a poor frequency resolution.

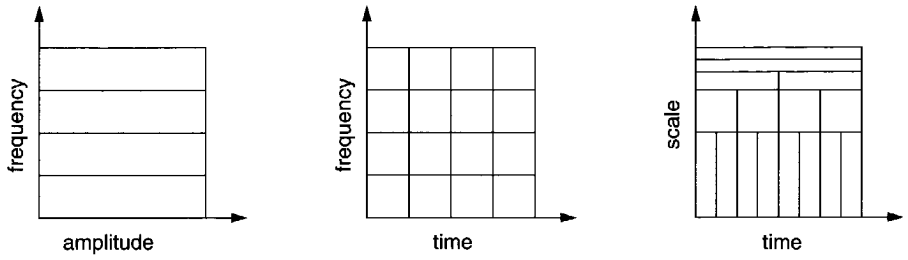

Figure 3-8. Fourier, Short-Time Fourier and Wavelet view of a signal

The advantage of the wavelet transform is that it uses short time windows at high frequencies and long time windows at low frequencies. In a sense, wavelets have a window that automatically adjusts to give the appropriate resolution. The wavelet view of a signal is compared with that of the FT and STFT in figure 3-8.

The wavelet transform of a time signal x is given in its continuous (CWT) and discrete (DWT) form as:

$$CWT(a,b) = \frac{1}{\sqrt{a}} \int_{-\infty}^{\infty} x(t) g\left(\frac{t-b}{a}\right) dt \tag{3-7}$$

a the scaling parameter. A value of $a > 1$ expands g in time and decreases the frequency of the oscillations in $g((t-b)/a)$. A value of $a < 1$ contracts g in time and increases the frequency of the oscillations in $g((t-b)/a)$.

b the translation parameter. The translation parameter delays or hastens the wavelet's onset.

$$DWT[k,m] = \frac{1}{\sqrt{a_0^m}} \sum_{n=0}^{N-1} x[n] g\left[\frac{k - n a_0^m b_0}{a_0^m}\right] \tag{3-8}$$

a_0, b_0 constants; the scaling and translation parameters a and b of equation 3-7 are functions of the integer parameter m: $a = a_0^m$ and $b = n a_0^m b_0$.

The signal x is transformed by an analyzing function $g((t-b)/a)$, analogous to the $w(t-\tau)\exp(-j2\pi ft)$ in the STFT (equation 3-4). The only restriction on g is that it must be short and oscillatory; i.e., it must have zero average and decay quickly at both ends. Therefore, the waveforms are called wavelets and the function g is referred to as the 'mother wavelet'. Some examples of the Daubechies wavelet family are shown in figure 3-9.

3.3.2 Continuous and discrete wavelet transform

As any signal on a computer is a discrete time signal, the term continuous wavelet transform can raise some questions. 'Continuous' should be interpreted as that the CWT can operate at every scale and that it is continuous in terms of shifting as described in the following CWT computational procedure [46]:

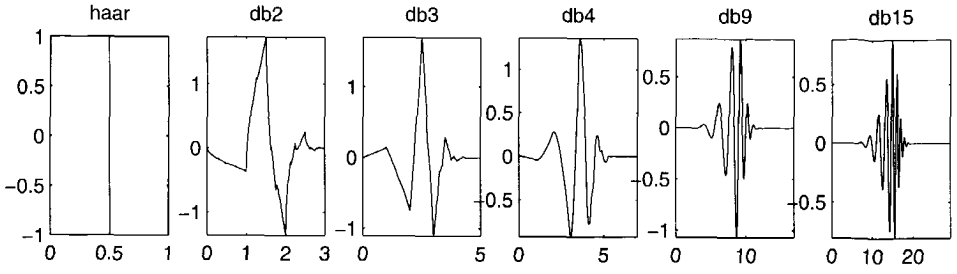

Figure 3-9. Some members of the Daubechies (db) wavelet family
The Haar wavelet (1 on [0 0.5] and -1 on [0.5 1]) is the same as db1.

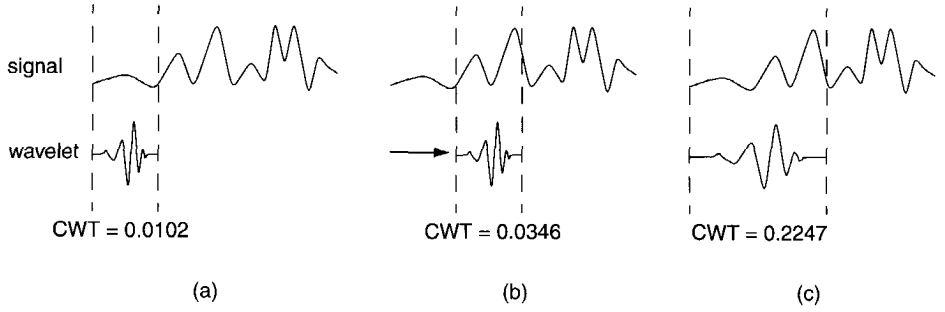

Figure 3-10. Continuous wavelet transform: consecutive steps for computation

1 Take a wavelet and compare it to a section at the start of the original signal

2 Calculate a number, CWT, that represents how closely correlated the wavelet is with this section of the signal. See figure 3-10 (a).

3 Shift the wavelet along the signal and repeat the steps 2 and 3 until the whole signal has been covered. See figure 3-10 (b).

4 Scale the wavelet and repeat steps 1 through 3. See figure 3-10 (c).

5 Repeat steps 1 through 4 for all scales.

The resulting coefficients at the various scales and for the various sections of the signal can be visualized in a three-dimensional and a two-dimensional plot, as in figure 3-16 and figure 3-17, respectively.

The DWT is based on dyadic scales and positions (based on powers of two). In that case the DWT is far more efficient than the CWT and just as accurate. The principle of the DWT is shown in figure 3-11. The original signal passes through a low-pass and high-pass filter leading to a detailed (high-frequency) component and an approximation (low-frequency component). In order to reduce the number of samples, downsampling is applied (figure 3-11, right). This means that every second data point is thrown away. Reconstructing the original signal works

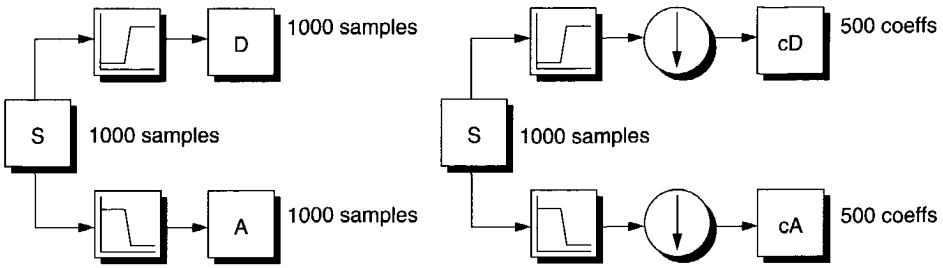

Figure 3-11. The process of the DWT
S = signal, D = detail, A = approximation, cD = detail coefficients, cA = approximation coefficients

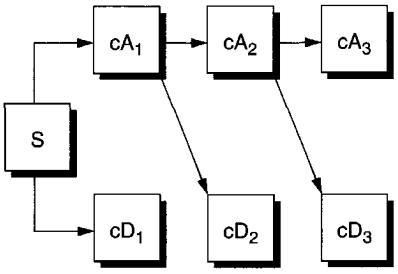

level	decomposition
1	$S = cA_1 + cD_1$
2	$S = cA_2 + cD_2 + cD_1$
3	$S = cA_3 + cD_3 + cD_2 + cD_1$

Figure 3-12. Multilevel DWT

the other way around: upsampling and filtering. The wavelet decomposition can be iterated with successive approximations decomposed in turn, so that one signal is broken up in lower-resolution components as shown in figure 3-12.

3.3.3 Two applications of the wavelet transform

Analysis of transient phenomena

In order to visualize the difference between the Fourier and the wavelet transform, we will analyze a capacitor switching transient. The signal is made up of a 60 Hz fundamental with a damped 900 Hz component superimposed as shown in figure 3-13 [61]. The signal contains four 60 Hz cycles and is sampled with a frequency of f_s = 10 kHz. The Fourier transform of this signal is shown in figure 3-14. The peaks at the frequencies of 60 Hz and 900 Hz can clearly be observed. However, from figure 3-14 no statement can be made on the time instant at which the 900 Hz component occurred.

When the STFT is applied, the size of the window must be determined in advance. When the signal is chopped up into four sections, the time period of each window equals one cycle T = 16.67 ms which fixes the frequency resolution at $\Delta f = 1/T$ = 60 Hz. The resulting time-frequency plot is shown in figure 3-15. The tint indicates the corresponding magnitude. Note that narrowing the window size yields a better time resolution but reduces the frequency

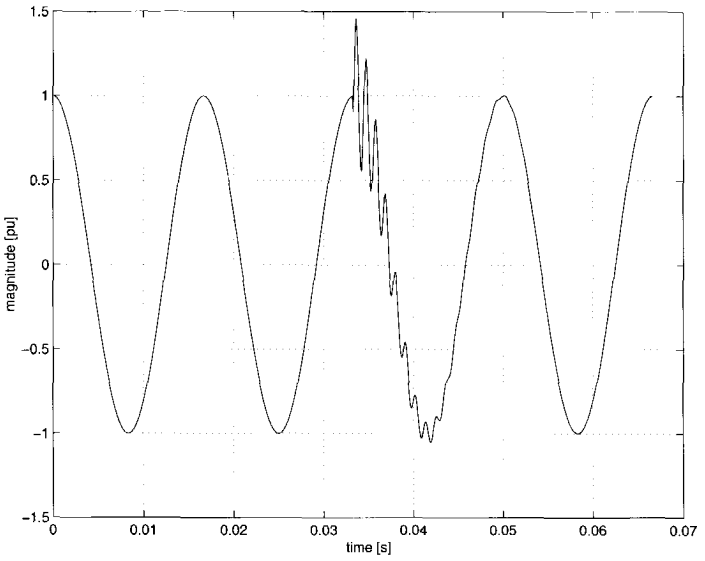

Figure 3-13. 60 Hz fundamental with a damped 900 Hz component superimposed

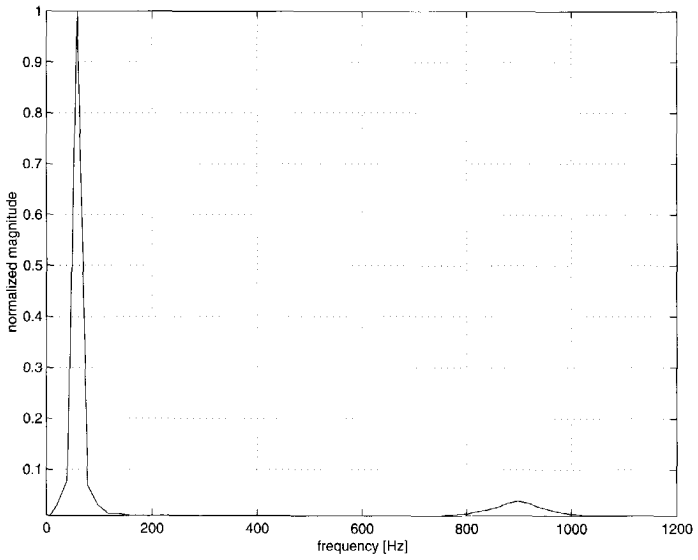

Figure 3-14. FT of the signal in figure 3-13

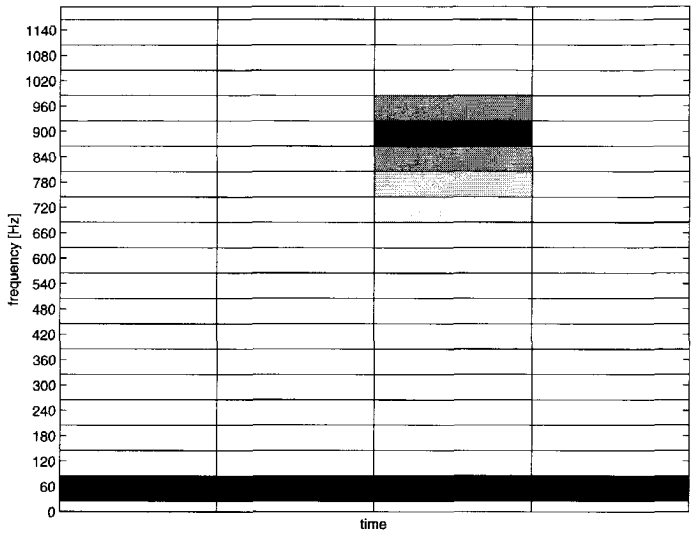

Figure 3-15. STFT with one-cycle window size of the signal in figure 3-13

resolution: e.g. 16 windows of a quarter of a cycle $T = 0.004167$ s fixes the frequency resolution at $\Delta f = 1/T = 240$ Hz.

It has become clear from this example that multiple resolution in time and frequency is a major advantage. A fine time resolution is used for high frequencies and a coarse time resolution for low frequencies. In such a way, transients are localized accurately whereas the information on the fundamental frequency is still available. This is accomplished by the wavelet transform. The CWT of the signal in figure 3-13 is shown in figure 3-16. The Morlet wavelet has been applied as mother wavelet; the absolute values of the wavelet coefficients are displayed. It is obvious from figure 3-16 that the lower scales correspond to the higher frequencies, as the peak in front corresponds to the 900 Hz component. The 'hills' in the middle correspond to the fundamental frequency. When the three-dimensional view of the CWT coefficients is displayed as a two-dimensional image (the three-dimensional graph is observed from above), and dyadic scaling is applied, as is the case with the DWT, figure 3-17 results. From this figure it appears that the darkest tint is in scale 8 and in scale 128. The corresponding frequency ranges for the scales at the 10 kHz sampling frequency (Nyquist frequency: 5 kHz) are displayed in figure 3-18. The scales 8 and 128 correspond to the 900 Hz and 60 Hz frequencies respectively.

Compression and filtering

As an example of wavelet compression, a simple digital signal consisting of eight numbers will be transformed [20]. As the example is meant for demonstration purposes only, the Haar or db1 wavelet transform will be applied (see also figure 3-9). The Haar wavelet transform is performed by computing averages and differences (divided by two) of neighboring pairs in the original signal. The Haar wavelet transform of the signal is shown in table 3-2. As an example,

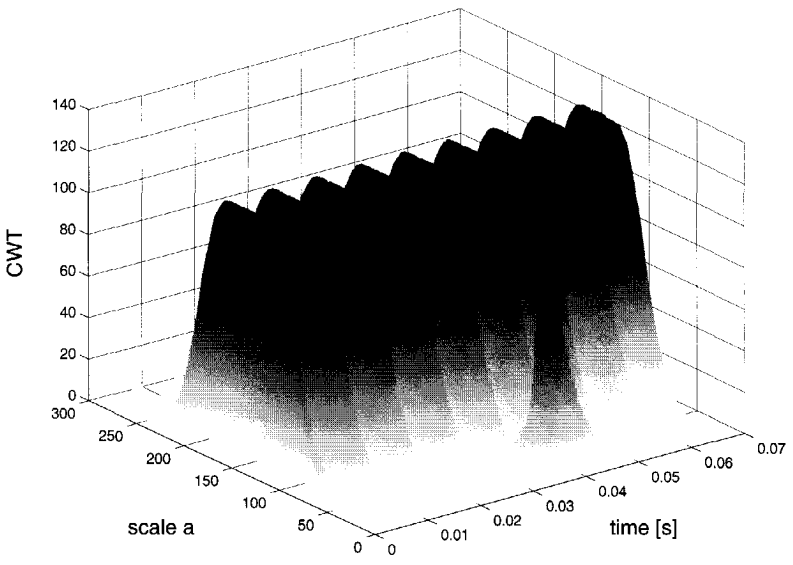

Figure 3-16. CWT (3D) of the signal in figure 3-13

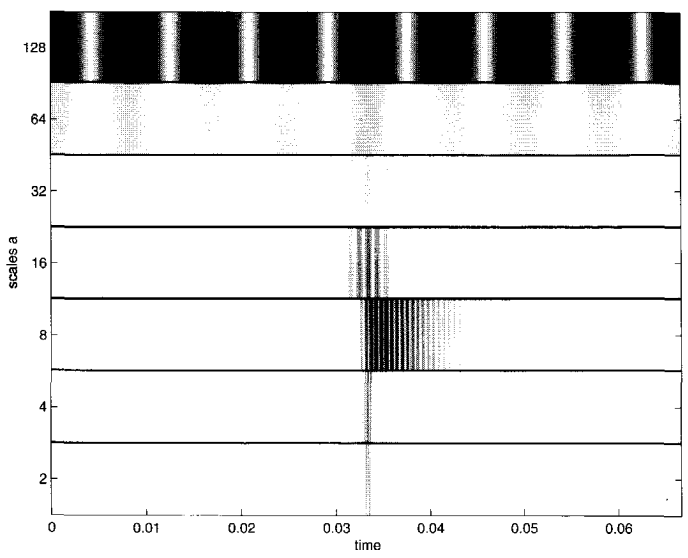

Figure 3-17. CWT (2D) of the signal in figure 3-13
Dyadic scaling (as with the DWT) has been applied

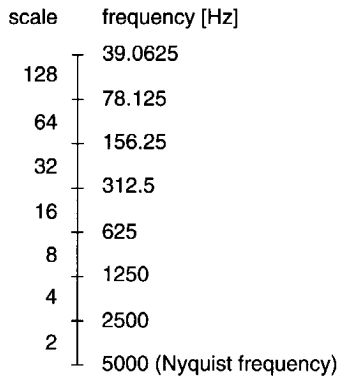

Figure 3-18. Relation between scales and frequency

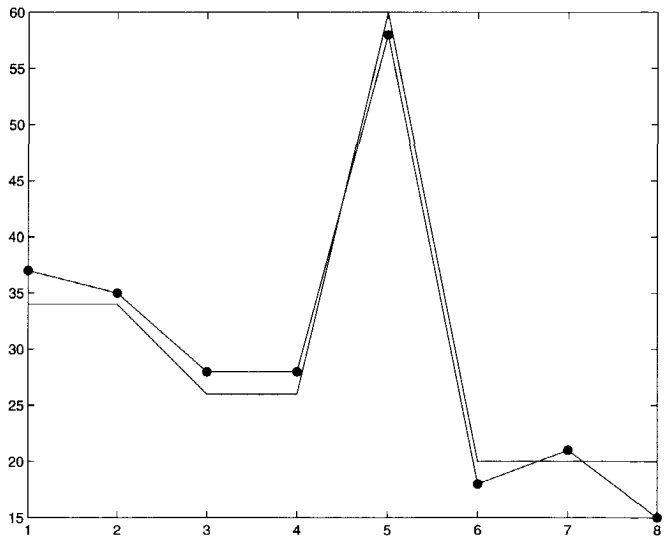

Figure 3-19. Original (line and dots) and compressed signal (line only)

the first pair {37 35} will be transformed: the average amounts to 36 while the difference (divided by two) totals 1. In the table, starting from the original signal, the three consecutive steps in taking the averages and differences (shown in the shaded cells) are shown. Looking at the table from the bottom row to the top would mean a reconstruction of the original signal.

From the wavelet decomposition, the various scales can be reconstructed separately. If for example the small-scale, i.e., high-frequency, behavior needs to be analyzed, the detail D_1 can be reconstructed as in table 3-3.

Table 3-2. Wavelet transform of a sample signal

S	37	35	28	28	58	18	21	15
$S = cA_1 + cD_1$	36	28	38	18	1	0	20	3
$S = cA_2 + cD_2 + cD_1$	32	28	4	10	1	0	20	3
$S = cA_3 + cD_3 + cD_2 + cD_1$	30	2	4	10	1	0	20	3
$S = cA_3 + cD_3 + cD_2 + cD_1$	**30**	**2**	**4**	**10**	**1**	**0**	**20**	**3**

Table 3-3. Small-scale reconstruction (D_1)

0	0	0	0	1	0	20	3
0	0	0	0	1	0	20	3
0	0	0	0	1	0	20	3
0	0	0	0	1	0	20	3
1	**-1**	**0**	**0**	**20**	**-20**	**3**	**-3**

The merit of this approach can be seen from table 3-2, by comparing the first row, i.e. the original signal, with the last row, i.e. the transformed signal. It is evident that the numbers in the shaded cells of the transformed signal are much smaller than the numbers in the original signal. This means that less storage is needed than would be required for the original signal.

Further compression of the original signal is achieved by tresholding. That means that numbers smaller than the treshold are discarded. When in our example a treshold of 4 is introduced, the signals contains only four (i.e. 50%) non-zero numbers, as shown in table 3-4. The result is that fewer computer resources or transmission capacity is required compared to that for the original signal.

Table 3-4. Signal reconstruction after tresholding

30	2	4	10	1	0	20	3
treshold = 4							
30	0	4	10	0	0	20	0
30	30	4	10	0	0	20	0
34	26	40	20	0	0	20	0
34	**34**	**26**	**26**	**60**	**20**	**20**	**20**

The resulting signal is the compressed version of the original signal. Both the original and the compressed signal are shown in figure 3-19.

3.4 Wavelet analysis of circuit breaker measurement data

The measured arc voltages are very capricious, with a lot of sudden jumps, as can be seen from the graphics in the appendix (e.g. figure A-6). As the arc voltage is correlated with the cooling

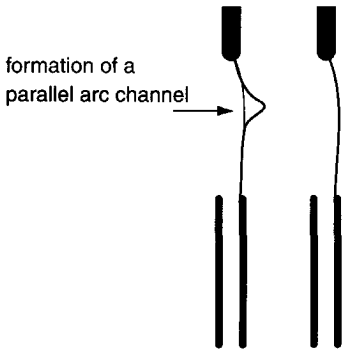

Figure 3-20. Formation of a parallel arc channel

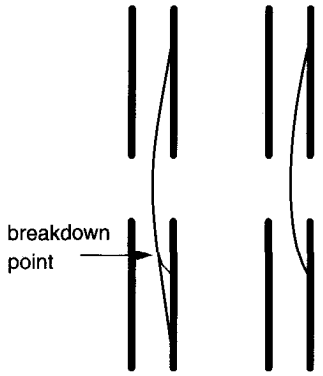

Figure 3-21. Breakdown between the arc and the nozzle (in case of a double-nozzle breaker)

process of the circuit breaker arc, it is interesting to see whether the jumps (or other high-frequent phenomena) in the arc voltage are related to the observed ageing of the contacts, the nozzle or the degradation of the SF_6 gas. As the arc is exposed to a highly pressurized gas flow, the arc is continuous in motion. The jumps in the arc voltage are caused by sudden shortening of the circuit breaker arc, by the formation of a parallel and more stable arc channel as visualized in figure 3-20. In case of a double-nozzle circuit breaker, a sudden breakdown can occur between the arc column and the nozzle [58] as shown in figure 3-21.

Wavelet analysis is applied in this section to quantify the voltage jumps and to locate them in time. The choice for a mother wavelet is not trivial: smooth wavelets indicate a better frequency resolution than wavelets with sharp steps; the opposite applies to time resolution [37]. As lower-order wavelets are more suitable for detecting sudden rapid changes within the signal, the Daubechies db2 (see also figure 3-9) wavelet has been chosen as the mother wavelet. In figure 3-22, it is shown that the sudden jumps in the arc voltage can be identified quite clearly. It is sufficient to compute only one scale in order to pinpoint the jumps in the arc voltage. In this case, the wavelet scale 50 has been used: too high scales have a lower time resolution, while too low scales may fail to detect smaller voltage jumps.

The wavelet transform is made on a 500 µs time window (i.e. 20000 samples) of the arc voltage that ends 25 µs before the arc voltage zero crossing. When the measured arc voltage is transformed by means of the scale 50, db2 wavelet, an appropriate treshold is selected such that only the relevant peaks are detected, while the noise is neglected. After that the number of samples with a non-zero value, i.e. the samples with a significant wavelet coefficient, are summed. The results for poles B (#503003 ... #503403) and C (#503503 ... #504803) of cb2 are shown in figure 3-23. Measurement #502803 of pole B has not been used, while this arc voltage was measured with a lower sensitivity. There is a clear border that separates the interruptions from the reignitions. The same is true for the measurements of pole A (#502103 ... #502503; measurements #502603 and #502703 were measured with a lower sensitivity). The measurements of pole A are not included in figure 3-23 while they were measured with a higher sensitivity than the arc voltages of poles B and C. Consequently, the results cannot be compared in a single plot.

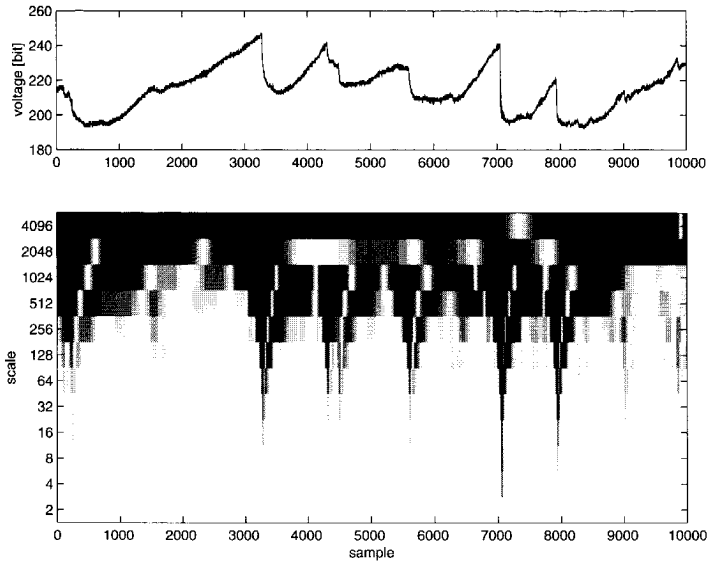

Figure 3-22. CWT (db2) of a piece of a measured arc voltage of cb2 (#502103; sample 20000:30000; 250 μs time window) Dyadic scaling has been applied

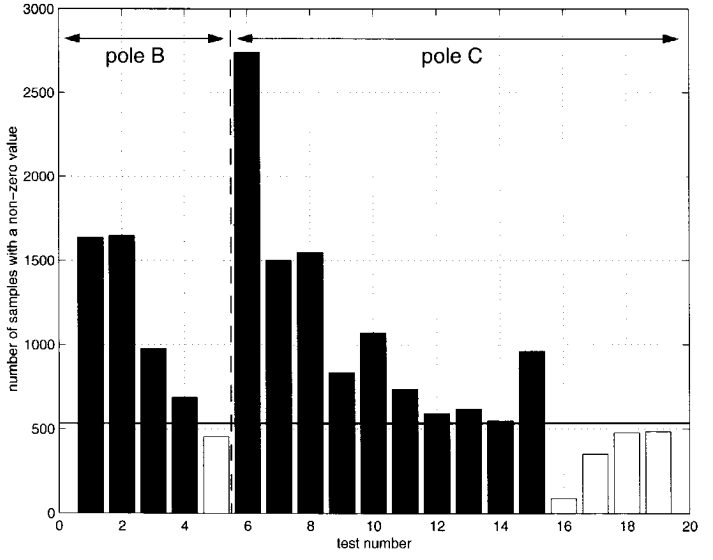

Figure 3-23. Number of samples with significant wavelet coefficients Black bar: interruption. White bar: reignition.

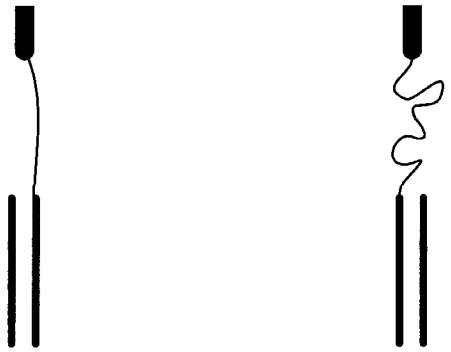

Figure 3-24. A steady arc and a turbulent arc

From the wavelet analysis it appears that the larger the number of (significant) voltage jumps - in a 500 μs time window that ends 25 μs before the arc voltage zero crossing - the more likely that cb2 interrupts the current. Physically, this result indicates that the more turbulent the arc voltage behaves, and the more powerful the cooling process is, the more likely that cb2 interrupts the current. When subjected to turbulent gas flows an arc of longer length and with a higher voltage results (see figure 3-24); this leads to a better interruption probability (see also section 3.2.1). Note however that a voltage jump in the last microseconds before current zero can be detrimental for the interruption probability due to the lower extinguishing peak as shown in figure 3-25.

It is not clear whether the observed phenomenon - the larger the number of voltage jumps the more likely it is that interruption takes place - is a property of this specific breaker only, as this tendency has not been found for cb3 or cb4. However, the voltages of cb3 and cb4 were measured with a lower sensitivity, with which it may have been impossible to detect the phenomenon. The sensitivity of the voltage measurements is shown in table 3-5.

Table 3-5. Sensitivity of the voltage measurements

circuit breaker	measurement	measurement range
cb2	#5021.. #5025	-5 kV.. 5 kV
	#5021.. #5028	-50 kV.. 50 kV
	#5030.. #5048	-10 kV.. 10kV
cb3	all	-50 kV.. 50 kV
cb4	all	-50 kV.. 50 kV

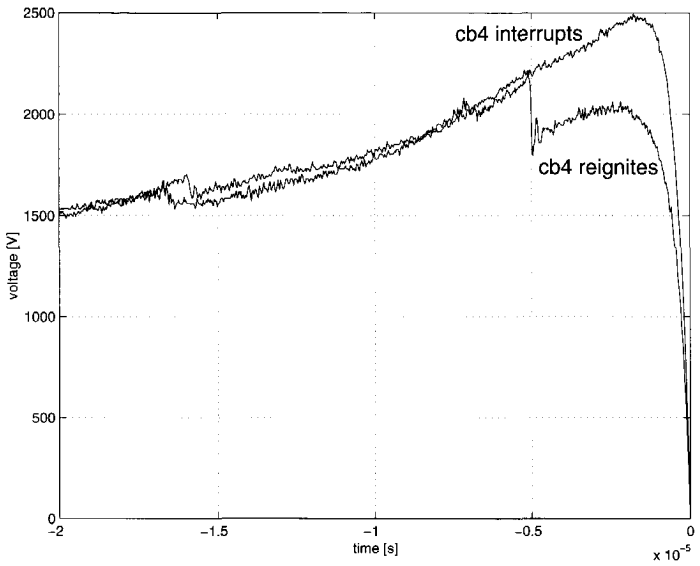

Figure 3-25. A jump in the arc voltage close to the voltage zero crossing can cause a reignition cb4, #5012 (reignition) and #5013 (interruption); identical arcing times and $(di/dt)_0$

3.5 Maxwell and the relation with lumped-circuit theory

In view of the high-frequency phenomena that have been observed in the measured data - such as the jumps in the arc voltage (e.g. figure 3-22) - and the physical dimensions in the high-power laboratory one can raise the question whether a lumped-element model of the test circuit can be applied in arc-circuit studies. It is the electrical size of the structure - its size in terms of the minimum wavelength of interest in the bandwidth over which the model must be valid - that dictates the sophistication and complexity of the required model.

All macroscopic electromagnetic phenomena can be described by Maxwell's equations. The equations express the distributed nature of the electromagnetic fields; the field quantities are functions of the spatial parameters as well as of the time.

Faraday's law relates the electromotive force generated around a closed contour C to the time rate of change of the total magnetic flux through the open surface S bounded by that contour. Or in other words: Faraday's law shows that a time-changing magnetic field can induce an electric field.

$$\oint_C \boldsymbol{E} \cdot d\boldsymbol{l} = -\frac{d}{dt}\int_S \boldsymbol{B} \cdot d\boldsymbol{s} \tag{3-9}$$

$\boldsymbol{E}$ the electric field intensity vector [V/m]
$\boldsymbol{B}$ the magnetic flux density vector [Wb/m^2]

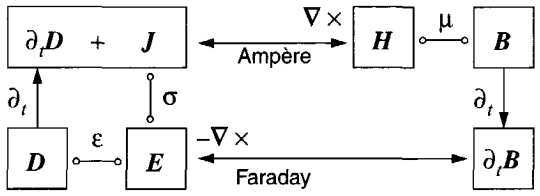

Figure 3-26. Schematical representation of the Maxwell relations

Ampère's law states just the opposite: a time-changing electric field can induce a magnetic field.

$$\oint_C \boldsymbol{H} \cdot d\boldsymbol{l} = \int_S \boldsymbol{J} \cdot d\boldsymbol{s} + \frac{d}{dt}\int_S \boldsymbol{D} \cdot d\boldsymbol{s} \tag{3-10}$$

$\boldsymbol{H}$ the magnetic field intensity vector [A/m]
$\boldsymbol{J}$ the current density vector [A/m^2]
$\boldsymbol{D}$ the electric flux density vector [C/m^2]

Gauss' law for the electric field states that the net flux of the electric flux density vector out of the closed surface S is equivalent to the net positive charge enclosed by the surface. In other words: electric field lines that begin on a positive charge must terminate on an equal amount of negative charge.

$$\oint_S \boldsymbol{D} \cdot d\boldsymbol{s} = \int_V \rho dv \tag{3-11}$$

ρ the volume-free charge density [C/m^3]

Gauss' law for the magnetic field outlines that all magnetic field lines form closed paths, i.e. there are no isolated sources of the magnetic field.

$$\oint_S \boldsymbol{B} \cdot d\boldsymbol{s} = 0 \tag{3-12}$$

In differential form, the Maxwell's equations are described hereunder and visualized in figure 3-26.

$$\nabla \times \boldsymbol{E} = -\frac{\partial \boldsymbol{B}}{\partial t} \tag{3-13}$$

$$\nabla \times \boldsymbol{H} = \boldsymbol{J} + \frac{\partial \boldsymbol{D}}{\partial t} \tag{3-14}$$

$$\nabla \cdot \boldsymbol{D} = \rho \tag{3-15}$$

$$\nabla \cdot \boldsymbol{B} = 0 \tag{3-16}$$

Circuit theory can be regarded as describing a restricted class of solutions of Maxwell's equations. In the following sections, power series approximations will be applied to describe the electromagnetic field. It is shown that the zero and first-order terms in these approximations (i.e. the quasi-static fields) form the basis for the lumped-circuit theory. By means of the second-order terms, the validity of the lumped-circuit theory at various frequencies can be estimated.

3.5.1 Power series approach to time-varying fields

The theory and applications in the following sections are mainly based on the text book of Magid [42].

All electromagnetic fields will, in general, alter their shape and behavior as a function of the frequency ω. The following series expansion can be made for all the field quantities (such as $\boldsymbol{E}$, $\boldsymbol{H}$, $\boldsymbol{J}$, ρ etc.).

$$\boldsymbol{E}(x, y, z, \tau, \omega) = \boldsymbol{e}_0(x, y, z, \tau) + \omega \boldsymbol{e}_1(x, y, z, \tau) + \omega^2 \boldsymbol{e}_2(x, y, z, \tau) + \ldots \tag{3-17}$$

Where τ is defined as $\tau = \omega t$. The expansion terms are independent of ω and the k^{th} term is given by

$$\boldsymbol{e}_k(x, y, z, \tau) = \frac{1}{k!}\left(\frac{\partial^k \boldsymbol{E}(x, y, z, \tau, \omega)}{\partial \omega^k}\right)_{\omega = 0} \tag{3-18}$$

Substitution of the power series into the field laws gives

$$\nabla \times \boldsymbol{E} = -\frac{\partial \boldsymbol{B}}{\partial t} = -\frac{\partial \boldsymbol{B}}{\partial \tau} \cdot \frac{\partial \tau}{\partial t} = -\omega \frac{\partial \boldsymbol{B}}{\partial \tau} \tag{3-19}$$

$$\begin{aligned} \nabla \times \boldsymbol{E} &= ((\nabla \times \boldsymbol{e}_0) + \omega(\nabla \times \boldsymbol{e}_1) + \omega^2(\nabla \times \boldsymbol{e}_2) + \ldots) = \\ &= -\omega \frac{\partial \boldsymbol{B}}{\partial \tau} = -\left(\omega\left(\frac{\partial \boldsymbol{b}_0}{\partial \tau}\right) + \omega^2\left(\frac{\partial \boldsymbol{b}_1}{\partial \tau}\right) + \omega^3\left(\frac{\partial \boldsymbol{b}_2}{\partial \tau}\right) + \ldots\right) \end{aligned} \tag{3-20}$$

Combining terms leads to

$$\left((\nabla \times \boldsymbol{e}_0) + \omega\left(\nabla \times \boldsymbol{e}_1 + \frac{\partial \boldsymbol{b}_0}{\partial \tau}\right) + \omega^2\left(\nabla \times \boldsymbol{e}_2 + \frac{\partial \boldsymbol{b}_1}{\partial \tau}\right) + \ldots\right) = 0 \tag{3-21}$$

This equation must hold for every possible frequency ω. Therefore, the coefficients of all the powers of ω are each separately equal to zero, leading to the following general equation

$$\nabla \times \boldsymbol{e}_k = -\frac{\partial \boldsymbol{b}_{k-1}}{\partial \tau} \tag{3-22}$$

Similar results follow from the corresponding equations obtained from each of the other basic field laws.

The power series notation can be simplified by absorbing the various powers of ω directly into each of the terms of the power series expansion.

$$\begin{aligned} \boldsymbol{E}(x, y, z, \tau, \omega) &= \boldsymbol{e}_0(x, y, z, \tau) + \omega \boldsymbol{e}_1(x, y, z, \tau) + \omega^2 \boldsymbol{e}_2(x, y, z, \tau) + \ldots \\ &= \boldsymbol{E}_0(x, y, z, \tau, \omega) + \boldsymbol{E}_1(x, y, z, \tau, \omega) + \boldsymbol{E}_2(x, y, z, \tau, \omega) + \ldots \end{aligned} \tag{3-23}$$

The k^{th} term of the series is taken as follows

$$\boldsymbol{E}_k(x, y, z, \tau, \omega) = \omega^k \boldsymbol{e}_k(x, y, z, \tau) \tag{3-24}$$

The field laws can be written in terms of only $\boldsymbol{E}_k$ and $\boldsymbol{B}_k$, without explicit appearance of ω^k.

$$\nabla \times \boldsymbol{E}_k = \nabla \times (\omega^k \boldsymbol{e}_k) = -\omega^k \frac{\partial \boldsymbol{b}_{k-1}}{\partial \tau} = -\omega \frac{\partial \boldsymbol{B}_{k-1}}{\partial \tau} = -\frac{\partial \boldsymbol{B}_{k-1}}{\partial t} \tag{3-25}$$

The resulting set of equations is shown in table 3-6.

Table 3-6. Electromagnetic-field relations expressed in zero, first and k^{th}-order terms

order	field laws
zero order	$\nabla \times \boldsymbol{E}_0 = 0$ $\nabla \times \boldsymbol{H}_0 = \boldsymbol{J}_0$ $\nabla \cdot \boldsymbol{D}_0 = \rho_0$ $\nabla \cdot \boldsymbol{B}_0 = 0$ $\nabla \cdot \boldsymbol{J}_0 = 0$
first order	$\nabla \times \boldsymbol{E}_1 = -\frac{\partial \boldsymbol{B}_0}{\partial t}$ $\nabla \times \boldsymbol{H}_1 = \boldsymbol{J}_1 + \frac{\partial \boldsymbol{D}_0}{\partial t}$ $\nabla \cdot \boldsymbol{D}_1 = \rho_1$ $\nabla \cdot \boldsymbol{B}_1 = 0$ $\nabla \cdot \boldsymbol{J}_1 = \frac{\partial \rho_0}{\partial t}$
k^{th} order	$\nabla \times \boldsymbol{E}_k = -\frac{\partial \boldsymbol{B}_{k-1}}{\partial t}$ $\nabla \times \boldsymbol{H}_k = \boldsymbol{J}_k + \frac{\partial \boldsymbol{D}_{k-1}}{\partial t}$ $\nabla \cdot \boldsymbol{D}_k = \rho_k$ $\nabla \cdot \boldsymbol{B}_k = 0$ $\nabla \cdot \boldsymbol{J}_k = \frac{\partial \rho_{k-1}}{\partial t}$

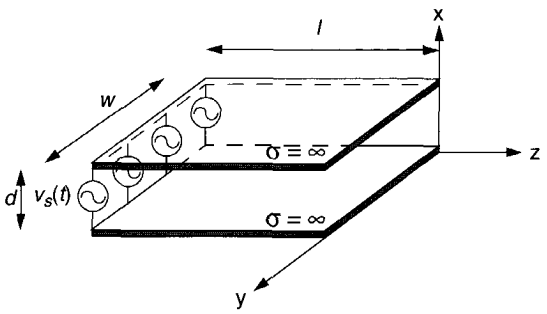

Figure 3-27. Parallel-plate capacitor in air
All fringing in the resulting fields can be neglected as $l >> d$ and $w >> d$

The series expansions should be solved as follows. First, the zero-order terms are determined. When the zero-order terms are known, the first-order terms can be computed. This step-by-step calculation goes on for all the higher-order terms until the required degree of accuracy has been reached.

The static field is described by only the zero-order terms, i.e. the time variation of the electromagnetic field is completely neglected. The quasi-static field is described by the zero-order and first-order terms. In the next section we will see that the base of circuit theory follows directly from Maxwell's equations as quasi-static approximations.

3.5.2 Quasi-static field of a parallel-plate capacitor

Consider the parallel-plate capacitor in air as shown in figure 3-27. The plates consist of perfectly conducting material ($\sigma = \infty$) and the length and width of the plates are much larger than their separation distance, so that all fringing in the resulting fields can be neglected. Therefore, all variation in $\boldsymbol{E}$ and $\boldsymbol{H}$ with both x and y can be neglected within this system:

$$\frac{\partial}{\partial x} = \frac{\partial}{\partial y} = 0 \tag{3-26}$$

The system is excited with a low-frequency sinusoidal excitation, which is uniformly distributed between the plates (at $z = -l$), such that a fixed reference voltage between the plates in the $z = 0$ plane is maintained:

$$v_r = A\cos(\omega t) \tag{3-27}$$

Since the reference voltage has an amplitude that is independent of the frequency ω, it follows that the power series expansion consists solely of a zero-order term equal in value to the reference voltage:

$$\begin{aligned} v_0(z = 0, t) &= v_r(t) = A\cos(\omega t) \\ v_k(z = 0, t) &= 0 \qquad \text{for} \quad k \geq 1 \end{aligned} \tag{3-28}$$

Quasi-static solution

The zero-order time-varying electromagnetic fields in this system are identical in form to their static (DC) counterparts:

$$\boldsymbol{E}_0 = -\boldsymbol{i}_x \frac{A\cos(\omega t)}{d} \tag{3-29}$$

$\boldsymbol{i}$ unit vector

$$\boldsymbol{H}_0 = 0 \tag{3-30}$$

The first-order contributions to the magnetic field can be derived from the first-order field laws in table 3-6.

$$\nabla \times \boldsymbol{H}_1 = \varepsilon_0 \frac{\partial \boldsymbol{E}_0}{\partial t} = \boldsymbol{i}_x \frac{\omega \varepsilon_0 A \sin(\omega t)}{d} \tag{3-31}$$

$$\nabla \cdot \mu_0 \boldsymbol{H}_1 = 0 \tag{3-32}$$

with

$$\nabla \times \boldsymbol{H}_1 = \boldsymbol{i}_x\left(\frac{\partial \boldsymbol{H}_{1z}}{\partial y} - \frac{\partial \boldsymbol{H}_{1y}}{\partial z}\right) + \boldsymbol{i}_y\left(\frac{\partial \boldsymbol{H}_{1x}}{\partial z} - \frac{\partial \boldsymbol{H}_{1z}}{\partial x}\right) + \boldsymbol{i}_z\left(\frac{\partial \boldsymbol{H}_{1y}}{\partial x} - \frac{\partial \boldsymbol{H}_{1x}}{\partial y}\right) \tag{3-33}$$

Combining equation 3-31 and 3-33 results in:

$$\underbrace{\frac{\partial \boldsymbol{H}_{1z}}{\partial y}}_{0} - \frac{\partial \boldsymbol{H}_{1y}}{\partial z} = \frac{\omega \varepsilon_0 A \sin(\omega t)}{d} \tag{3-34}$$

The first-order magnetic field within the enclosed air region in this system is:

$$\boldsymbol{H}_1 = \boldsymbol{i}_y \boldsymbol{H}_{1y} = -\boldsymbol{i}_y \frac{\omega \varepsilon_0 A \sin(\omega t)}{d} z \tag{3-35}$$

Note that equation 3-32 is satisfied, as $\boldsymbol{H}_{1y}$ is independent of y (and $\boldsymbol{H}_{1x} = \boldsymbol{H}_{1z} = 0$).

$$\nabla \cdot \mu_0 \boldsymbol{H}_1 = \mu_0\left(\frac{\partial \boldsymbol{H}_{1x}}{\partial x} + \frac{\partial \boldsymbol{H}_{1y}}{\partial y} + \frac{\partial \boldsymbol{H}_{1z}}{\partial z}\right) = 0 \tag{3-36}$$

The first-order contributions to the electric field can be derived from the first-order field laws in table 3-6.

$$\nabla \times \boldsymbol{E}_1 = -\mu_0 \frac{\partial \boldsymbol{H}_0}{\partial t} = 0 \tag{3-37}$$

$$\nabla \cdot \varepsilon_0 \boldsymbol{E}_1 = \rho_1 = 0 \tag{3-38}$$

Equation 3-37 equals zero as $\boldsymbol{H}_0$ equals zero for all time (equation 3-30) and so does its time derivative. Equation 3-38 equals zero as the enclosed air region is free of charge (for all fre-

quencies ω and time t) due to its insulating nature. The first-order electric field within the enclosed air region in this system, is:

$$\boldsymbol{E}_1 = 0 \tag{3-39}$$

As a result, the expressions for the non-fringing fields between the plates of the capacitor correct up to and including the first-order terms are

$$\boldsymbol{E}_{0,1} = \boldsymbol{E}_0 + \underbrace{\boldsymbol{E}_1}_{0} = -\boldsymbol{i}_x \frac{A\cos(\omega t)}{d} \tag{3-40}$$

$$\boldsymbol{H}_{0,1} = \underbrace{\boldsymbol{H}_0}_{0} + \boldsymbol{H}_1 = -\boldsymbol{i}_y \frac{\omega\varepsilon_0 A\sin(\omega t)}{d} z \tag{3-41}$$

For the voltage applied to the parallel-plate capacitor, correct up to and including the first-order contributions, it must hold that

$$[v_s(t)]_{0,1} = -\int_{x=0}^{d} (E_{0,1})_{z=-l}\, dx = A\cos(\omega t) \tag{3-42}$$

For the source current, correct up to and including the first-order contributions, it yields

$$[i_s(t)]_{0,1} = -\int_{y=0}^{w} (H_{0,1})_{z=-l}\, dy = -\frac{\varepsilon_0 lw}{d}\omega A\sin(\omega t) \tag{3-43}$$

The input impedance of the parallel-plate capacitor, correct up to and including first-order contributions, can be computed from the ratio between the phasor representations of v_s and i_s.

$$[V_s]_{0,1} = A \tag{3-44}$$

$$[I_s]_{0,1} = j\omega A\frac{\varepsilon_0 lw}{d} \tag{3-45}$$

$$Z_{0,1} = \frac{[V_s]_{0,1}}{[I_s]_{0,1}} = \frac{1}{j\omega\dfrac{\varepsilon_0 lw}{d}} = \frac{1}{j\omega C} \tag{3-46}$$

The lumped-element representation of the parallel-plate capacitor, correct up to and including first-order contributions, is a lumped capacitor C, where the value of the capacitance equals the DC or static capacitance of the parallel-plate system.

$$C = C_{dc} = \frac{\varepsilon_0 lw}{d} \tag{3-47}$$

Validity of the quasi-static approach

In order to check the validity of the quasi-static approximation, we compute the second-order contributions to the power series of the electric and magnetic field. The second-order magnetic field $\boldsymbol{H}_2$ is generated by the time rate of change of the first-order electric field $\boldsymbol{E}_1$ (table 3-6). But with $\boldsymbol{E}_1$ equal to zero at all points in the system, we can expect $\boldsymbol{H}_2$ to be equal to zero at all points in the system as well.

$$\boldsymbol{H}_2 = 0 \tag{3-48}$$

The second-order contributions to the electric field can be derived from the k^{th}-order ($k = 2$) field laws in table 3-6, and the first-order magnetic field in equation 3-35.

$$\nabla \times \boldsymbol{E}_2 = -\mu_0 \frac{\partial \boldsymbol{H}_1}{\partial t} = \boldsymbol{i}_y \frac{\omega^2 \mu_0 \varepsilon_0 A \cos(\omega t)}{d} z \tag{3-49}$$

$$\nabla \cdot \varepsilon_0 \boldsymbol{E}_2 = \rho_2 = 0 \tag{3-50}$$

with

$$\nabla \times \boldsymbol{E}_2 = \boldsymbol{i}_x \left(\frac{\partial \boldsymbol{E}_{2z}}{\partial y} - \frac{\partial \boldsymbol{E}_{2y}}{\partial z} \right) + \boldsymbol{i}_y \left(\frac{\partial \boldsymbol{E}_{2x}}{\partial z} - \frac{\partial \boldsymbol{E}_{2z}}{\partial x} \right) + \boldsymbol{i}_z \left(\frac{\partial \boldsymbol{E}_{2y}}{\partial x} - \frac{\partial \boldsymbol{E}_{2x}}{\partial y} \right) \tag{3-51}$$

Combining equation 3-49 and 3-51 results in:

$$\frac{\partial \boldsymbol{E}_{2x}}{\partial z} - \underbrace{\frac{\partial \boldsymbol{E}_{2z}}{\partial x}}_{0} = \frac{\omega^2 \mu_0 \varepsilon_0 A \cos(\omega t)}{d} z \tag{3-52}$$

The second-order electric field within the enclosed air region in this system is:

$$\boldsymbol{E}_2 = \boldsymbol{i}_x \boldsymbol{E}_{2x} = \boldsymbol{i}_x \frac{\omega^2 \mu_0 \varepsilon_0 A \cos(\omega t)}{d} \frac{z^2}{2} \tag{3-53}$$

Note that equation 3-50 is satisfied, as $\boldsymbol{E}_{2x}$ is independent of x (and $\boldsymbol{E}_{2y} = \boldsymbol{E}_{2z} = 0$).

$$\nabla \cdot \varepsilon_0 \boldsymbol{E}_2 = \varepsilon_0 \left(\frac{\partial \boldsymbol{E}_{2x}}{\partial x} + \frac{\partial \boldsymbol{E}_{2y}}{\partial y} + \frac{\partial \boldsymbol{E}_{2z}}{\partial z} \right) = 0 \tag{3-54}$$

The expressions for the non-fringing fields between the plates of the capacitor correct up to and including the second-order terms are

$$\boldsymbol{E}_{0,1,2} = \boldsymbol{E}_0 + \underbrace{\boldsymbol{E}_1}_{0} + \boldsymbol{E}_2 = -\boldsymbol{i}_x \frac{A \cos(\omega t)}{d} \left(1 - \frac{\omega^2 \mu_0 \varepsilon_0 z^2}{2} \right) \tag{3-55}$$

$$\boldsymbol{H}_{0,1,2} = \underbrace{\boldsymbol{H}_0}_{0} + \boldsymbol{H}_1 + \underbrace{\boldsymbol{H}_2}_{0} = -\boldsymbol{i}_y \frac{\omega\varepsilon_0 A \sin(\omega t)}{d} z \tag{3-56}$$

For the voltage applied to the parallel-plate capacitor, correct up to and including the second-order contributions, it must hold that

$$[v_s(t)]_{0,1,2} = -\int_{x=0}^{d} (E_{0,1,2})_{z=-l}\, dx = A\cos(\omega t)\left(1 - \frac{\omega^2\mu_0\varepsilon_0 l^2}{2}\right) \tag{3-57}$$

For the source current, correct up to and including second-order contributions, it yields

$$[i_s(t)]_{0,1,2} = -\int_{y=0}^{w} (H_{0,1,2})_{z=-l}\, dy = -\frac{\varepsilon_0 lw}{d}\omega A \sin(\omega t) \tag{3-58}$$

The input impedance of the parallel-plate capacitor, correct up to and including second-order contributions, can be computed from the ratio between the phasor representations of v_s and i_s.

$$[V_s]_{0,1,2} = A\left(1 - \frac{\omega^2\mu_0\varepsilon_0 l^2}{2}\right) \tag{3-59}$$

$$[I_s]_{0,1,2} = j\omega A \frac{\varepsilon_0 lw}{d} \tag{3-60}$$

$$Z_{0,1,2} = \frac{[V_s]_{0,1,2}}{[I_s]_{0,1,2}} = \frac{1}{j\omega\dfrac{\varepsilon_0 lw}{d}}\left(1 - \frac{\omega^2\mu_0\varepsilon_0 l^2}{2}\right) = \frac{1}{j\omega C}(1 - \omega^2 LC) \tag{3-61}$$

The lumped-element representation of the parallel-plate capacitor, correct up to and including second-order contributions, is an LC network, where the values of the capacitance and the inductance are specified as follows

$$C = C_{dc} = \frac{\varepsilon_0 lw}{d} \tag{3-62}$$

$$L = \frac{1}{2}\left(\frac{\mu_0 ld}{w}\right) \tag{3-63}$$

The quasi-static approach is valid only when the second-order contribution is negligible

$$\frac{\omega^2\mu_0\varepsilon_0 l^2}{2} << 1 \tag{3-64}$$

The wavelength of an EM wave is defined as:

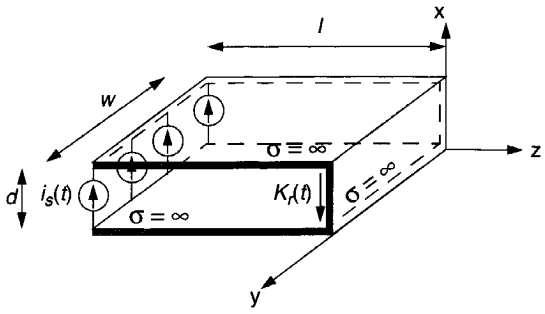

Figure 3-28. Single-turn inductor in air
All fringing in the resulting fields can be neglected as l >> d and w >> d

$$\lambda = \frac{2\pi}{\omega\sqrt{\mu_0\varepsilon_0}} \tag{3-65}$$

The use of the circuit theory model of a lumped capacitor for the parallel-plate system is justified as long as the values of the wavelength (λ) are much higher than the length of the plates (l):

$$\frac{\omega^2\mu_0\varepsilon_0 l^2}{2} = 2\pi^2\left(\frac{l}{\lambda}\right)^2 << 1 \tag{3-66}$$

3.5.3 Quasi-static field of a single-turn inductor

Consider the single-turn inductor in air as shown in figure 3-28. The plates consist of perfectly conducting material ($\sigma = \infty$) and the length and width of the plates are much larger than their separation distance, so that all fringing in the resulting fields can be neglected. Therefore, all variation in $\boldsymbol{E}$ and $\boldsymbol{H}$ with both x and y can be neglected within this system:

$$\frac{\partial}{\partial x} = \frac{\partial}{\partial y} = 0 \tag{3-67}$$

The system is fed by a low-frequency sinusoidal current source (at $z = -l$), such that the reference surface current density:

$$K_r = A\cos(\omega t) \tag{3-68}$$

Quasi-static solution

The zero-order time-varying electromagnetic fields in this system are identical in form to their static (DC) counterparts:

$$\boldsymbol{H}_0 = -\boldsymbol{i}_y K_r = -\boldsymbol{i}_y A\cos(\omega t) \tag{3-69}$$

$$\boldsymbol{E}_0 = 0 \tag{3-70}$$

The first-order contributions to the electric field can be derived from the first-order field laws in table 3-6.

$$\nabla \times \boldsymbol{E}_1 = -\mu_0 \frac{\partial \boldsymbol{H}_0}{\partial t} = -\boldsymbol{i}_y \mu_0 \omega A \sin(\omega t) \tag{3-71}$$

$$\nabla \cdot \varepsilon_0 \boldsymbol{E}_1 = \rho_1 = 0 \tag{3-72}$$

with

$$\nabla \times \boldsymbol{E}_1 = \boldsymbol{i}_x \left(\frac{\partial \boldsymbol{E}_{1z}}{\partial y} - \frac{\partial \boldsymbol{E}_{1y}}{\partial z} \right) + \boldsymbol{i}_y \left(\frac{\partial \boldsymbol{E}_{1x}}{\partial z} - \frac{\partial \boldsymbol{E}_{1z}}{\partial x} \right) + \boldsymbol{i}_z \left(\frac{\partial \boldsymbol{E}_{1y}}{\partial x} - \frac{\partial \boldsymbol{E}_{1x}}{\partial y} \right) \tag{3-73}$$

Combining equation 3-71 and 3-73 results in:

$$\frac{\partial \boldsymbol{E}_{1x}}{\partial z} - \underbrace{\frac{\partial \boldsymbol{E}_{1z}}{\partial x}}_{0} = -\mu_0 \omega A \sin(\omega t) \tag{3-74}$$

The first-order electric field within the enclosed air region in this system is:

$$\boldsymbol{E}_1 = \boldsymbol{i}_x \boldsymbol{E}_{1x} = -\boldsymbol{i}_x \mu_0 \omega z A \sin(\omega t) \tag{3-75}$$

Note that equation 3-72 is satisfied, as $\boldsymbol{E}_{1x}$ is independent of x (and $\boldsymbol{E}_{1y} = \boldsymbol{E}_{1z} = 0$).

$$\nabla \cdot \varepsilon_0 \boldsymbol{E}_1 = \varepsilon_0 \left(\frac{\partial \boldsymbol{E}_{1x}}{\partial x} + \frac{\partial \boldsymbol{E}_{1y}}{\partial y} + \frac{\partial \boldsymbol{E}_{1z}}{\partial z} \right) = 0 \tag{3-76}$$

The first-order contributions to the magnetic field can be derived from the first-order field laws in table 3-6.

$$\nabla \times \boldsymbol{H}_1 = \varepsilon_0 \frac{\partial \boldsymbol{E}_0}{\partial t} = 0 \tag{3-77}$$

$$\nabla \cdot \mu_0 \boldsymbol{H}_1 = 0 \tag{3-78}$$

The first-order magnetic field within the enclosed air region in this system is:

$$\boldsymbol{H}_1 = 0 \tag{3-79}$$

As a result, the expressions for the non-fringing fields of the inductor correct up to and including first-order terms are

$$\boldsymbol{E}_{0,1} = \underbrace{\boldsymbol{E}_0}_{0} + \boldsymbol{E}_1 = -\boldsymbol{i}_x \mu_0 \omega z A \sin(\omega t) \tag{3-80}$$

$$\boldsymbol{H}_{0,1} = \boldsymbol{H}_0 + \underbrace{\boldsymbol{H}_1}_{0} = -\boldsymbol{i}_y A \cos(\omega t) \tag{3-81}$$

For the voltage across the current source, correct up to and including first-order contributions, it must hold that

$$[v_s(t)]_{0,1} = -\int_{x=0}^{d} (E_{0,1})_{z=-l}\,dx = -\mu_0\omega l d A \sin(\omega t) \tag{3-82}$$

For the source current, correct up to and including first-order contributions, it yields

$$[i_s(t)]_{0,1} = -\int_{y=0}^{w} (H_{0,1})_{z=-l}\,dy = wA\cos(\omega t) \tag{3-83}$$

The input impedance of the single-turn inductor, correct up to and including first-order contributions, can be computed from the ratio between the phasor representations of v_s and i_s.

$$[V_s]_{0,1} = j\mu_0\omega l d A \tag{3-84}$$

$$[I_s]_{0,1} = wA \tag{3-85}$$

$$Z_{0,1} = \frac{[V_s]_{0,1}}{[I_s]_{0,1}} = \frac{j\mu_0\omega l d A}{wA} = j\omega\frac{\mu_0 l d}{w} = j\omega L \tag{3-86}$$

The lumped-element representation of the single-turn inductor, correct up to and including first-order contributions, is a lumped inductor L, where the value of the inductance equals the DC or static inductance of the single-turn inductor.

$$L = L_{dc} = \frac{\mu_0 l d}{w} \tag{3-87}$$

Validity of the quasi-static approach

In order to check the validity of the quasi-static approximation, we compute the second-order contributions to the power series of the electric and magnetic field. The second-order electric field $\boldsymbol{E}_2$ is generated by the time rate of change of the first-order magnetic field $\boldsymbol{H}_1$ (table 3-6). But with $\boldsymbol{H}_1$ equal to zero at all points in the system, we can expect $\boldsymbol{E}_2$ to be equal to zero at all points in the system as well.

$$\boldsymbol{E}_2 = 0 \tag{3-88}$$

The second-order contributions to the magnetic field can be derived from the k^{th}-order ($k = 2$) field laws in table 3-6, and the first-order electric field in equation 3-75.

$$\nabla \times \boldsymbol{H}_2 = \varepsilon_0\frac{\partial \boldsymbol{E}_1}{\partial t} = -\boldsymbol{i}_x\omega^2\mu_0\varepsilon_0 z A\cos(\omega t) \tag{3-89}$$

$$\nabla \cdot \mu_0\boldsymbol{H}_2 = 0 \tag{3-90}$$

with

$$\nabla \times \boldsymbol{H}_2 = \boldsymbol{i}_x\left(\frac{\partial \boldsymbol{H}_{2z}}{\partial y} - \frac{\partial \boldsymbol{H}_{2y}}{\partial z}\right) + \boldsymbol{i}_y\left(\frac{\partial \boldsymbol{H}_{2x}}{\partial z} - \frac{\partial \boldsymbol{H}_{2z}}{\partial x}\right) + \boldsymbol{i}_z\left(\frac{\partial \boldsymbol{H}_{2y}}{\partial x} - \frac{\partial \boldsymbol{H}_{2x}}{\partial y}\right) \tag{3-91}$$

Combining equation 3-89 and 3-91 results in:

$$\underbrace{\frac{\partial \boldsymbol{H}_{2z}}{\partial y}}_{0} - \frac{\partial \boldsymbol{H}_{2y}}{\partial z} = -\omega^2 \mu_0 \varepsilon_0 z A \cos(\omega t) \tag{3-92}$$

The second-order magnetic field within the enclosed air region in this system is:

$$\boldsymbol{H}_2 = \boldsymbol{i}_y \boldsymbol{H}_{2y} = \boldsymbol{i}_y \frac{\omega^2 \mu_0 \varepsilon_0 z^2}{2} A \cos(\omega t) \tag{3-93}$$

Note that equation 3-90 is satisfied, as $\boldsymbol{H}_{2y}$ is independent of y (and $\boldsymbol{H}_{2x} = \boldsymbol{H}_{2z} = 0$).

$$\nabla \cdot \mu_0 \boldsymbol{H}_2 = \mu_0\left(\frac{\partial \boldsymbol{H}_{2x}}{\partial x} + \frac{\partial \boldsymbol{H}_{2y}}{\partial y} + \frac{\partial \boldsymbol{H}_{2z}}{\partial z}\right) = 0 \tag{3-94}$$

The expressions for the non-fringing fields of the inductor correct up to and including second-order terms are

$$\boldsymbol{E}_{0,1,2} = \underbrace{\boldsymbol{E}_0}_{0} + \boldsymbol{E}_1 + \underbrace{\boldsymbol{E}_2}_{0} = -\boldsymbol{i}_x \mu_0 \omega z A \sin(\omega t) \tag{3-95}$$

$$\boldsymbol{H}_{0,1,2} = \boldsymbol{H}_0 + \underbrace{\boldsymbol{H}_1}_{0} + \boldsymbol{H}_2 = -\boldsymbol{i}_y A \cos(\omega t)\left(1 - \frac{\omega^2 \mu_0 \varepsilon_0 z^2}{2}\right) \tag{3-96}$$

For the voltage across the current source, correct up to and including second-order contributions, it must hold that

$$[v_s(t)]_{0,1,2} = -\int_{x=0}^{d} (E_{0,1,2})_{z=-l}\, dx = -\mu_0 \omega l d A \sin(\omega t) \tag{3-97}$$

For the source current, correct up to and including second-order contributions, it yields

$$[i_s(t)]_{0,1,2} = -\int_{y=0}^{w} (H_{0,1,2})_{z=-l}\, dy = wA\cos(\omega t)\left(1 - \frac{\omega^2 \mu_0 \varepsilon_0 l^2}{2}\right) \tag{3-98}$$

The input impedance of the single-turn inductor, correct up to and including second-order contributions, can be computed from the ratio between the phasor representations of v_s and i_s.

$$[V_s]_{0,1,2} = j\mu_0 \omega l d A \tag{3-99}$$

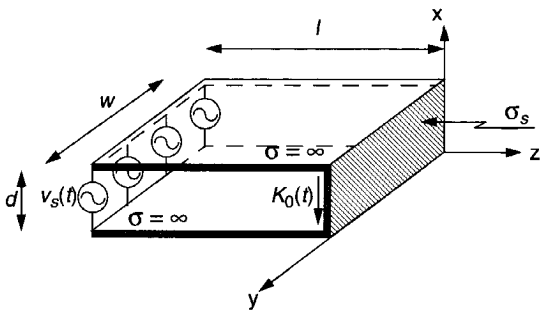

Figure 3-29. Resistor in air
All fringing in the resulting fields can be neglected as l >> d and w >> d

$$[I_s]_{0,1,2} = wA\left(1 - \frac{\omega^2\mu_0\varepsilon_0 l^2}{2}\right) \tag{3-100}$$

$$Z_{0,1,2} = \frac{[V_s]_{0,1,2}}{[I_s]_{0,1,2}} = \frac{j\omega\mu_0 ldA}{wA\left(1 - \frac{\omega^2\mu_0\varepsilon_0 l^2}{2}\right)} = \frac{j\omega L}{(1 - \omega^2 LC)} \tag{3-101}$$

The lumped-element representation of the single-turn inductor, correct up to and including second-order contributions, is an LC network, where the values of the capacitance and the inductance are specified as follows

$$L = L_{dc} = \frac{\mu_0 ld}{w} \tag{3-102}$$

$$C = \frac{1}{2}\left(\frac{\varepsilon_0 lw}{d}\right) \tag{3-103}$$

The quasi-static approach is valid only when the second-order contribution is negligible:

$$\frac{\omega^2\mu_0\varepsilon_0 l^2}{2} = 2\pi^2\left(\frac{l}{\lambda}\right)^2 << 1 \tag{3-104}$$

This result is identical to what we found in section 3.5.2 for the parallel-plate capacitor.

3.5.4 Quasi-static field of a resistor

Consider the resistor in air as shown in figure 3-29, formed by placing a resistive sheet of uniform surface conductivity σ_s at one end of two perfectly conducting plates ($\sigma = \infty$). The length and width of the plates are much larger than their separation distance, so that all fringing in the resulting fields can be neglected. Therefore, all variation in $\boldsymbol{E}$ and $\boldsymbol{H}$ with both x and y can be neglected within this system:

$$\frac{\partial}{\partial x} = \frac{\partial}{\partial y} = 0 \tag{3-105}$$

The system is excited with a low-frequency sinusoidal excitation, which is uniformly distributed between the plates (at $z = -l$), such that a fixed reference voltage across the resistive sheet (in the $z = 0$ plane) is maintained:

$$v_r = A\cos(\omega t) \tag{3-106}$$

Quasi-static solution

The zero-order time-varying electromagnetic fields in this system are identical in form to their static (DC) counterparts:

$$\boldsymbol{E}_0 = -\boldsymbol{i}_x \frac{v_r}{d} = -\boldsymbol{i}_x \frac{A\cos(\omega t)}{d} \tag{3-107}$$

$$\boldsymbol{H}_0 = -\boldsymbol{i}_y \frac{\sigma_s v_r}{d} = -\boldsymbol{i}_y \frac{\sigma_s A\cos(\omega t)}{d} \tag{3-108}$$

The first-order contributions to the electric field can be derived from the first-order field laws in table 3-6.

$$\nabla \times \boldsymbol{E}_1 = -\mu_0 \frac{\partial \boldsymbol{H}_0}{\partial t} = -\boldsymbol{i}_y \frac{\mu_0 \sigma_s \omega A \sin(\omega t)}{d} \tag{3-109}$$

$$\nabla \cdot \varepsilon_0 \boldsymbol{E}_1 = \rho_1 = 0 \tag{3-110}$$

with

$$\nabla \times \boldsymbol{E}_1 = \boldsymbol{i}_x\left(\frac{\partial \boldsymbol{E}_{1z}}{\partial y} - \frac{\partial \boldsymbol{E}_{1y}}{\partial z}\right) + \boldsymbol{i}_y\left(\frac{\partial \boldsymbol{E}_{1x}}{\partial z} - \frac{\partial \boldsymbol{E}_{1z}}{\partial x}\right) + \boldsymbol{i}_z\left(\frac{\partial \boldsymbol{E}_{1y}}{\partial x} - \frac{\partial \boldsymbol{E}_{1x}}{\partial y}\right) \tag{3-111}$$

Combining equation 3-109 and 3-111 results in:

$$\frac{\partial \boldsymbol{E}_{1x}}{\partial z} - \underbrace{\frac{\partial \boldsymbol{E}_{1z}}{\partial x}}_{0} = -\frac{\mu_0 \sigma_s \omega A \sin(\omega t)}{d} \tag{3-112}$$

The first-order electric field within the enclosed air region in this system is:

$$\boldsymbol{E}_1 = \boldsymbol{i}_x \boldsymbol{E}_{1x} = -\boldsymbol{i}_x \frac{\mu_0 \sigma_s \omega z A \sin(\omega t)}{d} \tag{3-113}$$

Note that equation 3-110 is satisfied, as $\boldsymbol{E}_{1x}$ is independent of x (and $\boldsymbol{E}_{1y} = \boldsymbol{E}_{1z} = 0$).

$$\nabla \cdot \varepsilon_0 \boldsymbol{E}_1 = \varepsilon_0\left(\frac{\partial \boldsymbol{E}_{1x}}{\partial x} + \frac{\partial \boldsymbol{E}_{1y}}{\partial y} + \frac{\partial \boldsymbol{E}_{1z}}{\partial z}\right) = 0 \tag{3-114}$$

The first-order contributions to the magnetic field can be derived from the first-order field laws in table 3-6.

$$\nabla \times \boldsymbol{H}_1 = \varepsilon_0 \frac{\partial \boldsymbol{E}_0}{\partial t} = \boldsymbol{i}_x \frac{\varepsilon_0 \omega A \sin(\omega t)}{d} \tag{3-115}$$

$$\nabla \cdot \mu_0 \boldsymbol{H}_1 = 0 \tag{3-116}$$

with

$$\nabla \times \boldsymbol{H}_1 = \boldsymbol{i}_x \left(\frac{\partial \boldsymbol{H}_{1z}}{\partial y} - \frac{\partial \boldsymbol{H}_{1y}}{\partial z} \right) + \boldsymbol{i}_y \left(\frac{\partial \boldsymbol{H}_{1x}}{\partial z} - \frac{\partial \boldsymbol{H}_{1z}}{\partial x} \right) + \boldsymbol{i}_z \left(\frac{\partial \boldsymbol{H}_{1y}}{\partial x} - \frac{\partial \boldsymbol{H}_{1x}}{\partial y} \right) \tag{3-117}$$

Combining equation 3-115 and 3-117 results in:

$$\underbrace{\frac{\partial \boldsymbol{H}_{1z}}{\partial y}}_{0} - \frac{\partial \boldsymbol{H}_{1y}}{\partial z} = \frac{\varepsilon_0 \omega A \sin(\omega t)}{d} \tag{3-118}$$

The first-order magnetic field within the enclosed air region in this system is:

$$\boldsymbol{H}_1 = \boldsymbol{i}_y \boldsymbol{H}_{1y} = -\boldsymbol{i}_y \frac{\varepsilon_0 \omega z A \sin(\omega t)}{d} \tag{3-119}$$

Note that equation 3-116 is satisfied, as $\boldsymbol{H}_{1y}$ is independent of y (and $\boldsymbol{H}_{1x} = \boldsymbol{H}_{1z} = 0$).

$$\nabla \cdot \mu_0 \boldsymbol{H}_1 = \mu_0 \left(\frac{\partial \boldsymbol{H}_{1x}}{\partial x} + \frac{\partial \boldsymbol{H}_{1y}}{\partial y} + \frac{\partial \boldsymbol{H}_{1z}}{\partial z} \right) = 0 \tag{3-120}$$

The expressions for the non-fringing fields within the enclosed air space in the system, correct up to and including first-order terms are

$$\boldsymbol{E}_{0,1} = \boldsymbol{E}_0 + \boldsymbol{E}_1 = -\boldsymbol{i}_x \left(\frac{v_r(t)}{d} - \frac{\mu_0 \sigma_s}{d} \frac{dv_r(t)}{dt} z \right) = -\boldsymbol{i}_x \left(\frac{A \cos(\omega t)}{d} + \frac{\mu_0 \sigma_s}{d} \omega z A \sin(\omega t) \right) \tag{3-121}$$

$$\boldsymbol{H}_{0,1} = \boldsymbol{H}_0 + \boldsymbol{H}_1 = -\boldsymbol{i}_y \left(\frac{\sigma_s v_r(t)}{d} - \frac{\varepsilon_0}{d} \frac{dv_r(t)}{dt} z \right) = -\boldsymbol{i}_y \left(\frac{\sigma_s A \cos(\omega t)}{d} + \frac{\varepsilon_0}{d} \omega z A \sin(\omega t) \right) \tag{3-122}$$

For the voltage applied to the resistor, correct up to and including first-order contributions, it must hold that

$$[v_s(t)]_{0,1} = -\int_{x=0}^{d} (E_{0,1})_{z=-l} dx = A \cos(\omega t) - \mu_0 \sigma_s \omega l A \sin(\omega t) \tag{3-123}$$

For the source current, correct up to and including first-order contributions, it yields

$$[i_s(t)]_{0,1} = -\int_{y=0}^{w} (H_{0,1})_{z=-l}\,dy = \frac{\sigma_s w A \cos(\omega t)}{d} - \frac{\varepsilon_0 w}{d}\omega l A \sin(\omega t) \tag{3-124}$$

The input impedance of the resistor, correct up to and including first-order contributions, can be computed from the ratio between the phasor representations of v_s and i_s.

$$[V_s]_{0,1} = A + j\mu_0\sigma_s\omega l A \tag{3-125}$$

$$[I_s]_{0,1} = \frac{\sigma_s w A}{d} + j\frac{\varepsilon_0 w}{d}\omega l A \tag{3-126}$$

$$Z_{0,1} = \frac{[V_s]_{0,1}}{[I_s]_{0,1}} = \frac{1 + j\mu_0\sigma_s\omega l}{\frac{\sigma_s w}{d} + j\frac{\varepsilon_0 w}{d}\omega l} = R\frac{1 + j\omega(L/R)}{1 + j\omega RC} \tag{3-127}$$

The lumped-element representation of the resistor, correct up to and including first-order contributions, is an RLC circuit, where the values of the resistance, inductance and capacitance are specified as follows

$$R = R_{dc} = \frac{d}{\sigma_s w} \tag{3-128}$$

$$L = L_{dc} = \frac{\mu_0 l d}{w} \tag{3-129}$$

$$C = C_{dc} = \frac{\varepsilon_0 l w}{d} \tag{3-130}$$

In case of a $\sigma_s = \infty$ ($R = 0$), the system changes into the single-turn inductor as described in section 3.5.3. In case of a $\sigma_s = 0$ ($R = \infty$), the system changes into the parallel-plate capacitor as described in section 3.5.2.

The lumped-element representation of the resistor is dependent on the actual value of the resistance R:

- $R << \sqrt{L/C}$. The lumped-element representation of the resistor equals a series LR circuit, as the input impedance is approximately

$$Z_{0,1} = R\frac{1 + j\omega(L/R)}{1 + j\omega RC} \approx R + j\omega L \tag{3-131}$$

- $R >> \sqrt{L/C}$. The lumped-element representation of the resistor equals a parallel RC circuit, as the input admittance is approximately

$$Y_{0,1} = \frac{1}{R}\frac{1 + j\omega RC}{1 + j\omega(L/R)} \approx \frac{1}{R} + j\omega C \tag{3-132}$$

- $R = \sqrt{L/C}$. The lumped-element representation of the resistor reduces to the DC resistance, as the input impedance equals

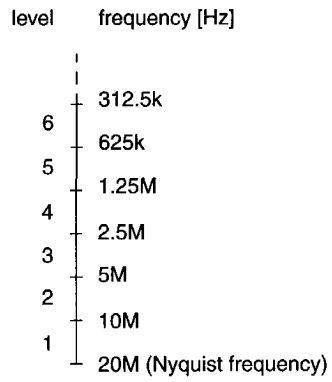

Figure 3-30. Wavelet levels corresponding to the measurement-data frequencies

$$Z_{0,1} = R\frac{1+j\omega(L/R)}{1+j\omega RC} = R \tag{3-133}$$

3.6 Modeling of the test circuit

It is the electrical size of the structure - its size in terms of the minimum wavelength of interest in the bandwidth over which the model must be valid - that dictates the sophistication and complexity of the required model. Although this is only an approximate criterion, which is closely related to the equations 3-66 and 3-104, an electromagnetic structure is said to be electrically small if its dimensions are smaller than one tenth of the smallest wavelength under consideration [53].

$$l < \frac{1}{10}\lambda \tag{3-134}$$

l the physical dimension [m]
λ the wavelength [m]

Because of the high-frequency phenomena that we observed in the measured arc voltages some of the voltage measurements have been analyzed for their frequency contents. A wavelet filter (db5) has been applied to filter the high-frequency components from the voltage measurements. The wavelet filter is in fact a signal compression procedure and works in the following way. The signal is decomposed by using the db5 wavelet. The levels 1 - 5 are completely tresholded after which the signal is reconstructed. The relation between the wavelet levels and the frequencies in our signal are given in figure 3-30. The effect is that the frequency components of 625 kHz and higher are removed from the signal. The results have been verified by using a Chebyshev IIR low-pass filter of order 11.

The following voltages of cb2, cb3 and cb4 have been analyzed.

- cb2: #502503 (direct test; reignition)
  The voltage has been measured twice (only with cb2 in case of 5 measurements). A

high-sensitivity voltage measurement was carried out in order to record the arc voltage very accurately, and a lower-sensitivity voltage measurement to record both the arc voltage and the first SLF peak (this sensitivity has also been used for the voltage measurements of cb3 and cb4, see table 3-5 (section 3.4)). The high-sensitivity voltage measurement has been analyzed for its frequency contents, as it contains the most information. A 1600 µs time window has been examined.

- cb3: #502303 (direct test; interruption)
  A 1000 µs time window has been analyzed. This time frame is shorter than the one used for #502503 (cb2). When the TRV builds up the end of the voltage measurement window is reached (see figure 1-9): this part of the data has been removed.
- cb4: #5014 (synthetic test; interruption)
  A 2000 µs time window has been analyzed. This time frame is longer than the ones used for the other two measurements: during a synthetic test the 4 memory blocks of the digitizing system are combined into 1 large block so that a longer time frame around the current zero crossing can be recorded. When the TRV builds up the end of the voltage measurement window is reached: this part of the data has been removed.

The difference between the filtered and the original voltage signal is further analyzed by determining the unbiased estimate of its autocorrelation [41].

$$R_x(\tau) = R_x(k \cdot \Delta t) = E(x(t) \cdot x(t+\tau)) \approx \frac{1}{N-k} \sum_{i=1}^{N-k} x_i \cdot x_{i+k} \tag{3-135}$$

x the signal vector
E the expected value operator
Δt the sampling time [s]
N the total number of samples

The autocorrelation as computed for the difference between the original and the filtered voltage data of measurement #502303 of cb3 is shown in figure 3-31. This can be interpreted to be zero-mean white noise:

$$R_x(\tau) = \begin{cases} \sigma_x^2 & \tau = 0 \\ 0 & \tau \neq 0 \end{cases} \tag{3-136}$$

Therefore, the applied (wavelet/Chebyshev) filter filtered out uncorrelated data only. No relevant information has been lost. The noise is not caused by the quantization process only; in that case the signal would be zero-mean white noise with a variance [41]:

$$\sigma^2 = \frac{\Delta^2}{12} = \frac{1}{12} \tag{3-137}$$

Δ the quantizer step size (in this case 1 bit)

Measurement #5014 of cb4 gives a similar picture as the measurement of cb3. In case of the high-sensitivity measurements of cb2, not only white noise is removed when the filters are applied. This becomes clear when the autocorrelation of the removed signal component is computed, as shown in figure 3-32. Therefore, the energy contents of the removed signal com-

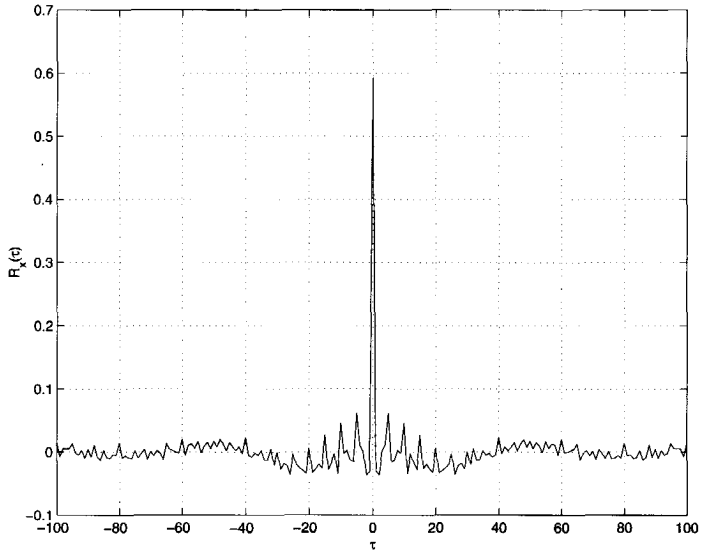

Figure 3-31. Autocorrelation of the removed signal component (#502303, cb3)

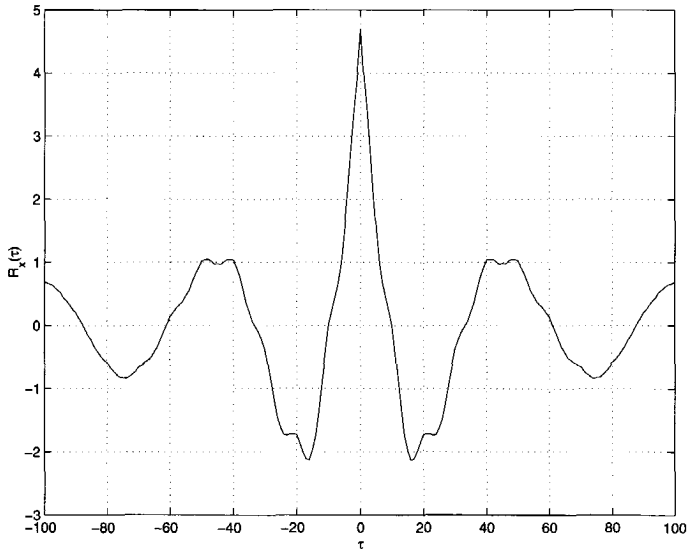

Figure 3-32. Autocorrelation of the removed signal component (#502503, cb2)

ponent are compared with that of the original signal, in order to decide whether it is relevant to take these high-frequency effects into account when modeling the test circuit. The energy contents of the removed signal component divided by the energy contents of the original signal is called the normalized mean-square error (NMSE) and is in fact a measure of the quality of compression.

$$\mathrm{NMSE} = 100 \cdot \frac{\|x - y\|^2}{\|x\|^2} \tag{3-138}$$

x the original signal
y the compressed/filtered signal
$\|.\|$ the norm of a signal; defined as the square root of its energy contents

The normalized mean-square error amounts to NMSE = 0.0034% for the high-sensitivity voltage measurement of cb2 (measurement #502503), while the NMSE of the 'low-sensitivity' voltage measurement of cb3 (measurement #502303) amounts to NMSE = 0.0015% and that of cb4 (measurement #5014) amounts to NMSE = 0.0034%. It is evident that the energy contents of the removed high-frequency signal components are so low that they do not play a significant role.

Therefore, the highest frequency of importance can be considered to be lower than 625 kHz. A signal with a frequency of 625 kHz has a wavelength of

$$\lambda = \frac{v}{f} = \frac{3\times10^8}{625\times10^3} = 480 \text{ m} \tag{3-139}$$

v the speed of light [m/s]
f the frequency [Hz]

Application of equation 3-134 shows us that the electromagnetic structure can be considered to be electrically small if its dimensions are smaller than one tenth of the smallest wavelength under consideration: $\lambda/10 = 48$ m. This distance is in the order of the distance between the circuit breaker and the short-circuit generator in the KEMA High-Power Laboratory. Therefore, the model of the laboratory test circuit can be build up by means of lumped network elements.

Chapter 4

Circuit breaker modeling: arc models

4.1 Introduction

In addition to the three states gas, liquid and solid, a substance may have a fourth state that is referred to as plasma. Maintaining a state, or changing it, generally depends on temperature and pressure. For example, a molecular gas dissociates gradually into an atomic gas if the thermal energy of some particles exceeds the molecular binding energy. An even more drastic change takes place as soon as the temperature of the gas is high enough so that some electrons can overcome the atomic binding energy. With increasing temperature, more and more atoms get stripped of their electrons until the gas becomes a mixture of freely moving electrons and ions. This ionized substance is called a plasma. Although the transition from a gas to a plasma takes place gradually and is therefore not a phase transition in the thermodynamic sense, it is often referred to as a 'fourth state of matter' [80].

The 'switching action', the basic function of the circuit breaker, refers to the mutual conversion of conductor and insulating material at a given potential. In power circuit breakers, the intensity of the current flowing through the conductors and the voltage levels that must be sustained by the insulating material are very high, and at present the only practical approach is the use of arc plasma. During an opening operation, the net result of the conservation of flux linkages is that the current, flowing in the system inductances prior to switching, continues to flow when the contacts part. The final touching surface area of the contacts carries an extremely high current density and, because of the local heating, the contact surface literally 'explodes', thus initiating a gaseous conduction path and an arc plasma channel. Because of the non-zero resistance of the arc channel, the (short-circuit) current causes a voltage across the contacts of the circuit breaker: the arc voltage. The arc behaves as a non-linear resistance. Thus, both the arc voltage and the arc current cross the zero value at the same time instant. If the arc is cooled sufficiently, at the time the current goes through zero, the circuit breaker interrupts the current

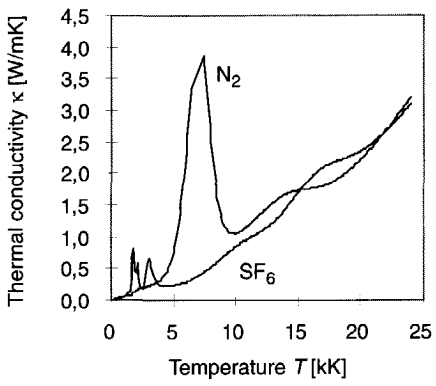

Figure 4-1. Thermal conductivity of SF_6 and N_2 as a function of the temperature [12]

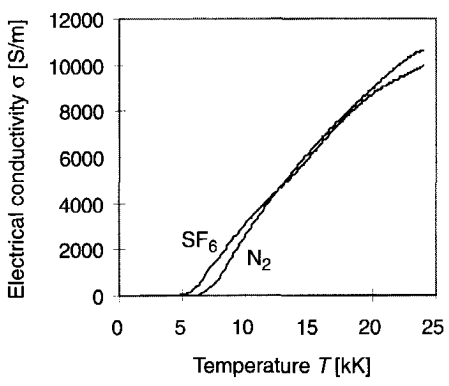

Figure 4-2. Electrical conductivity of SF_6 and N_2 as a function of the temperature [12]

because the electrical power input is zero. During current interruption, the arc resistance increases from practically zero to almost infinite in microseconds. Immediately after current interruption, the transient recovery voltage (TRV) builds up across the circuit breaker. As the gas mixture in the inter-electrode space does not change to a completely insulating state instantaneously, the arc resistance is finite at that time and a small current can flow: the post-arc current.

For an ideal circuit breaker, the resistance jumps from zero value to infinite resistance instantaneously for a circuit breaker opening operation. In most of the electrical-circuit computations, the circuit breaker can be modeled as a zero resistance in the closed state (i.e. a zero-voltage source) and an infinite resistance in the open state (i.e. a zero-current source). However, when detailed studies are to be made of the complicated interaction between the electrical network and the non-linear resistance of the circuit breaker, a mathematical model of the arcing phenomenon has to be made and incorporated into the circuit.

4.2 Properties of SF_6 arcs

Some properties that make SF_6 todays most applied arc quenching medium for the higher voltages are described hereunder.

In short, the formation of a plasma arc occurs in the following way [39]:

- a free electron is created by field emission-thermal emission from the electrodes, or by detachment or photo ionization from within the gas
- the electron is accelerated in the electromagnetic field
- the electron collides with heavy particles, resulting in dissociation of molecular species and finally ionization of the atoms.

SF_6 dissociates according to the following reaction $SF_6 \Leftrightarrow SF_4 + 2F$ around 1500 K [54]. The dissociation continues until around 2500 K, SF and F atoms result. These dissociation pro-

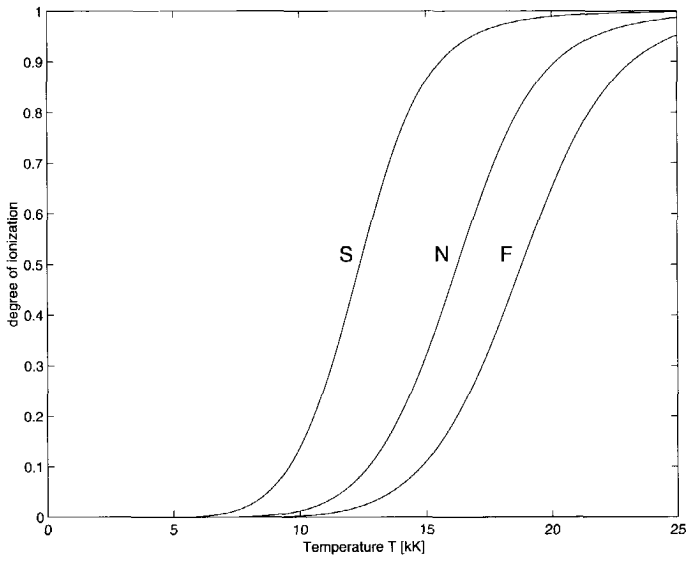

Figure 4-3. Degree of ionization as a function of the temperature

cesses result in a rather high thermal conductivity in the 2000 K - 3000 K region as shown in figure 4-1; the peaks in the thermal conductivity are caused by the dissociated particles that diffuse to the cold regions, carrying their energy of dissociation with them, while the undissociated particles diffuse from the cold to the hot regions, carrying no dissociation energy [19]. From 4000 K - 5000 K onwards, ionization takes place. First, the S atoms ionize, $S \Leftrightarrow S^+ + e^-$, because of the low ionization potential (10.357 eV). The ionization of the F atoms, $F \Leftrightarrow F^+ + e^-$, is noticeable after 7000 K (the ionization potential amounts to 17.42 eV). The ionization results in a rapidly increasing electrical conductivity, as shown in figure 4-2. If we assume thermal equilibrium the degree of space ionization can be derived with Saha's equation [65]:

$$\frac{x^2}{1-x^2} \cdot p = 3.16\text{e-}7 \cdot T^{5/2} \cdot e^{\frac{-eV_i}{kT}} \qquad (4\text{-}1)$$

x the degree of ionization
p the pressure [bar]
T the temperature [K]
e the charge of an electron: 1.6e-19 [C]
V_i the ionization potential [eV]
k the Boltzmann's constant: 1.38e-23 [J/K]

The degree of ionization of S, F and N (ionization potential: 14.54 eV) as computed by means of the Saha equation as a function of the temperature is shown in figure 4-3. From figure 4-2 and figure 4-3, it is clear that the arc can be fruitfully applied to switch between a conducting and an isolating state in a short period of time. Cooling by means of cold gas is the way to

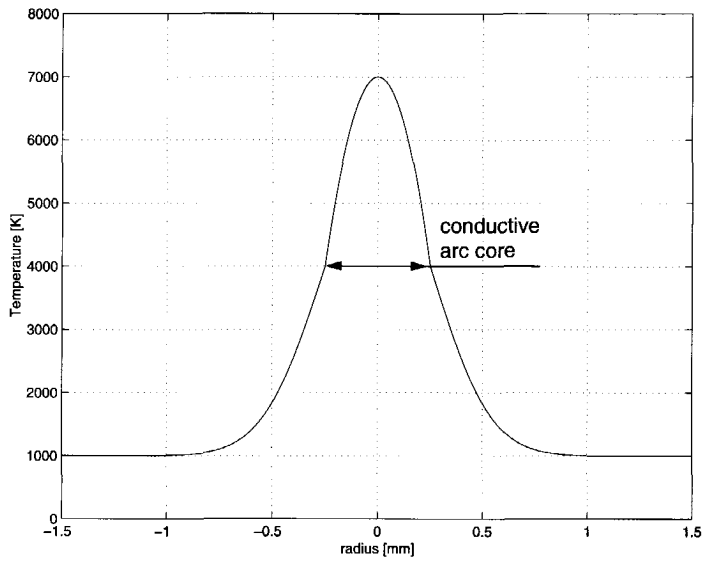

Figure 4-4. Arc temperature as a function of the radius

remove heat from the plasma channel and to change the conducting into a non-conducting state.

It is evident from figure 4-1 and figure 4-2 that the temperature where the thermal conductivity peaks due to the dissociation of SF_6 occur (1500 K - 3000 K) is substantially lower than the temperature where the rapid increase in electrical conductivity takes place (4000 K - 5000 K). The thermal conductivity peak of air (which contains 80% N_2) equals the temperature where the rapid increase in electrical conductivity takes place (7000 K). Therefore, when the arc current reaches zero, SF_6 behaves as an excellent heat conductor. As SF_6 is capable of cooling down the plasma channel much faster at lower temperatures, it will develop a substantially higher dielectric strength following the current zero.

Another profitable characteristic of SF_6 as extinguishing medium is its electronegative property [52]. Free electrons, which, because of their high mobility, carry most of the current, are strongly attracted by SF_6 molecules. When the free electrons attach to the gas molecules, heavy ions are formed and the mobility of the charged particles drops considerably. Therefore, the space conductivity disappears very quickly around current zero. Although an ionized gas with no free electrons is still slightly conducting, it is able to withstand high voltage gradients with relatively negligible currents [8].

In figure 4-4, a typical temperature profile of an SF_6 arc is shown (the 3-zone model of Hermann and Ragaller [29] has been used). The temperature profile of the arc can be calculated from the Elenbaas-Heller equation, which will be derived in section 4.3.2. The heat flow emitted radially, which is considered nearly constant along the radial direction within the temperature range of concern [52], is described by the following term (see also equation (4-6)):

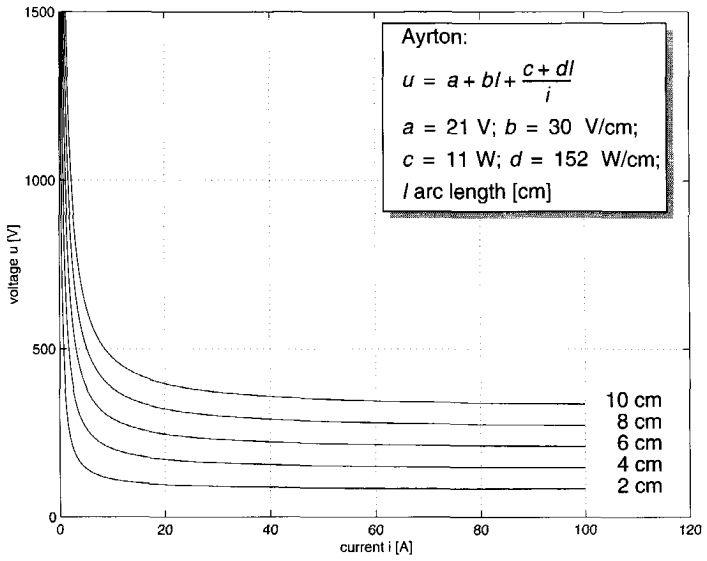

Figure 4-5. Static arc characteristics for copper electrodes in air

$$-2\pi r\kappa\frac{\partial T}{\partial r} \tag{4-2}$$

r the radius [m]
T the temperature [K]
κ the heat conductivity [W/mK]

We already concluded from figure 4-1 and figure 4-2 that the temperature where the thermal conductivity peaks due to the dissociation of SF_6 occur (1500 K - 3000 K) is substantially lower than the temperature where the rapid increase in electrical conductivity takes place (4000 K - 5000 K). Therefore, for the arc column at 4000 K - 5000 K or higher, κ is small and therefore $\partial T/\partial r$ is large. On the outside of the arc column, with temperatures around 2000 K, κ is large and therefore $\partial T/\partial r$ is small. These effects can be observed in the temperature profile in figure 4-4.

The relationship between arc current and arc voltage is called the arc characteristic. The static characteristic is valid when changes in the arc current take place slowly. The dynamic characteristic applies when changes in the arc current take place rapidly. In figure 4-5, various static arc characteristics for different arc lengths are shown as computed with the Ayrton equation [21,63]. Note that the arc characteristic shows a negative slope, because the arc tries to keep the electric power input equal to the (more or less) constant cooling power. When the arc channel length increases, a better cooling is established. In order to meet the power balance, a higher electric power input is necessary and a higher arc voltage is the result.

For an alternating current, the arc characteristic shows hysteresis and lies around the static arc characteristic as depicted in figure 4-6. This hysteresis originates from the heat capacity of the

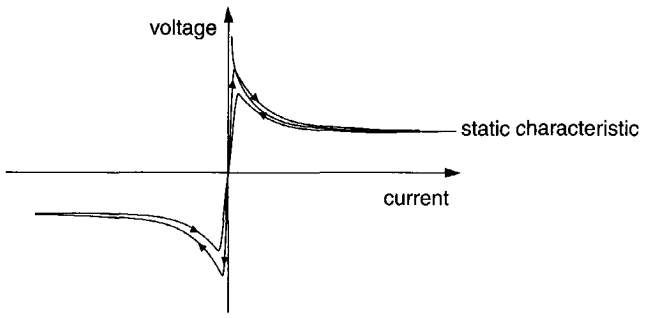

Figure 4-6. Dynamic arc characteristic

electrodes and the gas, which cannot follow a sudden change of the current. If the arc column conducts a current with an amplitude that continuously changes in time (as is the case with an AC current), the core conditions constantly lag the steady-state conditions. In the case of an increasing current amplitude, the arc voltage exceeds the steady-state arc voltage to create the necessary thermal energy. In the case of a decreasing current amplitude, the arc is forced to dissipate thermal energy, which results in a lower value of the arc voltage than the steady-state one [59].

In figure 4-2, it can be seen that the electrical conductivity for both SF_6 and N_2 is in the same order of magnitude over the range of temperatures shown. However, within the temperature range of 5000 K - 15000 K, the thermal conductivity of N_2 is larger than that of SF_6 (figure 4-1). In other words: N_2 is much more effective in removing heat than SF_6 within that specific temperature range. Therefore, the N_2 arc, which tries to keep the electrical power input balanced with the energy losses, has a higher arc voltage than an SF_6 arc conducting the same current [59].

4.3 Arc modeling: theory

Mathematical modeling of circuit breaker arcs is based on (simplifications of) complex physical processes. It merely depends on the type of application for which the arc model is to be used which simplifications can be made.

4.3.1 Physical description

The plasma in the arc column can be described by the equations of fluid dynamics and the laws of thermodynamics [8,52]:

Conservation of mass:

$$\frac{\partial \rho}{\partial t} = -\nabla \cdot (\rho v) \qquad (4\text{-}3)$$

change rate of density in a unit volume

net mass flow entering a unit volume

ρ the gas density [kg/m^3]
v the gas flow velocity [m/s]

Conservation of momentum:

$$\rho\frac{\partial v}{\partial t} = -\nabla p - \rho(v\nabla)v \qquad (4\text{-}4)$$

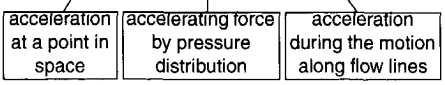

p the pressure [kg/ms^2, J/m^3]

Conservation of energy:

$$\rho\frac{\partial H}{\partial t} = -v\nabla(\rho H) + \nabla\cdot(pv) + \nabla\cdot(\kappa\nabla T) + \sigma E^2 + R(T,\rho) \qquad (4\text{-}5)$$

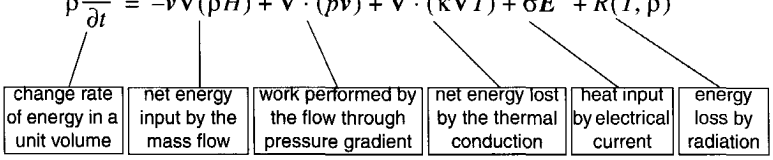

H the enthalpy of the gas [J/kg]
κ the thermal conductivity [W/mK]
T the gas temperature [K]
σ the electrical conductivity [S/m]
E the electrical field strength [V/m]
R the energy loss by radiation [W/m^3]

To find a solution to these equations is laborious and, therefore, simplifications have to be made in order to apply the equations for practical use.

4.3.2 Black-box models

Because of the heavy computations required to solve physical arc models as described by the equations in the previous section, and the uncertainty of the (time-dependent) parameters, their use for 'digital testing' purposes is limited. Black-box arc models are more suitable for this application [101,102]. The black-box type arc models are based on physical considerations but are in fact mathematical models; the correct electrical behavior of the arc is of greater importance than a description of the internal physical processes.

Black-box arc models are derived from the energy balance equation describing the arc under idealized conditions, i.e. a free-burning arc in a gaseous atmosphere, not subjected to external influences. The energy balance equation can be obtained as follows [100]. Assume an arc with a cylindrical shape as shown in figure 4-7, where the energy loss occurs only due to heat conduction in radial direction. The heat transfer through the circle at radius r, per unit time and per unit length, is given by:

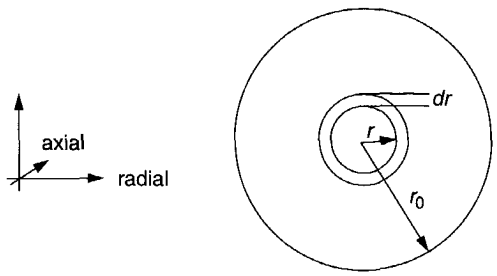

Figure 4-7. Cylindrical arc

$$\varphi(r) = -2\pi r\kappa\frac{\partial T}{\partial r} \tag{4-6}$$

φ the heat transfer per unit length [W/m]
r the radius [m]
T the temperature as a function of time and the coordinate in radial direction [K]
κ the heat conductivity [W/mK]

The heat transfer, per unit time and per unit length, through the circle at radius $r + dr$ is for an infinitely thin layer dr:

$$\varphi(r + dr) = \varphi(r) + \frac{\partial \varphi}{\partial r}dr \tag{4-7}$$

Therefore, the heat gain in the layer dr, per unit time and per unit length, can be written as:

$$\varphi(r) - \varphi(r + dr) = -\frac{\partial \varphi}{\partial r}dr = 2\pi\frac{\partial}{\partial r}\left(r\kappa\frac{\partial T}{\partial r}\right)dr \tag{4-8}$$

However, the heat production, per unit time and per unit length, as a result of the electric field in the layer dr amounts to:

$$2\pi rEJdr = 2\pi r\sigma E^2 dr \tag{4-9}$$

E the voltage gradient in the axial direction [V/m]
J the current density [A/m^2]
σ the electrical conductivity [S/m]

Accordingly, the total accumulated heat in the layer dr can be written as:

$$2\pi\frac{\partial}{\partial r}\left(r\kappa\frac{\partial T}{\partial r}\right)dr + 2\pi r\sigma E^2 dr \tag{4-10}$$

Integration over the total cross section of the arc between the boundaries 0 and r_0 gives for the total accumulated heat per unit length:

$$2\pi\left(r\kappa\frac{\partial T}{\partial r}\right)_{r_0} + E^2 g \tag{4-11}$$

g the conductance per unit length [Sm]

Therefore, the following equation results:

$$\frac{\partial Q}{\partial t} = 2\pi r_0 \kappa \left(\frac{\partial T}{\partial r}\right)_{r_0} + E^2 g \qquad \text{or} \qquad \frac{\partial Q}{\partial t} = -P + E^2 g \tag{4-12}$$

Q the internal energy per unit length [J/m]
P the cooling power per unit length [W/m]

This energy balance equation is often referred to as the Elenbaas-Heller equation. Note that this equation is in fact a simplified form of the conservation of energy equation (equation 4-5).

Mayr derived his arc model from the energy balance equation, equation 4-12, by making the following assumptions [47,48]:

- The arc has a constant cylindrical cross section
- The conductance is an exponential function of the internal energy of the arc column: $g = K\exp(Q/Q_0)$, with constants K and Q_0
- The heat flux towards the surroundings of the arc per unit time is constant and is caused only by thermal conduction: $P = -2\pi r_0 \kappa (\partial T/\partial r)_{r_0}$

When these assumptions are included in the Elenbaas-Heller equation (equation 4-12), the ensuing equation results.

$$E^2 g - P = \frac{d}{dt}(Q_0 \ln(g/K)) = Q_0 \frac{d}{dt}(\ln(g) - \ln(K)) = Q_0 \frac{d\ln g}{dt} \tag{4-13}$$

After we have rewritten equation 4-13, the Mayr equation results.

$$\frac{d\ln g}{dt} = \frac{1}{\tau}\left(\frac{E^2 g}{P} - 1\right) \tag{4-14}$$

τ the time constant $\tau = Q_0/P$ [s]
P the constant cooling power per unit length [W/m]

Another well-known arc model that is based on the energy balance equation is the Cassie arc model [10]. Cassie made the following assumptions:

- The arc has a cylindrical cross section that varies with the current and with time
- The temperature of the arc plasma is constant
- The heat flux is based on thermal convection

Under these assumptions, the conductivity, power loss and energy contents per unit volume are constants [7]. Therefore, the following equations hold:

$$\begin{aligned} g = g'A \rightarrow A &= \frac{g}{g'} \\ Q = Q'A \rightarrow Q &= \frac{Q'g}{g'} \\ P = P'A \rightarrow P &= \frac{P'g}{g'} \end{aligned} \tag{4-15}$$

g' the conductivity per unit volume [S/m]
Q' the energy contents per unit volume [J/m^3]
P' the power loss per unit volume [W/m^3]

When these expressions are incorporated in the Elenbaas-Heller equation (4-12), the following equation results:

$$-\frac{P'g}{g'} + E^2 g = \frac{d}{dt}\left(\frac{Q'g}{g'}\right) = \frac{Q'}{g'}\frac{dg}{dt}$$
$$\frac{1}{g}\frac{dg}{dt} = \frac{d\ln g}{dt} = \frac{g'}{Q'}\left(E^2 - \frac{P'}{g'}\right) = \frac{P'}{Q'}\left(\frac{E^2}{P'/g'} - 1\right) \quad (4\text{-}16)$$

Similar to Mayr's equation, a time constant can be introduced to account for the time lag that is due to the energy storage capacity and the finite rate of energy losses: $\tau = Q/P = Q'/P'$, which is a constant value. In the steady state, where the heat produced by the arc equals the losses, $P = gE^2 \rightarrow E = \sqrt{P/g} = \sqrt{P'/g'} = E_0$, a constant arc voltage gradient E_0 results. Therefore, the Cassie arc model can be written as:

$$\frac{d\ln g}{dt} = \frac{1}{\tau}\left(\frac{E^2}{E_0^2} - 1\right) \quad (4\text{-}17)$$

τ the time constant [s]
E_0 the constant arc voltage per unit length [V/m]

4.4 Arc modeling: a new arc model

4.4.1 Modified Mayr arc model

The Mayr arc model is described by the following equation (for the entire arc length):

$$\frac{1}{g}\frac{dg}{dt} = \frac{d\ln g}{dt} = \frac{1}{\tau}\left(\frac{ui}{P} - 1\right) \quad (4\text{-}18)$$

g the arc conductance [S]
u the arc voltage [V]
i the arc current [A]
τ the arc 'time constant' [s]
P the cooling power [W]

The 'time constant' τ and cooling power P can be either constant or can be assumed to be functions of the electrical quantities conductance, current or voltage. A lot of varieties can be found in literature and a comparison of these variants is given by Haupt [28]. In order to find the possible relations between the parameters of the arc model and the electrical quantities, assumptions are made to acquire a system with as many equations as there are parameters to be determined:

- Amsinck [1] assumes the parameters to be equal at points of equal conductance (therefore, a reignition is required to obtain the parameters)

- Hochrainer [31] assumes the parameters to be equal at points of equal current (therefore, a reignition is required to obtain the parameters)
- Zückler [105] assumes the parameters to be equal in two following time steps (therefore, no reignition is required)
- Sporckmann [90] and other authors seek to the parameters as a function of the time by using polynomials (note that the higher the degree of the polynomial, the more equations are required)

In fact, all of the above-mentioned methods can lead to good results. However, it will become clear from the following analysis that there is not a single unique relation between electrical quantities and arc parameters.

Equation 4-18 can be rewritten at a certain time instant k as:

$$\begin{bmatrix} -\left.\frac{d\ln g}{dt}\right|_k & \left. ui\right|_k \end{bmatrix} \begin{bmatrix} \left.\tau\right|_k \\ \left.1/P\right|_k \end{bmatrix} = 1 \qquad \text{or} \qquad \boldsymbol{A}\boldsymbol{x} = b \tag{4-19}$$

Equation 4-19 is an underdetermined system [93]: it consists of one equation and two unknowns. There is not a unique solution vector $\boldsymbol{x}$ for this equation. A particular solution to the system (equation 4-19) can be found rather easily:

$$\boldsymbol{x}_p = \begin{bmatrix} 0 \\ 1/(ui|_k) \end{bmatrix} \tag{4-20}$$

The solution to the homogeneous system $\boldsymbol{A}\boldsymbol{x}_h = 0$ has at least one non-trivial solution (i.e. $\boldsymbol{x}_h \neq \boldsymbol{0}$) because the number of equations is smaller than the number of unknowns. Since the matrix $\boldsymbol{A}$ has one row, there is only one non-trivial solution, which is called the nullspace of $\boldsymbol{A}$. The solutions of equation 4-19 can now be written as a sum of the particular solution and a solution to the homogeneous system:

$$\boldsymbol{x} = \boldsymbol{x}_p + c \cdot \boldsymbol{x}_h \tag{4-21}$$

c arbitrary number

It is easy to verify that for every c, this is a solution of the underdetermined system (equation 4-19):

$$\boldsymbol{A}\boldsymbol{x} = \boldsymbol{A}(\boldsymbol{x}_p + c \cdot \boldsymbol{x}_h) = \boldsymbol{A}\boldsymbol{x}_p + c \cdot \boldsymbol{A}\boldsymbol{x}_h = b + c \cdot 0 = b \tag{4-22}$$

Therefore, there is not one unique combination of (τ, P) values to describe the measured current and voltage traces. This explains why there are so many variations of the Mayr-type arc model that can be used successfully in simulations.

From the measurements, the particular and homogeneous solution can be determined for each sample point. Therefore, by choosing a certain relation for the time parameter τ, we prescribe the arbitrary number c in equation 4-21 at each sample point and the cooling power P as well. When the time constant τ is chosen to be constant, the cooling power P is computed at each

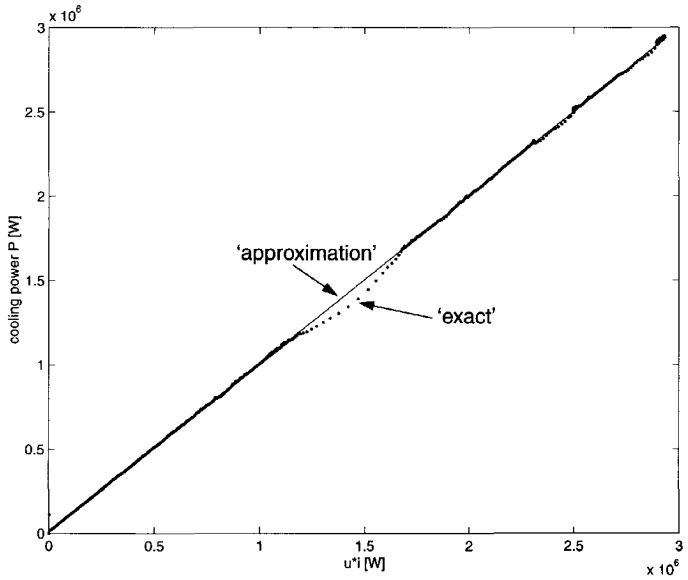

Figure 4-8. Cooling power P versus the electrical power input (#4005, cb1)

sample point such that equation 4-21 is fulfilled. With these parameters, the measured voltage trace can be recomputed exactly from $u = i_m/g$ if the following equation is solved:

$$\frac{1}{g}\frac{dg}{dt} = \frac{d\ln g}{dt} = \frac{1}{\tau}\left(\frac{i_m^2/g}{P} - 1\right) \tag{4-23}$$

i_m the measured arc current [A]

In figure 4-8, the 'exact' computed cooling power P is shown versus the electrical power input of the arc for measurement #4005 of cb1. From this figure it is evident that the cooling power shows a very strong linear relation with the electrical power input. Therefore, a new arc model is introduced with a constant time parameter τ and where the cooling power is a function of the electrical power input:

$$\frac{1}{g}\frac{dg}{dt} = \frac{d\ln g}{dt} = \frac{1}{\tau}\left(\frac{ui}{P_0 + P_1 ui} - 1\right) \tag{4-24}$$

P_0 cooling constant [W]
P_1 cooling constant

Although the arc model with the cooling power as a function of the electrical power input is a mathematical arc model, it does have a relation with arc physics, as the cooling power is built up of two components. The cooling constant P_0 represents the cooling power governed by the design of the circuit breaker (i.e. nozzle layout, pressure etc.). The cooling constant P_1 regulates the influence of the electrical power input on the cooling power and therefore embodies the pressure buildup in the breaker caused by ohmic heating of the arc plasma.

As the measured current data after current zero cannot be considered as physical post-arc currents (for the measurements used in this thesis; see section 1.4.2), the parameters are computed from a least-squares fit by using only the pre-current zero data in the last 100 μs before current zero. From the measured voltage and current the $d\ln g/dt$ is obtained. The τ, P_0 and P_1 parameters are determined such that the difference between this $d\ln g/dt$ trace and the one computed from equation 4-24 - by filling in the right-hand side in which u is the measured voltage and i is the measured current - is minimized. A simplex search method has been applied for the minimization. This approach has been validated by verifying that the arc model parameters that are determined from calculated voltage and current traces - obtained from arc model computations in a computer program - correspond to the arc model parameters in the computer program by means of which those voltage and current traces were computed. Two cases are shown in table 4-1, in which a small change in the P_1 parameter has been made in order to verify that the parameter determination is sensitive enough to deal with it.

Table 4-1. Verification of the arc parameter determination

	case 1		case 2	
arc parameters	**original**	**determined**	**original**	**determined**
P_0 [W]	7500	7554	7500	7532
P_1	0.9950	0.9949	0.9960	0.9960
τ [μs]	0.2500	0.2512	0.2500	0.2507

Despite the rather long time interval (100 μs) that is used for the arc model parameter determination - in order to reconstruct the rise to the arc voltage peak and accurately simulate the arc-circuit interaction - the method is not very sensitive to large arc voltage jumps that can occur in this period of time, as shown in figure 4-9. The $d\ln g/dt$ changes most in the time interval that starts around the arc voltage peak and ends at the current zero crossing: mismatches between the two $d\ln g/dt$ traces in this time interval add much more to the error of the curve-fitting process than mismatches in the area before the arc voltage peak.

The parameters determined for measurement #4005 of cb1 are: $\tau = 0.27$ μs, $P_0 = 15917$ W and $P_1 = 0.9943$. The approximate cooling power, $P_0 + P_1 ui$, is shown in figure 4-8 for the above-mentioned parameters. The measured and computed arc currents and voltages using the differential equation 4-24 with the above-mentioned parameters are shown in figure 4-9.

In the high-current interval, the arc voltages as computed with equation 4-24 are lower than the measured ones. This can be improved by adapting the arc model in the following way.

$$\frac{1}{g}\frac{dg}{dt} = \frac{d\ln g}{dt} = \frac{1}{\tau}\left(\frac{ui}{\max(U_{arc}|i|, P_0 + P_1 ui)} - 1\right) \qquad (4\text{-}25)$$

U_{arc} the constant arc voltage in the high-current area [V]; when this value is set to zero equation 4-24 results

In the high-current interval, equation 4-25 reduces to the following differential equation.

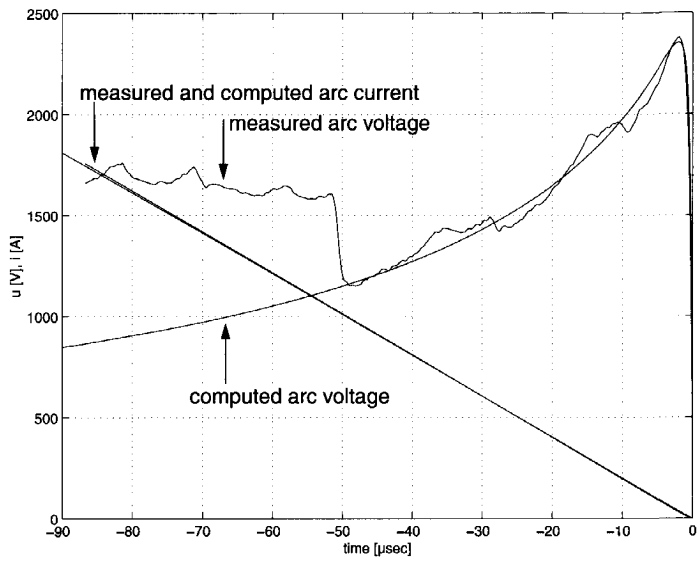

Figure 4-9. Computed (equation 4-24) and measured current and voltage traces for an interruption (#4005, cb1)

$$\frac{1}{g}\frac{dg}{dt} = \frac{d\ln g}{dt} = \frac{1}{\tau}\left(\frac{ui}{U_{arc}|i|} - 1\right) = \frac{1}{\tau}\left(\frac{u}{U_{arc}} - 1\right) \tag{4-26}$$

This equation shows a clear conformity with the Cassie arc model, which has proven its validity in the high-current area. At current zero, equation 4-25 (and equation 4-24) reduces to the following differential equation.

$$\frac{1}{g}\frac{dg}{dt} = \frac{d\ln g}{dt} = \frac{1}{\tau}\left(\frac{ui}{P_0} - 1\right) \tag{4-27}$$

This is exactly the Mayr arc model, which has proven its validity in the current-zero region. After current zero the constant P_1 is set to zero (the arc has been extinguished) and equation 4-27, i.e. the Mayr arc model, is used.

A reignition, measurement #4010 of cb1, has been recomputed with the following parameters: $\tau = 0.57\,\mu s$, $P_0 = 24281\,W$, $P_1 = 0.9942$ and $U_{arc} = 1135\,V$. The arc model shows a reignition too. Both measured and computed voltage and current traces around current zero are shown in figure 4-10. After the reignition a too low arc voltage is computed due to the use of the pure Mayr arc model after current zero. Our main interest is to have an arc model that shows good correspondence between the measured and computed traces before the current zero crossing - in order to accurately simulate the arc-circuit interaction - and that shows a good performance in predicting the outcome of a test. Therefore the fact that the model predicts a reignition is important; what happens after the reignition is - for our study - irrelevant. The use of the U_{arc} parameter is optional and is not used in the rest of the thesis.

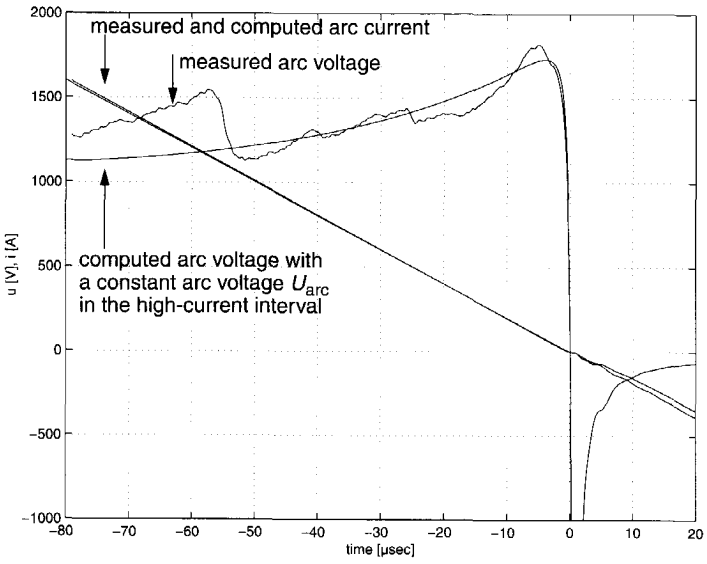

Figure 4-10. Computed (equation 4-25) and measured current and voltage traces for a reignition (#4010, cb1)

The arc model parameters τ and P_1 cover more or less the same range of values for the circuit breakers analyzed in this thesis, apart from cb3 (see section 4.4.2). The arc model parameter P_0 is a design parameter reflecting the difference in rated voltage of the circuit breakers, as becomes clear from the average P_0 values in table 4-2.

Table 4-2. Average P_0 values of the circuit breakers

	cb1	cb2	cb3	cb4
rated voltage [kV]	245	72.5	145	123
average P_0 [W]	27800	8235	18600	16200

The computations with the proposed arc model (equation 4-24) show good correspondence between the measured and computed current and voltage traces. Furthermore, the arc model shows an overall performance of 90% in predicting the outcome of the tests when the measurements of cb1, cb2 and cb4 are considered. That means that only in one out of ten cases an interruption is observed during the measurements for which the arc model shows a reignition, or vice versa (see also section 4.5.2). The proposed arc model is compared with two other arc models in section 4.5.3.

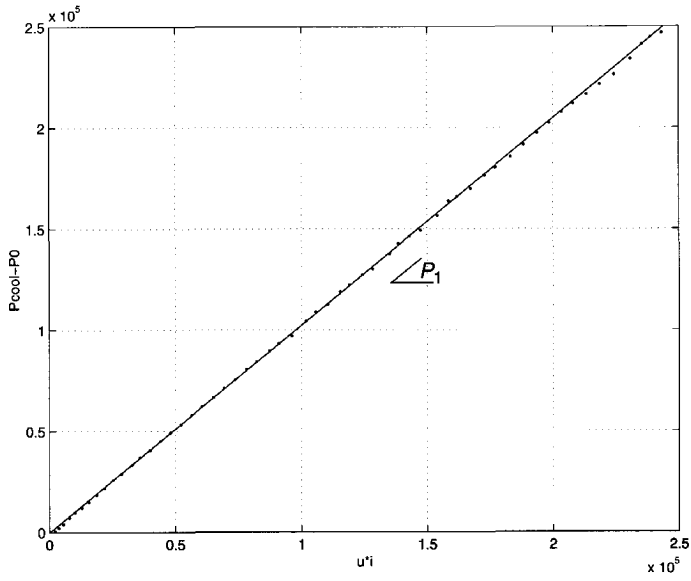

Figure 4-11. The cooling power P_1ui versus the electrical power input (#5115 / cb3)

4.4.2 Arc model limitations

The arc model, as described in the previous section, fails to reproduce most of the measurements of cb3. The mathematical reason for this failure can be discovered rather easily. The equation of the proposed arc model is:

$$\frac{1}{g}\frac{dg}{dt} = \frac{d\ln g}{dt} = \frac{1}{\tau}\left(\frac{ui}{P_0 + P_1 ui} - 1\right) \tag{4-28}$$

Let us assume that the Mayr arc model describes the circuit breaker behavior correctly.

$$\frac{1}{g}\frac{dg}{dt} = \frac{d\ln g}{dt} = \frac{1}{\tau}\left(\frac{ui}{P_{\text{cool}}} - 1\right) \tag{4-29}$$

If a fixed arc time constant τ is chosen, the cooling power P_{cool} in equation 4-29 can be derived in order to match the measured quantities exactly. When the constant P_0 in equation 4-28 is subtracted from this computed P_{cool}, the cooling power term $P_1 ui$ results. When $P_1 ui$ is plotted versus the electrical power input, figure 4-11 results. It is evident from this figure that the computed dots show a very strong linear relationship with the electrical power input, which is also the essence of this arc model. There is one problem, however, (in case of this specific circuit breaker): P_1, which is the slope of the depicted linear relation, is larger than one. The effect of a P_1 value larger than one can be analyzed from equation 4-28.

The denominator in the equation is, in this case, always larger than the nominator, which results in a negative $d\ln g/dt$ value in all cases. Therefore, the model only computes a decreasing conductance value.

A more physical explanation of the arc model's proper functioning for the breakers cb1, cb2, and cb4 while problems are encountered for cb3, is that cb3 is a divergent circuit-breaker type with a long-lasting gas blow. This difference can be clearly recognized in the measured arc voltages: the arc voltages of cb3 are higher with a less-pronounced extinguishing peak, that is located at a longer time interval before current zero. These characteristics can be observed from the average arc voltages of cb2, cb3, and cb4 as shown in figure 5-26 and the figures in the appendix.

In general, an arc model with a limited number of free parameters is not able to represent all classes/types of circuit breakers. Therefore, a more universal approach and alternative to the use of arc models is developed in Chapter 5.

4.5 Arc modeling: applications

4.5.1 Failure probability determination

Computations with arc models give the possibility to extend the information obtained during the cost-intensive tests in the high-power laboratory. One major difficulty with this approach is in the fact that the circuit breaker behavior as such is statistical, as described by Steel and Swift-Hook [92]. Therefore the circuit breaker cannot be described by a single (deterministic) set of arc model parameters, and a statistical arc model should be applied for certain 'digital testing' purposes. An example of digital testing by means of a statistical arc model is the determination of a fingerprint of the circuit breaker (within that specific test circuit and conditions) in the form of a failure probability distribution as a function of the arcing time.

Various papers on the inclusion of statistical behavior in arc models have been published [49,50,57,62,87,88,89]. In this section, the statistical properties of the arc model parameters, which are obtained from the current zero measurements of cb1 and cb2, will be used in a 'statistical version' of the proposed arc model [78]. Therefore, instead of a single computation with a deterministic arc model, of which we can only hope that it produces an approximation of the 50-percent failure probability, we have to perform multiple computations to be able to make statements about the interruption behavior of the breaker.

Statistical analysis of arc model parameters

The arc parameters of the applied arc model have been determined from a least-squares fit for each measurement. Therefore, for each circuit breaker, a list of arc model parameters results. Initially, the dependency between the arc model parameters and the arcing time and the applied current steepness $(di/dt)_0$ is investigated. As the contact separation speed relates the arcing time to the arc length, only the arc parameter P_0 (cooling constant per unit length [W/m]) is expected to be dependent on the arcing time: a longer arcing time results in a better pressure buildup and a more effective cooling in the breaker.

The Pearson's correlation coefficient is a conventional way of summarizing the strength of a correlation. Unfortunately, this is a rather poor statistic for deciding whether an observed cor-

relation is statistically significant and/or whether one observed correlation is significantly stronger than another. Therefore, nonparametric or rank correlation has been used: all values are replaced by their rank among the other values in the same data set [3,83]. Thus, the distribution function of the numbers is known exactly, i.e. a uniform distribution. The Spearman's rank correlation coefficient r_s can be computed and its significance can be tested by calculating the T value, which is approximately Student's t-distributed with $n-2$ degrees of freedom [3].

$$T = r_s \sqrt{\frac{n-2}{1-r_s^2}} \sim t(n-2) \tag{4-30}$$

n the number of samples

Additionally, a hypothesis testing can be performed to determine whether the computed absolute value of the correlation coefficient is large enough to conclude that the underlying population correlation coefficient (ρ_s) is some value other than zero.

H_0: uncorrelated: $\rho_s = 0$ (null hypothesis)

H_1: correlated: $\rho_s \neq 0$ (non-directional alternative hypothesis)

The null hypothesis H_0 is rejected when the absolute T value is larger than the critical value obtained from the Student's t-distribution with $n-2$ degrees of freedom and such that the likelihood of committing a Type I error (where a true null hypothesis is rejected) is α%.

$$|T| \geq t_{1-\alpha}(n-2) \tag{4-31}$$

α the (two-tailed) level of significance

The computed T values of Spearman's rank correlation coefficients for cb1 and cb2 are shown in table 4-3. The significant dependencies are shown in the shaded cells. The number of measurements of cb1 (13) is in fact much too small to make sound statements, and they are used mainly to verify the tendencies found for cb2. The data of cb4 are not used for this analysis as this breaker was tested exclusively with a fixed arcing time.

Table 4-3. Computed T values of Spearman's rank correlation coefficients

Dependency between	*T* values cb1	*T* values cb2
arcing time - P_0	2.2	4.3
arcing time - P_1	-0.8	-0.1
arcing time - τ	1.5	2.0
$(di/dt)_0$ - P_0	0.0	2.3
$(di/dt)_0$ - P_1	0.9	0.8
$(di/dt)_0$ - τ	-0.7	-1.6
P_0 - P_1	-1.8	-3.6
P_0 - τ	2.0	4.1
Critical value (level of significance)	**1.8 (α = 10%)**	**2.7 (α = 1%)**

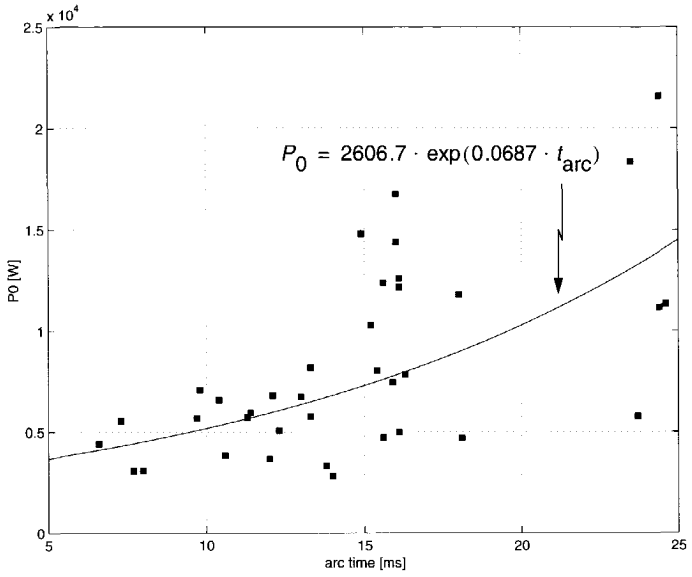

Figure 4-12. Arcing time versus cooling constant P_0 (cb2)

In correspondence to the theory, the hypothesis test shows that from the three arc parameters, only P_0 is dependent on the arcing time. It appears that the arc parameters are not correlated significantly with the applied current steepness $(di/dt)_0$. Thus, a relation between the arcing time and the cooling constant P_0 can be defined. Furthermore, it follows from the hypothesis tests that the arc model parameters P_1 and τ are related to P_0.

The computed arc model parameters are very much deviated - as shown in figure 4-12 for the cooling power P_0 of cb2 - and accordingly it is not possible to obtain a single set of parameters to describe the behavior of the circuit breaker. Therefore, multiple sets of arc model parameters have to be generated to describe the arc. Because of the dependency between the arcing time and P_0 (see figure 4-12 and table 4-3), it is even necessary to use multiple sets of arc model parameters at different arcing times.

First, a relation between the cooling constant P_0 and the arcing time is investigated. For this purpose the linear regression model is used.

$$y = \beta X + \varepsilon \tag{4-32}$$

y	the vector with the dependent variables (observations)
β	the vector with the regression coefficients
X	the matrix with the independent variables (explanatory variables)
ε	the residual vector

The linear relation is not exact but stochastic in nature. As the independent variables are assumed to be deterministic, the stochastic aspect of the linear model is completely covered by the residual terms. When we inspect the relation between the cooling constant P_0 and the arc-

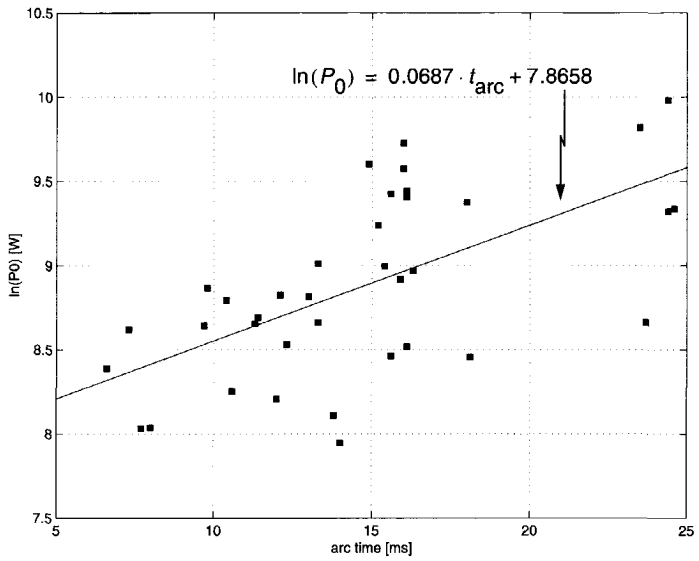

Figure 4-13. Arcing time versus the natural logarithm of the cooling constant P_0 (cb2)

ing time, as shown in figure 4-12, it is clear that the spread of the P_0 values increases for larger values of the arcing time. This phenomenon is called heteroscedasticity and indicates that the variance of the residuals is not equal for all the observations. This is in contradiction with the linear model, where the residuals always have the same distribution in spite of the independent variables. This problem can be tackled by transforming the dependent variables, as shown in figure 4-13, which results in the following linear regression model for cb2.

$$\ln(P_0) = 0.0687 \cdot t_{arc} + 7.8658 + \varepsilon_{P_0} \tag{4-33}$$

t_{arc} the arcing time [ms]

When the resulting residuals are plotted against the independent variables, as shown in figure 4-14, no clear patterns can be recognized. This is essential as the residues and the independent variables need to be uncorrelated.

Both P_1 and τ are dependent on P_0 (as shown in table 4-3), and the following linear regression models can be derived for cb2

$$\ln(1 - P_1) = 4.95\text{e-}5 \cdot P_0 - 5.8230 + \varepsilon_{P_1} \tag{4-34}$$

$$\ln(\tau) = 5.29\text{e-}5 \cdot P_0 - 1.4634 + \varepsilon_{\tau} \tag{4-35}$$

The independent variables have been transformed in order to prevent that the values of P_1 become larger than or equal to one and to prevent that the values of τ become smaller than or equal to zero.

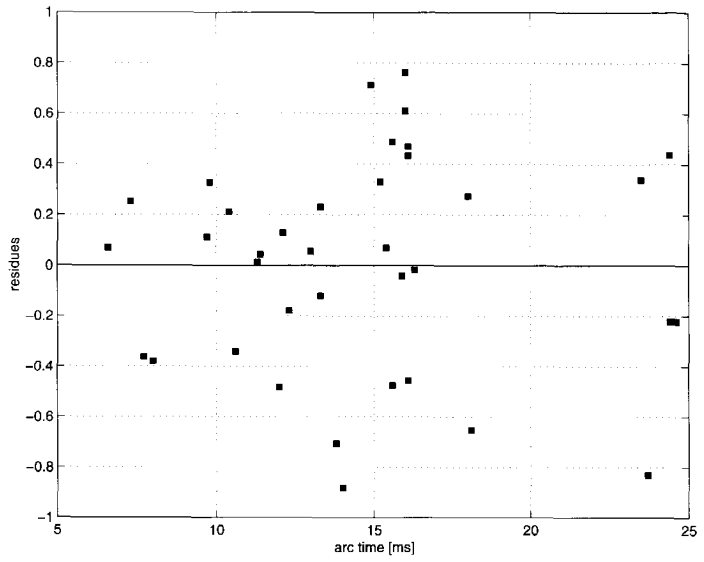

Figure 4-14. Arcing time versus the residues ε_{P_0} (cb2)

As the deterministic part of the three linear regression models has been specified, the residue vector in each model is known and its distribution can be determined. Because the normal distribution is the appropriate model when a measurement can be thought of as arising from the cumulative effect of a large number of factors (central limit theorem), a test on normality of the residue vectors is performed. In the first place, the residue vectors can be plotted in a normal probability plot to verify the normal distribution, as shown in figure 4-15 for the residues in equation 4-33. When the data (indicated with the plus signs) fall near the straight line, which is the case here, the assumption of normality is reasonable. In order to have a more sound statement on the presumed normally distributed residues, one can carry out EDF (empirical distribution function) tests. The basic principle is to see how closely the observed sample cumulative distribution agrees with the hypothesized theoretical cumulative distribution as shown in figure 4-16 for the residues in equation 4-33. Besides, the EDF tests are more suited for smaller data cases (which we have here) than the more familiar chi-squared test.

There are several ways to measure the amount of disagreement between the sample and hypothesized cumulative distribution functions (CDFs). The Kolmogorov-Smirnov test statistic is based on the maximum difference between the sample CDF and the hypothesized CDF. The Cramer-Von Mises test statistic is based on the integrated mean-square difference between the sample CDF and the hypothesized CDF. Both Cramer-Von Mises and Kolmogorov-Smirnov tests have been applied to test the normality of the residue vectors of the linear models of the arc model parameters.

The test of normality of the residue vectors is a hypothesis test.

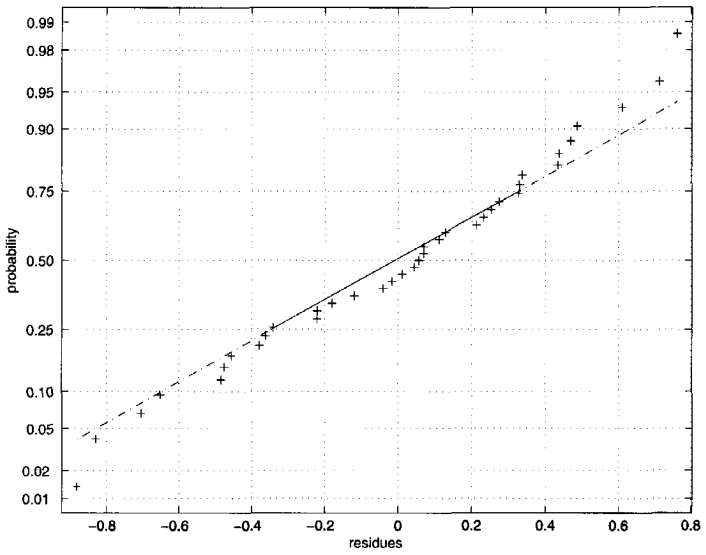

Figure 4-15. Normal probability plot of the residues ε_{P_0} (cb2)

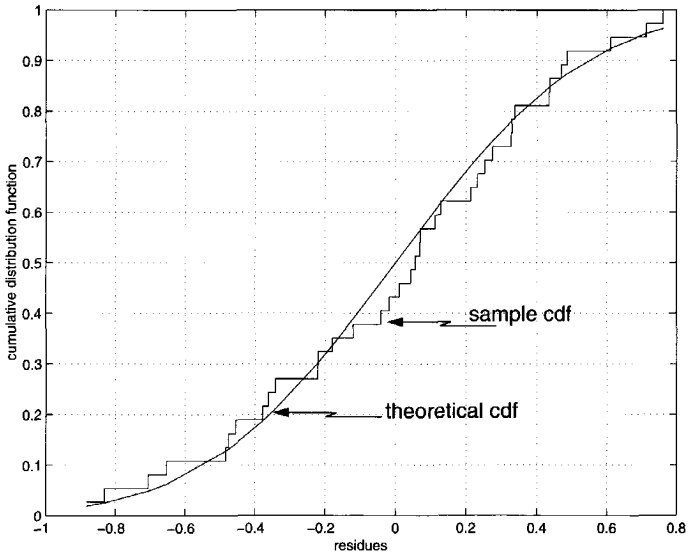

Figure 4-16. Cumulative distribution of the residues ε_{P_0} compared with the hypothesized theoretical cumulative distribution (cb2)

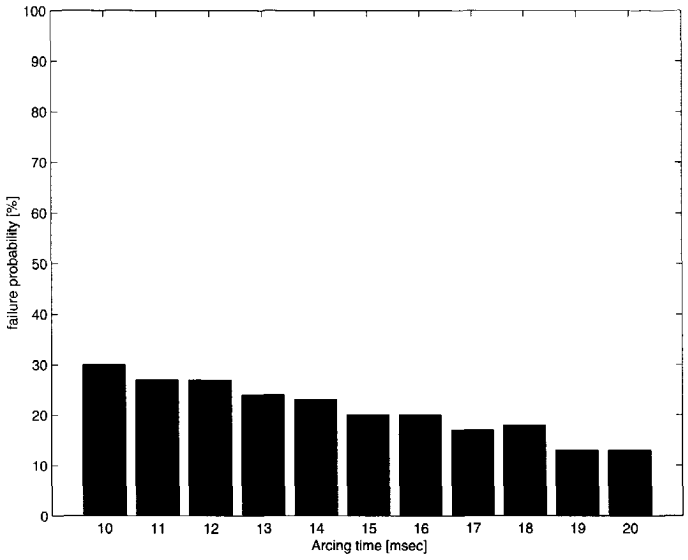

Figure 4-18. Failure probability of cb1 vs. the arcing time at a $(di/dt)_0$ = 18.9 A/μs (85% SLF)

H_0: normally distributed (null hypothesis)
H_1: not normally distributed (alternative hypothesis)

The null hypothesis (i.e. normally distributed residue vectors) cannot be rejected at a 10% level of significance for both breakers.

Thus, the circuit breaker can be modeled at various arcing times by the derived linear regression models (equations 4-33, 4-34 and 4-35), where the residue vectors are drawn from a normal distribution (characterized by its mean $\mu = 0$ and its variance σ^2).

Failure probability computation

To obtain the failure probability distribution as a function of the arcing time, we performed 100 arc-circuit interaction computations at each arcing time, as shown in the flowchart in figure 4-17. Both the transient program XTrans and the MATLAB Power System Blockset have been used for the computations and for mutual comparison.

In figure 4-18 and figure 4-19 we see the failure probability distributions of cb1 in a synthetic SLF test with $(di/dt)_0$ = 18.9 A/μs (85% SLF) and $(di/dt)_0$ = 20 A/μs (90% SLF), respectively. Figure 4-20, 4-21, and 4-22 show the failure probability distributions of cb2 in a direct SLF test with $(di/dt)_0$ = 9.2 A/μs (55% SLF), $(di/dt)_0$ = 11.7 A/μs (70% SLF) and $(di/dt)_0$ = 15.1 A/μs (90% SLF), respectively.

The trends - as they can be observed from the figures - agree with what we expected to find:

- the longer the arcing times, the lower the failure probability (at least in the range of arcing times used here)

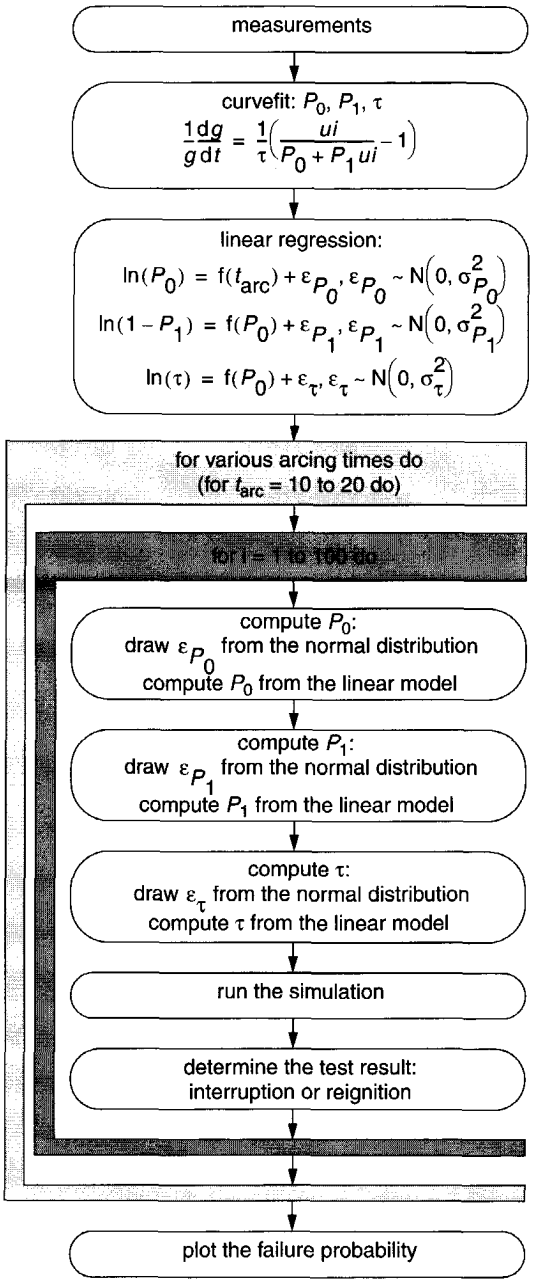

Figure 4-17. Flowchart of the statistical arc-circuit interaction computations

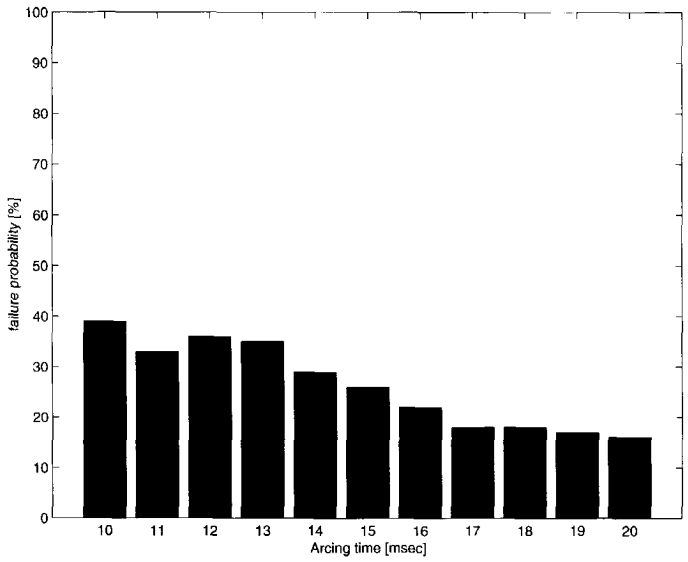

Figure 4-19. Failure probability of cb1 vs. the arcing time at a $(di/dt)_0$ = 20 A/μs (90% SLF)

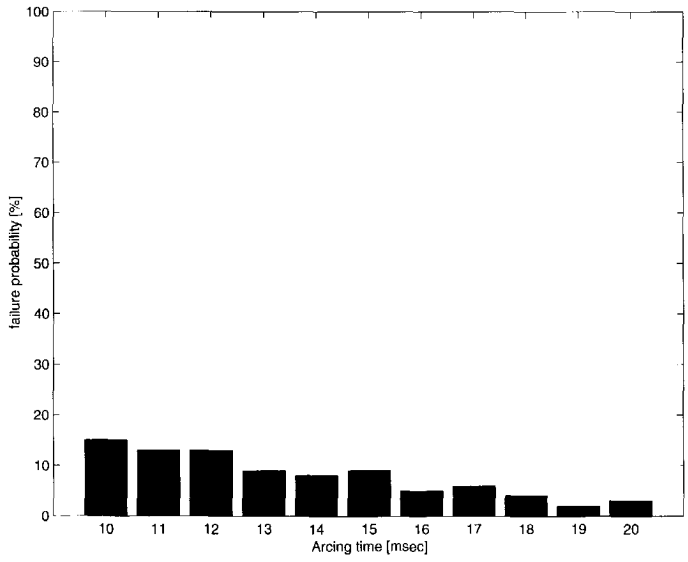

Figure 4-20. Failure probability of cb2 vs. the arcing time at a $(di/dt)_0$ = 9.2 A/μs (55% SLF)

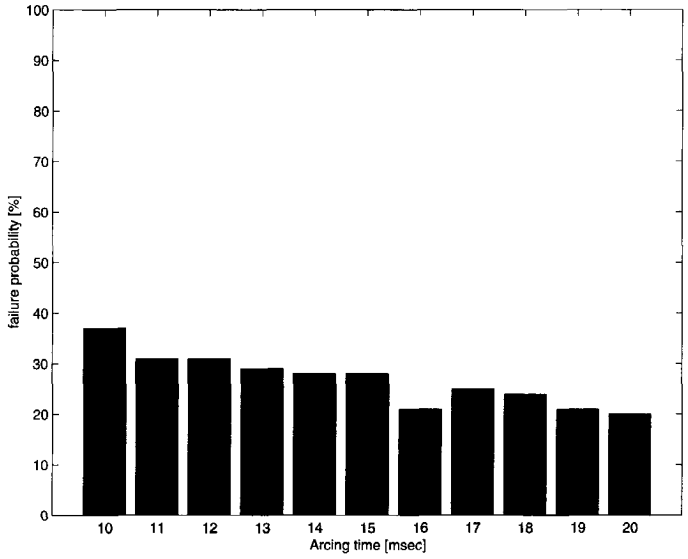

Figure 4-21. Failure probability of cb2 vs. the arcing time at a $(di/dt)_0$ = 11.7 A/μs (70% SLF)

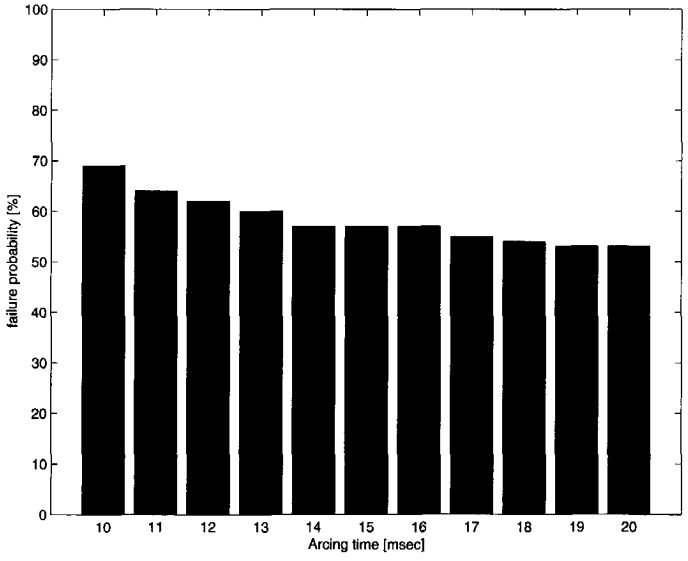

Figure 4-22. Failure probability of cb2 vs. the arcing time at a $(di/dt)_0$ = 15.1 A/μs (90% SLF)

- the higher the applied current steepness $(di/dt)_0$, the higher the failure probability distribution (at least in the range of SLF percentages used here [74])

Unfortunately, it is not possible to compare one of the obtained figures with the testing results directly. Because the measurements are spread over various arcing times, too few measurements at a specific arcing time are available to verify the computations. This is also one of the reasons why we perform this computation. The performance of two different circuit breakers can be compared by means of the failure probability distribution, while the arcing times during the tests were different. Therefore, the failure probability distributions can be used to compare various circuit breakers and/or designs.

4.5.2 Quality of interruption

An important feature of arc models is that they can be used to compute the 'quality of interruption' or, in other words, 'the margin of interruption', being the margin between interruption and failure. Furthermore, this parameter indicates how successful an interruption was (i.e. a comparison of interruptions) or how severe a failure was (i.e. a comparison of failures). After having performed a test on a circuit breaker, one can use the measurement data to determine the arc model parameters for this single measurement. Now, the arc model with the accompanying parameters can be used in a suitable computer program (see Chapter 6) to determine the maximum current slope $(di/dt)_{max}$ that the arc model is able to clear without reignition. The quality of interruption, as introduced by Habedank and Knobloch [27], is defined as the ratio between the $(di/dt)_{max}$ over the current slope $(di/dt)_0$ (i.e. the average value of the arc current derivative from an interval of 100 µs before current zero to 5 µs before current zero (see figure 3-4)) applied during the test: $(di/dt)_{max}/(di/dt)_0$. When this ratio exceeds one, the maximum *di/dt* the breaker could possibly clear is higher than the interrupted *di/dt* during the test, and this ratio corresponds to an interruption. In case of a ratio less than one, the situation corresponds to a reignition and the *di/dt* should be decreased so that the breaker interrupts. The quantity $(di/dt)_{max}/(di/dt)_0$ gives us a good indication of the interruption performance of the circuit breaker. The computed $(di/dt)_{max}$ is, however, larger than we expected based on experience gained from testing. This might be caused by the fact that the influence of the *di/dt* on the arc model parameters is neglected. Although it was concluded that the arc model parameters of cb1 and cb2 are not significantly correlated with the $(di/dt)_0$ at the chosen level of significance (see section 4.5.1), for cb2 there exists a (weak) positive correlation between P_0 and $(di/dt)_0$ and a weak negative correlation between τ and $(di/dt)_0$ (see table 4-3). An alternative method to determine more realistic $(di/dt)_{max}/(di/dt)_0$ values is investigated in section 5.4.

The $(di/dt)_{max}/(di/dt)_0$ for cb2, as computed with the proposed arc model, is shown in figure 4-23. In only two cases, the arc model gives an incorrect prediction:

- pole A: we have an observed reignition, while the arc model predicts an interruption (white square above the $(di/dt)_{max}/(di/dt)_0 = 1$ line)
- pole C: we have an observed interruption, while the arc model predicts a reignition (black diamond below the $(di/dt)_{max}/(di/dt)_0 = 1$ line)

Some remarkable observations can be made from figure 4-23:

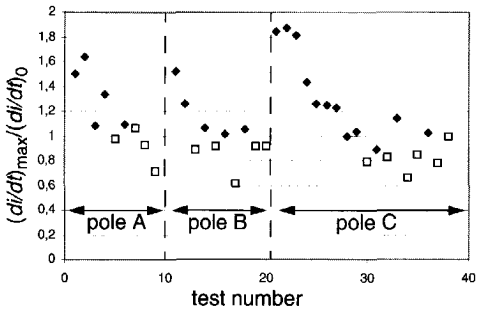

Figure 4-23. Test number versus the $(di/dt)_{max}/(di/dt)_0$ (cb2)
◆ = observed interruptions
□ = observed reignitions

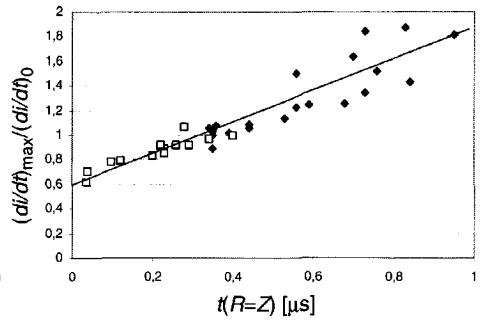

Figure 4-24. t(R=Z) versus the $(di/dt)_{max}/(di/dt)_0$ (cb2) (obtained from measurements)
◆ = observed interruptions
□ = observed reignitions

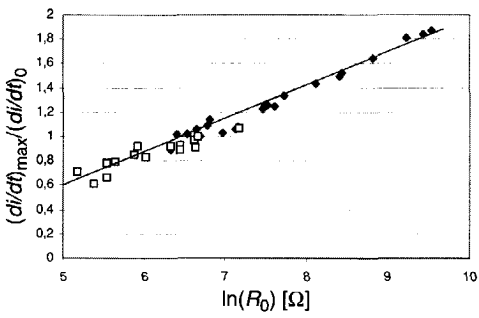

Figure 4-25. $ln(R_0)$ versus the $(di/dt)_{max}/(di/dt)_0$ (cb2) (obtained from computations)
◆ = observed interruptions
□ = observed reignitions

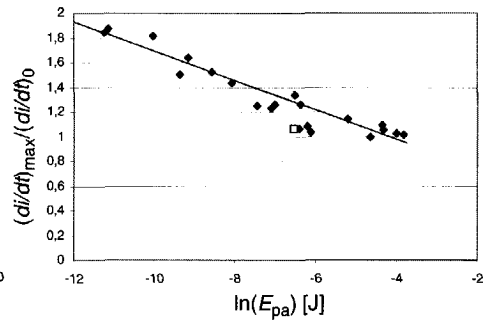

Figure 4-26. $ln(E_{pa})$ versus the $(di/dt)_{max}/(di/dt)_0$ (cb2) (obtained from computations)
◆ = observed interruptions
□ = observed reignitions

- There is a clear overall decrease in the quality of interruption during the progress of tests on every pole, reflecting the degradation of the circuit breaker by the tests.
- The rate of degradation clearly depends on the amount of power frequency current stress (pole A: 26.3 kA_{RMS}, pole B: 22.1 kA_{RMS}, pole C: 17.4 kA_{RMS}).

Another interpretation of the $(di/dt)_{max}/(di/dt)_0$ value is that it gives an indication of the stress that the circuit breaker encountered during a test. A high $(di/dt)_{max}/(di/dt)_0$ value indicates that the circuit breaker had a high margin of interruption and a relatively easy job in interrupting the current. Or in other words: the circuit breaker in its specific state encountered relatively low stress. The advantage of the $(di/dt)_{max}/(di/dt)_0$ is that it is an absolute value: if we have a value of 0.9, we know that it is a reignition. However, to obtain the $(di/dt)_{max}/(di/dt)_0$, we need to make multiple arc-circuit interaction computations. The three following indicators, active at different time intervals - before current zero, at current zero and after current zero - can be applied to quantify the stress, directly from the measurement or by computation (see also section 3.2).

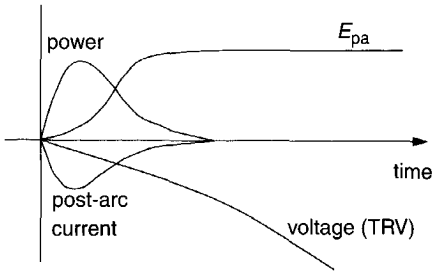

Figure 4-27. The post-arc energy (E_{pa})

- *before current zero.* The time before current zero where the arc resistance equals the characteristic impedance of the transmission line: $t(R=Z)$. The relation between the $(di/dt)_{max}/(di/dt)_0$ and the $t(R=Z)$ is shown in figure 4-24. In the figure, a rather strong linear relation can be observed between the two quantities and a clear distinction between the interruptions and failures. The closer the $t(R=Z)$ is to current zero, the more severely the breaker is stressed by the test circuit.
- *at current zero.* Knobloch and Habedank [38] applied the arc resistance at the current zero crossing: R_0. In our opinion this value can be obtained accurately from computations only (see section 3.2.2). The relation between the $(di/dt)_{max}/(di/dt)_0$ and the $\ln(R_0)$ is shown in figure 4-25. In the figure, a rather strong linear relation can be observed between the two quantities and a clear distinction between the interruptions and failures. The smaller the R_0 at the current zero crossing, the more the breaker is stressed by the test circuit.
- *after current zero.* Rieder [60] introduced the post-arc energy (E_{pa}), which is applied and thoroughly investigated by De Lange [15]. E_{pa} is the integral of the multiplication of the small post-arc current and the transient recovery voltage (TRV) as illustrated in figure 4-27. It is clear that only for interruptions an E_{pa} value can be calculated. As the post-arc currents are too small to be measured, the E_{pa} can only be obtained from computations. The relation between the $(di/dt)_{max}/(di/dt)_0$ and $\ln(E_{pa})$ is shown in figure 4-26. In the figure, a rather strong linear relation can be observed between the two quantities. The higher the E_{pa}, the more severely the breaker is stressed by the test circuit.

4.5.3 Critical line-length computation

In this section, three arc models are applied to determine the critical line length, i.e. the short line fault percentage, which stresses the circuit breaker most. The three indicators proposed in the previous section have been utilized to determine the stress on the breaker.

Arc models

The three arc models are listed hereunder. The first arc model is introduced in section 4.4 of this thesis: a modified Mayr type arc model with a constant time parameter τ and whose cooling power is a function of the electrical power input [73].

$$\frac{1}{g}\frac{dg}{dt} = \frac{1}{\tau}\left(\frac{ui}{P_0 + P_1 ui} - 1\right) \tag{4-36}$$

g the arc conductance [S]
u the arc voltage [V]
i the arc current [A]
τ the arc time constant [s]
P_0 cooling constant [W]
P_1 cooling constant

The second arc model is a series connection of a Cassie and Mayr arc model [26].

$$\begin{aligned} \frac{1}{g_c}\frac{dg_c}{dt} &= \frac{1}{\tau_c}\left(\frac{u_c^2}{U_0^2} - 1\right) \\ \frac{1}{g_m}\frac{dg_m}{dt} &= \frac{1}{\tau_m}\left(\frac{u_m i}{P_0} - 1\right) \\ \frac{1}{g} &= \frac{1}{g_c} + \frac{1}{g_m} \end{aligned} \tag{4-37}$$

g the total arc conductance [S]
g_c the conductance of the arc described by the Cassie equation [S]
g_m the conductance of the arc described by the Mayr equation [S]
u_c the voltage across the Cassie arc [V]
u_m the voltage across the Mayr arc [V]
i the arc current [A]
τ_c the Cassie arc time constant [s]
U_0 the Cassie steady state arc voltage [V]
τ_m the Mayr arc time constant [s]
P_0 the Mayr steady-state power-loss of the arc [W]

The third arc model consists of three arc models in series [86]. The first arc is a Mayr-Cassie type arc, the second one is a Mayr type arc, and the third one is a pure Mayr arc.

$$\begin{aligned} \frac{1}{g_1}\frac{dg_1}{dt} &= \frac{1}{\tau_1}\left(\frac{u_1 i}{g_1^{0.5625}/A_1} - 1\right) \\ \frac{1}{g_2}\frac{dg_2}{dt} &= \frac{1}{\tau_2}\left(\frac{u_2 i}{g_2^{0.1}/A_2} - 1\right) \\ \frac{1}{g_3}\frac{dg_3}{dt} &= \frac{1}{\tau_3}\left(\frac{u_3 i}{1/A_3} - 1\right) \\ \frac{1}{g} &= \frac{1}{g_1} + \frac{1}{g_2} + \frac{1}{g_3} \end{aligned} \tag{4-38}$$

g the total arc conductance [S]
g_n the conductance of the n^{th} arc [S]

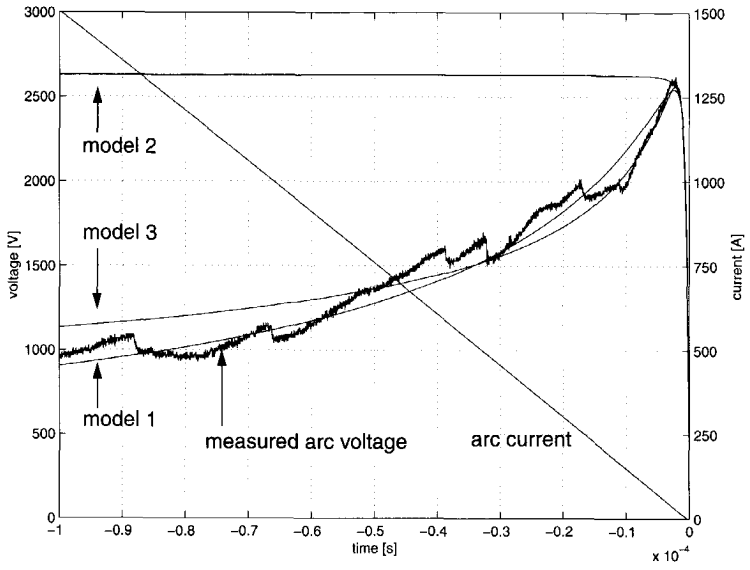

Figure 4-28. Comparison of three arc models: arc voltage reproduction (#5016, cb4)

u the total arc voltage [V]
u_n the voltage across the n^{th} arc [V]
i the arc current [A]
τ_n the time constant of the n^{th} arc [s]
A_1 the constant of the first arc $[1/A^{0.4375}V^{1.5626}]$
A_2 the constant of the second arc $[1/A^{0.9}V^{1.1}]$
A_3 the (inverted cooling) constant of the third arc [1/W]

All three arc models are able to reproduce the arc voltage, as illustrated in figure 4-28. In the last 100 µs before current zero, the deviation between the different traces is rather large (see figure 4-28). However in the last 2 µs before current, which is the most important period for the arc-circuit interaction, all three models create more or less the same voltage trace (see figure 4-29). At and after current zero, the models are in fact Mayr arc models. In the first arc model, the constant P_1 is set to zero from the current zero crossing on and transforms into a Mayr arc. For the second and the third arc model, it is only the pure Mayr equation that plays a role close to the current zero crossing.

Indicators for circuit severity

In order to determine which situation is the most severe for the circuit breaker, we used three different indicators, active at different time intervals - before current zero, at current zero and after current zero - to quantify the stress on the circuit breaker model (see section 4.5.2).

- *before current zero.* The time before current zero where the arc resistance equals the characteristic impedance of the transmission line: $t(R=Z)$. The closer the value is to current zero, the more severely the breaker is stressed by the test circuit.

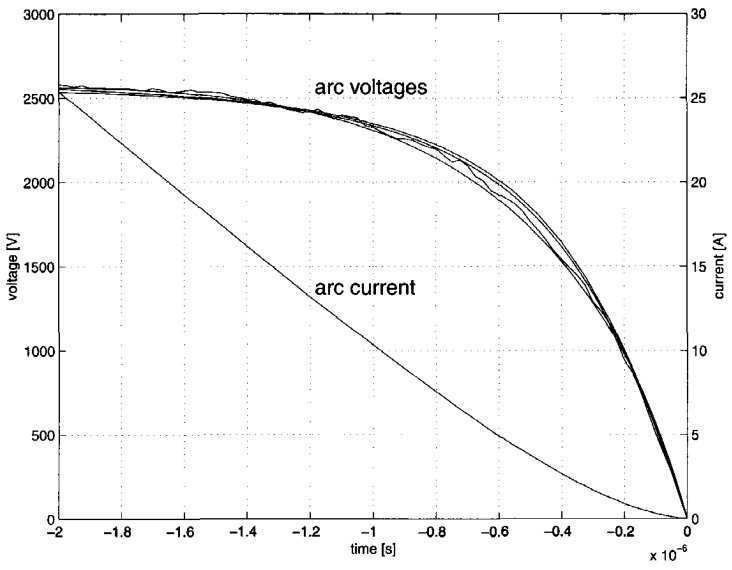

Figure 4-29. Comparison of three arc models: arc voltage reproduction detail (#5016, cb4)

- *at current zero.* The arc resistance: R_0. The smaller the arc resistance value at the current zero crossing, the more the breaker is stressed by the test circuit.
- *after current zero.* The post-arc energy: E_{pa}. The higher the E_{pa} value, the more severely the breaker is stressed by the test circuit.

Computational procedure

For the three specified arc models, arc model parameters have been determined for all of the measurements that were performed on the breakers under test. As one single set of parameters only describes the behavior of the arc during one specific test, a list of arc model parameters results for each breaker and each arc model. Each single set of arc model parameters, corresponding to one measurement, is used in the critical line-length determination. The computational procedure for each circuit breaker and each arc model is visualized by the flowchart in figure 4-30.

After a completed computation, we have obtained a list of stress indicators, i.e. $t(R=Z)$, R_0 and E_{pa} values, for the specific arc model and circuit breaker. In order to determine the most severe percentage SLF, based on the measurements of a specific breaker, we make the stress indicators relative for each measurement and compute the overall stress as the mean of the relative stress indicators per percentage SLF. An example of this approach is outlined in table 4-4 and in table 4-5 for three 'measurements'.

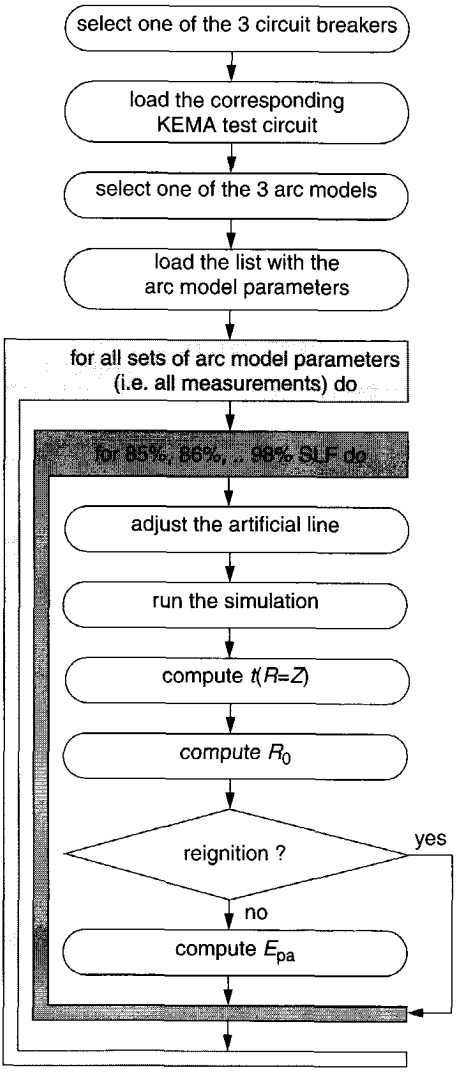

Figure 4-30. Flowchart of the critical line-length computation

Table 4-4. Example of absolute (R_0 [Ω]) stress indicators

measurement nr.	90%	91%	92%	93%	94%	95%
1	1000	900	800	700	800	900
2	900	800	700	800	900	1000
3	1100	1000	900	800	900	1000

Table 4-5. Example of relative and overall stress indicators

measurement nr.	90%	91%	92%	93%	94%	95%
1	1.4	1.3	1.1	1.0	1.1	1.3
2	1.3	1.1	1.0	1.1	1.3	1.4
3	1.4	1.3	1.1	1.0	1.1	1.3
overall stress	**1.4**	**1.2**	**1.1**	**1.0**	**1.2**	**1.3**

In table 4-5, the critical SLF percentage is shaded and amounts to 93%; the lower the (relative) arc resistance value at the current zero crossing, the more severely the breaker is stressed by the test circuit.

In total, more than 5000 arc-circuit interaction computations have been carried out. The results are summarized in table 4-6.

Table 4-6. Critical SLF percentages

circuit breaker	arc model	t(R=Z)	R_0	E_{pa}
cb2	1	95	95	91
	2	94	93	92
	3	94	93	92
cb3	2	94	93	93
	3	93	93	92
cb4	1	95	95	92
	2	95	95	92
	3	94	94	94

From table 4-6, it appears that the difference in outcome between the three arc models is rather small. Also, there is not a great difference in critical SLF percentages as predicted by the three stress indicators. Yet the critical SLF percentage as indicated by E_{pa} is in general smaller than the values predicted by the other two indicators. This might be caused by the fact that the E_{pa} value is sometimes based on less than half of the measurements because of reignitions.

The results for circuit breaker cb4, as computed with the three arc models, are shown graphically in figure 4-31, figure 4-32 and figure 4-33.

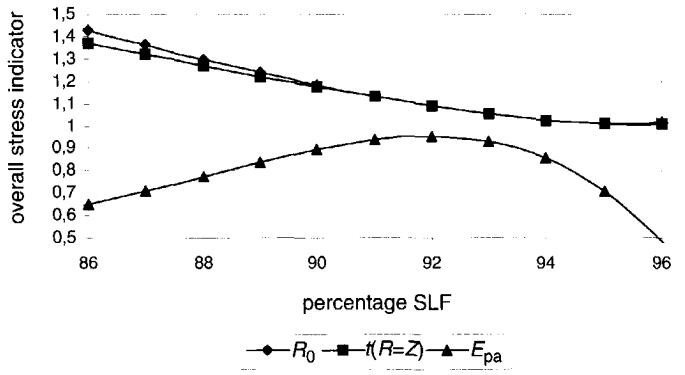

Figure 4-31. Critical line length / arc model 1 / cb4

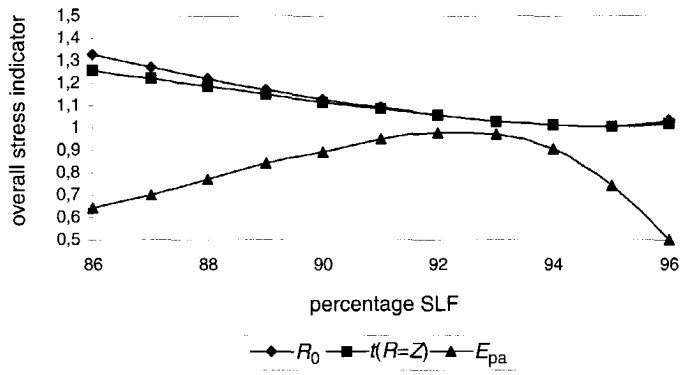

Figure 4-32. Critical line length / arc model 2 / cb4

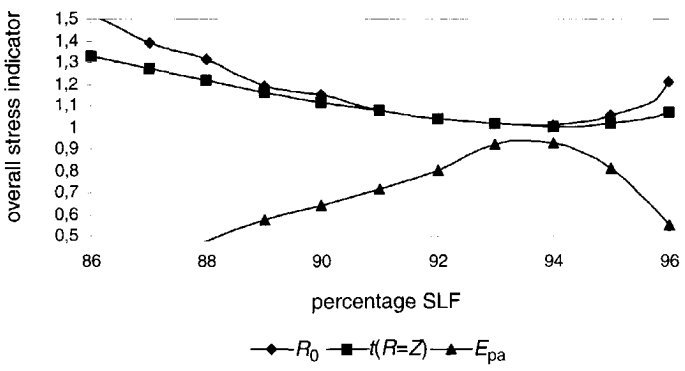

Figure 4-33. Critical line length / arc model 3 / cb4

The outcome is remarkable in the sense that rather independent of the circuit breaker, arc model and/or stress indicator, it appears that an SLF percentage higher than 90% puts more stress on the circuit breakers than the 90% SLF prescribed in the IEC standard. Although there is some scattering in the results, it appears that a 93-94% SLF is the most severe for the circuit breakers to interrupt.

Chapter 5

Voltage injection

5.1 Introduction

When arc models are applied for digital testing purposes, the measurement data of the circuit-breaker test are used to find the parameters of a (mathematical) arc model. In combination with a lumped-element representation of the test circuit, that particular measurement can be reconstructed. Furthermore, an arc model can be used to obtain additional information about the breaker under test; e.g. the margin of interruption, as described in section 4.5.2. On the other hand, this approach has also a few disadvantages and the following questions can be raised:

- As everybody uses their own arc model, and believes in the results obtained with it, why trust results obtained with other arc models?
- Why does the use of (Mayr-type) arc models often result in a noticeable computed post-arc current, while most of the recorded post-arc currents for the SF_6 circuit breakers in this thesis are in fact too small to be recorded?
- Is it correct to use an arc model and its parameters in a variety of circuits while the arc model parameters were obtained under different conditions in a different circuit?
- Is the arc behavior accurately described by an arc model of which the parameters are determined by means of the measured arc voltage and arc current traces before current zero only, while the measured current data can be rather inaccurate close to the current zero crossing?

Moreover, the application of a specific type of arc model is not generally valid, as an arc model with a limited number of free parameters is not able to represent all classes/types of circuit breakers; e.g. the arc model as proposed in this thesis fails to reproduce most of the measurements of cb3 (see section 4.4.2). Therefore, in this chapter, the measured data will be applied in

a more direct way. In the lumped-element representation of the laboratory test circuit the circuit breaker is modeled by means of a voltage source that injects the measured voltage across the circuit breaker into the network.

This voltage injection method is based on the substitution theorem [11,16]:
Consider an arbitrary network containing a number of independent sources. Suppose that for these sources and for the given initial conditions, the network has a unique solution for all its branch voltages and branch currents. Consider an uncoupled branch k, with the unique solutions $i_k(t)$ and $v_k(t)$ for the current and voltage waveform respectively. Suppose that this branch k is replaced by either an independent current source with waveform $i_k(t)$ or an independent voltage source with waveform $v_k(t)$. If the modified network has a unique solution for all its branch currents and branch voltages, then these branch currents and branch voltages are identical with those of the original network.

Therefore, we need to check that the modified network has a unique solution. When the circuit breaker in the test circuit is replaced by a voltage source, we obtain an RLC circuit with independent voltage sources. Given any initial state and any set of inputs, any linear time-invariant network made of passive R, L and C-components has a unique solution. Therefore, replacing the circuit breaker by a voltage source that injects the measured arc voltage into the test circuit should result in the same branch currents and branch voltages in the network as those caused by the circuit breaker within the original circuit.

The voltage injection method will be used in the following sections for 'digital testing' purposes. It will become clear that this approach is a useful tool in addition to the use of arc models.

5.2 Post-arc current verification

After the extinction of the arc, the inter-electrode space does not change into a complete insulating state instantaneously. The post-arc current is the current that continues to flow after the arc current has been interrupted and the transient recovery voltage builds up. From laboratory test results, there appears to be a relation between the amplitude of the post-arc current and the aging and/or degradation of a circuit breaker [84]. Therefore, the post-arc current is an important characteristic of the breaker.

Measuring the post-arc current poses some special problems (see also section 2.2). In the high-current interval, the transducers should be able to withstand currents of tens of kAs. Yet, after the current zero crossing, post-arc currents with a magnitude of about 1 A or less should be recorded. Additionally, the measurements are performed in an electromagnetically hostile environment. This problem is sometimes tackled by using a Rogowski coil for the current measurement: not the current itself is measured, but the time derivative of the current. The current is obtained by integrating the signal from the Rogowski coil (see also section 2.4.2 and section 2.4.3).

For one breaker only (cb2), post-arc currents have been detected. For all the measurements performed on the three poles of the specific circuit breaker, no physical post-arc currents could be detected in the measurement data (see for example the 'post-arc current' in figure 1-10), except for two cases. Both 'post-arc currents' occurred as the last interruption of a circuit-breaker pole, and thereafter, the circuit-breaker poles were degraded so far that only reignitions

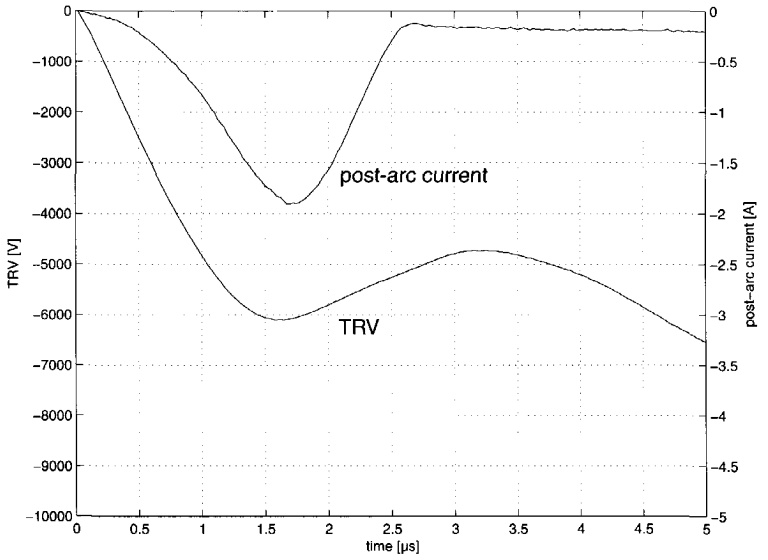

Figure 5-1. Post-arc current and TRV measurement of the last interruption of the 2nd pole (#503303, cb2)

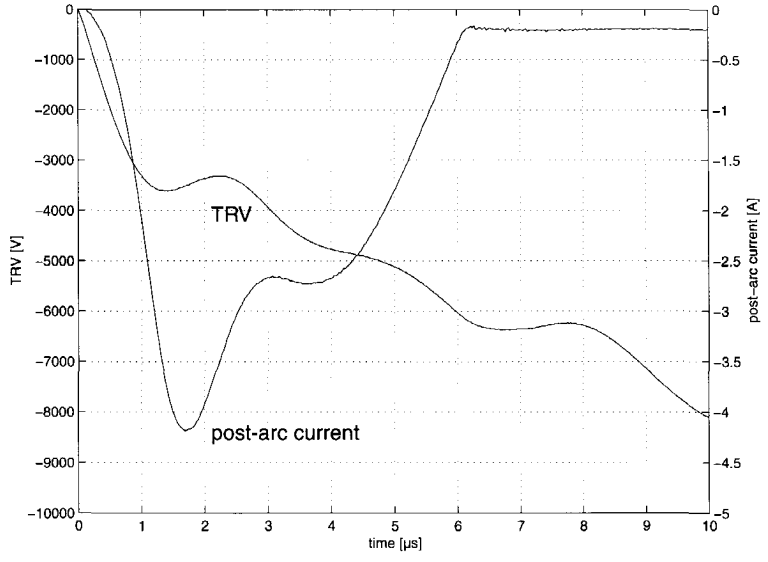

Figure 5-2. Post-arc current and TRV measurement of the last interruption of the 3th pole (#504704, cb2)

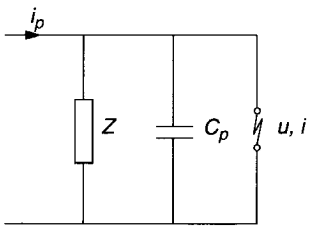

Figure 5-3. Simplified SLF circuit

occurred. Therefore, a large post-arc current could indicate that the circuit-breaker pole approaches its end of life. The measured 'post-arc currents' and TRVs are shown in figure 5-1 and figure 5-2.

5.2.1 Post-arc current computation

In order to verify those remarkably large post-arc currents that we measured, we did computations that are based on the more accurate voltage measurement [76]. Widl et al. [103] have already applied a similar approach to a simplified SLF test circuit as shown in figure 5-3. The arc current is computed with the following equation:

$$i = i_p - \frac{u}{Z} - C_p \frac{du}{dt} \tag{5-1}$$

i the arc current to be computed [A]
u the measured arc voltage [V]
i_p the prospective current [A]
Z the characteristic impedance of the line [Ω]
C_p the capacitance parallel to the breaker [F]

In this thesis, the complete test circuit will be considered. In the lumped-element representation of the laboratory test circuit the circuit breaker is modeled by means of a voltage source that injects the measured voltage across the circuit breaker into the network (see figure 5-4). The voltage injection consists of a block that injects a time-voltage array, being the measured data, into a (controlled) voltage source. The current flowing from the voltage source is determined and is equal to the current through the arc channel. MATLAB Simulink/Power System Blockset has been used for the voltage injection computations.

Because the arc voltage is only measured during the actual test around current zero, we extrapolate the arc voltage to obtain a linearly rising or constant arc voltage during the high-current phase of the interrupting process. Due to the resistive character of the arc, both the arc voltage and the arc current must be zero at the same time instant. As the arc current is calculated from the interaction between the circuit and the injected arc voltage, the instant of the current zero crossing is not known in advance. The voltage injection computation should therefore be repeated iteratively in order to make sure that the current and voltage zero crossing coincide. The procedure for calculating the current from the voltage measurement is depicted in figure 5-5, and is explained hereunder.

- The measurement data are loaded

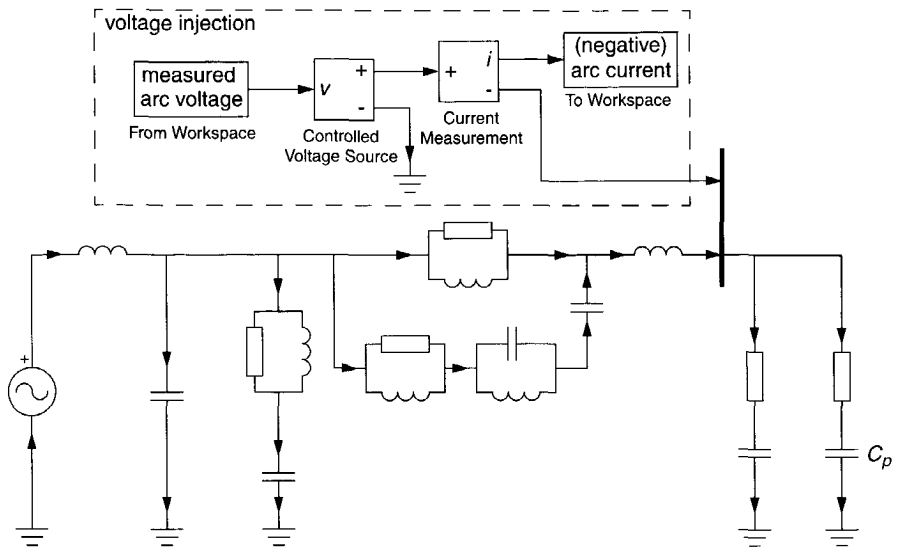

Figure 5-4. Voltage injection in a direct SLF test circuit (MATLAB Simulink/Power System Blockset)

- The accompanying test circuit is loaded
- Around voltage zero, a polynomial approximation is applied to the voltage measurement data. This is necessary while during the voltage injection computation a variable step size solver is used to reduce the computation time and because of the functionality of the Simulink block ('From Workspace') that injects the data into the circuit. The Simulink block uses linear interpolation when the variable step-size solver takes a step at a time that is not specified in the available data. This causes discontinuities in the *du/dt*. The capacitor C_p that is parallel to the voltage injection (see figure 5-4) and has a very small series resistance causes bursts in the computed current due to the abruptly changing arc voltage: $i = C_p du/dt$. By applying a polynomial approximation around the voltage zero crossing, we acquire global smoothness and obtain additional 'data points' to overcome this problem.
- If the exact time of the voltage zero crossing is unknown, this instant can be calculated with the polynomial approximation. When the time instant of the voltage zero crossing is already known, a weighted polynomial approximation can be applied and the voltage zero crossing gets a high weight factor.
- Because the arc voltage is only measured during the actual test around current zero, we extrapolate the arc voltage to obtain a linearly rising or constant arc voltage during the high-current phase of the interrupting process.
- Next the iterative computation starts. In fact, the voltage zero crossing is shifted until the zero crossing of the computed current is below a certain treshold value (e.g. the current at the voltage zero crossing must be smaller than 10 mA).

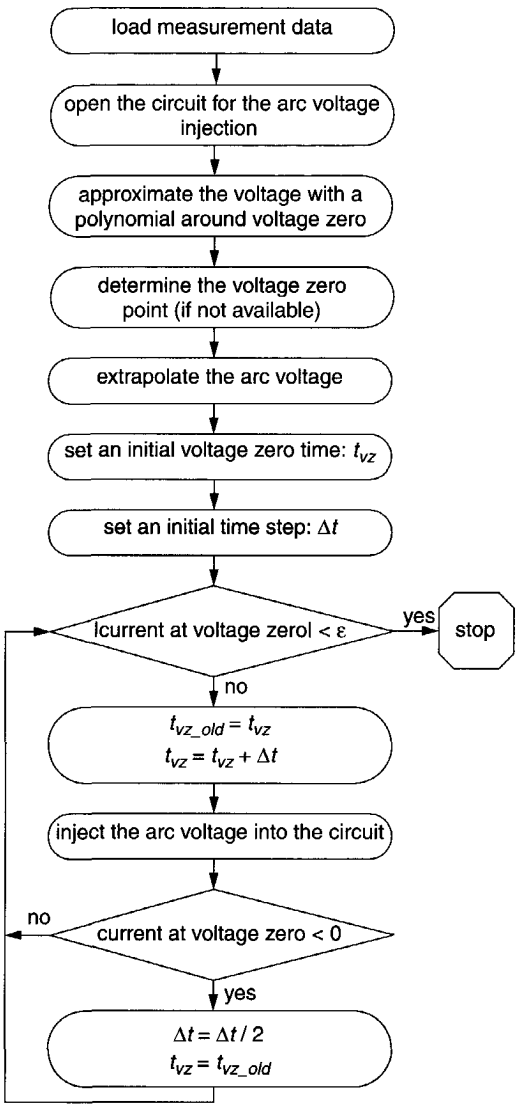

Figure 5-5. Flowchart of the voltage-injection method

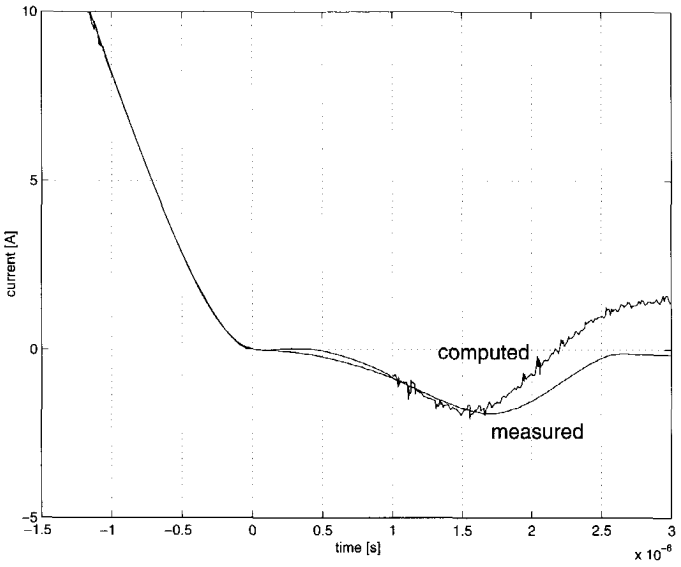

Figure 5-6. Reconstructed current of the last interruption of the 2nd pole (#503303, cb2)

When we realize that the test circuit, as shown in figure 5-4, is only a lumped-element representation of the laboratory test circuit used during the testing in the high-power laboratory, it is understandable that measured and computed results are not completely identical. The capacitance C_p (figure 5-4), parallel to the circuit breaker, in the test circuit of cb2 (see figure A-5 (section A.2)) was increased to 300 pF instead of 50 pF in order to obtain good agreement between the measured and computed traces.

A few of the results of the voltage injection computations are shown in figure 5-6, figure 5-7, figure 5-8 and figure 5-9, and it can be concluded that the currents are reconstructed rather well. The rather large post-arc current amplitudes that are measured for the last interruptions of the second and third circuit-breaker poles are reconstructed as well. This indicates that the observed 'post-arc currents' are in fact physical post-arc currents and shows that the circuit representation and the measurement data are reliable. In the cases where no post-arc currents could be detected in the measurement data, the computation gives no indication of a physical post-arc current either. The computational procedure is not suitable for calculating 'normal' post-arc currents; the iteration stops when the current at voltage zero is smaller than 10 mA (see the flowchart in figure 5-5), which is in the order of magnitude of a 'normal' post-arc current.

The reconstructed current trace contains some noise, and is smooth from one microsecond before until one microsecond after the current zero crossing. The noise is absent here because of the polynomial approximation and the availability of additional 'data points' around the voltage zero crossing.

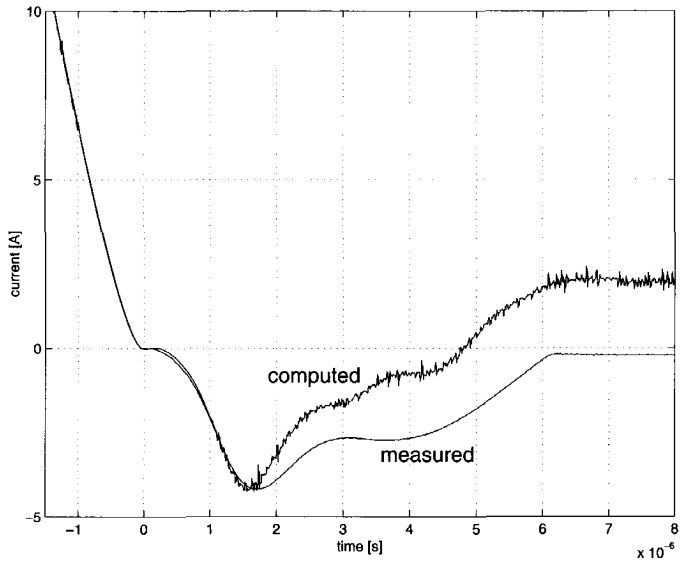

Figure 5-7. Reconstructed current of the last interruption of the 3th pole (#504704, cb2)

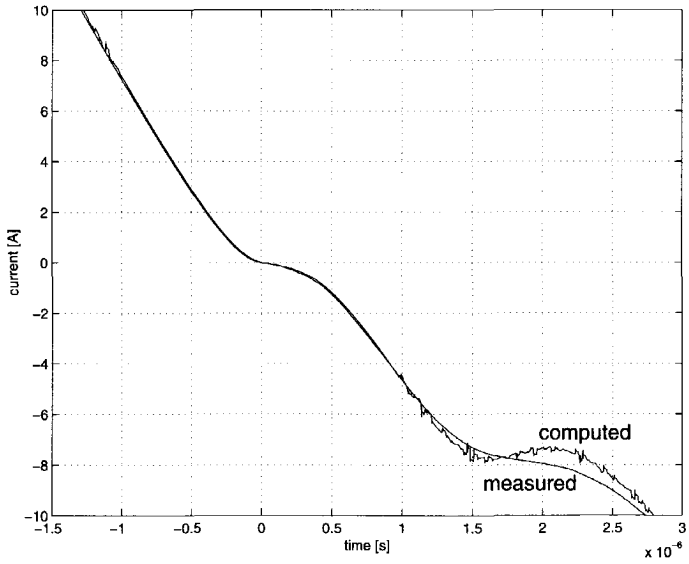

Figure 5-8. Reconstructed current of a reignition (#504703, cb2)

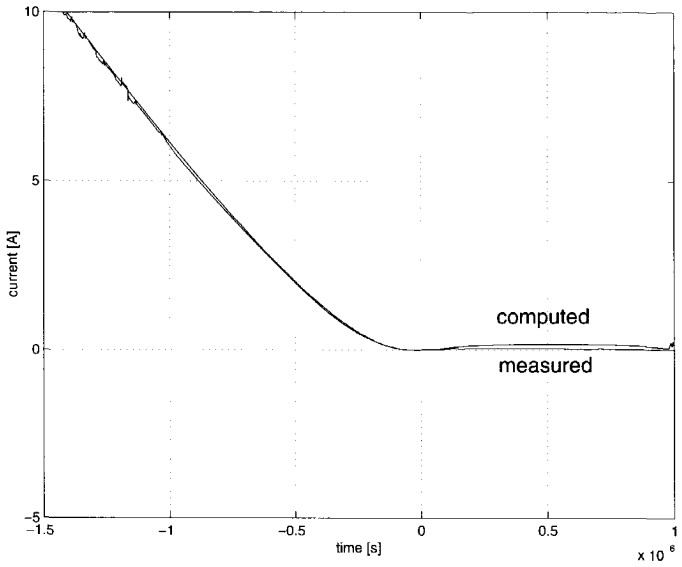

Figure 5-9. Reconstructed current of an interruption (#504604, cb2)

5.2.2 Undamped TRV computation

Another way to obtain information about the post-arc current is to compare the measured TRV with one that is computed by assuming the post-arc current to be zero. The post-arc current causes damping of the TRV waveform. This damping is usually negligible as the post-arc currents for SF_6 breakers are very small.

To compute the undamped transient recovery voltage, one needs to have calculated accurately the state variables of the circuit (capacitor voltages and inductor currents) at current zero, including arc-circuit interaction. This is the case when one has completed the iterative computation of the voltage injection method, as described in the previous section, and the time instants of voltage zero and current zero coincide.

Another simulation is performed for the after current zero domain, for which the obtained state variables at current zero are used as the initial conditions. For this computation, the voltage injection is removed from the circuit (in other words: the 'circuit breaker' is removed from the network), which implies that the circuit breaker has an infinite resistance after current zero and the computed transient recovery voltage is not damped by a post-arc current.

The difference between the measured (damped) and the calculated (undamped) transient recovery voltage gives us information about the presence or absence of a post-arc current. A few of the measured and computed TRVs are shown in figure 5-10, figure 5-11 and figure 5-12. The damping in the two cases when a large 'post-arc current' was measured is considerably larger than for the other cases. This can be observed clearly when one looks at the first TRV peaks: in

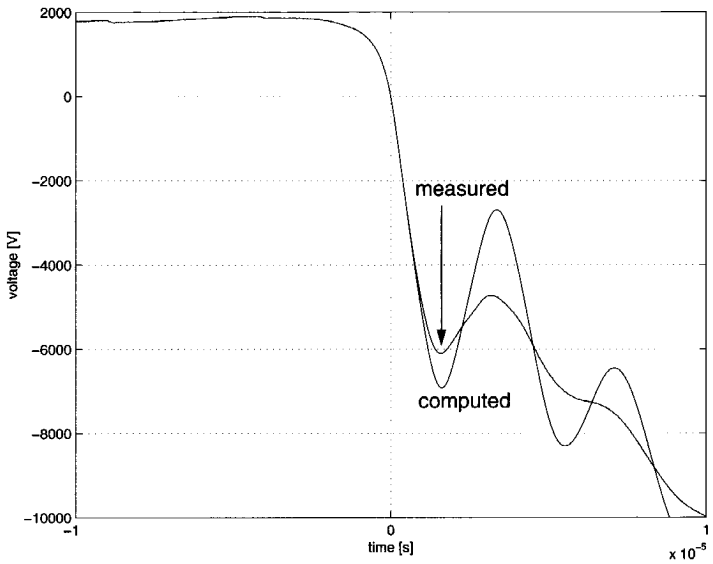

Figure 5-10. Measured and computed (undamped) TRVs of the last interruption of the 2nd pole (#503303, cb2)

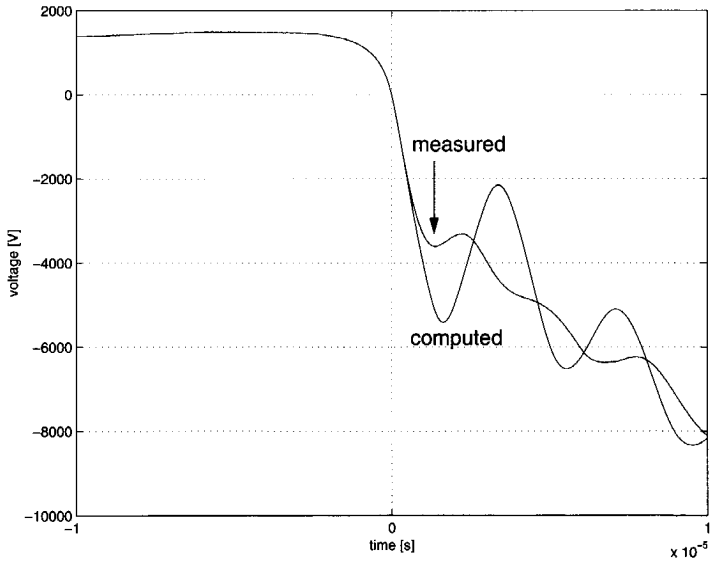

Figure 5-11. Measured and computed (undamped) TRVs of the last interruption of the 3th pole (#504704, cb2)

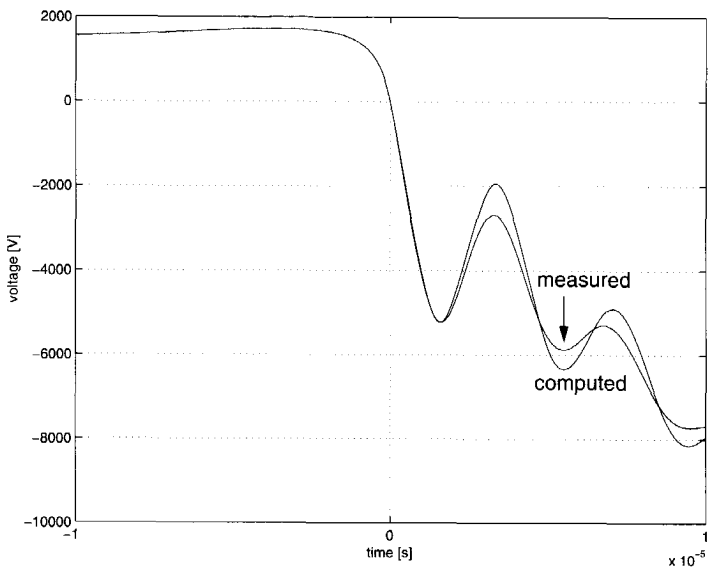

Figure 5-12. Measured and computed (undamped) TRVs of an interruption (#504604, cb2)

figure 5-10 and figure 5-11, the two cases where a large post-arc current was distinguished, considerable differences in peak values occur; in figure 5-12, where no post-arc current could be detected, hardly any difference is seen.

5.3 Artificial-line comparison

The voltage injection method can be fruitfully applied to investigate arc-circuit interaction in different circuits. In this section the measured voltages of cb2, cb3 and cb4 will be used to compare 4 types of lines (artificial lines) for SLF tests. That means that the artificial lines are not compared by means of (models of) the three circuit breakers cb2, cb3 and cb4, but the artificial lines are compared when they are subjected to arc voltages that are equal to the ones that have been measured for cb2, cb3 and cb4. This enables us to investigate the difference between the arc-circuit interaction of the various lines in a transparent way. Note that, due to this approach, the influence of the test circuit on the arc voltage is neglected. This assumption can - to some extent - be supported by comparing the average arc voltages of pole A and B of cb3, as shown in figure 5-13. These two poles of the breaker were tested in different test circuits whereas the same $(di/dt)_0$ was applied: pole A was tested in a direct SLF test circuit (figure A-12), while pole B was subjected to a synthetic SLF test (figure A-15). The average arc voltage trace of pole B is somewhat higher than that of pole A. This corresponds to the fact that the average arcing time of the test series of pole B (11.7 ms) is higher than that of pole A (11 ms). The shape of the average arc voltage traces is identical: 0.8 times the average arc voltage trace of pole B equals the average arc voltage trace of pole A.

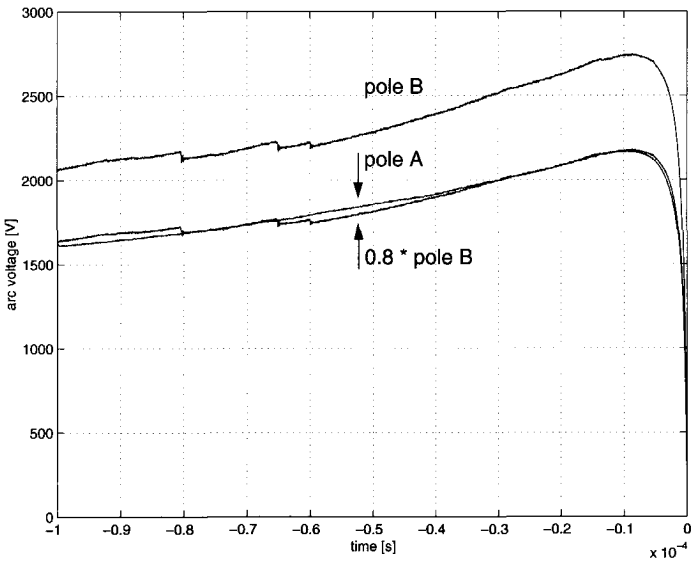

Figure 5-13. Average arc voltages of pole A and B of cb3
Note that the average arc voltage of pole A is about 0.8 times the average arc voltage of pole B

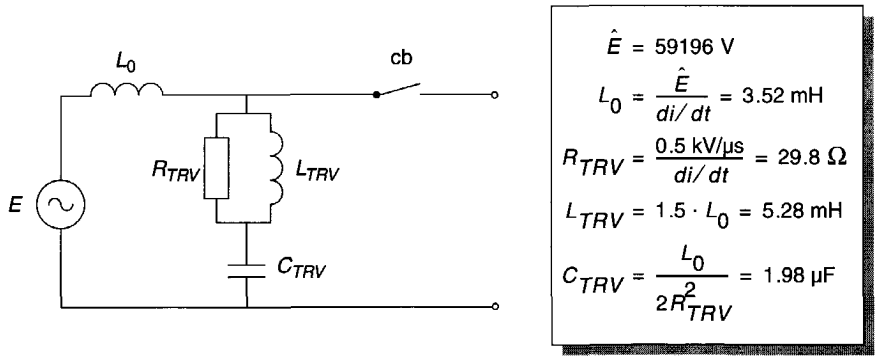

Figure 5-14. Two-parameter TRV circuit [9]

5.3.1 Artificial lines

The test circuits have been dimensioned for a 72.5 kV, 31.5 kA, 60 Hz circuit breaker. The direct test circuit used to represent the power system at the supply side of the circuit breaker is shown in figure 5-14. For the characteristics of an ideal line, resulting in a 90% SLF, it holds that:

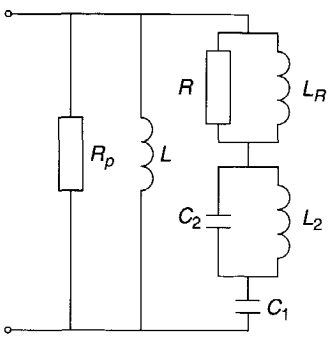

$$L = 0.391 \text{ mH}$$
$$L_R = 0.145 \cdot L = 5.67\text{e-}5 \text{ H}$$
$$L_2 = 0.0725 \cdot L = 2.83\text{e-}5 \text{ H}$$
$$C_1 = \frac{1}{3} \cdot \frac{L}{Z_c^2} = 521.3 \text{ pF}$$
$$C_2 = 2C_1 = 1.04 \text{ nF}$$
$$R = Z_c = 500\ \Omega$$
$$R_p = 10Z = 4500\ \Omega$$
$$Z_c = \frac{R_p Z}{R_p - Z} = 500\ \Omega$$

Figure 5-15. KEMA artificial line [96]
R_p is put in parallel to reduce the peak factor from 1.8 to 1.6.

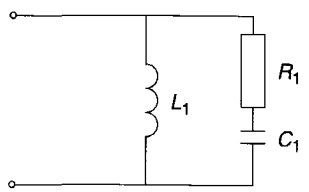

$$L_1 = 1.6 \cdot L = 6.256\text{e-}4 \text{ H}$$
$$C_1 = C = 1.93 \text{ nF}$$
$$R_1 = Z = 450\ \Omega$$

Figure 5-16. RLC artificial line [91]

$$L = L_0\left(\frac{1}{0.9} - 1\right) = 0.391 \text{ mH} \tag{5-2}$$

L_0 the inductance of the source-side circuit in figure 5-14 [H]

$$C = \frac{L}{Z^2} = 1.93 \text{ nF} \tag{5-3}$$

Z the characteristic impedance: $Z = 450\ \Omega$

The artificial lines considered are depicted in figure 5-15, figure 5-16, figure 5-17 and figure 5-18. The npi artificial line, shown in figure 5-18, serves as a reference because of its good correspondence to an ideal piece of transmission line. The inherent SLF wave shapes produced by the four artificial lines are plotted in figure 5-19.

5.3.2 Computational results

The indicator $t(R=Z)$, used earlier in section 3.2.2 and section 4.5.2, is applied to quantify the arc-circuit interaction. Therefore, only the arc-circuit interaction before current zero is studied. All the measured arc voltages for cb2, cb3 and cb4 have been injected into the four SLF cir-

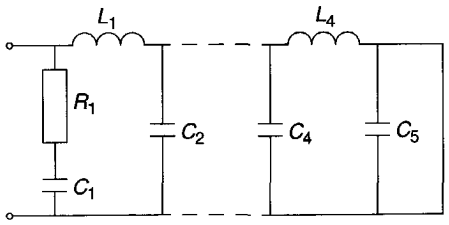

$L_{1...4} = L/4 = 9.775\text{e-}5$ H
$C_{1,5} = C/8 = 0.241$ nF
$C_{2...4} = C/4 = 0.482$ nF
$R_1 = Z = 450\ \Omega$

Figure 5-17. npiR artificial line; 4 pi-sections [91]

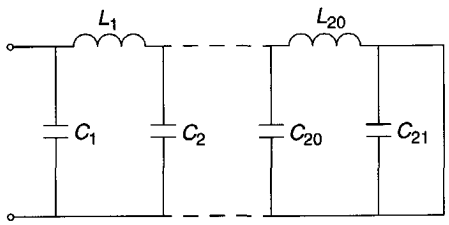

$L_{1...20} = L/20 = 1.955\text{e-}5$ H
$C_{1,21} = C/40 = 48.25$ pF
$C_{2...20} = C/20 = 96.5$ pF

Figure 5-18. npi artificial line; 20 pi-sections; serves as a reference [91]

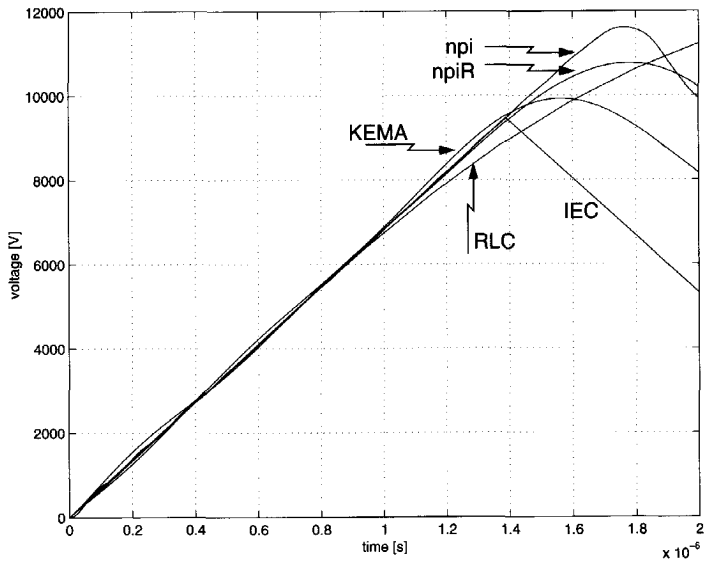

Figure 5-19. Inherent SLF wave shapes

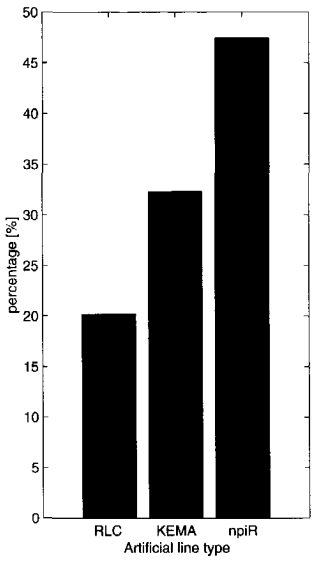

Figure 5-20. Artificial line that shows the closest correspondence to the reference npi line

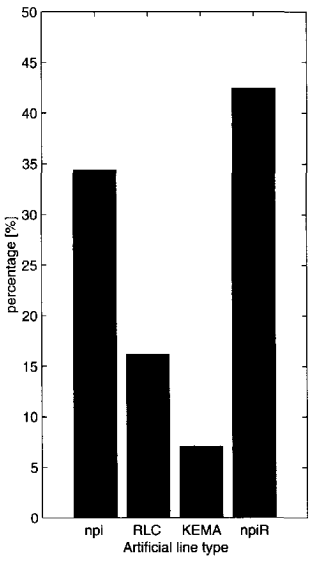

Figure 5-21. Artificial line that stresses the circuit breaker most

cuits and the $t(R=Z)$ values have been computed. Based on the indicator $t(R=Z)$, the npiR artificial line has an arc-circuit interaction that corresponds most to that of the reference npi line. This can be observed from figure 5-20 in which the percentage of all injected arc voltages is shown where the $t(R=Z)$ value of the RLC, KEMA or npiR SLF circuit is closest to that of the reference npi circuit. This result could have been expected, as a frequency scan of the four SLF circuits (displayed in figure 5-22), shows the best agreement between the npiR and the reference npi circuit.

Based on the indicator $t(R=Z)$, the npiR artificial line stresses the circuit breaker most, while the KEMA artificial line is the least severe for the breaker, as shown in figure 5-21. In order to explain these results, we must analyze the arc-circuit interaction before current zero; as the arc-circuit interaction differs for the four SLF circuits, a different arc resistance development and interruption probability results (see also [67]). The arc-circuit interaction before current zero is analyzed in the next section.

5.3.3 Arc-circuit interaction

When a simplified SLF circuit with only the source, the arc and the main inductances is studied, insight can be gained on the voltage distribution. Because we focus on a 90% SLF in this case, $L = L_0/9$ (see equation 5-2), the voltage distribution for the simplified SLF circuit in figure 5-23 is:

$$u_{L0} = \frac{9}{10}(E + u_{\text{arc}}) \tag{5-4}$$

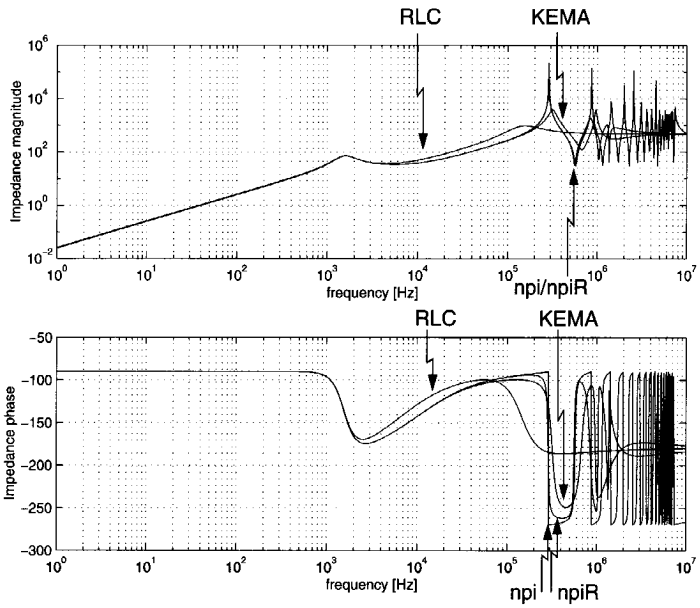

Figure 5-22. Frequency scan of the four SLF circuits

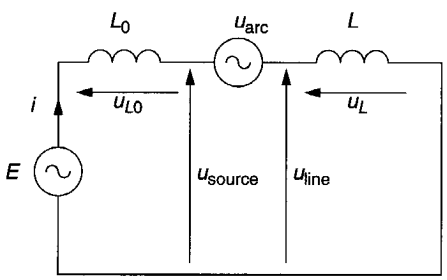

Figure 5-23. Simplified SLF circuit (1)

$$u_L = \frac{1}{10}(E + u_{arc}) \tag{5-5}$$

The current i, from figure 5-23, is a 100% inductive current. The current lags the driving voltage by 90 degrees and is zero when the supply voltage is at its peak value. Therefore, the *di/dt*, with the peak driving voltage $\hat{E} >> u_{arc}$, can be considered to be constant in the interval around the current zero crossing.

$$\frac{di}{dt} \approx \frac{\hat{E}}{L_0 + L} \tag{5-6}$$

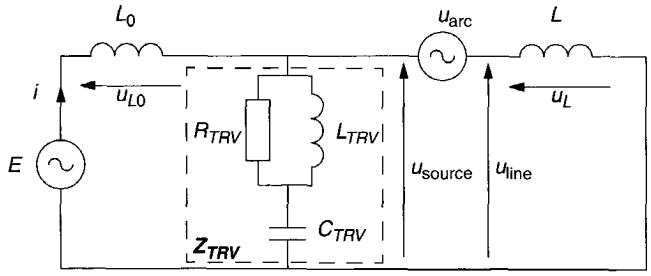

Figure 5-24. Simplified SLF circuit (2)

When the TRV branch is added at the supply side, we obtain the circuit in figure 5-24. For the voltage source and during the static part of the arc voltage, i.e. for low frequencies, the impedance of the TRV branch is large and can be neglected compared to the impedances of the inductances. Therefore, the voltage distribution is more or less the same as in equation 5-4 and equation 5-5. However, close to current zero, the arc voltage changes rapidly and higher frequencies start to play a role. Now the influence of the TRV branch cannot be neglected anymore. For the higher frequencies, the impedance of the TRV branch reaches the value of R_{TRV}. The impedances of the inductances increase linearly with the frequency. At the higher frequencies, the parallel connection of L_0 and Z_{TRV}, as seen from the arc, is predominantly determined by Z_{TRV}. Consequently, the dynamic part of the arc voltage distributes over Z_{TRV} and over L. As the impedance of the line inductance is much higher than that of the TRV branch, the voltage builds up across the line inductance L. The current i, as shown in figure 5-24, is approximately purely inductive. As the dynamic part of the arc voltage builds up across the line inductance, the constant di/dt (equation 5-6) around the current zero crossing is hardly influenced by the presence of the TRV branch.

When, at the line side of the circuit breaker, the artificial line is considered instead of only the line inductance, the low-frequency behavior remains the same. For the higher frequencies, the impedance of the artificial line tends towards the characteristic impedance $Z = 450\ \Omega$. The dynamic part of the arc voltage distributes over $Z_{TRV} = R_{TRV} = 29.8\ \Omega$ and $Z = 450\ \Omega$. As approximately 15/16 part of the dynamic arc voltage builds up across the line, in the following it will be assumed that the complete dynamic part of the arc voltage builds up at the line side only. The voltages and current in an SLF circuit are schematically depicted in figure 5-25. The current i, as shown in figure 5-25, is approximately inductive. As the dynamic part of the arc voltage builds up at the line side of the breaker, the constant di/dt (equation 5-6) around the current zero crossing is hardly influenced by the presence of the TRV branch. However, due to the interaction between the arc and the artificial line, the current steepness before current zero is heavily distorted. It is the deviation from the current through the line inductance (i_L), which crosses zero with a constant di_L/dt (equivalent to equation 5-6), that will be studied hereunder.

The arc-circuit interaction will be analyzed based on one characteristic arc voltage for each set of arc voltages. This characteristic arc voltage has been obtained by creating an average arc voltage based on all of the measured arc voltages of a specific breaker. Therefore, three characteristic arc voltages result, each related to one of the circuit breakers (cb2, cb3 and cb4). The average arc voltages are shown in figure 5-26. In order to be able to make analytic computa-

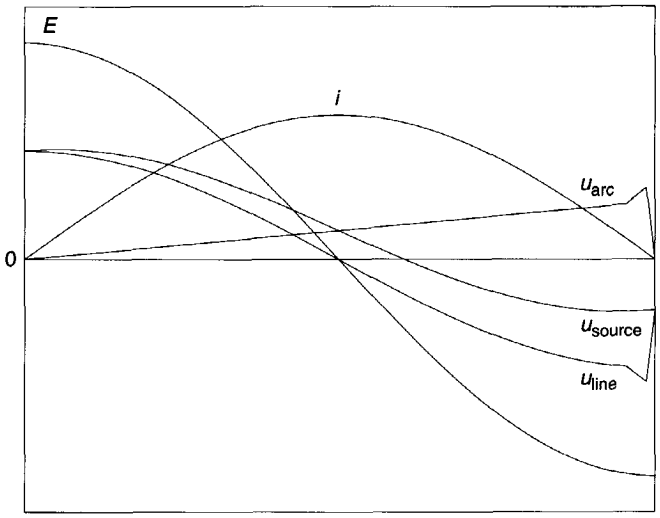

Figure 5-25. Voltage and current traces in a SLF circuit (amplitudes and time scales are exaggerated)

tions for the time interval where the arc voltage is changing rapidly, we approximate the dynamic parts of the average arc voltages by the following, relatively simple, functions:

$$u_{cb2} = \frac{1425}{\exp(6.25)} \cdot \exp(2.5e6 \cdot t) \qquad t = 0...2.5\ \mu s \tag{5-7}$$

$$u_{cb3} = \frac{1550}{\exp(12.5)} \cdot \exp(2.5e6 \cdot t) + 3e13 \cdot t^2 \qquad t = 0...5\ \mu s \tag{5-8}$$

$$u_{cb4} = \frac{2450}{\exp(6.25)} \cdot \exp(2.5e6 \cdot t) \qquad t = 0...2.5\ \mu s \tag{5-9}$$

These functions describe the departure of the arc voltage from the more or less constant arc voltage value indirectly. As the artificial line sees the dynamic part of the arc voltage as a divergence from the more or less constant (in this case: negative) u_{line} value, as shown in figure 5-25, the equations describe this sudden change (in this case: increase) in voltage. The approximations compared with the mean arc voltages are shown in figure 5-27; the time $t = 0$ used in equations 5-7, 5-8, and 5-9, corresponds to the blacks dots at the onset of the computed voltages whereas the time $t = 2.5\ \mu s$ (cb2 and cb4) and $t = 5\ \mu s$ (cb3) corresponds to the arc-voltage zero crossing.

As the exponential functions in the dynamic arc voltage approximating equations have the same powers and differ only in multiplication factor, the response of the artificial lines to equation 5-8 (cb3) will be investigated. By means of superposition, the response of the artificial lines to this equation can be studied in two parts. First, the response of the artificial lines to the

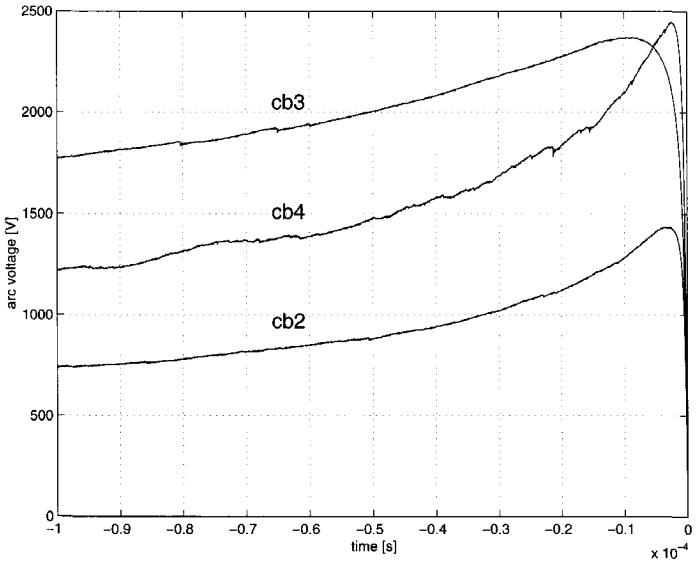

Figure 5-26. Average arc voltages of cb2, cb3 and cb4
Note that the average arc voltage of cb4 is about 1.7 times the average arc voltage of cb2

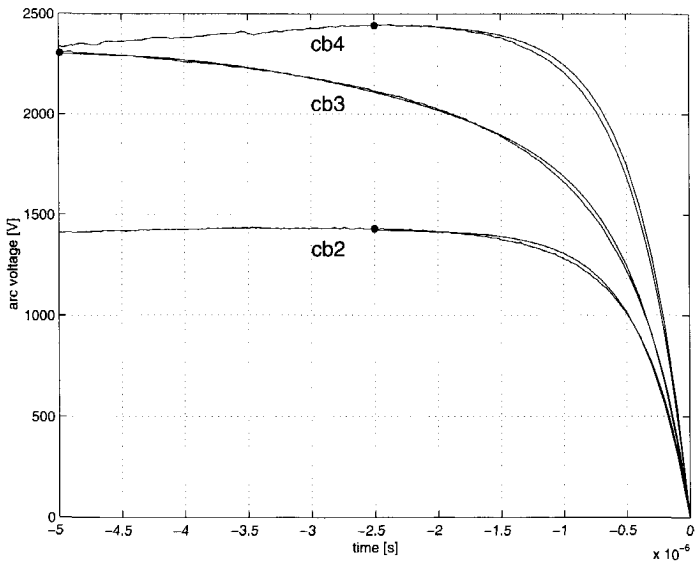

Figure 5-27. Simple approximations of the dynamic part of the arc voltage

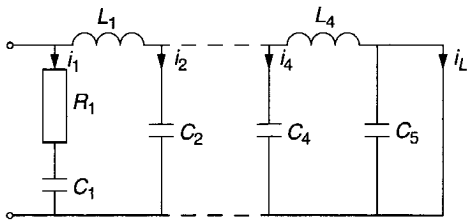

$L_{1...4} = L/4 = 9.775\text{e-}5$ H
$C_{1,5} = C/8 = 0.241$ nF
$C_{2...4} = C/4 = 0.482$ nF
$R_1 = Z = 450\ \Omega$

Figure 5-28. Currents in the npiR artificial line; 4 pi-sections

exponential voltage term and second, the response to the quadratic term. The response of the artificial lines, when exposed to the dynamic arc voltage of cb2 or cb4, will be equivalent to the response of the lines when exposed to the exponential voltage term of cb3. The currents differ only by a constant factor.

RLC artificial line (figure 5-16)

When the exponential voltage term is applied, the currents through the line inductance L (i_L) and the branch in parallel (i) are approximately:

$$i_L(t) \approx \frac{a}{L} \cdot \frac{\exp(2.5\text{e}6 \cdot t)}{2.5\text{e}6} \approx 3.7\text{e-}6 \cdot \exp(2.5\text{e}6 \cdot t) \tag{5-10}$$

$$i(t) \approx a \cdot C \cdot 2.5\text{e}6 \cdot \frac{\exp(2.5\text{e}6 \cdot t)}{2.5\text{e}6 \cdot R \cdot C + 1} \approx 8.8\text{e-}6 \cdot \exp(2.5\text{e}6 \cdot t) \tag{5-11}$$

a constant; 1550/exp(12.5)
t time; $t = 0...5$ µs
L $L = 6.256\text{e-}4$ H
C $C = 1.93$ nF
R $R = 450\ \Omega$

When the quadratic voltage term is applied, the currents through the line inductance L (i_L) and the branch in parallel (i) are approximately:

$$i_L(t) \approx \frac{b \cdot t^3}{6 \cdot L} \tag{5-12}$$

$$i(t) \approx b \cdot C \cdot t \tag{5-13}$$

b constant; $b = 6\text{e}13$

npiR artificial line (figure 5-28)

When we apply the exponential voltage term, the inductive short-circuit current (i_L) and the total current through the capacitance branches of the artificial line (i) are approximately:

$$i_L(t) \approx \left(\frac{a}{L} \cdot 0.1\text{e-}6 \cdot \exp(2.5\text{e}6 \cdot t)\right) /$$

$$\left(\left(1 + \frac{1}{2} \cdot (2.5\text{e}6)^2 LC\right) \cdot \left(2 \cdot (2.5\text{e}6)^2 LC + \frac{1}{2} \cdot (2.5\text{e}6)^4 L^2 C^2 + 1\right)\right) \approx \tag{5-14}$$

$$\approx 3.1\text{e-}6 \cdot \exp(2.5\text{e}6 \cdot t)$$

$$i_1(t) \approx \frac{a \cdot C \cdot 1.25\text{e}6 \cdot \exp(2.5\text{e}6 \cdot t)}{1.25\text{e}6 \cdot R \cdot C + 1} \approx 2.7\text{e-}6 \cdot \exp(2.5\text{e}6 \cdot t) \tag{5-15}$$

$$i_2(t) \approx a \cdot C \cdot \exp(2.5\text{e}6 \cdot t) \cdot \left(\frac{3}{4} \cdot 2.5\text{e}6 + 3 \cdot (2.5\text{e}6)^3 LC + \frac{1}{4} \cdot (2.5\text{e}6)^5 L^2 C^2\right) /$$

$$\left(\left(1 + \frac{1}{2} \cdot (2.5\text{e}6)^2 LC\right) \cdot \left(2 \cdot (2.5\text{e}6)^2 LC + \frac{1}{2} \cdot (2.5\text{e}6)^4 L^2 C^2 + 1\right)\right) \approx \tag{5-16}$$

$$\approx 4.0\text{e-}6 \cdot \exp(2.5\text{e}6 \cdot t)$$

$$i_3(t) \approx \frac{a \cdot C \cdot 1.25\text{e}6 \cdot \exp(2.5\text{e}6 \cdot t)}{2 \cdot (2.5\text{e}6)^2 LC + \frac{1}{2} \cdot (2.5\text{e}6)^4 L^2 C^2 + 1} \approx 2.1\text{e-}6 \cdot \exp(2.5\text{e}6 \cdot t) \tag{5-17}$$

$$i_4(t) \approx a \cdot C \cdot \frac{1}{4} \cdot 2.5\text{e}6 \cdot \exp(2.5\text{e}6 \cdot t) /$$

$$\left(\left(1 + \frac{1}{2} \cdot (2.5\text{e}6)^2 LC\right) \cdot \left(2 \cdot (2.5\text{e}6)^2 LC + \frac{1}{2} \cdot (2.5\text{e}6)^4 L^2 C^2 + 1\right)\right) \approx \tag{5-18}$$

$$\approx 0.9\text{e-}6 \cdot \exp(2.5\text{e}6 \cdot t)$$

$$i(t) \approx i_1(t) + i_2(t) + i_3(t) + i_4(t) \approx 9.7\text{e-}6 \cdot \exp(2.5\text{e}6 \cdot t) \tag{5-19}$$

a constant; 1550/exp(12.5)
t time; $t = 0...5$ µs
L $L = 9.775\text{e-}5$ H
C $C = 0.482$ nF
R $R = 450\ \Omega$

When we apply the quadratic voltage term, the inductive short-circuit current (i_L) and the total current through the capacitance branches of the artificial line (i) are approximately:

$$i_L(t) \approx -\frac{5}{8} \cdot b \cdot C \cdot t + \frac{b \cdot t^3}{24 \cdot L} \tag{5-20}$$

$$i(t) \approx 2 \cdot b \cdot C \cdot t \tag{5-21}$$

b constant; $b = 6\text{e}13$

npi artificial line (figure 5-18)

The results of an npi artificial line with $n = 4$ are comparable with those of the npiR artificial line. As the resistance in the first capacitance branch is not present, a slightly higher current results in this branch.

$$i_1(t) \approx a \cdot C \cdot 1.25e6 \cdot \exp(2.5e6 \cdot t) \approx 3.5e\text{-}6 \cdot \exp(2.5e6 \cdot t) \tag{5-22}$$

a constant; 1550/exp(12.5)
t time; $t = 0...5$ µs
C $C = 0.482$ nF

When the exponential voltage term is applied, this leads to a total current through the capacitance branches of the artificial line that is slightly higher than the one of the npiR artificial line.

$$i(t) \approx i_1(t) + i_2(t) + i_3(t) + i_4(t) \approx 10.5e\text{-}6 \cdot \exp(2.5e6 \cdot t) \tag{5-23}$$

When the number of pi sections - in our case 20 - is increased, the current decreases.

When the quadratic voltage term is applied, the total current through the capacitance branches of the artificial line is equal to the one derived for the npiR artificial line.

KEMA artificial line (figure 5-15)

Because of the resistance in parallel with the main inductance of the artificial line, this artificial line draws a resistive current during the static period of the arc voltage. The current through the resistance R_p amounts to:

$$i_{Rp}(t) \approx \frac{\hat{E}\cos(\omega t)}{10 \cdot R_p} \approx 1.3\cos(\omega t) \tag{5-24}$$

R_p $R_p = 4500\ \Omega$

When the exponential voltage term is applied, the currents through the line inductance L (i_L) and the two branches in parallel (i and i_{Rp}) are approximately:

$$i_L(t) \approx a \cdot \frac{\exp(2.5e6 \cdot t)}{2.5e6 \cdot L} \approx 5.9e\text{-}6 \cdot \exp(2.5e6 \cdot t) \tag{5-25}$$

$$\begin{aligned} i(t) \approx a \cdot C_1 \cdot \Big\{ & (2.5e6 \cdot R + (2.5e6)^2 L_R + (2.5e6)^3 R C_2 L_2 + (2.5e6)^4 C_2 L_2 L_R)/ \\ & [(2.5e6)^2 R C_1 L_2 + (2.5e6)^2 R C_1 L_R + (2.5e6)^2 R C_2 L_2 + R + 2.5e6 \cdot L_R + \\ & (2.5e6)^4 R C_1 C_2 L_2 L_R + (2.5e6)^3 C_1 L_2 L_R + (2.5e6)^3 C_2 L_2 L_R] \Big\} \cdot \exp(2.5e6 \cdot t) \approx \\ & \approx 6.2e\text{-}6 \cdot \exp(2.5e6 \cdot t) \end{aligned} \tag{5-26}$$

$$i_{Rp}(t) \approx \frac{a \cdot \exp(2.5e6 \cdot t)}{R_p} \approx 1.3e\text{-}6 \cdot \exp(2.5e6 \cdot t) \tag{5-27}$$

a constant; 1550/exp(12.5)

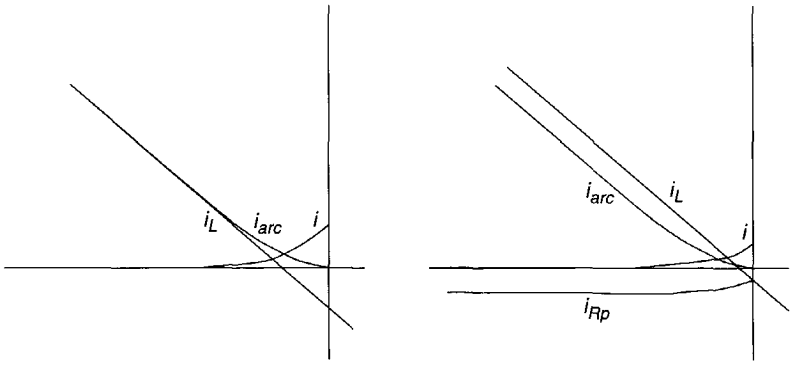

Figure 5-29. Current traces close to (arc) current zero, resulting from arc-circuit interaction
Left: situation applicable to the RLC, npiR and npi artificial line: $i_{arc} = i_L + i$
Right: situation applicable to the KEMA artificial line: $i_{arc} = i_L + i + i_{Rp}$

t	time; $t = 0...5$ µs
C_1	$C_1 = 521.3$ pF
C_2	$C_2 = 1.04$ nF
L	$L = 0.391$ mH
L_2	$L_2 = 2.83e\text{-}5$ H
L_R	$L_R = 5.67e\text{-}5$ H
R	$R = 500\ \Omega$
R_p	$R_p = 4500\ \Omega$

When the quadratic voltage term is applied, the currents through the line inductance L (i_L) and the two branches in parallel (i and i_{Rp}) are approximately:

$$i_L(t) \approx \frac{b \cdot t^3}{6 \cdot L} \tag{5-28}$$

$$i(t) \approx b \cdot C_1 \cdot t \tag{5-29}$$

$$i_{Rp}(t) \approx \frac{b \cdot t^2}{2 \cdot R_p} \tag{5-30}$$

b	constant; 6e13

Artificial lines compared

The arc-circuit interaction makes it easier for the circuit breaker to interrupt the current. Due to the rapidly changing arc voltage close to the arc current zero crossing, the artificial lines give a 'flat foot' to the otherwise with a constant *di/dt* reducing arc current. This effect is depicted in figure 5-29. As a result, the arc resistance increases more rapidly to higher values, which also results in larger *t(R=Z)* values. As we have two types of arc voltages here, one consisting of an exponential term only and one described by both a quadratic and an exponential term, the effect of the arc-circuit interaction will be described separately.

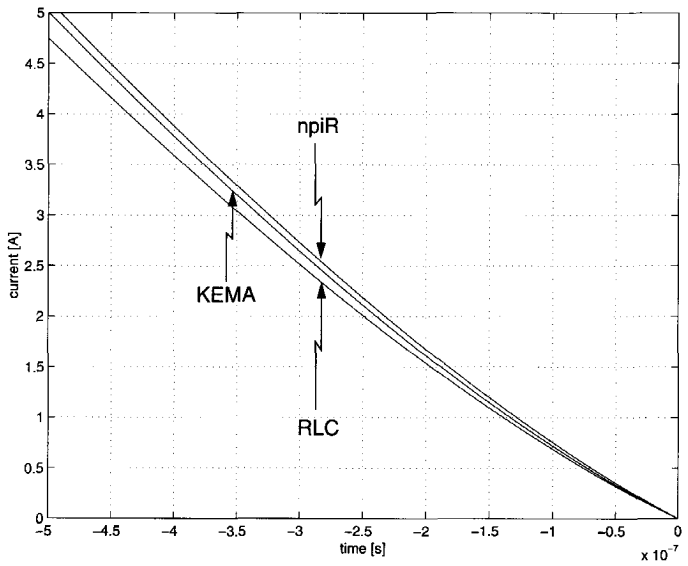

Figure 5-30. Arc currents close to current zero, when the dynamic part of the arc voltage is only described by an exponential function

When an arc voltage is considered where the dynamic part of the voltage is only described by an exponential term (as is the case for cb2 and cb4), it is evident that the order of the artificial line drawing the largest current is as follows:

- KEMA: $i(t) + i_L(t) + i_{Rp}(t) \approx 13.4\text{e-}6 \cdot \exp(2.5\text{e}6 \cdot t)$
- npi: slightly higher than the current drawn by the npiR artificial line but smaller than $i(t) + i_L(t) < 13.6\text{e-}6 \cdot \exp(2.5\text{e}6 \cdot t)$
- npiR: $i(t) + i_L(t) \approx 12.8\text{e-}6 \cdot \exp(2.5\text{e}6 \cdot t)$
- RLC: $i(t) + i_L(t) \approx 12.5\text{e-}6 \cdot \exp(2.5\text{e}6 \cdot t)$

This ranking needs to be nuanced. The line inductance of the RLC circuit is 1.6 times higher than that of the other artificial lines. Therefore, the di_L/dt of the stationary short-circuit current is considerably less (about 6%) than that in the other SLF circuits. Therefore, the arc resistance builds up more quickly and the RLC circuit tends out to be the least taxing artificial line. The arc currents in the KEMA, npiR and RLC SLF circuits are shown in figure 5-30.

When an arc voltage is considered for which the dynamic part of the voltage is only described by a quadratic term, the order of the artificial line drawing the largest current at the instant of the arc current zero crossing is as follows (note that all the line inductances and capacitances have been set to a reference value for easy comparison):

- KEMA: $i(t) + i_L(t) + i_{Rp}(t) \approx 0.27 \cdot b \cdot C \cdot t + \frac{b \cdot t^3}{6 \cdot L} + \frac{b \cdot t^2}{2 \cdot R_p}$

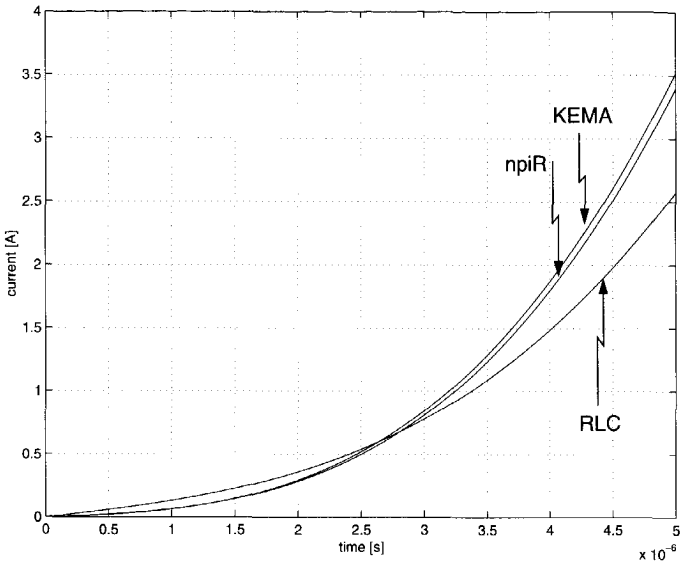

Figure 5-31. Currents through the artificial lines when the dynamic part of the arc voltage is described by a quadratic function

- npiR/npi: $i(t) + i_L(t) \approx \frac{11}{32} \cdot b \cdot C \cdot t + \frac{b \cdot t^3}{6 \cdot L}$
- RLC: $i(t) + i_L(t) \approx b \cdot C \cdot t + \frac{b \cdot t^3}{6 \cdot 1.6 \cdot L}$

b constant; 6e13
t time; $t = 0...5$ µs
L $L = 0.391$ mH
C $C = 1.93$ nF
R_p $R_p = 4500\ \Omega$

The currents are visualized in figure 5-31.

Therefore, when the results are combined, and the response of the artificial lines is studied when the dynamic part of the arc voltage is described by both an exponential and a quadratic term (as is the case for cb3), the KEMA line turns out to be the least taxing. The RLC artificial line, which showed to be the easiest on a circuit breaker with a dynamic arc voltage described by an exponential term only, is now almost as taxing as the npi and npiR artificial line. The resulting arc currents in the KEMA, npiR and RLC SLF circuits are shown in figure 5-32.

5.4 Quality of interruption

The possibility to obtain an indicator for the interruption performance of circuit breakers under test is an important property of arc models. The computed $(di/dt)_{max}/(di/dt)_0$ ratio gives an

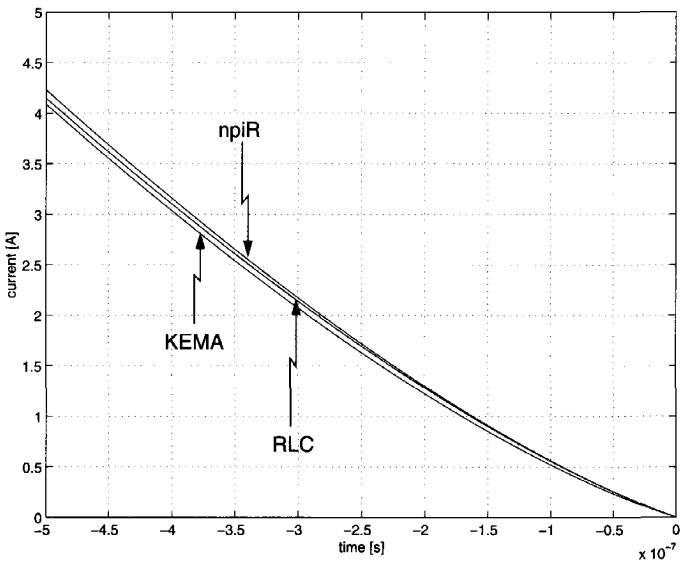

Figure 5-32. Arc currents close to current zero when the dynamic part of the arc voltage is described by both an exponential and quadratic function

expression for the quality of interruption for each test. The computed $(di/dt)_{max}$ is, however, larger than we expected based on experience gained from testing (see section 4.5.2).

The voltage injection method can also be applied to determine the quality of interruption: $(di/dt)_{max}/(di/dt)_0$. For this purpose the relation between the measured arc voltage and the *di/dt* applied during the test must be investigated. In figure 5-33 and figure 5-34, the *di/dt* applied during the test is displayed versus the measured peak arc voltage of cb2 and cb4, respectively (cb3 has been tested with an almost constant *di/dt* and does not add useful information for this purpose). It is clear from the figures that the peak arc voltage seems to be spread over the same range of values when the *di/dt* varies. Of course, the peak arc voltage is strongly influenced by the arcing time. The arcing time in the synthetic tests of cb4 has been kept more or less constant and does not influence the peak arc voltage. The arcing time for cb2 varies throughout the test series, but that influence is present in all three clusters (around di/dt = 9 A/µs, di/dt = 12 A/µs and di/dt = 14 A/µs) in figure 5-33. The large spread of the arc voltage peaks in a cluster originates mainly from the non-constant arcing time.

Accordingly, it is straightforward to apply the arc voltage injection method here [79]; the measured arc voltage is injected, and remains therefore constant, while the *di/dt* is adjusted (by means of the generator voltage in a direct test or the capacitor bank voltage in a synthetic test scheme) in order to determine the critical boundary between interruption and failure. This can be achieved by combining the two following approaches: the voltage injection method before current zero and the use of an arc model after current zero. As all arc models used in section 4.5.3 reduce to the original Mayr arc model at current zero and immediately thereafter, the choice for a Mayr arc model in combination with the voltage injection method is plausible.

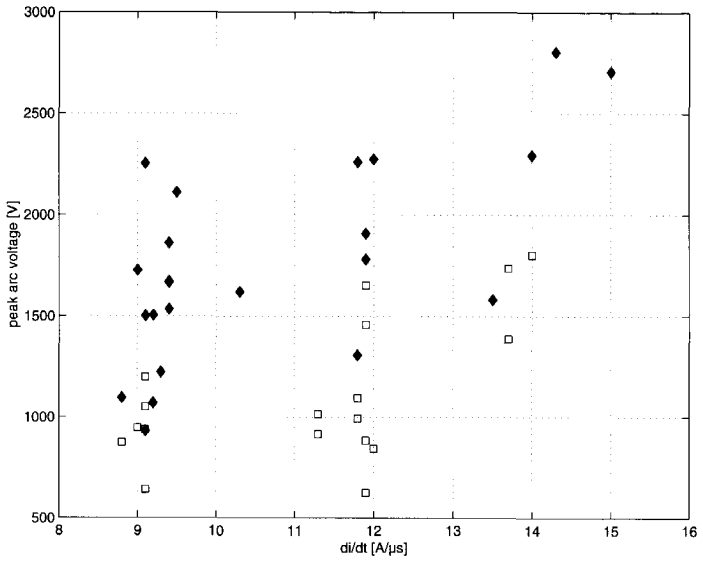

Figure 5-33. $(di/dt)_0$ versus peak arc voltage (cb2)
◆ = observed interruptions, □ = observed reignitions

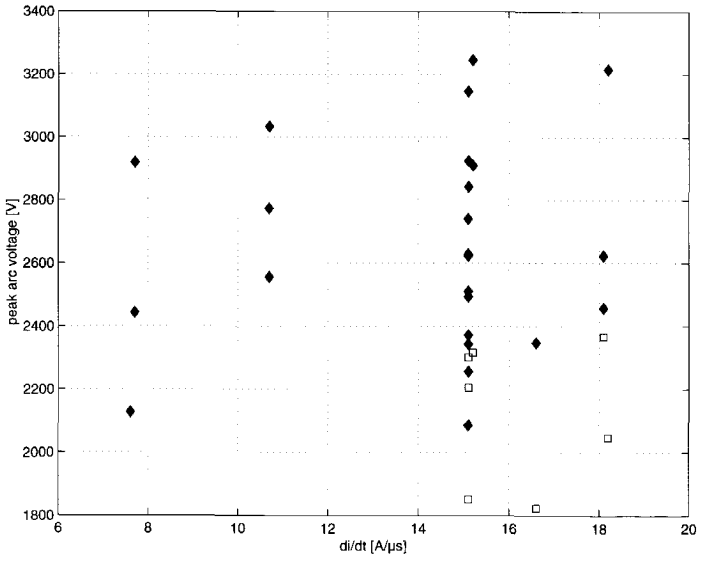

Figure 5-34. $(di/dt)_0$ versus peak arc voltage (cb4)
◆ = observed interruptions, □ = observed reignitions

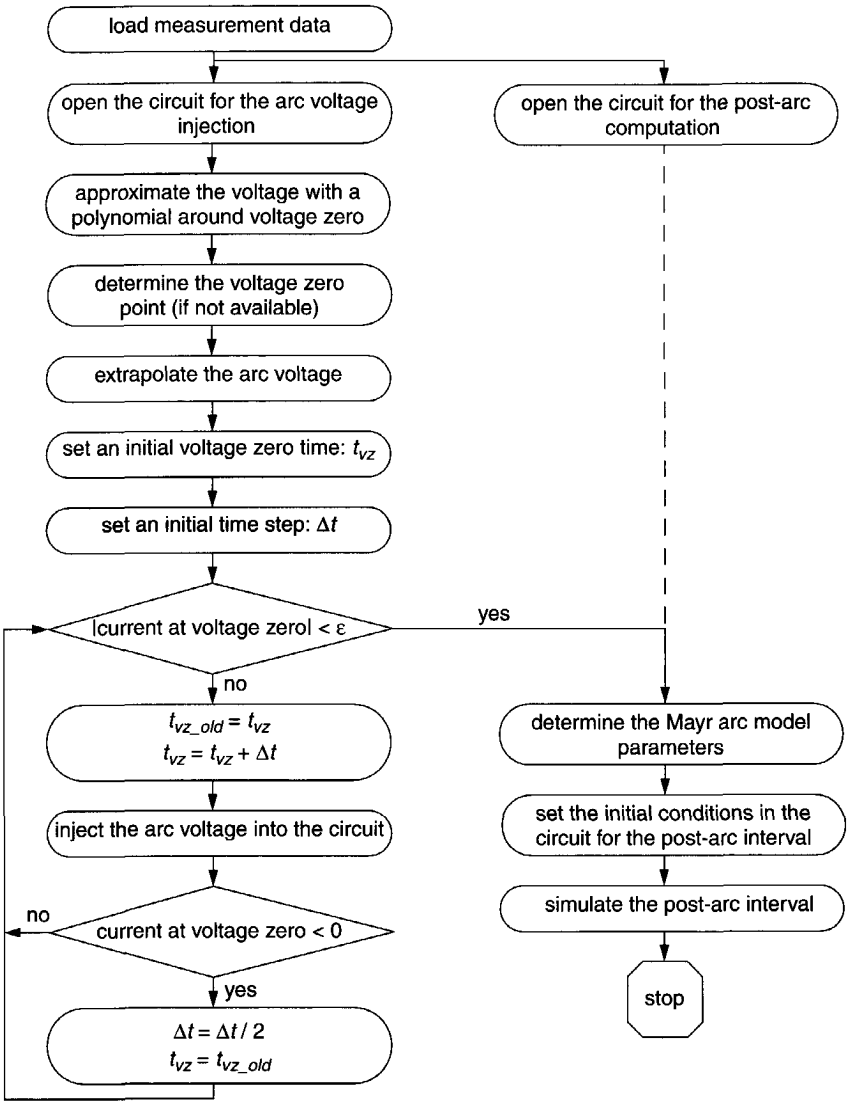

Figure 5-35. Flowchart of the voltage injection method before current zero in combination with a Mayr arc model for the post-arc period

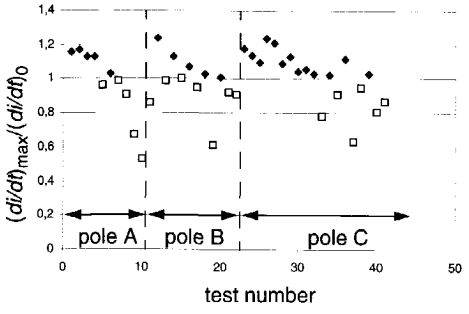

Figure 5-36. Test number versus the $(di/dt)_{max}/(di/dt)_0$ (cb2)
◆ = observed interruptions
□ = observed reignitions

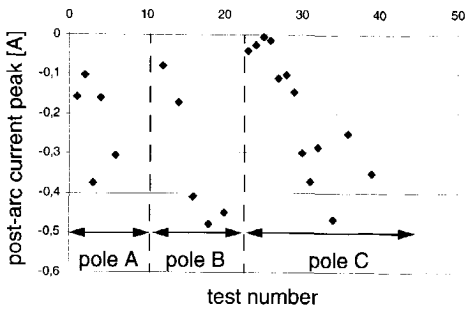

Figure 5-37. Test number versus the post-arc current peak (cb2)
(obtained from computations)
◆ = observed interruptions

The computational procedure is depicted in the flowchart in figure 5-35. The computation requires two circuits.

- *before current zero.* Voltage injection: in the lumped-element representation of the laboratory test circuit the circuit breaker is modeled by means of a voltage source that injects the measured voltage across the circuit breaker into the network. An example of this approach is shown in figure 5-4. Due to the resistive character of the arc, both arc voltage and arc current must be zero at the same instant. As the arc current is calculated from the interaction between the circuit and the injected arc voltage, the instant of the current zero is not known in advance. The voltage injection computation should therefore be repeated iteratively in order to let the current and voltage zero crossing coincide. When the computed current value at the voltage zero point lies within the preset margins, the measured voltage and the computed current before current zero are used to determine the Mayr arc model parameters for the post-arc computation.

- *after current zero.* Mayr arc model: the circuit breaker under test is represented by the Mayr arc model. The initial values for the circuit elements are the capacitor voltages and inductor currents of the circuit elements in the lumped-element representation of the test circuit at the voltage zero crossing, calculated with the voltage injection.

This process has to be repeated for every measurement several times before the $(di/dt)_{max}$ can be determined. For every *di/dt* adjusted, the calculation steps of the flowchart in figure 5-35 have to be executed. The Mayr arc model parameters are determined only once, when the $(di/dt)_0$ is applied. The repeated computations with the adjusted *di/dt* values in order to determine the $(di/dt)_{max}$ use these Mayr parameters. The arc conductance at current zero, which varies under the influence of the applied *di/dt*, is used as initial condition for the Mayr arc model in the post-arc computation.

The $(di/dt)_{max}/(di/dt)_0$ for cb2, as a result of the combined voltage injection / Mayr arc model computation, is shown in figure 5-36. It does not give a single incorrect prediction: all reigni-

tions and interruptions that were computed, occurred also during testing. From figure 5-36, similar observations can be made as those in section 4.5.2:

- There is a clear overall decrease in the quality of interruption during the progress of tests on every pole, reflecting the degradation of the circuit breaker by the tests.
- The rate of degradation clearly depends on the amount of power frequency current stress (pole A: 26.3 kA_{RMS}, pole B: 22.1 kA_{RMS}, pole C: 17.4 kA_{RMS}).

The number of tests used in section 4.5.2 is less than the number that is used here. The explanation for this is that the measured arc voltage is, in some cases, too low (in comparison with the resolution of the measurement system) to calculate the arc model parameters with a sufficient accuracy. This problem does not occur when the voltage injection method is applied.

The $(di/dt)_{max}/(di/dt)_0$ figures (figure 4-23 versus figure 5-36) look similar, but there is a significant difference with respect to the obtained $(di/dt)_{max}/(di/dt)_0$ values. In section 4.5.2, $(di/dt)_{max}/(di/dt)_0$ values of 1.9 were calculated. In figure 5-36, the maximum $(di/dt)_{max}/(di/dt)_0$ value is 1.24, which means that, for that specific test, the *di/dt* could have been 1.24 times higher than the *di/dt* applied during the test to cause circuit-breaker failure. Therefore, the $(di/dt)_{max}/(di/dt)_0$ values obtained with the combined voltage injection / Mayr arc model method are more realistic than the values obtained by using only an arc model and indicate the maximum current that the circuit breaker can interrupt.

In figure 5-37, the test number versus the computed post-arc current peak is shown. The figure visualizes the theory that the post-arc current peak increases when the circuit breaker degrades (see also section 5.2). Note that only the post-arc current peaks of the interruptions can be computed.

Chapter 6

Numerical computations

6.1 Introduction

It is hardly possible to analyze transient phenomena by hand; this is only feasible for simple circuits containing a small number of elements. Therefore, through the years, tools have been developed to 'automate' these computations [68]. Before the introduction of the (digital) computer, transient phenomena in an electrical power system were analyzed by means of TNAs (Transient Network Analyzers). The TNA consists of analog building blocks with which a complete network can be built up and simulated. Because of the rapid progression of advanced digital computer hardware, digital simulation enormously evolved. Therefore, the analog TNA is often replaced by fully digital simulators, such as the RTDS (Real Time Digital Simulator), developed at the Manitoba HVDC Research Centre [40]. Because of the real-time property, these digital simulators can now be used for areas that were restricted to TNAs, such as the testing of protective relays. The computational engine of these digital simulators is comparable to the one used in the EMTP (the Electro Magnetic Transient Program, see section 6.2).

Historically, the first computer programs for the computation of transients in power systems used techniques to simulate the travelling waves on transmission lines. The first computer programs for solving the problems related to the travelling waves were based on the application of lossless lines. For the different nodes, the reflection and refraction coefficients were computed from the characteristic impedances. The degree to which the travelling waves were reflected and refracted on the nodes was administered and could be made visible by means of a so-called lattice diagram. An example of such a lattice diagram is shown in figure 6-1, where an ideal single-phase line is charged by a DC voltage.

Another well-known approach that is based on lossless lines is the Bergeron method. Lumped elements, like a C or L, are represented by short lines. An inductance L is represented as a loss-

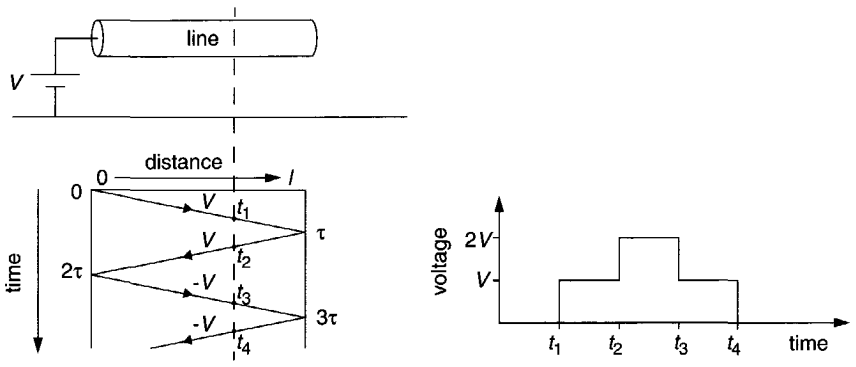

Figure 6-1. Lattice diagram
τ = travel time, V = voltage of the DC source, l = length of the line

less line with a characteristic impedance $Z = L/\tau$ and a travel time τ. A parallel capacitance C is represented as a lossless line with a characteristic impedance $Z = \tau/C$ and a travel time τ. However, a series capacitance poses a problem.

Almost all of the programs for the computation of transient phenomena solve the equations in the time domain. However, programs have been developed that apply a frequency domain method, such as the FTP (Frequency-domain Transient Program) [51]. The great advantage of a transient analysis method based on the Fourier or Laplace transform is that the frequency-dependent effects of lines and cables are automatically included. Nevertheless, a transformation to the Laplace or Fourier domain poses some special problems: a circuit breaker interrupts the current at the current zero crossing, but how can we translate this to the other domains? Furthermore, difficulties arise when we are dealing with discontinuous and nonlinear elements.

In the following sections, several (time domain) computer programs will be highlighted that can be used for computations involving arc models.

6.2 EMTP

The Electro Magnetic Transient Program (EMTP) is the creation of H.W. Dommel, who started to work on the program at the Munich Institute of Technology in the early 1960s [17]. He continued his work at BPA (Bonneville Power Administration) [18]. It became popular when Dommel (as its creator) and Scott-Meyer, both with the BPA, made the source code public. This was both its strength and its weakness, for many people spent time on program development. However, their actions were not always as concerted as they should have been. This resulted in a huge amount of code for every conceivable circuit element, which at times was rather unreliable and lacked documentation. This problem has now been amended in the EPRI/EMTP version. The EPRI Group has re-coded, tested and extended most parts of the program over and over again in a concerted effort to improve its reliability and functionality. Circuit-breaker models are an example of the extended functionality. They were added in 1987 [56] and improved in 1997 [43] and are not available in the public-domain version of the program: the ATP (Alternative Transient Program). Nowadays, the EMTP - and other programs of

which the computational engine is based on the same principles - is the most widely used and accepted program for the computation of transients in power systems.

6.2.1 Solution method

The EMTP is based on the application of the trapezoidal rule to convert the differential equations of the network components into algebraic equations. This approach is demonstrated hereunder for the inductance, capacitance and for a lossless line.

Inductance

For the inductance L of a branch between the nodes k and m, it holds that:

$$i_{k,m}(t) = i_{k,m}(t-\Delta t) + \frac{1}{L}\int_{t-\Delta t}^{t}(v_k - v_m)dt \tag{6-1}$$

Integration by means of the trapezoidal rule gives the following equations.

$$\begin{aligned} i_{k,m}(t) &= \frac{\Delta t}{2L}(v_k(t) - v_m(t)) + I_{k,m}(t-\Delta t) \\ I_{k,m}(t-\Delta t) &= i_{k,m}(t-\Delta t) + \frac{\Delta t}{2L}(v_k(t-\Delta t) - v_m(t-\Delta t)) \end{aligned} \tag{6-2}$$

Capacitance

For the capacitance C of a branch between the nodes k and m, it holds that:

$$v_k(t) - v_m(t) = v_k(t-\Delta t) - v_m(t-\Delta t) + \frac{1}{C}\int_{t-\Delta t}^{t} i_{k,m}(t)dt \tag{6-3}$$

Integration by means of the trapezoidal rule gives the following equations.

$$\begin{aligned} i_{k,m}(t) &= \frac{2C}{\Delta t}(v_k(t) - v_m(t)) + I_{k,m}(t-\Delta t) \\ I_{k,m}(t-\Delta t) &= -i_{k,m}(t-\Delta t) - \frac{2C}{\Delta t}(v_k(t-\Delta t) - v_m(t-\Delta t)) \end{aligned} \tag{6-4}$$

Lossless line

For a single-phase lossless line between the terminals k and m, the following equation must be true.

$$u_m(t-\tau) + Zi_{m,k}(t-\tau) = u_k(t) - Zi_{k,m}(t) \tag{6-5}$$

τ the travel time [s]
Z the characteristic impedance [Ω]

In words: the expression $u + Zi$ encountered by an observer when he leaves the terminal m at time $t - \tau$ must still be the same when he arrives at terminal k at time t. From equation 6-5, the following two-port equations can be deduced.

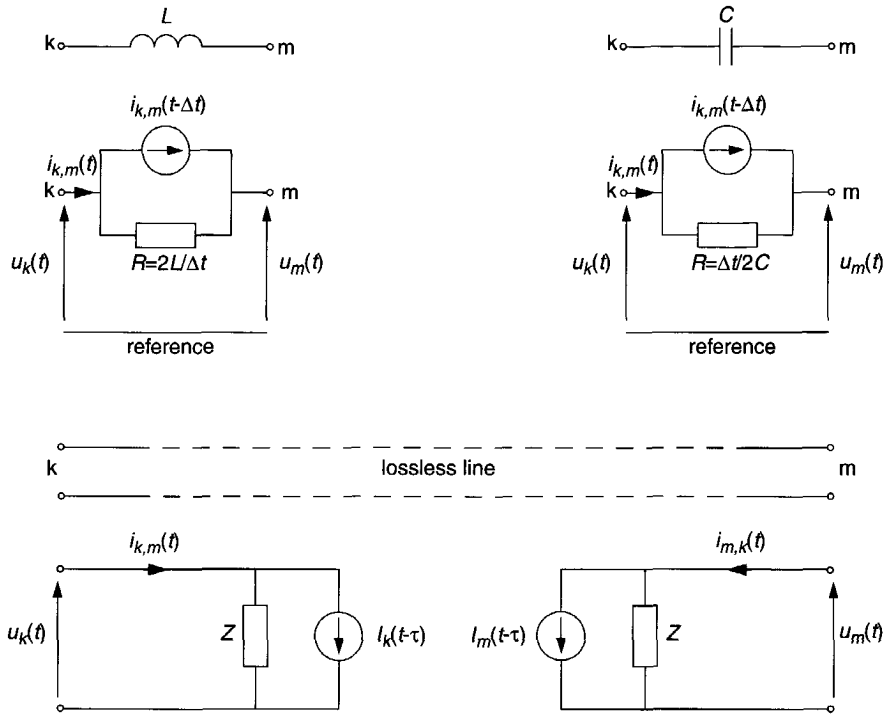

Figure 6-2. EMTP representation of the inductance, capacitance and a lossless line by current sources and parallel resistances.
Δt is the step size of the computation. τ is the travel time of the line. Z is the characteristic impedance of the line.

$$
\begin{aligned}
i_{k,m}(t) &= \frac{u_k(t)}{Z} + I_k(t-\tau) \\
I_k(t-\tau) &= -\frac{u_m(t-\tau)}{Z} - i_{m,k}(t-\tau) \\
i_{m,k}(t) &= \frac{u_m(t)}{Z} + I_m(t-\tau) \\
I_m(t-\tau) &= -\frac{u_k(t-\tau)}{Z} - i_{k,m}(t-\tau)
\end{aligned}
\qquad (6\text{-}6)
$$

The resulting models for the inductance, capacitance and the lossless line are shown in figure 6-2.

They consist of current sources, which are determined by current values from previous time steps, and resistances in parallel. Thus, a network can be built up of current sources and resistances by using the equivalent circuits as shown in figure 6-2. This approach will be demonstrated on the simple RLC network, which is shown in figure 6-3.

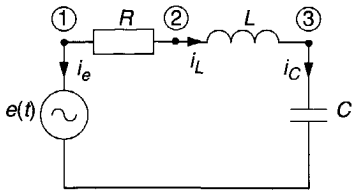

Figure 6-3. Sample RLC circuit

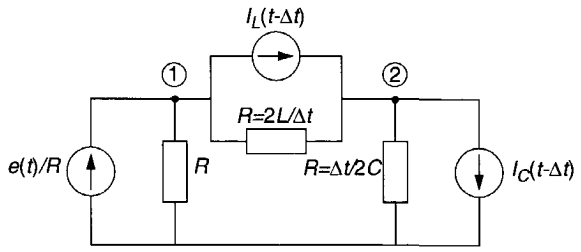

Figure 6-4. Equivalent EMTP circuit

By means of the equivalent models for the inductance and the capacitance, shown in figure 6-2, and the replacement of the voltage source and the series impedance by a current source with a parallel resistance, the RLC circuit can be converted into the equivalent circuit shown in figure 6-4. In order to compute the unknown node voltages, we need to formulate a set of equations by applying the NA method (Nodal Analysis).

$$\begin{bmatrix} \frac{1}{R}+\frac{\Delta t}{2L} & -\frac{\Delta t}{2L} \\ -\frac{\Delta t}{2L} & \frac{\Delta t}{2L}+\frac{2C}{\Delta t} \end{bmatrix} \begin{bmatrix} u_1(t) \\ u_2(t) \end{bmatrix} = \begin{bmatrix} \frac{e(t)}{R} \\ 0 \end{bmatrix} - \begin{bmatrix} I_L(t-\Delta t) \\ I_C(t-\Delta t) - I_L(t-\Delta t) \end{bmatrix} \tag{6-7}$$

In general, the following equation holds:

$$\boldsymbol{Yu} = \boldsymbol{i}-\boldsymbol{I} \tag{6-8}$$

$\boldsymbol{Y}$	the nodal admittance matrix
$\boldsymbol{u}$	the vector with unknown node voltages
$\boldsymbol{i}$	the vector with current sources
$\boldsymbol{I}$	the vector with current sources, that are determined by current values from previous time steps

The actual computation works as follows.

- The building up and inversion of the $\boldsymbol{Y}$-matrix. This step has to be taken only once. However, when switching is applied, the step has to be repeated if the topology of the network changes.
- The time-step loop is entered and the vector of the right-hand side of equation 6-8 is computed after a time step Δt.
- The set of linear equations is solved by means of the inverted matrix $\boldsymbol{Y}$ and the vector with the nodal voltages $\boldsymbol{u}$ is known.
- The vector in the right-hand side of equation 6-8 is computed for a time step Δt further in time and we keep continuing this procedure until we reach the final time.

The advantages of the 'Dommel/EMTP' method, as described above, are among others:

- Simplicity. The network is reduced to a number of current sources and resistances from which the **Y**-matrix can be constructed easily.
- Robustness. The EMTP makes use of the trapezoidal rule, which is a numerically stable and robust integration routine.

However, the method has some disadvantages too:

- A voltage source poses a problem. This becomes clear from the sample RLC-circuit: a small series resistance will result in an ill-conditioned **Y**-matrix (see equation 6-7).
- It is difficult to change the computational step size dynamically during the calculation: the resistance values and the current sources should be recomputed at each change (see equation 6-7) which entails **Y**-matrix re-inversion. This takes too much time for larger networks.
- The **Y**-matrix is ill conditioned. The treatment of resistances in the representations of the capacitance and the inductance (see figure 6-2 and equation 6-7) is opposite with regard to the computational step size Δt. Thus, if the computational step size is decreased, it affects the inductances and capacitances in opposite ways. This can lead to numerical instabilities.

6.2.2 Arc model implementation

The arc models within the EMTP are implemented by means of the compensation method [43,56]. The non-linear elements are essentially simulated as current injections, which are superimposed on the linear network after a solution without the non-linear elements has been found.

The procedure is as follows. The non-linear element is open-circuited and the Thevenin voltage and Thevenin impedance are computed. Now, the two following equations have to be satisfied. First, the equation of the linear part of the network (the instantaneous Thevenin equivalent circuit as seen from the arc model), which is:

$$V_{th} - iR_{th} = iR \tag{6-9}$$

V_{th} the Thevenin (open-circuit) voltage [V]
R_{th} the Thevenin impedance [Ω]
i the arc current [A]
R the arc resistance [Ω]

Second, the relationship of the non-linear element itself. Application of the trapezoidal method of integration yields for the arc resistance at the simulation time t:

$$R(t) = R(t-\Delta t) + \frac{\Delta t}{2}\left(\left.\frac{dR}{dt}\right|_{t} + \left.\frac{dR}{dt}\right|_{t-\Delta t}\right) \tag{6-10}$$

Δt the time step [s]

The dR/dt is described by the differential equation of the arc model. In order to find a simultaneous solution of the equations 6-9 and 6-10, the equations have to be solved by means of an iterative process (e.g. Newton-Raphson).

Therefore, the solution process is as follows:

- The node voltages are computed without the non-linear branch.
- The equations 6-9 and 6-10 are solved iteratively.
- The final solution is found by superimposing the response to the current injection i.

In the EMTP96, three arc models have been implemented: the Avdonin/Schwarz, Urbanek and Kopplin model.

6.3 MNA

Ho e.a. [30] introduced the MNA method (Modified Nodal Analysis) to circumvent the large shortcoming of the NA method, i.e. the inefficient treatment of voltage sources. Van der Sluis used this approach to build a network-independent transient computer program called MNA [97]. The MNA method is based on the usage of state equations: the voltages over the capacitances and the current through the inductances are continuous.

6.3.1 Solution method

The set of equations to solve the sample RLC-circuit as shown in figure 6-3, formulated by means of the MNA method, is described hereunder.

$$\begin{bmatrix} \frac{1}{R} & -\frac{1}{R} & 0 & 1 & 0 \\ -\frac{1}{R} & \frac{1}{R} & 0 & 0 & 0 \\ 0 & 0 & 0 & 0 & 1 \\ 1 & 0 & 0 & 0 & 0 \\ 0 & 0 & 1 & 0 & 0 \end{bmatrix} \begin{bmatrix} u_1(t) \\ u_2(t) \\ u_3(t) \\ i_e(t) \\ i_C(t) \end{bmatrix} = \begin{bmatrix} 0 & 0 \\ -1 & 0 \\ 1 & 0 \\ 0 & 0 \\ 0 & 1 \end{bmatrix} \begin{bmatrix} i_L(t) \\ u_C(t) \end{bmatrix} + \begin{bmatrix} 0 \\ 0 \\ 0 \\ e(t) \\ 0 \end{bmatrix} \tag{6-11}$$

The vector with the state variables, in this case containing the current through the inductance and the voltage over the capacitance, can be obtained by integration of the following equation.

$$\begin{bmatrix} i_L'(t) \\ u_C'(t) \end{bmatrix} = \begin{bmatrix} 0 & \frac{1}{L} & -\frac{1}{L} & 0 & 0 \\ 0 & 0 & 0 & 0 & \frac{1}{C} \end{bmatrix} \begin{bmatrix} u_1(t) \\ u_2(t) \\ u_3(t) \\ i_e(t) \\ i_C(t) \end{bmatrix} \tag{6-12}$$

In general, the following equations hold.

$$\boldsymbol{x}_1'(t) = \boldsymbol{A}\boldsymbol{x}_2(t) \tag{6-13}$$

$$\boldsymbol{B}(t)\boldsymbol{x}_2(t) = \boldsymbol{C}\boldsymbol{x}_1(t) + \boldsymbol{f}(t) \tag{6-14}$$

x_1 the n-vector of differential variables
x_2 the m-vector of algebraic variables
A the nxm-matrix that represents the linear relation between x_1' and x_2
$B(t)$ the mxm-MNA matrix; the matrix can be time dependent
C the mxn-matrix that represents the linear relation between x_1 and x_2
$f(t)$ the m-vector with the (time-dependent) contributions from voltage and current sources

Normally, the MNA matrix will not be time dependent. However, it will be when, e.g., an arc model is incorporated as a non-linear conductance. Such a time-dependent MNA matrix should be inverted or factorized at each time step which is not recommendable because of the long computation times.

To solve equation 6-13 and 6-14, the following method is used.

- The right-hand side vector of equation 6-14 is calculated with the initial values of x_1.
- If the MNA matrix is time dependent, the matrix is updated and inverted or factorized.
- From equation 6-14, x_2 is computed.
- The values of x_1 at the new time step are computed by solving equation 6-13 with a numerical integration method. This process is repeated until the final simulation time is reached.

The advantages of the MNA method, as described above, are among others:

- Voltage sources are easily included (as shown in the case of the sample RLC circuit)
- The computational step size is not present within the MNA matrix (see equation 6-11). If the step size is adjusted during the calculation, the MNA matrix does not need to be inverted or factorized once more (assumed that the MNA matrix is not time dependent).

However, the method also has one disadvantage:

- The matrices A, B and C require linearity and it is necessary that the two sets of unknowns can be defined and solved separately from the corresponding set of equations. Therefore, the MNA method only deals with linear models. Non-linear diodes, arc models and so on, can only be incorporated by means of tricks.

6.3.2 Arc model implementation

An arc model can be implemented within the MNA method in various ways.

The arc model can be modeled as a non-linear conductance. However, then the MNA matrix becomes time dependent and should be inverted or factorized at each time step. This involves a heavy computational burden and is not recommended. An alternative can be found in applying so-called partial matrix (factor) updating. Now the changes are not made within the MNA matrix itself, but in the inverted MNA matrix [34] or the MNA matrix factors [36]. Although this introduces additional computation time for the updating, the MNA matrix has to be inverted or factorized only once.

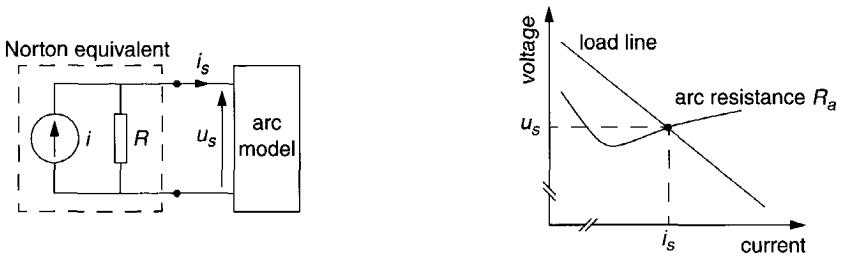

Figure 6-5. Arc model connected to a linear network

Another approach is the one that Van der Sluis followed to implement the Mayr arc model in the MNA computer program [97]. The arc model is treated as a voltage source. This technique is depicted in figure 6-5. The linear network to which the arc model is connected, can be replaced by the Norton equivalent with its corresponding load line.

Each time step, the arc resistance R_a is computed from the arc model's differential equation. At the point of intersection of the momentary arc resistance and the load line, both the network and the arc model have the same voltage u_s and current i_s. If two points of the load line, (u_1, i_1) and (u_2, i_2), are known, the voltage u_s and current i_s are computed from the following equation.

$$u_s = u_1 + \frac{(R_a i_1 - u_1)(u_2 - u_1)}{u_2 - u_1 + R_a(i_1 - i_2)}$$
$$i_s = \frac{u_s}{R_a} \tag{6-15}$$

There is one arc model incorporated within the MNA computer program: the Mayr arc model.

6.4 XTrans

The Power Systems Laboratory of the Delft University of Technology introduced the transient program XTrans [4,5,69,70]. The program was developed especially for analysis of arc-circuit interaction, which involves non-linear elements in relation to stiff differential equations. The calculations are performed with a variable step size and adjustable accuracy of the computed currents, voltages and e.g. conductances.

6.4.1 Solution method

The application of the NA and MNA method has some drawbacks, especially when non-linear elements such as arc models are used, as described in the previous sections. A more general representation of a set of first-order differential equations and algebraic equations (DAEs) is given by:

$$\boldsymbol{F}(\boldsymbol{x}'(t), \boldsymbol{x}(t), t) = \boldsymbol{0} \tag{6-16}$$

The set of equations to solve the sample RLC-circuit as shown in figure 6-3, formulated by means of the DAEs, is described hereunder.

$$\begin{bmatrix} i_e(t) + \dfrac{u_1(t) - u_2(t)}{R} \\ \dfrac{u_1(t) - u_2(t)}{R} - i_L \\ i_L - i_C \\ u_1(t) - e(t) \\ i_L'(t) - \dfrac{u_2(t) - u_3(t)}{L} \\ u_3'(t) - \dfrac{i_C(t)}{C} \end{bmatrix} = \mathbf{0} \tag{6-17}$$

The solution of the DAEs (equation 6-16) is achieved by using the BDF method (Backward Differentiation Formula method). This method was first proposed by Gear in 1971 [22] and has been studied and developed by mathematicians since then. The solution is performed in two steps:

- Suppose the solution $\boldsymbol{x}^n$ at $t = t^n$ is given. Then one must select an appropriate step size $h = t^{n+1} - t^n$ to be able to compute an approximation of $\boldsymbol{x}'(t^{n+1})$ using the multi-step BDF formula:

$$\boldsymbol{x}'^{n+1} = \frac{1}{h^n} \sum_{i=0}^{k} \alpha_i \boldsymbol{x}^{n+1-i} \tag{6-18}$$

  k the order of the method
  α_i the coefficients of the method
  h the step size of the computation

  This is called a multi-step method because the calculation results of the last k time steps are used. In the special case that $k = 1$, equation 6-18 yields the one-step Euler formula:

$$\boldsymbol{x}'^{n+1} = \frac{\boldsymbol{x}^{n+1} - \boldsymbol{x}^n}{h^n} \tag{6-19}$$

  The determination of the step size and the coefficients α_i is based on a strategy which is described in detail in [6].

- In equation 6-16, $\boldsymbol{x}'$ is replaced by the backward difference (equation 6-18) and this gives us the following nonlinear set of equations.

$$\boldsymbol{F}(\boldsymbol{x}'^{n+1}, \boldsymbol{x}^{n+1}, t^{n+1}) = \boldsymbol{g}(\boldsymbol{x}^{n+1}, t^{n+1}) = \mathbf{0} \tag{6-20}$$

These equations can be solved by the Newton-Raphson method, which consists of the following iteration formulas:

$$\boldsymbol{J}\Delta\boldsymbol{x}_i^{n+1} = \boldsymbol{g}(\boldsymbol{x}_i^{n+1}, t^{n+1}) \tag{6-21}$$

$$\boldsymbol{x}_{i+1}^{n+1} = \boldsymbol{x}_i^{n+1} + \Delta\boldsymbol{x}_i^{n+1} \tag{6-22}$$

$\boldsymbol{J}$ the Jacobian matrix of $\boldsymbol{g}$
$\boldsymbol{x}_i^{n+1}$ the i^{th} approximation of $\boldsymbol{x}^{n+1}$

This iteration process is started with initial guesses $\boldsymbol{x}_0^{n+1}$ to make sure that the desired solution is reached. These initial guesses are found by extrapolating the earlier solution points. Subsequently the mismatch vector (i.e. the right-hand side of equation 6-21) is computed by filling in these values in $\boldsymbol{g}$. Then the correction vector, $\Delta\boldsymbol{x}_i^{n+1}$, is solved from equation 6-21. The vector $\boldsymbol{x}^{n+1}$ is updated as shown in equation 6-22 and the process is repeated until convergence has been achieved. This solution process may seem time consuming compared with the NA or MNA method but this is not necessarily the case. The use of a multi-step method makes it possible to take larger time steps than can be done using a single-step method. The possibility to adjust the step size during calculation makes it possible to solve stiff equations and to avoid the cumulation of errors.

An electrical network consists of elements connected to each other in nodes. The elements and nodes both have their own related equations and unknowns. The equations related to the nodes represent the connections between the elements. They are obtained by applying Kirchhoff's current law (KCL) to every node except the datum node. The corresponding unknowns are the voltages at these nodes. The NA method uses only these equations and unknowns, but the MNA method allows network elements to introduce extra unknowns and equations. These equations have to be linear and algebraic when the MNA method is used, but can also be non-linear and first-order differential if the BDF method is used.

6.4.2 Arc model implementation

When using the DAEs, an arc model, such as the Mayr arc model, can easily be implemented by extending the system of equations (such as given in the equations 6-16 and 6-17) as follows:

$$\begin{bmatrix} \vdots \\ i - gu \\ \vdots \\ g' - \frac{1}{\tau}\left(\frac{u^2 g^2}{P} - g\right) \end{bmatrix} = \mathbf{0} \tag{6-23}$$

i the arc current [A]
u the arc voltage [V]
g the arc conductance [S]
τ the Mayr arc time constant [s]
P the Mayr arc cooling power [W]

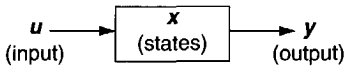

Figure 6-6. Simulink Block

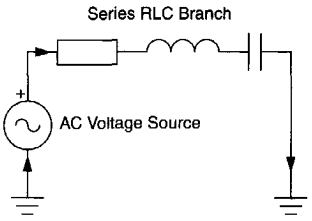

Figure 6-7. Sample RLC circuit in the MATLAB PSB

Within the XTrans program, the author has implemented a large number of arc models, such as: Cassie, KEMA/Rutgers, KEMA/Kertész, Mayr, multiple Modified Mayr's, Schavemaker, Schwarz (Avdonin), Siemens/Habedank.

6.5 MATLAB Power System Blockset

After the introduction of the Power System Blockset (PSB) for modeling and simulating electric power systems within the MATLAB Simulink environment, one can use the general-purpose mathematical program MATLAB for simulating power-system transients. The Power System Blockset is developed at TEQSIM Inc. and Hydro-Québec [44,94]. Simulink is a software package for modeling, simulating and analyzing dynamic systems [45]. It provides a graphical user interface for building models as block diagrams. The PSB block library contains Simulink blocks that represent common components and devices found in electrical power networks. The measurement blocks and the controlled sources in the PSB block library act as links between electrical signals (voltages across elements and currents flowing through lines) and Simulink blocks (transfer functions).

6.5.1 Solution method

Simulink is based on the interconnection of blocks to build up a system. Each block has three general elements: a vector of inputs $\boldsymbol{u}$, a vector of outputs $\boldsymbol{y}$ and a vector of state variables $\boldsymbol{x}$ (see figure 6-6). Before the computation, the system is initialized: the blocks are sorted in the order in which they need to be updated. Then, by means of numerical integration with one of the implemented ODE (Ordinary Differential Equation) solvers, the system is simulated. The computation consists of the following steps.

- The block output is computed in the correct order.
- The block calculates the derivatives of its states based on the current time, the inputs and the states.
- The derivative vector is used by the solver to compute a new state vector for the next time step. These steps continue until the final simulation time is reached.

The PSB block library contains Simulink blocks that represent common components and devices found in electrical-power networks. Therefore, systems can be built consisting of both Simulink and PSB blocks. However, the measurement blocks and the controlled sources in the

PSB block library act as links between electrical signals (voltages across elements and currents flowing through lines) and Simulink blocks (transfer functions). Before the computation, the system is initialized: the state-space model of the electric circuit is computed and the equivalent Simulink system is built up. The computation itself is analogous to the previously mentioned Simulink computational process.

The sample RLC circuit, previously used in this chapter, built up in the PSB, is shown in figure 6-7. It is important to note that the arrows in the diagram do not indicate causality, as is the case in the Simulink block diagrams. The state-space model of this sample circuit is described hereunder.

$$\dot{\boldsymbol{x}} = \begin{bmatrix} -\frac{R}{L} & -\frac{1}{L} \\ \frac{1}{C} & 0 \end{bmatrix} \boldsymbol{x} + \begin{bmatrix} \frac{1}{L} \\ 0 \end{bmatrix} V_{AC} \qquad \text{with} \qquad \boldsymbol{x} = \begin{bmatrix} i_L \\ u_c \end{bmatrix} \tag{6-24}$$

MATLAB contains a large number of ODE solvers [82], some with fixed and others with variable step size. The ode15*s* solver, which can be used to solve stiff systems, is a variable-order solver based on the Numerical Differentiation Formulas (NDFs). These are more efficient than the BDFs (as described in section 6.4.1), though a couple of the higher-order formulas are somewhat less stable.

6.5.2 Arc model implementation

The arc models have been implemented by the author as voltage-controlled current sources. This approach is visualized in figure 6-8, where both the Mayr arc model block and the underlying system are shown. Some of the elements in figure 6-8 will be clarified hereunder.

DEE: Differential Equation Editor

The equations of the Mayr arc model have been incorporated by means of the Simulink DEE (Differential Equation Editor) block, as shown in figure 6-9. Therefore, the following system of equations is solved:

$$\begin{array}{l|l} \dfrac{dx(1)}{dt} = \dfrac{u(2)}{\tau}\left(\dfrac{e^{x(1)}u(1)^2}{P} - 1\right) & \dfrac{d\ln g}{dt} = \dfrac{u(2)}{\tau}\left(\dfrac{gu^2}{P} - 1\right) \\ y = e^{x(1)}u(1) & i = gu \end{array} \tag{6-25}$$

$x(1)$ the state variable of the differential equation which is the natural logarithm of the arc conductance: $\ln(g)$.

$x0$ the initial value of the state variable, i.e. the initial value of the arc conductance: $g(0)$.

$u(1)$ the first input of the DEE block which is the arc voltage: u.

$u(2)$ the second input of the DEE block which represents the contact separation of the circuit breaker: $u(2) = 0$ when the contacts are closed and $u(2) = 1$ when the contacts are being opened.

y the output of the DEE block which is the arc current: i.

g the arc conductance [S]

u the arc voltage [V]

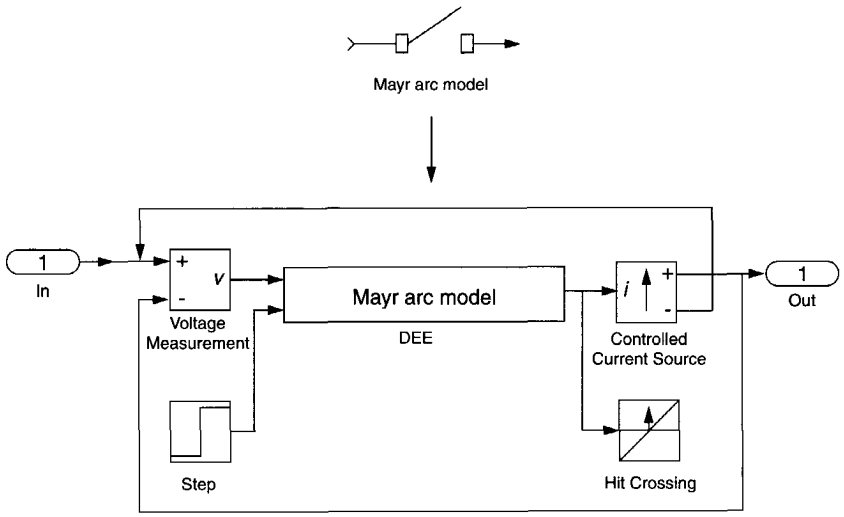

Figure 6-8. Mayr arc model implementation in MATLAB Simulink/Power System Blockset

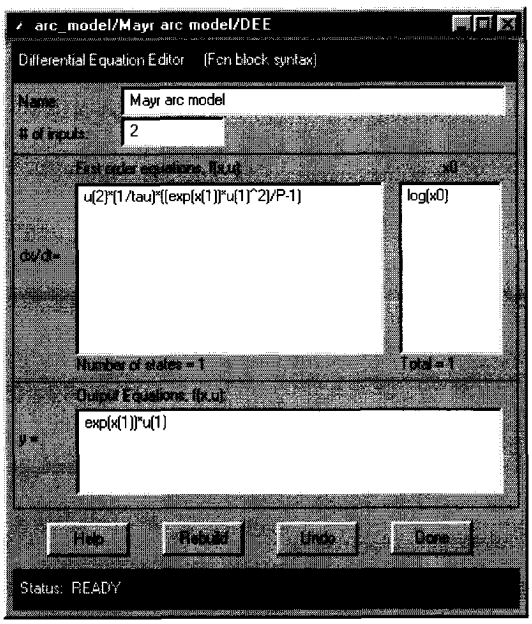

Figure 6-9. Mayr equation in the Simulink Differential Equation Editor (DEE)

i the arc current [A]
τ the arc time constant [s]
P the cooling power [W]

Hit Crossing

The Simulink 'Hit crossing' block detects when the input, in this case the current, crosses the zero value. Therefore, by adjusting the step-size, the block ensures that the simulation finds the zero crossing point. This is of importance because the voltage and current zero crossing of the circuit breaker, which behaves as a non-linear resistance, is a crucial moment in the interruption process, which should be computed accurately.

Step

The Simulink 'Step' block is used to control the contact separation of the circuit breaker. A step is made from a value zero to one at the specified contact separation time. When the contacts are closed, the following differential equation is solved:

$$\frac{d\ln g}{dt} = 0 \tag{6-26}$$

Therefore, the arc model behaves as a conductance with the value $g(0)$. Starting from the contact separation time, the Mayr equation is solved:

$$\frac{d\ln g}{dt} = \frac{1}{\tau}\left(\frac{gu^2}{P} - 1\right) \tag{6-27}$$

Within the PSB, arc models can be implemented rather easily when the approach as described in this section is followed. The author developed the Arc Model Blockset [77] which contains a large number of arc models, such as: Cassie, KEMA/Kertész, Mayr, multiple Modified Mayr's, Schavemaker, Schwarz (Avdonin), Siemens/Habedank.

6.6 Comparison by means of computational results

Due to the limited number of arc models implemented in the MNA program, this program has not been considered for use in this thesis. The other three programs (EMTP v3.0, XTrans and MATLAB PSB) have been compared in order to check their applicability for the type of computations required in this thesis. Because of the fast phenomena involved, the interruption process of the circuit breaker is an ideal test case to compare the use of various programs for transient computations [71]. The Schwarz/Avdonin arc model [81] is used to represent the circuit breaker, while the arc model is available in EMTP96 v3.0, and the author implemented it in both XTrans and MATLAB PSB:

$$\frac{1}{g}\frac{dg}{dt} = \frac{d\ln g}{dt} = \frac{1}{\tau_0 g^{\alpha}}\left(\frac{ui}{P_0 g^{\beta}} - 1\right) \tag{6-28}$$

g	the arc conductance [S]
u	the arc voltage [V]
i	the arc current [A]
τ_0	the 'time constant'; free parameter [s/S^{α}]
α	free parameter
P_0	the 'cooling constant'; free parameter [W/S^{β}]
β	free parameter

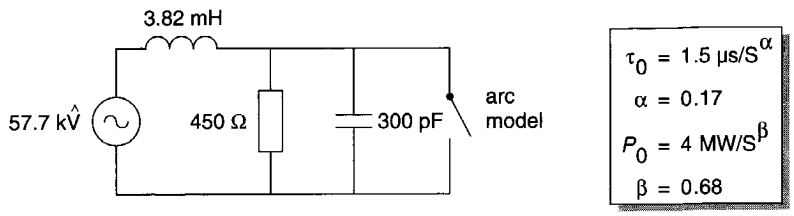

Figure 6-10. Benchmark circuit used for comparison (frequency: 60 Hz)

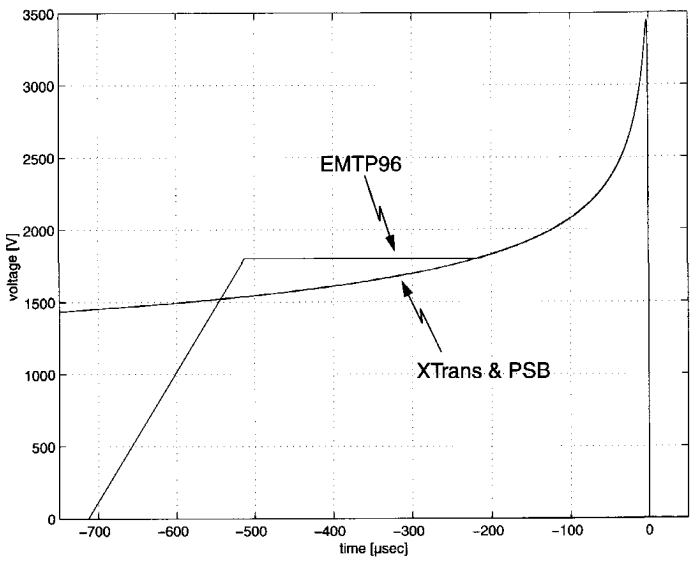

Figure 6-11. Computed arc voltages

The benchmark circuit, in which the circuit breaker interrupts the fault current, is kept as simple as possible and is shown in figure 6-10. As the arc 'time constant' is a function of the arc conductance, at the current zero crossing we find a 'time constant' of about 0.4 μs with the arc model parameters and the circuit specified in figure 6-10.

The computed arc voltage peaks and post-arc currents are shown in figure 6-11, figure 6-12 and figure 6-13, respectively. It is evident from the figures that all three programs produce (more or less) the same results, but one has to be cautious when using the EMTP96 because of its fixed time step. Both XTrans and MATLAB Simulink/PSB have variable step-size solvers. This is a great advantage when dealing with the non-linear arc models. In the high-current interval, the arc-circuit interaction does not change very rapidly and relatively large computational steps can be taken without loss of accuracy. Around current zero, the arc resistance

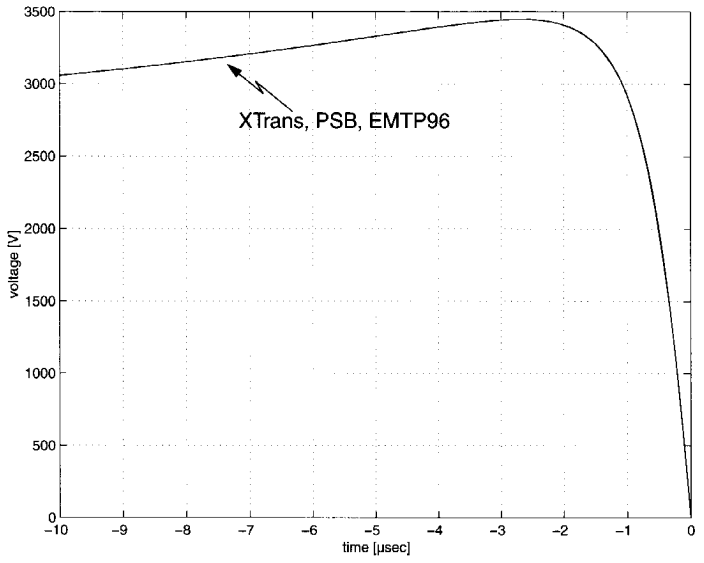

Figure 6-12. Computed arc voltages (detail)

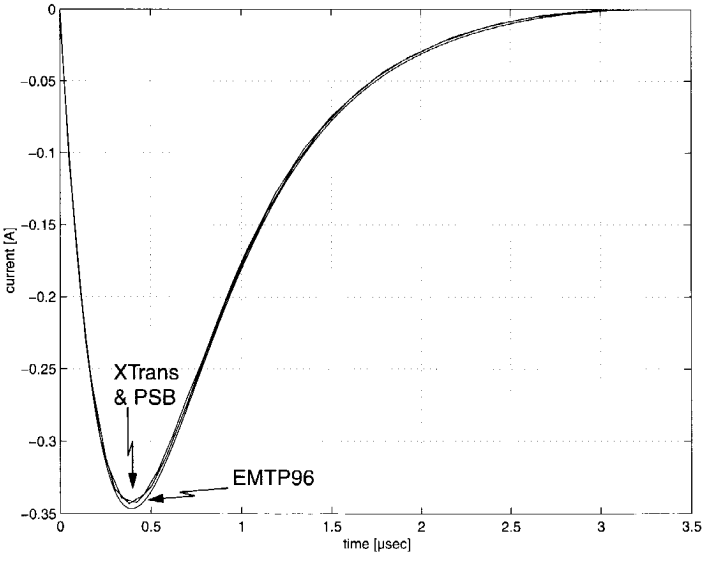

Figure 6-13. Computed post-arc currents (EMTP96: Δt = 1.e-8 s)

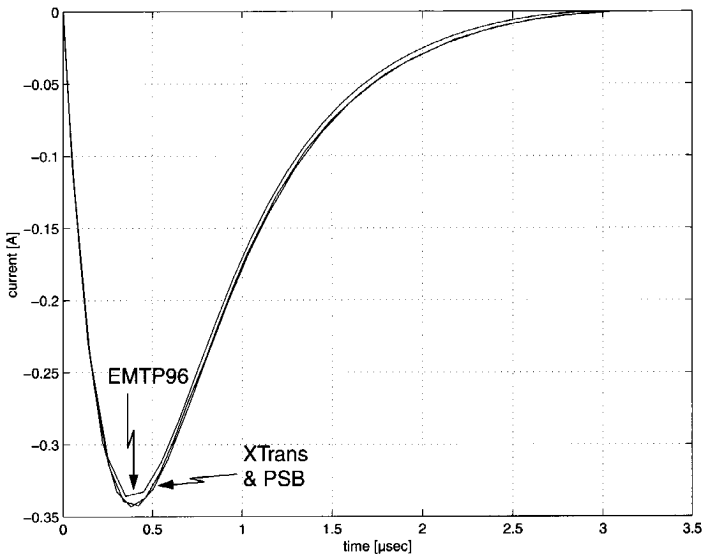

Figure 6-14. Computed post-arc currents (EMTP96: Δt = 1.e-7 s)

changes very fast and small time steps must be taken to preserve the computational accuracy. In such a way, the computation time is reasonable while the accuracy is guaranteed. The EMTP96 uses a fixed step-size solver and the user has to choose the step-size. In figure 6-11, figure 6-12 and figure 6-13, in the EMTP96 a step-size of Δt = 1.e-8 s has been selected whereas for figure 6-14, a step-size of Δt = 1.e-7 s has been chosen: it can be seen that the result of the EMTP96 already begins to diverge. In the EMTP96, the arc model is implemented in a different way than in the other two programs: the arc model is activated only a short time before current zero, whereas in the other two programs the arc model is active during the high-current phase as well, as can be seen from figure 6-11. This can result in a different arc-circuit interaction and subsequently in different outcomes.

Both XTrans and the MATLAB PSB show identical results and have been used complementary in this thesis for the arc-circuit interaction studies. Because of the implementation of the arc models and the fixed step-size solver, the EMTP96 can give (slightly) different results and is less suitable for studying arc-circuit interaction in detail. Therefore, the EMTP96 has not been used in this thesis.

Chapter 7

Conclusions

In this thesis computational techniques are applied to extend the information obtained during laboratory tests on high-voltage SF_6 circuit breakers. Thus 'digital testing' of circuit breakers is introduced. All computations and results in this thesis, are based on actual measurements that have been performed on various circuit breaker types of different manufacturers.

The most direct method to obtain extra information from the tests in the high-power laboratory is by analyzing the measurement data directly. Several indicators are presented that give some additional information about the circuit-breaker interrupting performance, such as the value of the peak arc voltage, the value of the time derivative of the arc current at current zero and the time before current zero where the arc resistance equals the characteristic impedance of the transmission line. Especially this last indicator, $t(R=Z)$, is very powerful. The prediction power of the $t(R=Z)$ indicator - its ability to separate the interruptions from the reignitions - is higher than 95% for the four breakers considered in this thesis. Furthermore it gives an indication of the circuit-breaker performance and degradation during a test series and can be used to differentiate between circuit breakers.
Wavelet analysis of the measurement data shows that for one of the tested breakers the jumps observed in the arc voltage are related to the interrupting performance: the larger the number of voltage jumps - on a 500 μs time window that ends 25 μs before the arc voltage zero crossing - and the more turbulent the arc behaves, the more likely it is that interruption takes place.
From the analysis of the frequency contents of the measured voltages, it is demonstrated that it is valid to model the laboratory test circuit by means of lumped circuit elements for arc-circuit interaction computations.

Because of the heavy computational burden of physical arc models, and the uncertainty of the (time-dependent) parameters, their use for 'digital testing' purposes is limited. In this thesis, a new Mayr-type arc model is introduced with a constant time parameter (τ) and where the cooling power is a function of the electrical power input ($P_0 + P_1 ui$). The arc model parameter P_0

is a design parameter reflecting the difference in rated voltage of the circuit breakers. The cooling constant P_1 regulates the influence of the electrical power input on the cooling power and therefore embodies the pressure buildup in the breaker caused by ohmic heating of the arc plasma. The arc model shows good correspondence between the measured and computed current and voltage traces and an overall performance of 90% in predicting the outcome of the tests. That means that only in one out of ten cases an interruption has been observed during the measurements for which the arc model showed a reignition, or vice versa. The arc model has its limitations; it can't be used for one of the four circuit breakers studied in this thesis.
Several applications of arc models for digital testing purposes are outlined, such as the determination of the failure probability, the quality of interruption and the critical line length. The failure probability distributions can be used to compare various circuit breakers and/or designs, although the arcing times during the laboratory tests were spread. The quality of interruption or, in other words, the margin of interruption, is the margin between interruption and failure; it indicates how successful an interruption was (i.e. a comparison of interruptions) or how severe a failure was (i.e. a comparison of failures) as well. Furthermore, it gives an indication of the circuit-breaker performance and degradation during a test series. In order to calculate the critical line length, i.e. the short line fault percentage which stresses the circuit breaker most, three arc models and three indicators have been utilized to determine the stress on the breaker. Rather independent of the circuit breaker, arc model and/or stress indicator, it appears that the critical line length corresponds to a 93-94% SLF which is higher than the 90% SLF prescribed in the IEC standard.

The use of arc models has certain drawbacks, which can be overcome by applying a method that is presented in this thesis: the voltage injection method. In the lumped-element representation of the laboratory test circuit the circuit breaker is modeled by means of a voltage source that injects the measured voltage across the circuit breaker into the network. This method has been applied successfully for an indirect verification of the current zero measurement system of KEMA. In combination with a Mayr arc model, the voltage injection method has been used for computing the quality of interruption. The results obtained are more realistic than the results obtained by using only an arc model and indicate the maximum current that the circuit breaker can interrupt. The voltage injection method has also been applied to compare various artificial lines. They are not compared by means of models of the circuit breakers, but the artificial lines are compared when they are subjected to the measured arc voltages. Therefore, the difference between the arc-circuit interaction of the various lines has been studied in a transparent way.

Computer programs used for arc-circuit interaction computations must be able to deal with non-linear arc models in relation to stiff differential equations. Three different programs that can be used for arc-circuit interaction studies have been compared, namely EMTP96 v3.0, XTrans and MATLAB Simulink/Power System Blockset in combination with the Arc Model Blockset (developed by the author). Programs with a fixed step-size solver, such as the EMTP96, are less suitable for detailed arc-circuit interaction studies than programs with variable step-size solvers, such as XTrans and MATLAB Simulink/Power System Blockset. In the high-current interval, the arc-circuit interaction does not change very rapidly and relatively large computational steps can be taken without a negative influence on the accuracy. Around current zero, however, the arc conductance changes very fast and small time steps must be taken to preserve the computational accuracy. In such a way, the computation time is limited while the accuracy is guaranteed.

References

[1] Amsinck, R.: 'Verfahren zur Ermittlung der das Ausschaltverhalten Bestimmenden Lichtbogenkenngrößen', *ETZ-A*, Bd. 98 (1977) H. 8, pp. 566-567. (In German)

[2] ANSI/IEEE: *C37.100, IEEE Standard Definitions for Power Switchgear*, 1981, The Institute of Electrical and Electronics Engineers.

[3] Bain, Lee J., and Engelhardt, Max: *Introduction to Probability and Mathematical Statistics*, PWS Publishers, 1987, ISBN 0-87150-067-1.

[4] Bijl, N.D.H., and Van der Sluis, L.: 'New Approach to the Calculation of Electrical Transients, Part I: Theory', *European Transactions on Electrical Power Engineering (ETEP)*, Vol. 8, No. 3, May/June 1998, pp. 175-179.

[5] Bijl, N.D.H., and Van der Sluis, L.: 'New Approach to the Calculation of Electrical Transients, Part II: Applications', *European Transactions on Electrical Power Engineering (ETEP)*, Vol. 8, No. 3, May/June 1998, pp. 181-186.

[6] Brenan, Kathryn E., Campbell, Stephen L., and Petzold, Linda R.: *Numerical Solutions of Initial-Value Problems in Differential-Algebraic Equations*, North Holland, New York, 1989, ISBN 0-444-01511-6.

[7] Browne Jr., T. E.: 'A Study of AC Arc Behavior Near Current Zero by Means of Mathematical Models', *AIEE Transactions*, Vol. 67, 1948, pp. 141-153.

[8] Browne Jr., Thomas E. (editor): *Circuit Interruption - Theory and Techniques*, Marcel Dekker, New York, 1984, ISBN 0-8247-7177-X.

[9] Bystruev, A.K., Chernyshev, N.M., Gontchar, V.C., Ilyin, P.A., Kaplan, V.V., and Sheheglov, I.P.: 'Some Aspects of Reproducing the Standard Test Conditions in Laboratories', *CIGRE*, Report 13-77(SC)33, 1977.

[10] Cassie, A.M.: 'Theorie Nouvelle des Arcs de Rupture et de la Rigidité des Circuits', *CIGRE*, Report 102, 1939, pp. 588-608. (In French)

[11] Chua, Leon O., Desoer, Charles A., and Kuh, Ernest S.: *Linear and Nonlinear Circuits*, McGraw-Hill, Inc., 1987, ISBN 0-07-100685-0.

[12] Cliteur, Gerard J.: *Non-equilibrium SF_6 Arc Plasma Modelling and Numerical Simulation Around Current-Zero*, Dissertation Kanazawa University, Japan, 1999.

[13] Damstra, G.C.: 'A New Synthetic Test Plant at KEMA High-Power Laboratory', *Symposium on High Voltage Switching Equipment*, May 29-30, 1979, Sydney, Australia.

[14] Damstra, G.C., and Kertész, V.: 'Development and Application of a 10 MHz Digital System for Current-Zero Measurements', *IEE Proc.-Sci. Meas. Technol.*, Vol. 142, No. 2, March 1995, pp. 125-132.

[15] De Lange, Adriaan J.P.: *High Voltage Circuit Breaker Testing with a Focus on Three Phases in One Enclosure Gas Insulated Type Breakers*, Dissertation Delft University of Technology, 2000.

[16] Desoer, Charles A., and Kuh, Ernest S.: *Basic Circuit Theory*, McGraw-Hill, Inc., 1969.

[17] Dommel, H.W.: 'A Method for Solving Transient Phenomena in Multiphase Systems', *Proceedings of the second Power System Computation Conference*, Stockholm, Sweden, 1966, Report 5.8.

[18] Dommel, H.W.: 'Digital Computer Solution of Electromagnetic Transients in Single- and Multiphase Networks', *IEEE Transactions on Power Apparatus and Systems*, Vol. PAS-88, No. 4, April 1969, pp. 388-399.

[19] Flurscheim, Charles H. (editor): *Power Circuit Breaker Theory and Design*, Peter Peregrinus, London, 1975, ISBN 0-901223-62-X.

[20] Galli, A.W., and Nielsen, O.M.: 'Wavelet Analysis for Power System Transients', *IEEE Computer Applications in Power*, Vol. 12, No. 1, January 1999, pp. 16-25.

[21] Garzon, Ruben D.: *High-Voltage Circuit Breakers*, Marcel Dekker, New York, 1997, ISBN 0-8247-9821-X.

[22] Gear, C.W.: 'Simultaneous Numerical Solution of Differential-Algebraic Equations', *IEEE Transactions on Circuit Theory*, Vol. 18, No. 1, January 1971, pp. 89-95.

[23] Greenwood, Allan: *Electrical Transients in Power Systems*, John Wiley & Sons, New York, 1991, ISBN 0-471-62058-0.

[24] Guilloux, C., Therme, Y., and Scarpa, P.G.: 'Measurement of the Post Arc Current of HV Circuit Breakers - Application to Short Circuit Tests with ITRV', *IEEE Transactions on Power Delivery*, Vol. 8, No. 3, July 1993, pp. 1148-1153.

[25] Haar, A.: 'Zur Theorie der Orthogonalen Funktionensysteme', *Math. Annal.*, Vol. 69, pp. 331-371, 1910. (In German)

[26] Habedank, U.: 'On the Mathematical Description of Arc Behaviour in the Vicinity of Current Zero', *etzArchiv*, Bd. 10, H. 11, pp. 339-343, 1988.

[27] Habedank, U., and Knobloch, H.: 'Procedure for the Optimization of SF_6 Circuit-Breakers', *European Transactions on Electrical Power Engineering (ETEP)*, Vol. 2, No. 5, pp. 315-320, 1992.

[28] Haupt, Michael: *Untersuchung der Anwendungsmöglichkeiten von Lichtbogenzweipolmodellen zur Beschreibung des Thermischen Schaltverhaltens von SF6-Leistungsschaltern*, Dissertation RWTH Aachen, 1988. (In German)

[29] Hermann, W., and Ragaller, K.: 'Theoretical Description of the Current Interruption in HV Gas Blast Breakers', *IEEE Transactions on Power Apparatus and Systems*, Vol. PAS-96, No. 5, September/October 1977, pp. 1546-1555.

[30] Ho, C.W, Ruehli, A.E., and Brennan, P.A.: 'The Modified Nodal Approach to Network Analysis', *IEEE Transactions on Circuits and Systems*, Vol. CAS-22, No. 6, June 1975, pp. 501-509.

[31] Hochrainer, A.: 'Study of Arcs in Breakers with the Help of a Cybernetic Model and Under the Influence of Turbulence', *CIGRE*, Report 13-10, 1972.

[32] IEC: *IEC-62271-100, High-Voltage Switchgear and Controlgear - Part 100: High-Voltage Alternating-Current Circuit-Breakers*, 2001, International Electrotechnical Commission. (Previously: *IEC-60056, High-Voltage Alternating-Current Circuit-Breakers*, 1987, International Electrotechnical Commission.)

[33] IEC: *IEC-60427, Synthetic Testing of High-Voltage Alternating Current Circuit-Breakers*, 1989, International Electrotechnical Commission. (Upcoming: *IEC-62271-101, High-Voltage Switchgear and Controlgear - Part 101: Synthetic Testing*, International Electrotechnical Commission.)

[34] Irisarri, G.D., and Sasson, A.M.: 'An Automatic Contingency Selection Method for On-Line Security Analysis', *IEEE Transactions on Power Apparatus and Systems*, Vol. PAS-100, No. 4, April 1981, pp. 1838-1844.

[35] Kertész, Viktor: *CZM User's Guide*, version 3.9, July 1999, KEMA High-Power Laboratory, Utrechtseweg 310, 6812 AR Arnhem, the Netherlands.

[36] Kezunovic, M, Aganagic, M., Bladow, J.K., and Hamai, D.M.: 'Transients Computation for Relay Testing in Real-Time', *IEEE Transactions on Power Delivery*, Vol. 9, No. 3, July 1994, pp. 1298-1307.

[37] Kim, C.H., and Aggarwal, R.: 'Wavelet Transforms in Power Systems', *Power Engineering Journal*, Vol. 14, No. 2, April 2000, pp. 81-87.

[38] Knobloch, H., and Habedank, U.: 'Arc Resistance at Current Zero: a Tool to Describe the Breaking Capacity of SF_6 Circuit-Breakers at Short-Line Faults', *Proceedings of the 11th International Symposium on High-Voltage Engineering (ISH 99)*, Vol. 3, 1999, pp. 205-208.

[39] Kreuger, Fred H.: *Industrial High Voltage, 1. Electric fields, 2. Dielectrics, 3. Constructions*, Delft University Press, 1991, ISBN 90-6275-561-5.

[40] Kuffel, R., Giesbrecht, J., Maguire, T., Wierckx, R.P., and McLaren, P.: 'RTDS - A Fully Digital Power System Simulator Operating in Real Time', *Conference Proceedings of ICDS'95*, College Station, Texas, USA, April 1995, pp. 19-24.

[41] Leon-Garcia, Alberto: *Probability and Random Processes for Electrical Engineering - Second Edition*, Addison-Wesley Publishing Company, 1994, ISBN 0-201-50037-X.

[42] Magid, Leonard M.: *Electromagnetic Fields, Energy and Waves*, John Wiley and Sons, New York, 1972, ISBN 0-471-56334-X.

[43] Mahseredjian, J., Landry, M., and Khodabakhchian, B.: 'The New EMTP Breaker Arc Model', *Proceedings of the IPST (International Conference on Power Systems Transients)*, 1997, pp. 245-249.

[44] Mathworks, The: *Power System Blockset, For Use with Simulink - User's Guide*, version 1, January 1999, The Mathworks, Inc., 24 Prime Park Way, Natick, MA 01760-1500.

[45] Mathworks, The: *Simulink, Dynamic System Simulation for MATLAB - Using Simulink*, version 3, January 1999, The Mathworks, Inc., 24 Prime Park Way, Natick, MA 01760-1500.

[46] Mathworks, The: *Wavelet Toolbox for use with MATLAB - User's Guide*, version 1, March 1996, The Mathworks, Inc., 24 Prime Park Way, Natick, MA 01760-1500.

[47] Mayr, O.: 'Beitrage zur Theorie des Statischen und des Dynamischen Lichtbogens', *Archiv für Elektrotechnik*, Band 37, Heft 12, 1943, pp. 588-608. (In German)

[48] Mayr, O.: 'Über die Theorie des Lichtbogens und seiner Löschung', *Elektrotechnische Zeitschrift*, Jahrgang 64, Heft 49/50, 16 Dezember 1943, pp. 645-652. (In German)

[49] Meirelles, M.P., and Dupont, C.J.: 'Stochastic Arc Modelling', *Seventh International Conference on Switching Arc Phenomena (SAP-93)*, September 1993, Lódz, Poland.

[50] Möller, K., Schmidt, R., and Sporckmann, B.: 'Theoretical and Experimental Investigation of the Stochastic Behavior of an SF6 Blast-Switching Arc', *IEEE Transactions on Plasma Science*, Vol. PS-8, No. 4, December 1980, pp. 352-356.

[51] Nagaoka, N., and Ametani, A.: 'A Development of a Generalized Frequency-Domain Transient Program - FTP', *IEEE Transactions on Power Delivery*, Vol. 3, No. 4, October 1988, pp. 1996-2004.

[52] Nakanishi, Kunio (editor): *Switching Phenomena in High-Voltage Circuit Breakers*, Marcel Dekker, New York, 1991, ISBN 0-8247-8543-6.

[53] Paul, Clayton R.: *Introduction to Electromagnetic Compatibility*, John Wiley & Sons, New York, 1992, ISBN 0-471-54927-4.

[54] Paul, K.C., Sakuta, T., and Takashima, T.: 'Transport and Thermodynamic Properties of SF_6 Gas Contaminated by PTFE Reinforced with Al_2O_3 and BN Particles', *IEEE Transactions on Plasma Science*, Vol. 25, No. 4, August 1997, pp. 786-798.

[55] Pettinga, J.A.J., and Siersema, J.: 'A Polyphase 500kA Current Measuring System with Rogowski Coils', *IEE Proceedings*, Vol. 130, Pt. B, No. 5, September 1983, pp. 360-363.

[56] Phaniraj, V., and Phadke, A.G.: 'Modelling of Circuit-Breakers in the Electromagnetic Transients Program', *IEEE Proceedings on Power Industry Computer Applications (PICA)*, 1987, pp. 476-482.

[57] Portela, C., Dupont, C., and Meirelles, M.P.: 'Deterministic and Statistic Arc Modelling', *CIGRE*, 13-107, 1994.

[58] Ragaller, K., Plessl, A., Hermann, W., and Egli, W.: 'Calculation Methods for the Arc Quenching System of Gas Circuit Breakers', *CIGRE*, Report 13-03, 1984.

[59] Reid, W.E.: 'Effect of Transient Recovery Voltage (TRV) on Power Circuit Interruption', *IEEE Seminar/Report Power System Transient Recovery Voltages - Chapter 1*, 87TH0176-8-PWR, 1987, pp. 5-14.

[60] Rieder, W., and Kuhn, H.D.: 'Bedeutung und Schwierigkeiten der sogenannten «Nachstrom»-Messungen', *Schweizerisches Technische Zeitschrift (STZ)*, Nr. 29/30, July 1961, pp. 609-619. (In German)

[61] Robertson, D.C., Camps, O.I., Mayer, J.S., and Gish, W.B.: 'Wavelets and Electromagnetic Power System Transients', *IEEE Transactions on Power Delivery*, Vol. 11, No. 2, April 1996, pp. 1050-1058.

[62] Rothardt, L.: 'Stochastische Modellierung des Schaltlichtbogens', *Elektrie*, Berlin 38, 2, 1984, pp. 57-59. (In German)

[63] Rüdenberg, Reinholdt: *Elektrische Schaltvorgänge*, Springer-Verlag, New York, 1974, ISBN 3-540-05766-8. (In German)

[64] Rutgers, W.R., Hulshof, H.J.M., Laurensse, I.J., and Van der Wey, A.H.: 'Optical Sensors for the Measurement of Electric Current and Voltage', *KEMA Scientific & Technical Reports*, Vol. 5, No. 11, 1987, pp. 281-292.

[65] Saha, M.N.: 'Ionization in the Solar Chromosphere', *Phil. Mag.*, S. 6, Vol. 40, No. 238, October 1920, pp. 472-488.

[66] Santos, J.C., Taplamacioglu, M.C., and Hidaka, K.: 'Pockels High-Voltage Measurement System', *IEEE Transactions on Power Delivery*, Vol. 15, No. 1, January 2000, pp. 8-13.

[67] Schavemaker, P.H., and Van der Sluis, L.: 'The Influence of the Topology of Test Circuits on the Interrupting Performance of Circuit Breakers', *IEEE Transactions on Power Delivery*, Vol. 10, No. 4, October 1995, pp. 1822-1828.

[68] Schavemaker, P.H., and Van der Sluis, L.: 'Berekenen van Transiënten', *Energietechniek*, Vol. 76, No. 7/8, July/August 1998, pp. 418-421. (In Dutch)

[69] Schavemaker, P.H., and Van der Sluis, L.: 'Theorie achter XTrans', *Energietechniek*, Vol. 76, No. 9, September 1998, pp. 498-500. (In Dutch)

[70] Schavemaker, P.H., and Van der Sluis, L.: 'Werken met XTrans', *Energietechniek*, Vol. 76, No. 10, October 1998, pp. 576-579. (In Dutch)

[71] Schavemaker, P.H., De Lange, A.J.P., and Van der Sluis, L.: 'A Comparison between Three Tools for Electrical Transient Computations', *Proceedings of the IPST (International Conference on Power Systems Transients)*, June 20-24, 1999, Budapest, Hungary, pp. 13-18.

[72] Schavemaker, P.H., Van der Sluis, L., Smeets, R.P.P., and Kertész, V.: 'Digital Testing of High-Voltage Circuit Breakers', *IEEE Computer Applications in Power*, Vol. 13, No. 2, April 2000, pp. 52-56.

[73] Schavemaker, P.H., and Van der Sluis, L.: 'An Improved Mayr-Type Arc Model Based on Current-Zero Measurements', *IEEE Transactions on Power Delivery*, Vol. 15, No. 2, April 2000, pp. 580-584.

[74] Schavemaker, P.H., De Lange, A.J.P., and Van der Sluis, L.: 'Circuit Breaker Arc Model Computations for Critical Line Length Determination', *Proceedings of the PowerCon2000 (International Conference on Power System Technology)*, December 4-7, 2000, Perth, Australia, pp. 915-920.

[75] Schavemaker, P.H., Van der Sluis, L., Smeets, R.P.P., and Kertész, V.: 'Vermogenschakelaars Digitaal Beproefd', *Energietechniek*, No. 3, Jaargang 79, Maart 2001, pp. 132-135. (In Dutch)

[76] Schavemaker, P.H., Van der Sluis, L., and Pharmatrisanti, A.: 'Post-Arc Current Reconstruction Based on Actual Circuit Breaker Measurements', *IEE Proc.-Sci. Meas. Technol.*, Vol. 149, No. 1, January 2002, pp. 17-21.

[77] Schavemaker, P.H., and Van der Sluis, L.: 'The Arc Model Blockset', *Proceedings of the Second IASTED International Conference POWER AND ENERGY SYSTEMS (EuroPES)*, June 25-28, 2002, Crete, Greece, pp. 644-648.

[78] Schavemaker, P.H., and Van der Sluis, L.: 'A Statistical Arc Model for Digital Testing of Circuit Breakers', *Proceedings of the Second IASTED International Conference POWER AND ENERGY SYSTEMS (EuroPES)*, June 25-28, 2002, Crete, Greece, pp. 655-660.

[79] Schavemaker, P.H., and Van der Sluis, L.: 'Quantification of the Interrupting Performance of High-Voltage Circuit Breakers', *IEE Proc.-Sci. Meas. Technol.*, Vol. 149, No. 4, July 2002, pp. 153-157.

[80] Schmidt, George: *Physics of High Temperature Plasmas - an Introduction*, Academic Press, New York, 1966.

[81] Schwarz, J.: 'Dynamisches Verhalten eines Gasbeblasenen, Turbulenzbestimmten Schaltlichtbogens', *ETZ-A*, Bd. 92 (1971), pp. 389-391. (In German)

[82] Shampine, F.S, and Reichelt, M.W.: 'The Matlab ODE Suite', *SIAM Journal on Scientific Computing*, Vol. 18, No. 1, January 1997, pp. 1-22.

[83] Sheskin, David J.: *Handbook of Parametric and Nonparametric Statistical Procedures*, CRC Press, 1997, ISBN 0-8493-3119-6.

[84] Smeets, R.P.P., Even, A., Habedank, U., Kertész, V., Neumann, C., Scarpa, P., and Van der Sluis, L.: 'Progress Towards 'Digital Testing', a Novel Additional Tool to Investigate the Performance of HV Circuit Breakers for the Benefit of Utility, Manufacturer and Standardizing Body', *CIGRE*, Report 13-107, 1998.

[85] Smeets, R.P.P., Eenink, A.H., and Kertész, V.: 'A New High-Resolution High-Frequency Current-Zero Measuring System', *Proceedings of the ERA Conference on High Voltage Measurement and Calibration*, 1998, pp. 1.2.1-1.2.12.

[86] Smeets, R.P.P., and Kertész, V.: 'Evaluation of High-Voltage Circuit Breaker Performance with a New Validated Arc Model', *IEE Proc.-Gener. Transm. Distrib.*, Vol. 147, No. 2, March 2000, pp. 121-125.

[87] Sporckmann, B.: 'Ein Stochastisches Lichtbogenmodell zur Berechnung von Ausschaltvorgängen von Hochspannungsleistungsschaltern', *ETZ-A*, Bd. 99, H. 12, 1978, pp. 758-759. (In German)

[88] Sporckmann, Bernd: *Ein Stochastisches Lichtbogenmodell zur Berechnung der Versagerwahrscheinlichkeit von Hochspannungsleistungsschaltern beim Unterbrechen von Kurzschlußströmen*, Dissertation RWTH Aachen, 1981. (In German)

[89] Sporckmann, B.: 'Ein Stochastisches Lichtbogenmodell zur Berechnung der Versagerwahrscheinlichkeit von Hochspannungsleistungsschaltern bei Kurzschlußausschaltungen', *ETZ-Archiv*, Bd. 5, H. 11, 1983, pp. 347-351. (In German)

[90] Sporckmann, B.: 'Auswerteverfahren zur Bestimmung der Kenngrößen Phänomenologischer Lichtbogenmodelle', *Archiv für Elektrotechnik*, 66, 1983, pp. 135-141. (In German)

[91] St-Jean, G., and Landry, M.: 'Comparison of Waveshape Quality of Artificial Lines used for Short-Line Fault Breaking Tests on HV Circuit Breakers', *IEEE Transactions on Power Delivery*, Vol. 4, No. 4, October 1989, pp. 2109-2113.

[92] Steel, J.G., and Swift-Hook, D.T.: 'Statistics of Circuit-Breaker Performance', *Proceeding of the IEE*, Vol. 117, No. 7, July 1970, pp. 1337-1345.

[93] Strang, Gilbert: '*Linear Algebra and its Applications*', Harcourt Brace Jovanovich, San Diego, ISBN 0-15-551005-3.

[94] Sybille, G., Brunelle, P., Le-Huy, H., Dessaint, L.A., and Al-Haddad, K.: 'Theory and Applications of Power System Blockset, a MATLAB/Simulink-Based Simulation Tool for Power Systems', *IEEE Winter Meeting*, Singapore, January 23-27, 2000.

[95] Thorén, B.: 'Short-Line Faults', *Elteknik*, 9, No. 2, February 1966, pp. 25-33.

[96] Van der Linden, W.A., and Van der Sluis, L.: 'A New Artificial Line for Testing High-Voltage Circuit Breakers', *IEEE Transactions on Power Apparatus and Systems*, Vol. PAS-102, No. 4, April 1983, pp. 797-804.

[97] Van der Sluis, L.: 'A Network Independent Computer Program for the Computation of Electrical Transients', *IEEE Transactions on Power Delivery*, Vol. PWRD-2, No. 3, July 1987, pp. 779-784.

[98] Van der Sluis, L., Damstra, G.C., Kempen, H.W., and Van der Linden, W.A.: 'Synthetic Test Methods: Experience and Future Developments', *CIGRE*, Report 13-203, 1992.

[99] Van der Sluis, Lou: *Transients in Power Systems*, John Wiley & Sons, Chichester, 2001, ISBN 0-471-48639-6.

[100] Vermij, L., and Ter Horst, D. Th. J.: 'Considerations Regarding Switching Arc Phenomena', *Holectechniek*, No. 2, 1972, pp. 77-92.

[101] W.G. 13.01: 'Practical Application of Arc Physics in Circuit Breakers. Survey of Calculation Methods and Application Guide', *Electra*, No. 118, 1988, pp. 65-79.

[102] W.G. 13.01: 'Applications of Black Box Modelling to Circuit Breakers', *Electra*, No. 149, August 1993, pp. 41-71.

[103] Widl, W., Kirchesch, P., and Egli, W.: 'Use of Integral Arc Models in Circuit Breaker Testing and Development', *IEEE Transactions on Power Delivery*, Vol. 3, No. 4, October 1988, pp. 1685-1691.

[104] Yonezawa, T., Sugiyama, T., and Hidaka, M.: 'Development of a 1,000kV SF_6 Gas Circuit Breaker', *Mitsubishi Electric Advance*, Vol. 77, Dec. 1996, pp. 10-13.

[105] Zückler, K.: 'Untersuchungen zum Dynamischen Verhalten von Schalterlichtbögen', *ETZ-A*, Bd. 99 (1978) H. 9, pp. 546-548. (In German)

List of Abbreviations

AC	Alternating Current
ANSI	American National Standards Institute
ATP	Alternative Transient Program
BDF	Backward Differentiation Formula
CB	Circuit Breaker
CDF	Cumulative Distribution Function
CT	Current Transformer
CWT	Continuous Wavelet Transform
DAE	Differential Algebraic Equation
DB	Daubechies (type of wavelet)
DC	Direct Current
DEE	Differential Equation Editor
DFT	Discrete Fourier Transform
DWT	Discrete Wavelet Transform
EC	European Commission
EDF	Empirical Distribution Function
EM	Electro Magnetic
EMC	Electro Magnetic Compatibility
EMF	ElectroMotive Force
EMI	Electro Magnetic Interference
EMTP	Electro Magnetic Transient Program
EU	European Union
FT	Fourier Transform
FTP	Frequency-domain Transient Program
HV	High Voltage
IEC	International Electrotechnical Commission
IEEE	Institute of Electrical and Electronics Engineers
KCL	Kirchoff Current Law
MNA	Modified Nodal Analysis
NA	Nodal Analysis
NDF	Numerical Differentiation Formula

NMSE	Normalized Mean-Square Error
ODE	Ordinary Differential Equation
PSB	Power System Blockset
RMS	Root Mean Square
RTDS	Real Time Digital Simulator
SF_6	Sulfur hexafluoride
SLF	Short Line Fault
STFT	Short-Time Fourier Transform
TNA	Transient Network Analyzer
TRV	Transient Recovery Voltage
WDFT	Windowed Discrete Fourier Transform

List of Figures

List of Tables

Acknowledgements

First of all, I would like to thank Prof. ir. Lou van der Sluis for his effort, enthusiasm and support during this Ph.D. work. I am indebted to all my colleagues of the Power Systems Laboratory and especially to Dr. ir. Adriaan de Lange: we had and have great discussions on this topic.

Furthermore, I would like to thank Prof. dr. ir. René Smeets of the KEMA High-Power Laboratory for his healthy criticism and appreciated discussions.

I am grateful to Dr. Hartmut Knobloch and Dr. Ulrich Habedank for the possibility offered to work at the Siemens Switchgear Works in Berlin, Germany, for two months.

I would like to thank all the partners within the EU project for their valuable contributions and pleasant cooperation:

- KEMA: René Smeets, Viktor Kertész, Roel Mikx and Ewald van Dorst
- Siemens AG: Hartmut Knobloch and Ulrich Habedank
- RWE Energie: Claus Neumann, Burkhard Krampe, Mr. Luhmann and Mr. Huhsemann
- Laborelec cv.: Andre Even, Mr. Moulaert, Patrick Scarpa (ULG) and Mrs. Defays (ULG)

I am indebted to Mrs. Anita Pharmatrisanti and Mr. Foek Chin-Joe, who graduated on topics discussed in this thesis, for their valuable contributions to this work.

Dr. H.P. Lopuhaä of the Control, Risk, Optimization, Systems and Stochastics (CROSS) department of the Delft University of Technology is thanked for his valuable comments on the material described in section 4.5.1.

Prof. dr. ir. R.L. Lagendijk of the Mediamatics (MM) department of the Delft University of Technology is thanked for his valuable comments on the material described in section 3.6.

Curriculum Vitae

Pieter H. Schavemaker was born on November 30, 1970, in Velsen (the Netherlands). After having finished secondary school in Velsen in 1989, he studied electrical engineering at the Delft University of Technology. He graduated 'cum laude' from the Electrical Power Systems group in 1994. After graduation, he performed research on power system state estimation at the Electrical Power Systems group for one year. In 1995, he started as an application engineer at ABB in The Netherlands. He did projects on Substation Control Systems, involving functional and detailed design descriptions, engineering, the factory acceptance test, operator training, installation and the sight acceptance test.

Since 1996 he has been with the Electrical Power Systems group where he is currently assistant professor. He started working on 'digital testing of high-voltage circuit breakers' within the framework of a European project. The results of this research are described in this Ph.D. thesis. In 1999, he performed research at the Siemens Switchgear Works in Berlin Germany, for two months.

As an assistant professor, he is/was involved with the following courses:

- Power systems
- Power system analysis I
- Transient phenomena in power systems
- Linear algebra
- Integrated design project

Furthermore, he co-taught in several post-academic courses, such as:

- Planning, design and operation of electric networks
- Stationary network analysis - from modeling to loadflow
- Power circuit breakers in electrical power systems

Appendix: Test circuits and measurement data

A.1 Circuit breaker cb1: 245 kV, 50 kA, 50 Hz, SF_6 puffer

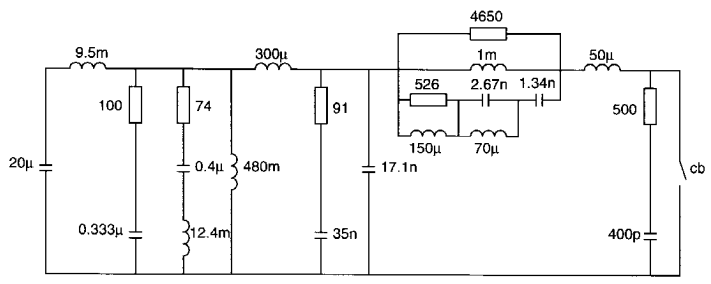

Figure A-1. Synthetic SLF test circuit, cb1

During these tests, a 10 MHz measurement system was used.

Table A-1. Test data of cb1

measurement	pole	$(di/dt)_0$ [A/µs]	arcing time [ms]	I(nterruption) R(eignition)
4005	A	20.5	10.4	I
4006	A	20.5	9.5	R
4008	A	20.5	19.8	I
4009	A	20.5	15	I
4010	A	20.5	12.5	R
4011	A	20.5	17.6	I
4012	A	20.5	22.6	I

Table A-1. Test data of cb1 (Continued)

measurement	pole	$(di/dt)_0$ [A/µs]	arcing time [ms]	I(nterruption) R(eignition)
4013	A	20.5	13.7	I
4017	B	21.3	11.2	I
4020	B	21.3	14.1	I
4022	B	19.5	12.5	I
4023	B	19.5	17.8	I
4024	B	19.5	15.9	I

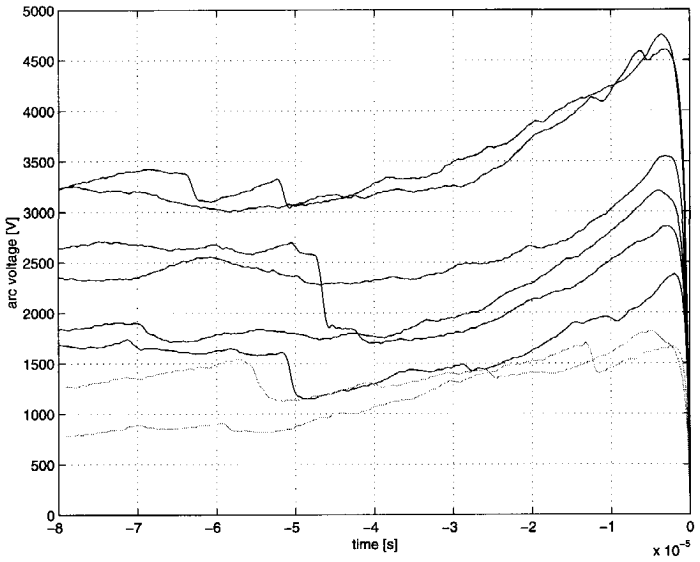

Figure A-2. Arc voltages of pole A, cb1 (last 80 µs)
black: interruptions, grey: reignitions

Figure A-2 and A-3 show the measured arc voltages in the last 80 µs before current zero for pole A and B of the circuit breaker, respectively. The current traces of the reignitions from -0.5 µs to 1.5 µs around current zero for pole A of the circuit breaker are shown in figure A-4. Pole B did not reignite.

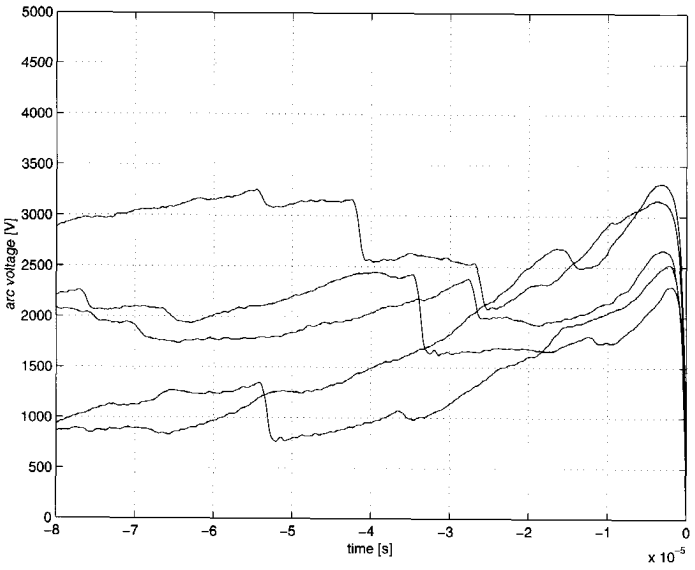

Figure A-3. Arc voltages of pole B, cb1 (last 80 μs)
black: interruptions

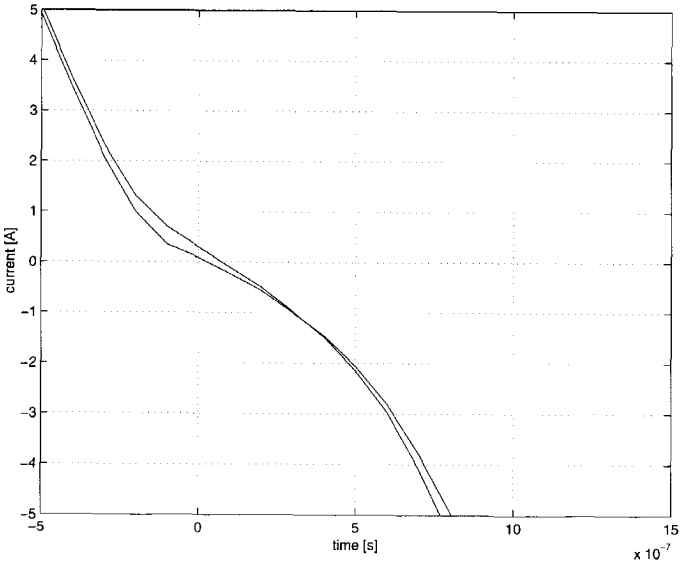

Figure A-4. Current traces of the reignitions of pole A, cb1 (from -0.5 μs to 1.5 μs)

A.2 Circuit breaker cb2: 72.5 kV, 31.5 kA, 60 Hz, SF_6 puffer

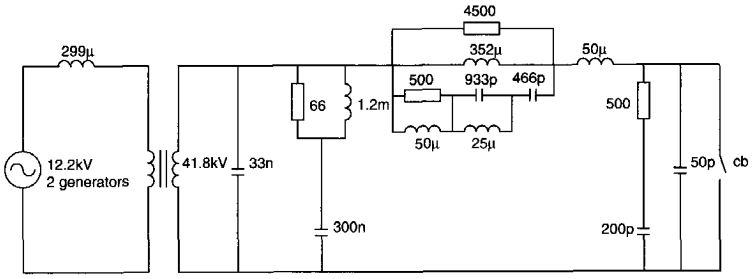

Figure A-5. Direct SLF test circuit, cb2

During these tests, a 40 MHz measurement system was used.

Table A-2. Test data of cb2

measurement	pole	$(di/dt)_0$ [A/µs]	arcing time [ms]	I(nterruption) R(eignition)
5021	A	10.3	12	I
5022	A	15	13.3	I
5023	A	13.5	10.4	I
5024	A	14.3	16	I
5025	A	14	24.4	I
5026	A	13.7		R
5027	A	11.3		R
5028	B	11.8	15.9	I
5030	B	12	15.6	I
5031	B	11.8	15.6	I
5032	B	11.9	16	I
5033	B	11.9	14.9	I
5034	B	11.9		R
5035	C	9.4	14	I
5036	C	9.4	13.8	I
5037	C	9.1	13.3	I
5038	C	9.5	13	I
5039	C	9.4	12.1	I
5040	C	9.4	12.3	I

Table A-2. Test data of cb2 (Continued)

measurement	pole	$(di/dt)_0$ [A/µs]	arcing time [ms]	I(nterruption) R(eignition)
5041	C	9.2	11.3	I
5042	C	9.3	11.4	I
5043	C	9.1	10.1	I
5044	C	9.2	10.6	I
5045	C	8.8	18.1	I
5046	C	9	18	I
5047	C	9.1	24.6	I
5048	C	9.1		R

= 'post-arc current' observed

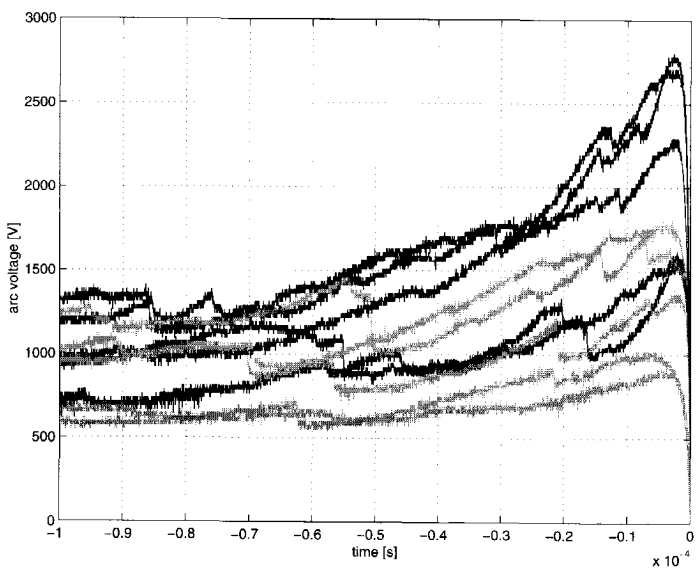

Figure A-6. Arc voltages of pole A, cb2 (last 100 µs)
black: interruptions, grey: reignitions

Figure A-6, A-7, and A-8 show the measured arc voltages in the last 100 µs before current zero for the three poles of the circuit breaker, respectively. The current traces of the reignitions from -0.5 µs to 1.5 µs around current zero for the three poles of the circuit breaker are shown in figure A-9, figure A-10 and figure A-11, respectively.

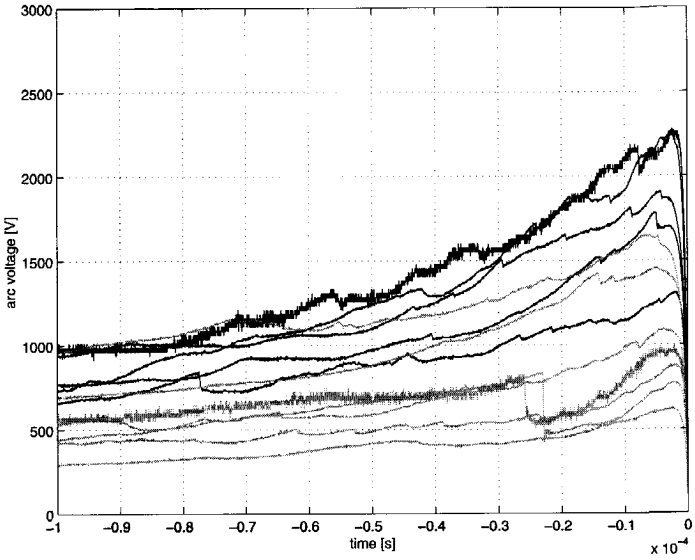

Figure A-7. Arc voltages of pole B, cb2 (last 100 μs)
black: interruptions, grey: reignitions

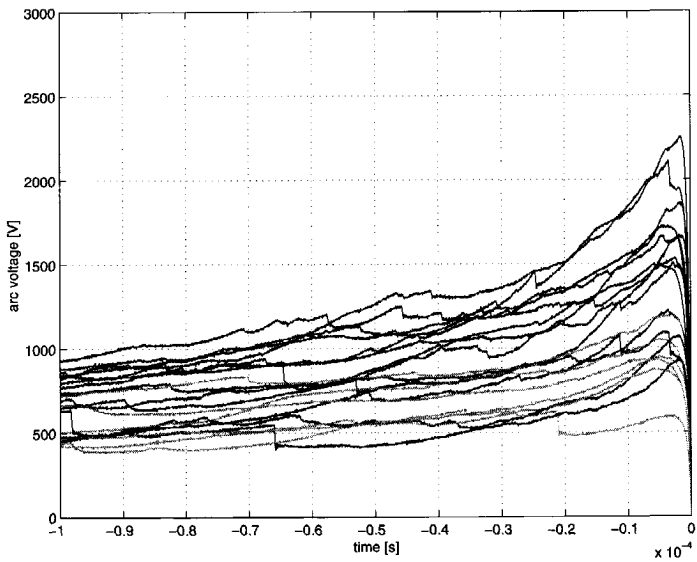

Figure A-8. Arc voltages of pole C, cb2 (last 100 μs)
black: interruptions, grey: reignitions

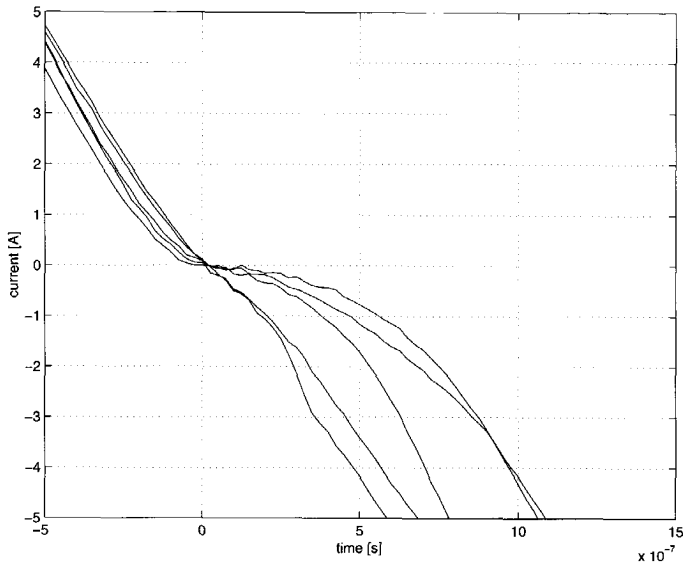

Figure A-9. Current traces of the reignitions of pole A, cb2 (from -0.5 μs to 1.5 μs)

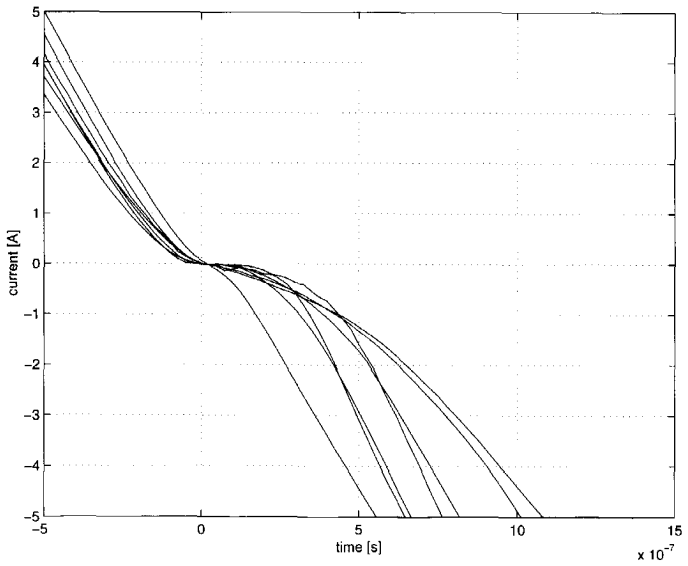

Figure A-10. Current traces of the reignitions of pole B, cb2 (from -0.5 μs to 1.5 μs)

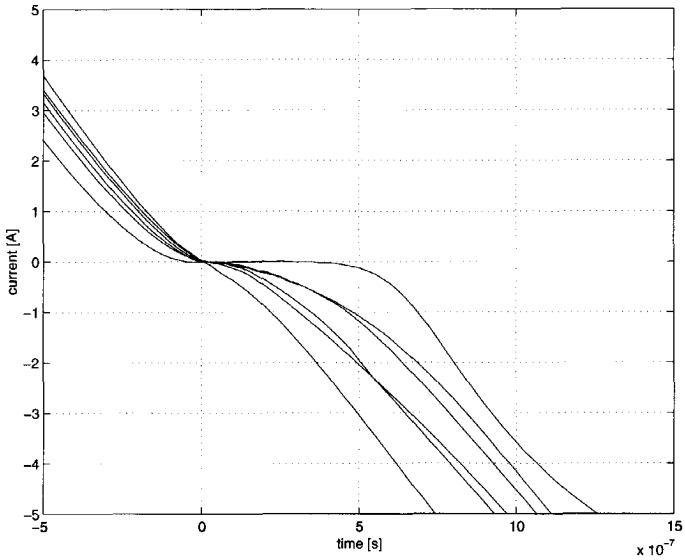

Figure A-11. Current traces of the reignitions of pole C, cb2 (from -0.5 μs to 1.5 μs)

A.3 Circuit breaker cb3: 145 kV, 31.5 kA, 60 Hz, SF_6 puffer

A.3.1 Circuit breaker cb3: direct SLF test

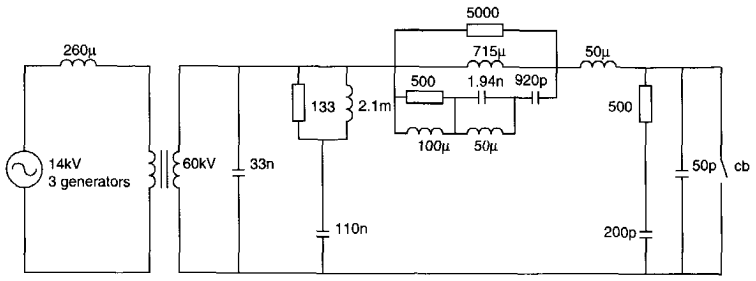

Figure A-12. Direct SLF test circuit, cb3

During these tests, a 40 MHz measurement system was used.

Table A-3. Direct test data of cb3

measurement	pole	$(di/dt)_0$ [A/µs]	arcing time [ms]	I(nterruption) R(eignition)
5006	A	14.6	11.9	I
5007	A	15.2	9.5	I
5008	A	14.9	16.1	I
5009	A	14.4	16.1	I
5010	A	14.2	16.1	I
5011	A	14.1	16.1	I
5012	A	14	16.1	I
5013	A	14	15	I
5014	A	14	13.9	I
5015	A	14	13	I
5016	A	14.1	12.1	I
5017	A	14.1	11.1	I
5018	A	14.2	10	I
5019	A	14	9	I
5020	A	14.2	16.4	I
5021	A	14.1	8.1	I
5022	A	14.2	15.5	I

Table A-3. Direct test data of cb3 (Continued)

measurement	pole	$(di/dt)_0$ [A/µs]	arcing time [ms]	I(nterruption) R(eignition)
5023	A	14	15.5	I
5024	A	14.1	15.3	I
5025	A	14.1	15.4	I
5026	A	14.2	15.4	I
5027	A	14.2	15.4	I
5028	A	14.2	15.5	I
5029	A	14.2	7	I
5030	A	14.2		R

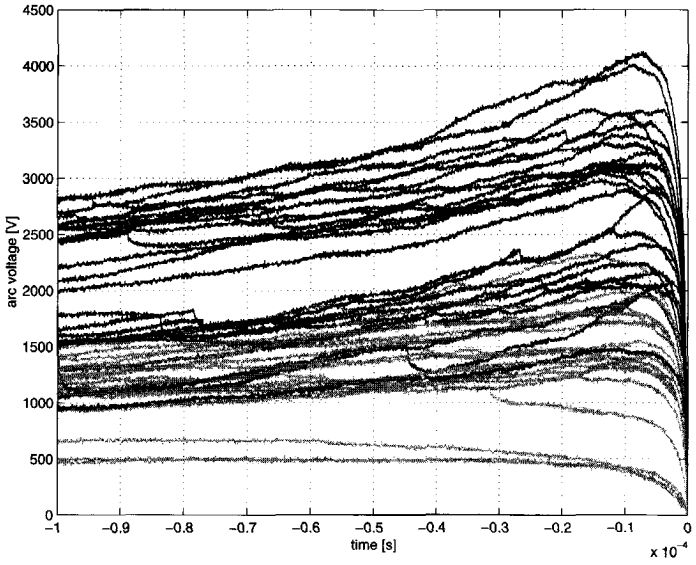

Figure A-13. Arc voltages of pole A, cb3 (last 100 µs)
black: interruptions, grey: reignitions

Figure A-13 shows the measured arc voltages in the last 100 µs before current zero for pole A of the circuit breaker. The current traces of the reignitions from -0.5 µs to 1.5 µs around current zero for pole A of the circuit breaker are shown in figure A-14.

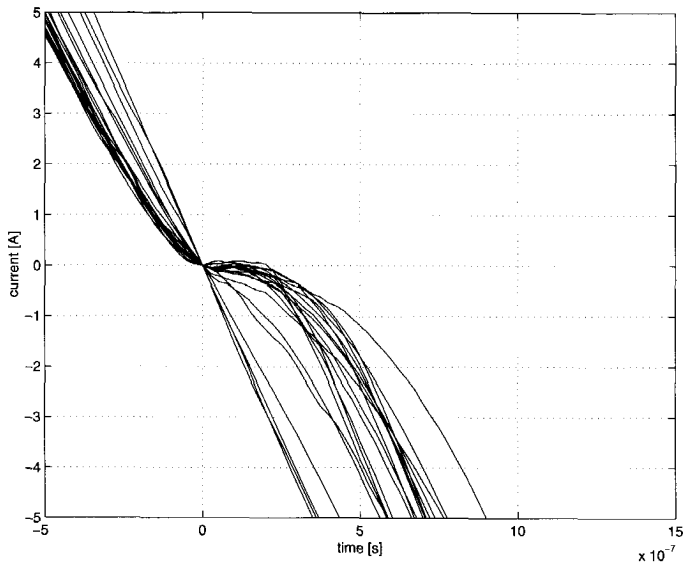

Figure A-14. Current traces of the reignitions of pole A, cb3 (from -0.5 μs to 1.5 μs)

A.3.2 Circuit breaker cb3: synthetic SLF test

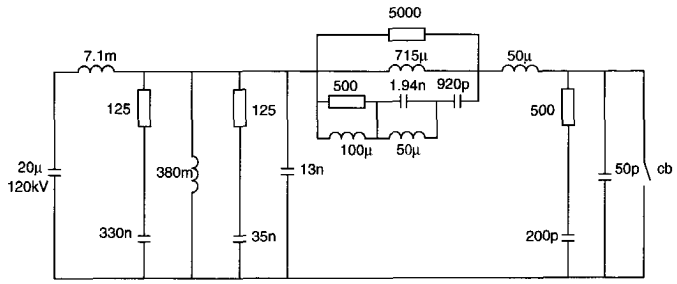

Figure A-15. Synthetic SLF test circuit, cb3

During these tests, a 40 MHz measurement system was used.

Table A-4. Synthetic test data of cb3

measurement	pole	$(di/dt)_0$ [A/µs]	arcing time [ms]	I(nterruption) R(eignition)
5104	B	14.2	12	I
5105	B	14.2	10.9	I
5106	B	14.2	10.1	I
5107	B	14.2	9.1	I
5109	B	14.2	set for 8.2	R
5110	B	14.2	set for 8.2	R
5111	B	14.2	set for 8.2	R
5112	B	14.2	9	I
5113	B	14.2	set for 9	R
5114	B	14.2	8.9	I
5115	B	14.2	set for 8.9	R
5116	B	14.2	16.5	I
5117	B	14.2	16.5	I
5118	B	14.2	16.5	I
5119	B	14.2	16.5	I
5120	B	14	16.5	I
5121	B	14	15.4	I
5122	B	14	14.5	I
5123	B	14	13.5	I

Table A-4. Synthetic test data of cb3 (Continued)

measurement	pole	$(di/dt)_0$ [A/µs]	arcing time [ms]	I(nterruption) R(eignition)
5124	B	14	12.6	I
5125	B	14	11.6	I
5126	B	14	10.5	I
5127	B	14	9.7	I
5128	B	14	9.7	I
5129	B	14	8.6	I
5130	B	14	set for 7.6	R

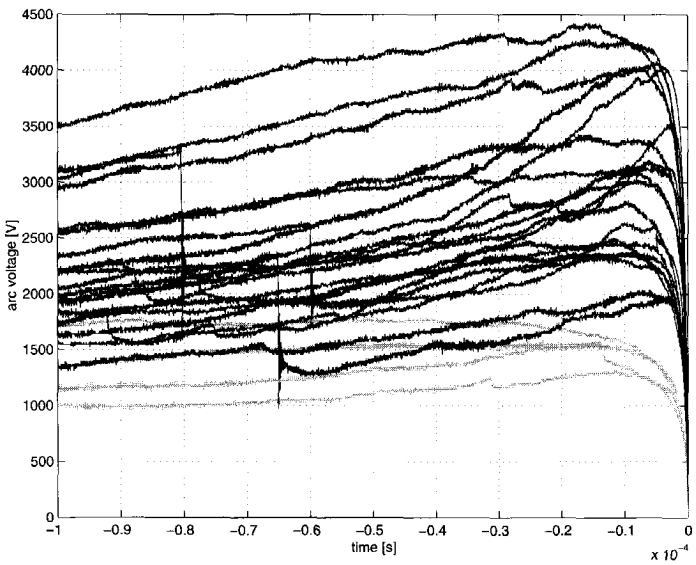

Figure A-16. Arc voltages of pole B, cb3 (last 100 µs)
black: interruptions, grey: reignitions

Figure A-16 shows the measured arc voltages in the last 100 µs before current zero for pole B of the circuit breaker. The current traces of the reignitions from -0.5 µs to 1.5 µs around current zero for pole B of the circuit breaker are shown in figure A-17.

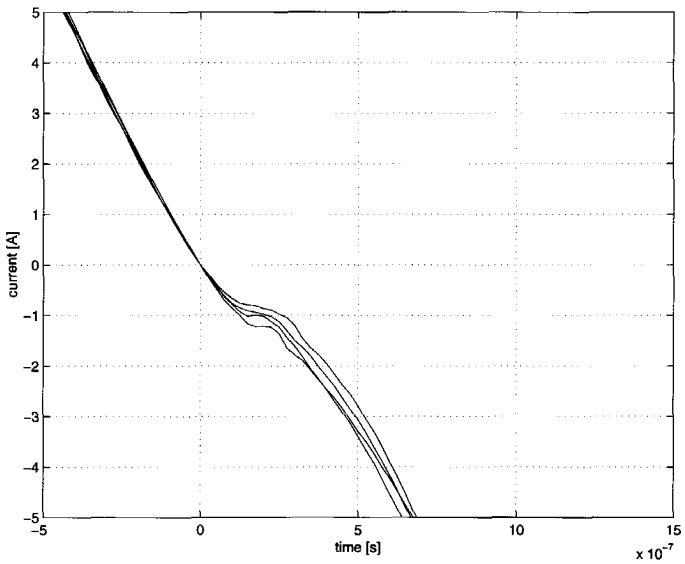

Figure A-17. Current traces of the reignitions of pole B, cb3 (from -0.5 μs to 1.5 μs)

A.4 Circuit breaker cb4: 123 kV, 31.5 kA, 60 Hz, SF_6 selfblast

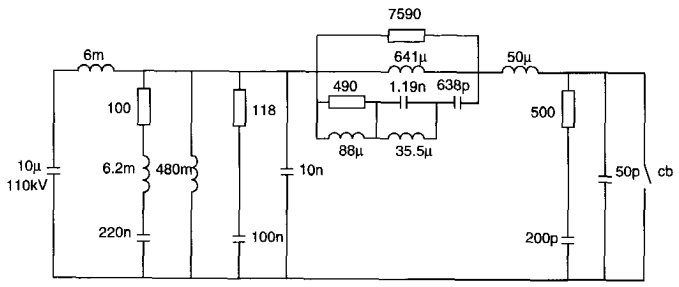

Figure A-18. Synthetic SLF test circuit, cb4

During these tests, a 40 MHz measurement system was used.

Table A-5. Test data of cb4

measurement	pole	$(di/dt)_0$ [A/µs]	arcing time [ms]	I(nterruption) R(eignition)
5011	A	15.1	18	I
5012	A	15.1	18	R
5013	A	15.1	18.2	I
5014	A	15.2	18.1	I
5015	A	15.1	18.2	R
5016	A	15.1	18	I
5017	A	15.1	18.3	I
5019	A	15.1	18.2	I
5020	A	15.1	18.2	I
5021	A	15.1	18	R
5022	A	15.2	18	R
5024	B	7.6	17.2	I
5025	B	7.7	17.4	I
5026	B	7.7	17.4	I
5027	B	10.7	17.7	I
5028	B	10.7	17.6	I
5029	B	10.7	17.6	I
5030	B	15.2	18.3	I
5031	B	15.1	18.2	I

Table A-5. Test data of cb4 (Continued)

measurement	pole	$(di/dt)_0$ [A/µs]	arcing time [ms]	I(nterruption) R(eignition)
5032	B	15.1	18.2	I
5033	B	16.6	18.2	R
5034	B	16.6	18.5	I
5036	C	15.1	17.9	I
5037	C	15.1	18.2	I
5038	C	15.1	18.2	I
5039	C	18.1	18.3	I
5040	C	18.1	18	I
5041	C	18.2	18.1	I
5042	C	18.2	14.2	R
5043	C	18.1	21.9	R
5044	C	15.1	17.7	I

Figure A-19, A-20, and A-21 show the measured arc voltages in the last 100 µs before current zero for the three poles of the circuit breaker, respectively. The current traces of the reignitions from -0.5 µs to 1.5 µs around current zero for the three poles of the circuit breaker are shown in figure A-22, figure A-23 and figure A-24, respectively.

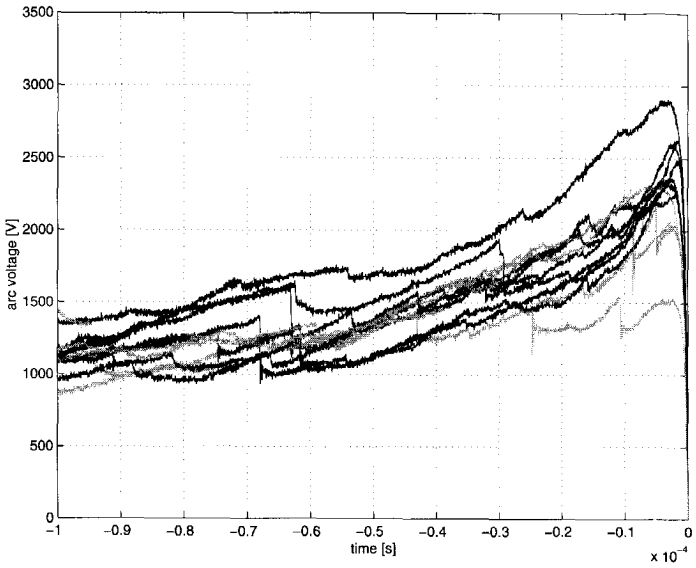

Figure A-19. Arc voltages of pole A, cb4 (last 100 μs)
black: interruptions, grey: reignitions

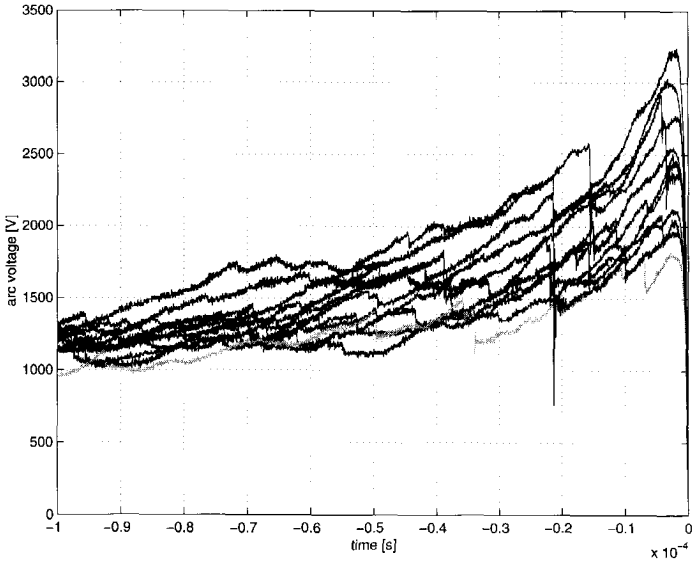

Figure A-20. Arc voltages of pole B, cb4 (last 100 μs)
black: interruptions, grey: reignitions

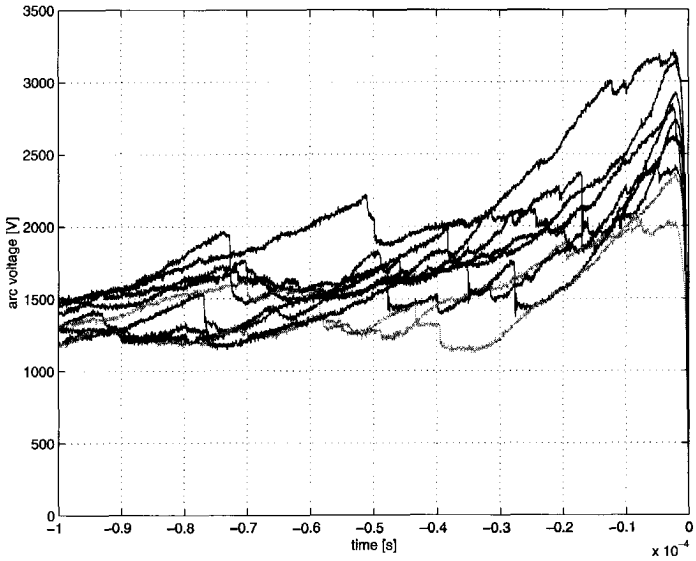

Figure A-21. Arc voltages of pole C, cb4 (last 100 μs)
black: interruptions, grey: reignitions

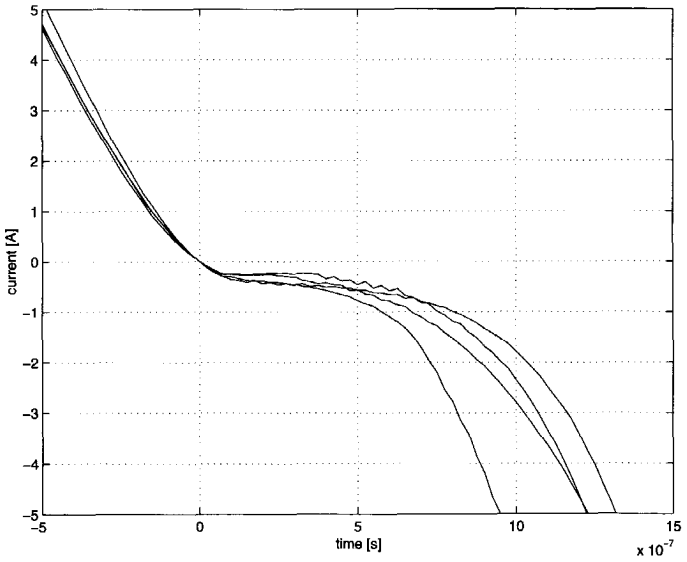

Figure A-22. Current traces of the reignitions of pole A, cb4 (from -0.5 μs to 1.5 μs)

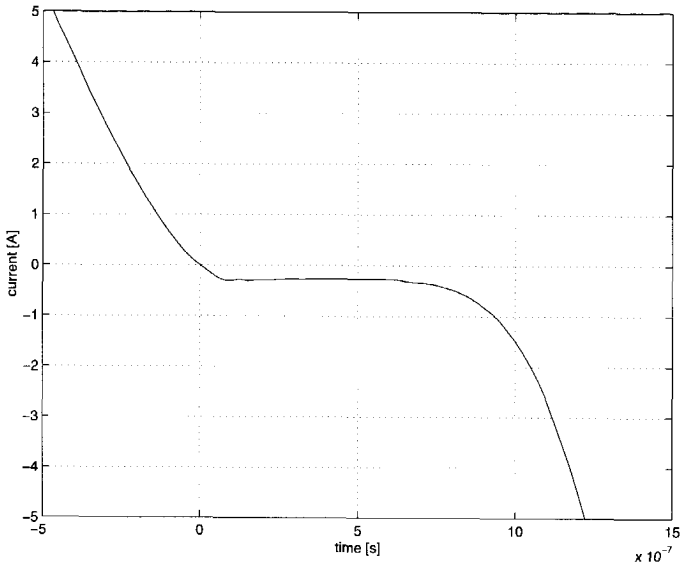

Figure A-23. Current traces of the reignitions of pole B, cb4 (from -0.5 μs to 1.5 μs)

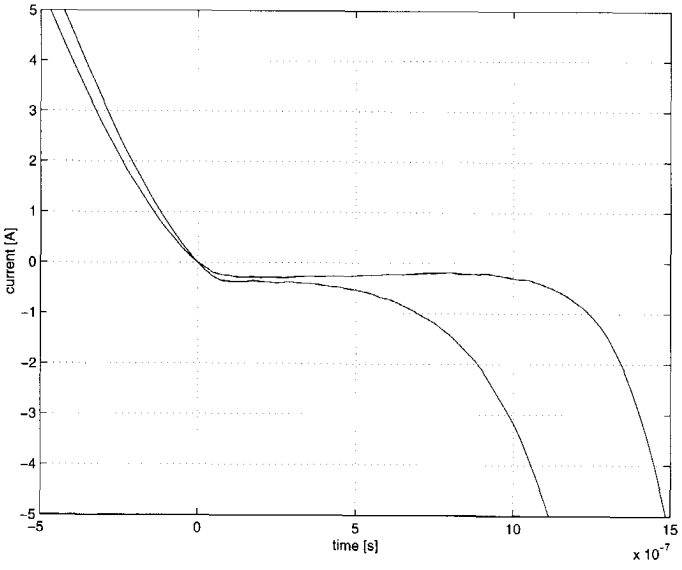

Figure A-24. Current traces of the reignitions of pole C, cb4 (from -0.5 μs to 1.5 μs)